UNIVERSITY OF CALIFORNIA
SANTA CRUZ

EXCITED-STATE DYNAMICS IN SOLID-STATE SPIN DEFECTS AND SPIN DYNAMICS OF CARRIERS IN SOLIDS FROM FIRST-PRINCIPLES

A dissertation submitted in partial satisfaction of the
requirements for the degree of

DOCTOR OF PHILOSOPHY

in

PHYSICS

by

Kejun Li

September 2024

The Dissertation of Kejun Li
is approved:

Professor Jairo Velasco Jr., Chair

Professor Aiming Yan

Professor Yuan Ping

Peter F. Biehl
Vice Provost and Dean of Graduate Studies

Table of Contents

List of Figures

List of Tables

Abstract

Excited-State Dynamics in Solid-State Spin Defects and Spin Dynamics of Carriers in Solids from First-Principles

by

Kejun Li

The spin degree of freedom can be controlled in systems of solid-state spin defects or via the spin of carriers in solids. To achieve effective control, it requires in-depth understanding of the excited-state dynamics in spin defects, and the mechanisms by which carrier spin relaxes and dephases in solids. This thesis presents the development and application of advanced first-principles methods that accurately describe the electronic structures and interaction processes, providing a comprehensive understanding of excited-state dynamics.

For the solid-state spin defects, the challenges include identifying the chemical structure of spin defects and predicting their spin-dependent photoluminescence (PL) contrast. Regarding the defect identification, we use the density functional theory (DFT) and many-body perturbation theory to calculate a complete set of static and dynamical properties of spin defects, including exciton-defect coupling and electron-phonon coupling. We demonstrate that certain spin defects candidates that can explain experimental observations. For predicting the spin-dependent PL contrast, we develop and implement the first-principles optically-detected magnetic resonance (ODMR). We show the prediction of spin-orbit coupling (SOC) and intersystem-crossing (ISC) with

multi-reference electronic states. With this first-principles tool and accurate description of the excited-state dynamics, we achieve accurate prediction of the ODMR of spin defects.

For the spin of carriers in solids, understanding the mechanisms of spin dynamics and the intrinsic properties of solids requires accurate simulation of spin lifetimes (τ_s) for spin relaxation and dephasing. We utilize our developed first-principles real-time density-matrix (FPDM) approach to simulate spin dynamics in general solid-state systems. This approach provides a complete first-principles description of light–matter interactions and scattering processes, including electron–phonon, electron–impurity, and electron–electron scatterings with self-consistent spin-orbit coupling. By employing this method, we successfully reproduce experimental results for spin relaxation lifetime (T_1) and spin dephasing time (T_2^*). Our findings demonstrate that the Frohlich interaction, which primarily governs carrier relaxation, has minimal impact on spin relaxation. We also show that the dynamical Rashba effect results in anisotropy of spin lifetime and provide insights into how symmetry affects spin relaxation and transport.

Acknowledgments

First, I would like to thank my advisor, Prof. Yuan Ping, who is full of passion and insight to science. I am very grateful to get the opportunity to start a journey in the computational physics research. Her support and advice allow me to continue to pursue my research goal throughout my Ph.D.

I would like to thank Dr. Tyler Smart, who was a great mentor and patient to guide me into computational research and the collaborative researches on spin defects. I would like to thank Prof. Junqing Xu for his many suggestions in research and the close conversations both in and out of work. I would like to thank Chunhao Guo, Shimin Zhang, Andrew Grieder and Valentin Urena Baltazar, who are great group members and friend to work with on research and have fun with. I would also like to thank other group members for fruitful discussion.

I am thankful to Prof. Jairo Velasco, Jr. and Prof. Aiming Yan for serving on my committee and support for my study and research at UCSC. I am also thankful to many other professors and the graduate coordinators in the physics department, Prof. David Lederman, Dr. Ben Miller and Jeremy Parker, who provides great help to me to make academic progress.

For the out-of-compus collaboration, I am thankful to my theory colaborators Prof. Sergey A. Varganov, Dr. Vsevolod D. Dergachev and Ilya D. Dergachev for the help with the quantum chemistry calculations. I am thankful to my experiment collaborators, Xingyu Gao, Dr. Lilia Xie, who are wonderful to work with and from whom I learn more about the connection between theory and experiment. I would like

to thank Prof. Ravishankar Sundararaman for his genuine advice in both research and life.

I am grateful to Dr. Takeda Yoshihiko, Dr. Zhou Yang and Dr. Annemi Strydom for their care and support. I am grateful to my Ph.D friends from my first day at UCSC, Dun Lin, Yannong He, Yiluan Song, Qiuxia Tang, Qiming Liu, Yan Zhang, Shijun Sun, Wencheng Shao, Yuzhan Zhao and Siyu Zhu.

Finally, I am grateful to my family for their strong support. During difficult times, their shared life experiences and care have been a source of strength for me.

Chapter 1

Introduction

Solid-state spin defects and the spin of carriers in solids are two different platforms for the control of spin degree of freedom in solid-state systems. A defect can be created by vacancies, substitutions, or interstitial atoms in a solid. When the net spin is nonzero in a defect, it is referred to spin defect, characterized by localized spin. In contrast, spin of carriers is an ensemble excitation in solid, which is delocalized and can transfer across solids. To achieve effective control of the spins in the two platforms, it requires a deep understanding of the excited-state dynamics within spin defects and the mechanisms governing spin relaxation and dephasing in solids, respectively.

For solid-state spin defect, one of the primary challenges in studying solid-state spin defects is identifying their chemical structures. The complexity of identifying the chemical structures can be due to the following factors. First, a large number of spin defects have been observed from experiments in both two dimensional (2D) and three dimensional (3D) semiconductors, including but not limited to hexagonal boron

nitride [21, 22], TMD [23], silicon carbide [24], diamond [25, 26]. Second, there are a great number of spin defect candidates possibly responsible for the single-photon emission [27, 28]. Besides defect identification, optical approaches, which characterize spin-dependent photoluminescence (PL) contrast, are crucial for controlling spin in spin defects. There is a lack of a general theoretical tool for predicting their spin-dependent PL contrast. To overcome the challenges, we not only need to understand the static properties of spin defects, such as their excitation energies, zero field splitting, hyperfine interactions, but also their dynamical properties, including their excited state lifetimes and transition rates.

For spin of carriers, many types of solids, including 2D materials and their heterostructures [29, 30], topological and magnetic materials [31, 32] and perovskites [33, 34], have been considering as the platform for controlling spin in order to realize spintronics, which is a new generation of electronics that possesses low-energy dissipation. However, there is a lack of a predictive tool for new materials design. In addition, understanding the mechanisms of spin dynamics and the intrinsic spin properties of materials requires precise simulations of spin lifetimes.

This thesis reports the first-principles studies of the solid-state spin defects and spin of carriers, motivated by the above challenges. The focus of the thesis is on the development and application of advanced first-principles computational methods that provide accurate descriptions of electronic structures and interaction processes. In the following sections, the thesis offers a comprehensive understanding of excited-state dynamics in solid-state spin defects and an in-depth exploration of the mechanisms

governing spin relaxation and dephasing for carrier spins in solids.

The structure of this thesis as follows. Chapter 2 introduces the density functional theory for electronic structure, many-body-perturbation theory, and the methods for transition rates and ODMR. Chapter 3 introduces the fundamental of group theory and its application to spin defects, specifically for defects of C_{3v} symmetry. Chapter 4 presents the work on the identification of spin defects based on the comparison between theory and experimental observations in terms of many aspects of the optical properties. Chapter 5 presents the study of excited-state dynamics of solid-state spin defects, particularly the prototypical NV center in diamond. Chapter 6 presents the study of spin relaxation and dephasing in perovskites using the FPDM approach, which is general for spin of carriers in solids. Chapter 7 presents the study of the anistropy of spin lifetime due to symmetry breaking of perovskites.

Chapter 2

Theoretical Methods

2.1 Density Functional Theory for Electronic Structure

2.1.1 The Many-Body Problem

The solid-state systems involve a large number of interacting particles, including nuclei and electrons that make up atoms. The physical properties of the solids are determined by the complex many-body interactions, which can be well described and solved by the time-independent many-body Schrödinger equation,

$$\hat{H}\Psi = E\Psi \tag{2.1}$$

$$\hat{H} = \hat{T}_N + \hat{V}_{N-N} + \hat{T}_e + \hat{V}_{e-e} + \hat{V}_{\text{ext}} \tag{2.2}$$

where $\hat{H}$ is the Hamiltonian operator, Ψ is the many-body wavefunction that depends on electronic position $\mathbf{r}$ and nuclear position $\mathbf{R}$, and E is the energy of the state. The Hamiltonian contains many terms for different interactions, including $\hat{T}_N$ the kinetic energy of nuclei, $\hat{V}_{N-N}$ the nucleus-nucleus Coulomb repulsion, $\hat{T}_e$ the kinetic energy of

electrons, $\hat{V}_{e-e}$ the repulsive electron-electron Coulomb interaction, and $\hat{V}_{\text{ext}}$ the external potential which includes $\hat{V}_{e-N}$ as the attractive interaction between the negatively charged electron and positively charged nucleus. Writing the interactions explicitly in the SI unit, we can have

$$\hat{T}_N = -\sum_I \frac{\hbar^2}{2M_I}\nabla_I^2 \tag{2.3}$$

$$\hat{V}_{N-N} = \frac{1}{2}\sum_{I,J} \frac{Z_I Z_J e^2}{4\pi\varepsilon_0|\mathbf{R}_I - \mathbf{R}_J|} \tag{2.4}$$

$$\hat{T}_e = -\frac{\hbar^2}{2m_e}\sum_i \nabla_i^2 \tag{2.5}$$

$$\hat{V}_{e-e} = \frac{1}{2}\sum_{i\neq j} \frac{e^2}{4\pi\varepsilon_0|\mathbf{r}_i - \mathbf{r}_j|} \tag{2.6}$$

$$\hat{V}_{e-N} = -\sum_{i,I} \frac{Z_I e^2}{4\pi\varepsilon_0|\mathbf{r}_i|} \tag{2.7}$$

where $\hbar$ is the Planck's constant, M is the mass of nucleus, ∇^2 is the Laplacian operator, Z is the charge of nucleus, $\mathbf{R}$ is the nuclear coordinate, ε_0 is the permittivity of the free space, e is the electron unit change and $\mathbf{r}$ is the electron position. The i and j indices sum over the interactions involving electrons, and the I index sums over the interaction involving nuclei.

The Schrödinger equation in Eq. (2.1) is fundamental and adequate for understanding materials. However, the exact solution of the many-body Schrödinger equation is almost an impossible task due to the tremendous degree of freedom of a solid-state system. Some practical approximations are desired to enable the solutions of the quantum mechanics while retaining the main features of the complex solid-state systems [35].

The first approximation widely adopted is the Born-Oppenheimer approxima-

tion that allows the separation of nuclear degree of freedom from the electronic degree of freedom, considering that the mass of a nucleus is a lot heavier than the mass of electron and that nuclei are nearly frozen while electrons are moving in solids. With this approximation, With this approximation, we can drop off the $\hat{T}_N$ term in Eq. (2.2), and the remaining problem is find the solution of the many-electron Schrödinger equation,

$$\left(\hat{T}_e + \hat{V}_{e-e} + \hat{V}_{\text{ext}} + \hat{V}_{N-N}\right)\Psi(\mathbf{r_1}, \mathbf{r_2}, ...\mathbf{r_N}) = E\Psi(\mathbf{r_1}, \mathbf{r_2}, ...\mathbf{r_N}) \tag{2.8}$$

The ground state energy of the electronic Hamiltonian, therefore, depends on the nuclear coordinates and forms a potential energy surface (PES) as a function of the nuclear coordinate.

Second, the large degree of freedom of electrons still is still a big challenge for a practical solution of the many-electron system. As will be discussed in Sec. 2.1.2, this big challenge is resolved by the density functional theory (DFT).

2.1.2 Density Functional Theory

Instead of solving Eq. (2.8), the density functional theory [36], which is proved by Hohenberg and Kohn, together with the Kohn-Sham (KS) ansatz [37], offers a practical solution for the ground state of an electronic system by minimizing electronic energy. The well-known Hohenberg-Kohn theorem shows that

- The electron density $n_0(\mathbf{r})$, which is the probability of finding an electron at position $\mathbf{r}$, can uniquely determine all the information in the ground state many-electron wavefunctions. This uniqueness ensures the one-to-one correspondence between the V_{ext} (or Hamiltonian) and electron density.

- The total energy of a system is a functional of the electron density for any given external potential V_{ext}. The ground state electron density can be obtained by minimizing the total energy globally. This provides a variational principle for looking for the ground state electron density.

On the other hand, the Kohn-Sham ansatz maps the many-body problem in the interacting picture onto an independent-particle problem in the non-interacting picture. This mapping essentially requires an auxiliary Hamiltonian ($\hat{H}_{\text{KS}}$) consist of the kinetic operator ($-\frac{1}{2}\nabla^2$) and an effective potential ($V_{\text{eff}}(\mathbf{r})$) for the independent electron. Without specifically writing spin, the Hamiltonian is expressed as

$$\hat{H}_{\text{KS}} = -\frac{1}{2}\nabla^2 + V_{\text{eff}}(\mathbf{r}) \tag{2.9}$$

$$V_{\text{eff}}(\mathbf{r}) = V_{\text{ext}}(\mathbf{r}) + V_{\text{Hartree}}[n] + V_{\text{xc}}[n] \tag{2.10}$$

where the effective potential contains the external potential $V_{\text{ext}}(\mathbf{r})$, the potential for the Hartree interaction $V_{\text{Hartree}}[n]$, and the potential of the exchange-correlation energy $V_{\text{xc}}[n]$. The potentials are functionals of the independent electron density. The many-body Schrödinger equation is replaced by so-called Kohn-Sham equation,

$$\Big[-\frac{1}{2}\nabla^2 + V_{\text{eff}}(\mathbf{r})\Big]\psi_i(\mathbf{r}) = \varepsilon_i\psi_i(\mathbf{r}) \tag{2.11}$$

The solution of this equation is the electron density of independent particle $n(\mathbf{r})$ and total energy $E_{\text{KS}}[n]$,

$$n(\mathbf{r}) = \sum_i f_i|\psi_i(\mathbf{r})|^2 \tag{2.12}$$

$$E_{\text{KS}}[n] = T_s[n] + E_{\text{ext}}[n] + E_{\text{Hartree}}[n] + E_{\text{xc}}[n] + E_{N-N} \tag{2.13}$$

where f_i is the electron occupation number of i-th KS state and ψ_i is the wavefunction of the i-th KS state. $T_s[n]$, $E_{\text{ext}}[n]$, $E_{\text{Hartree}}[n]$, $E_{\text{xc}}[n]$ and E_{N-N} are the kinetic energy, energy due to the external potential, Hartree energy, exchange-correlation energy and nuclear-nuclear interaction energy, respectively. All the energy are functionals of the electron density except E_{N-N}, which is in general treated classically. Explicitly, their functionals are written as

$$T_s[n] = -\frac{1}{2}\sum_i f_i \int d\mathbf{r}|\nabla\psi_i(\mathbf{r})|^2 \tag{2.14}$$

$$E_{\text{ext}}[n] = \int d\mathbf{r} V_{\text{ext}}(\mathbf{r})n(\mathbf{r}) \tag{2.15}$$

$$E_{\text{Hartree}}[n] = \frac{1}{2}\int d\mathbf{r}d\mathbf{r}'\frac{n(\mathbf{r})n(\mathbf{r}')}{|\mathbf{r}-\mathbf{r}'|} \tag{2.16}$$

$$E_{N-N} = \frac{1}{2}\sum_{I,J}\frac{Z_I Z_J}{|\mathbf{R}_I - \mathbf{R}_J|} \tag{2.17}$$

It can be found that only the exchange-correlation energy, which describes the many-body exchange-correlation interaction, does not have an exact expression in the non-interacting picture. Therefore, it is indispensable to get an approximate form of exchange-correlation functional. When the approximate form is adequate to reproduce the true exchange-correlation in the interacting picture, the electron density of the independent particle can exactly describe the ground state of the many-body problem. More details can be found in Sec. 2.1.3.

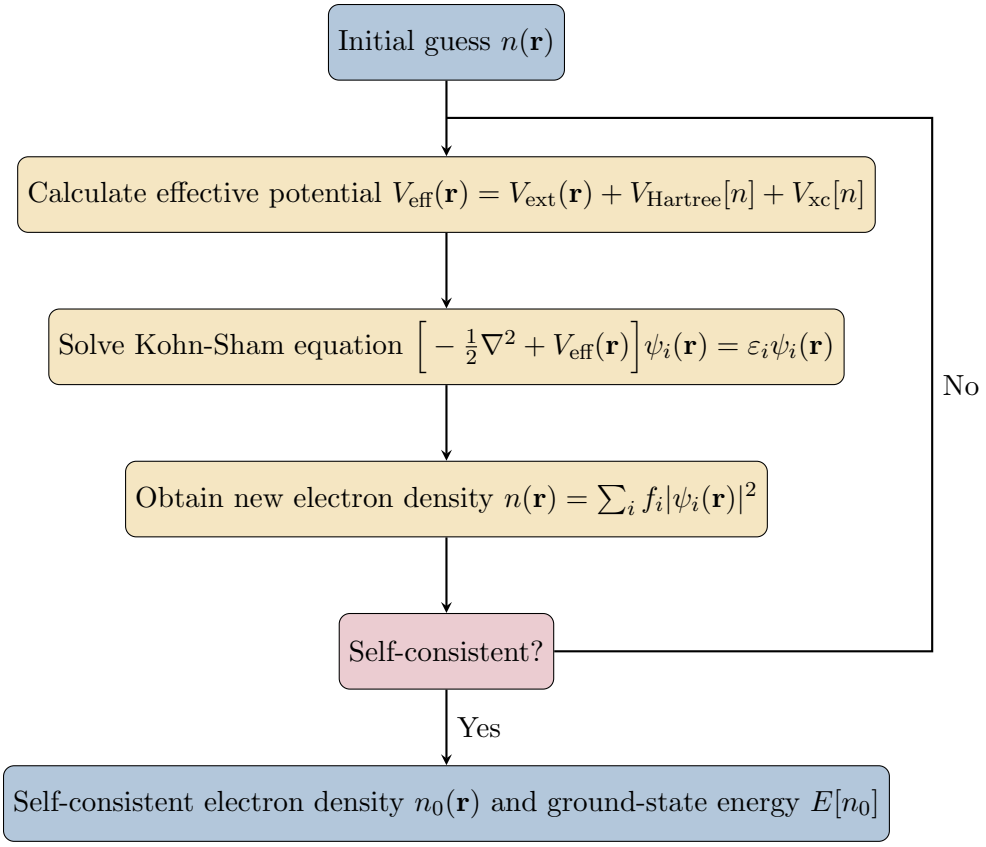

Figure 2.1: Self-consistent cycle for first-principle calculations.

With the Hohenberge-Kohn theorem and the Kohn-Sham ansatz, the electron density can be solved with the Kohn-Sham equation over sufficient number of self-consistent cycles until the self-consistent condition of energy threshold is satisfied, as shown in Fig. 2.1. All information of the ground state can be obtained subsequently with the ground-state electron density.

2.1.3 Exchange and Correlation Functionals

Currently, we can only approximate the form of the exchange-correlation functional in the Kohn-Sham equation to capture the true many-body exchange-correlation interaction. It becomes important to find the form that provides best description. The most frequently adopted functionals include the local density approximation (LDA) [38] and the generalized gradient approximation (GGA) [39].

The common feature between LDA and GGA is the ability to separate the exchange and correlation terms.

$$E_{\mathrm{xc}} = E_{\mathrm{x}} + E_{\mathrm{c}} \tag{2.18}$$

The LDA is a local exchange-correlation approximation with a homogeneous electron gas of density n [40]. It is expressed as

$$E_{\mathrm{xc}} = \int d\mathbf{r} \epsilon_{\mathrm{xc}}^{\mathrm{LDA}}(n(\mathbf{r}))n(\mathbf{r}) \tag{2.19}$$

where $\epsilon_{\mathrm{xc}}^{\mathrm{LDA}}(n(\mathbf{r}))$ is the exchange-correlation energy density that represents the energy per electron at $\mathbf{r}$. The LDA is generated with an analytical exchange energy and a highly accurate correlation energy calculated from Monte Carlo [38, 41]. It has been successful in describing the lattice constants of solids, but it highly overestimates the atomization energies [42].

The semi-local GGA functional is developed, which further includes the gradient of electron density to account for the variation or inhomogeneity of electron den-

sity [42].

$$E_{\mathrm{xc}} = \int d\mathbf{r} \epsilon_{\mathrm{xc}}^{\mathrm{GGA}}(n(\mathbf{r}), \nabla n(\mathbf{r})) n(\mathbf{r}) \tag{2.20}$$

The well-known and widely used functional PBE [39] have been successfully providing reasonable atomization energy and accurate description of geometries of solids. However, there is a known issue that PBE underestimates bandgap because of the derivative discontinuity of the exchange-correlation energy and inaccurate correction to the self-interaction energy[43, 44]. Consequently, the excitation energies of spin defects, which are a focus of this thesis, can be inaccurate.

Hybrid functional, which incorporates the Hartree-Fock (exact exchange) and and an exchange-correlation functional, can greatly improve the accuracy by eliminating the self-interaction error in the exchange interaction [45]. One of the commonly used hybrid functionals is PBE0(α), which is expressed as

$$E_{\mathrm{xc}}^{\mathrm{PBE0}(\alpha)} = \alpha E_{\mathrm{x}}^{\mathrm{HF}} + (1-\alpha) E_{\mathrm{x}}^{\mathrm{PBE}} + E_{\mathrm{c}}^{\mathrm{PBE}} \tag{2.21}$$

where α is the fraction of the exact exchange $E_{\mathrm{x}}^{\mathrm{HF}}$ that mixes with the exchange $E_{\mathrm{x}}^{\mathrm{PBE}}$ of the PBE exchange part, and $E_{\mathrm{c}}^{\mathrm{PBE}}$ is the correlation part. Another hybrid functional HSE(α) separates the short-range (SR) and long-range (LR) exchange in the PBE and only mixes the short-range exchange with the Hartree-Fock [46, 47],

$$E_{\mathrm{xc}}^{\omega\mathrm{PBEh}(\alpha)} = \alpha E_{\mathrm{x}}^{\mathrm{HF,SR}}(\omega) + (1-\alpha) E_{\mathrm{x}}^{\mathrm{PBE,SR}}(\omega) + E_{\mathrm{x}}^{\mathrm{PBE,LR}}(\omega) + E_{\mathrm{c}}^{\mathrm{PBE}} \tag{2.22}$$

where SR and LR stand for short-range and long-range interactions, respectively. ω is a parameter used for adjusting the extent of the short-range interaction.

The hybrid functionals show significant improvement in the description of the excitation energies with the trade-off of higher computational cost and poor convergence with the k-point sampling in the Brillouin zone. Nevertheless, they have been shown to provide better prediction for many spin defects in solids with respect to their excitation energies, compared to PBE [48, 49, 50, 51, 52]. A appropriate fraction α needs to be determined for the hybrid functionals for spin defects. Koopman's theorem provides a way for this determination. With the assumption that α depends on the long-range dielectric screening of the host materials rather than the specific defects, Koopman's theorem states that the electron affinity (EA) of the system with one less charge should equal the ionization energy (IP) of the system of one more charge, expressed as $\mathrm{EA}_{q+1} = \mathrm{IP}_q$ [2].

2.2 Many-Body Perturbation Theory

The exchange-correlation interaction in the non-interacting picture is accounted by the V_{xc} in Eq. (2.9). However, the approximation of the exchange-correlation functionals may not be sufficiently accurate to account for the error due to the self-interaction. Moreover, DFT that describe well for the ground state of an electronic system, but may be inadequate to describe the excited state properties from measurements such as electron loss spectrum and optical absorption.

To address the above issues, the many-body perturbation theory beyond the Hartree-Fock approximation in DFT is usually applied. The basic idea of many-body perturbation theory is to map the strong bare Coulomb interaction between electrons

into a weaker effective interaction between a dressed electron and its surrounding environment. This dressed electron is known as a quasiparticle, which results from the strong electron-electron repulsion. Due to the repulsion, a positive charge cloud surrounding the electron is created such that electrons are screened or dressed. Using the quasiparticle concept, there is immediate similarity between the quasiparticle equation below compared to Eq. (2.9),

$$[T + V_{\mathrm{h}} + V_{\mathrm{ext}}]\Psi_i(\mathbf{r}) + \int d\mathbf{r}'\Sigma(\mathbf{r}, \mathbf{r}'; E_i)\Psi_i(\mathbf{r}') = E_i\Psi_i(\mathbf{r}) \tag{2.23}$$

where Σ is the self-energy operator replacing with the exchange-correlation energy $V_{\mathrm{xc}}(\mathbf{r})\delta(\mathbf{r} - \mathbf{r}')$ in DFT, and E_i is the quasiparticle energy at state i. The Hamiltonian describing the quasiparticle is non-Hermitian, leading to the quasiparticle having a finite lifetime.

The challenge turns to solve the self-energy of the excitation of quasiparticle, and a general solution is the Green's function [53, 54]. The one-particle Green's function is sufficient for calculating the self-energy. However, when coming to the optical measurement where electron and hole quasiparticles are excited and form excitons, the one-particle Green's funciton is not suffient to account for the interaction between the electron and hole. At his point, it needs two-particle Green's function, which is also called Bethe-Salpeter equation (BSE) [55] to further account for the excitonic effect due to the interaction between electron and hole. The derivation in this section follows the derivation in Ref. [53, 54, 55, 56, 57].

2.2.1 Hedin's Equations

The solution of one-particle Green's function for the many-body problem starts from the many-body Hamiltonian in Eq. (2.2), which is simplified with only the electronic terms as below

$$H_0 = \int d\mathbf{r}\psi^\dagger(\mathbf{r})h(\mathbf{r})\psi(\mathbf{r}) + \frac{1}{2}\int d\mathbf{r}d\mathbf{r}'\psi^\dagger(\mathbf{r})\psi^\dagger(\mathbf{r}')v(\mathbf{r},\mathbf{r}')\psi(\mathbf{r}')\psi(\mathbf{r}) \tag{2.24}$$

with the perturbation Hamiltonian given by

$$H'(t) = \int d\mathbf{r}\psi^\dagger(\mathbf{r})v_p(\mathbf{r},t)\psi(\mathbf{r}) \tag{2.25}$$

where $\psi^\dagger(\mathbf{r})$ and $\psi(\mathbf{r})$ are the creation and annihilation field operators, respectively. $h(\mathbf{r})$ is the one-particle Hamiltonian, $v(\mathbf{r},\mathbf{r}')$ is the bare Coulomb potential between two particles, and $v_p(\mathbf{r},t)$ is the time-dependent perturbative potential.

As can be seen in Sec. 2.3.1, in the interaction picture, the time-dependent perturbation can cause the time-dependent states by the time-evolution operator Eq. (2.72), and affects the field operators,

$$\psi(\mathbf{r},t) = U_I(t_0,t)\psi(\mathbf{r})U_I(t,t_0) \tag{2.26}$$

Also, the time-evolution operator allows to define the S matrix, which will be used later in writing the Green's function,

$$S = S(t,t') = T\exp\Big[-i\int_{t'}^{t} dt_1 H'(t_1)\Big] \tag{2.27}$$

where T is the Wick time-ordering operator which places the operators with larger time on the left. The Schrödinger equation of the time-dependent field operator is

$$i\frac{\partial\psi(\mathbf{r},t)}{\partial t} = U_I(t_0,t)\Big[\psi(\mathbf{r}), H_o + H'\Big]U_I(t,t_0) \tag{2.28}$$

Then, the following equation of motion can be derived with considering the anticommutation relationship between the field operators $\{\psi(\mathbf{r}), \psi^\dagger(\mathbf{r}')\} = \delta(\mathbf{r}, \mathbf{r}')$,

$$\begin{aligned}
&\left[i\frac{\partial}{\partial t} - h(\mathbf{r}) - v_p(\mathbf{r}, t)\right] T\left[\psi(\mathbf{r}, t)\psi^\dagger(\mathbf{r}', t')\right] \\
&- \int d\mathbf{r}'' v(\mathbf{r}, \mathbf{r}') T\left[\psi^\dagger(''\mathbf{r}, t)\psi(\mathbf{r}'', t)\psi(\mathbf{r}, t)\psi^\dagger(\mathbf{r}', t')\right] \\
&= i\delta(\mathbf{r}, \mathbf{r}')\delta(t, t')
\end{aligned} \tag{2.29}$$

This operator has the following effect on the field operators,

$$T\left[\psi(\mathbf{r}, t)\psi^\dagger(\mathbf{r}', t')\right] = \theta(t - t')\psi(\mathbf{r}, t)\psi^\dagger(\mathbf{r}', t') - \theta(t' - t)\psi^\dagger(\mathbf{r}', t')\psi(\mathbf{r}, t) \tag{2.30}$$

where $\theta(t)$ is the Heaviside step function, whose time derivative results in delta function $d\theta(t)/dt = \delta(t)$.

By defining the one-particle and two-particle Green's functions with the time operator and S matrix in Eq. (2.27),

$$G(1, 2) = -i\frac{\langle N|T[S\psi(1)\psi^\dagger(2)]|N\rangle}{\langle N|T[S]|N\rangle} \tag{2.31}$$

$$G(1, 2; 1', 2') = (-i)^2\frac{\langle N|T[S\psi(1)\psi(2)\psi^\dagger(2)\psi^\dagger(1)]|N\rangle}{\langle N|T[S]|N\rangle} \tag{2.32}$$

where $|N\rangle$ represents the ground state of N electrons, the indices 1 and 2 stand for space-time coordinates $1 = (\mathbf{r_1}, t_1)$ and $2 = (\mathbf{r_2}, t_2)$. Then, the equation of motion can

be simplified to the equations below [56],

$$\left[i\frac{\partial}{\partial t_1} - h(1)\right]G(1,2) - \int d(3)v_p(1,3)G(3,2) + i\int d(3)v(1,3)G(1,3^+;2,3^{++}) = \delta(1,2)$$
$$\left[-i\frac{\partial}{\partial t_2} - h(2)\right]G(1,2) - \int d(3)G(1,3)v_p(3,2) + i\int d(3)v(2,3)G(1,3^{--};2,3^-) = \delta(1,2) \tag{2.33}$$

(2.34)

The expressions show that the one-particle Green's function depends on the two-particle Green's function, and the two-poarticle Green's function has dependency on higher-order Green's function and so on. This dependency is simplified and resolved by introducing the expression of two-particle Green's function by the one-particle Green's function plus the external potential derivative of the one-particle Green's function,

$$G(1,3;2,3') = G(1,2)G(3,3^+) - \frac{\delta G(1,2)}{\delta v_p(3)} \tag{2.35}$$

This expression enables to write the equation of motion for the one-particle Green's function,

$$\left[i\frac{\partial}{\partial t_1} - h(1) - V(1) - i\int d(3)v(1^+,3)\frac{\delta}{\delta v_p(3)}\right]G(1,2) = \delta(1,2) \tag{2.36}$$

where $V(1)$ is the total potential,

$$V(1) = v_p(1) + \int d(2)v(1,2)G(2,2^+) \tag{2.37}$$

Using the total potential with the following inverse of the Green's function, the inverse dielectric matrix ε^{-1}, the irreducible polarizability χ_0, electron density n and the chain

rule,

$$\int d(3)G(1,3)G^{-1}(3,2) = \delta(1,2) \tag{2.38}$$

$$\varepsilon^{-1}(1,2) = \frac{\delta V(1)}{v_p(2)} \tag{2.39}$$

$$\chi_0(1,2) = \frac{\delta n(1)}{\delta V(2)} = -i\frac{\delta G(1,1^+)}{\delta V(2)} \tag{2.40}$$

we can define a few quantities, including the vertex function Γ, the polarizability χ, the screened Coulomb potential W, and the self-energy Σ as below,

$$\Gamma(1,2;3) = -\frac{\delta G^{-1}(1,2)}{\delta V(3)} \tag{2.41}$$

$$\begin{aligned}\chi(1,2) = \frac{\delta n(1)}{\delta v_p(2)} &= -i\frac{\delta G(1,1^+)}{\delta v_p(2)} = -i\int d(3)\frac{\delta G(1,1^+)}{\delta V(3)}\frac{\delta V(3)}{\delta v_p(2)} \\ &= \chi_0(1,2) + \int d(3)\chi_0(1,3)\varepsilon^{-1}(3,2) \\ &= \chi_0(1,2) + \int d(34)\chi_0(1,3)v(3,4)\chi(4,2)\end{aligned} \tag{2.42}$$

$$W(1,2) = \int d(3)\varepsilon^{-1}(1,3)v(3,2) = \int d(3)v(1,3)\varepsilon^{-1}(2,3) \tag{2.43}$$

$$\Sigma(1,2) = i\int d(34)G(1,3)\Gamma(3,2;4)W(4,1^+) \tag{2.44}$$

These quantities allow the equation of motion to be rewritten as

$$\left[i\frac{\partial}{\partial t_1} - h(1) - V(1)\right]G(1,2) - i\int d(3)\Sigma(1,3)G(3,2) = \delta(1,2) \tag{2.45}$$

Finally, the well-known Hedin's equations can be derived as below,

$$\Sigma(1,2) = i \int d(34) G(1,3) \Gamma(3,2;4) W(4,1^+) \tag{2.46}$$

$$G(1,2) = G_0(1,2) + \int d(34) G_0(1,3) \Sigma(3,4) G(4,2) \tag{2.47}$$

$$\Gamma(1,2;3) = \delta(1,2)\delta(1,3) + \int d(4567) \frac{\delta \Sigma(1,2)}{\delta G(4,5)} G(4,6) G(7,5) \Gamma(6,7;3) \tag{2.48}$$

$$\chi_0(1,2) = -i \int d(34) G(1,3) G(4,1^+) \Gamma(3,4;2) \tag{2.49}$$

$$W(1,2) = v(1,2) + \int d(34) v(1,3) \chi_0(3,4) W(4,2) \tag{2.50}$$

The loop of Hedin's equations can be solved self-consistently but is difficult. Some approximations need to make to reduce the complexity of the solution, including the random phase approximation (RPA) and GW approximation.

2.2.2 Random Phase Approximation and GW Approximation

By neglecting the vertex corrections and retaining the first term in Eq. (2.48), we make the random phase approximation,

$$\Gamma(1,2;3) = \delta(1,2)\delta(1,3) \tag{2.51}$$

and the polarizability becomes

$$\chi_0(1,2) = -iG(1,2^+)G(2,1^+) \tag{2.52}$$

$$\chi(1,2) = \chi_0(1,2) + \int d(3) \chi_0(1,3) [1 - v\chi_0]^{-1}(3,2) \tag{2.53}$$

It is clear that χ_0 is the response of density to total potential is from the one-particle Green's function of the non-interacting electron-hole pair. χ is the RPA response func-

tion of electron density to the perturbation potential, which is useful for optical response and electron screening. By plugging Eq. (2.52) into Eq. (2.46), we can find the self-energy is reduced to

$$\Sigma(1,2) = iG(1,2)W(1^+,2) \tag{2.54}$$

which contains only G and W. Thus, the approximation is called GW approximation.

The Green's function is implemented with the Lehmann representation,

$$G(\mathbf{r},\mathbf{r}';\omega) = \frac{\psi_i(\mathbf{r})\psi_i^*(\mathbf{r}')}{\omega - E_i + i\eta} \tag{2.55}$$

where $\psi_i(\mathbf{r})$ and $\psi_i^*(\mathbf{r}')$ are the i-th KS wavefunctions at DFT, E_i is the corresponding eigenvalue of the KS state, η is a real infinitesimal that takes a negative value for occupied states and a positive value for unoccupied states. Subsequently, the self-energy can be evaluated.

2.2.3 Bethe-Salpeter Equation

The optical absorption is an excitation process of electron-hole pair, which contains the interaction between electron and hole. This is so-called excitonic effect and can be described by the two-particle Green's function, also known as Bethe-Salpeter Equation, which is defined as

$$L(1,2;1',2') = -G(1,2;1',2') + G(1,1')G(2,2') \tag{2.56}$$

It includes the correlated propagation of an electron and a hole in the first term, while the second term eliminates the uncorrelated propagation of the two particles, which

can be electron and electron, hole and hole, electron and hole, or hole and electron, depending on the time ordering of the field operators. By Eq. (2.35), the equation can be rewritten as

$$\begin{aligned} L(1,2;1',2') = \frac{\delta G(1,1')}{\delta v_p(2',2)} &= -\int d(33')G(1,3)\frac{\delta G^{-1}(3,3')}{\delta v_p(2',2)}G(3',1') \\ &= G(1,2')G(2,1') + \int d(33')G(1,3)\frac{\delta \Sigma(3,3')}{\delta v_p(2',2)}G(3',1') \end{aligned} \tag{2.57}$$

where the self-energy contains the Hartree potential and exchange-correlation self-energy, i.e. $\Sigma = v_{\text{Hartree}} + \Sigma_{\text{xc}}$. With defining the two-particle propagator L_0 and the two-particle interaction kernel Ξ as below,

$$L_0(1,2;1',2') = G(1,2')G(2,1') \tag{2.58}$$

$$\Xi(3,2,3',2') = -i\delta(3,3')\delta(2,2'^{+})v(3^{+},2) + \frac{\delta\Sigma(3,3')}{\delta G(2',2)} \tag{2.59}$$

we can obtain the BSE

$$L(1,2;1',2') = L_0(1,2;1',2') + \int d(33'44')L_0(1,3';1',3)\Xi(3,4,3',4')L(4',2;4,2') \tag{2.60}$$

which is a Dyson equation of the two-particle propagator. In the solution of the BSE on top of GW, the kernel can be simplified with the GW approximation in Sec. 2.2.2.

2.3 Transition Rate Formula

The optical measurement of spin defects is involves many transition processes, including excitation, radiative recombination, intersysten crossing and internal conversion. During the excitation, spin defects absorb photons and promote from the ground

state to excited states. Subsequently, radiative recombination occurs with emitting photons in the process. Besides, spin defects in the excited state can undergo nonradiative recombination processes to electronic states of lower energy via heat dissipation to lattice vibration. One is intersystem crossing (ISC), a nonradiative recombination process between states of different spin multiplicity. The other is internal conversion (IC), a spin-conserving nonradiative recombination process. These processes are critical in the excited-state dynamics of spin defects and collectively influence their optical properties and measurements.

We use Fermi's golden rule, a fundamental theory derived from time-dependent perturbation theory, to calculate excited-state transition rates by determining the probability of quantum state transitions induced by perturbations.

2.3.1 Time-Dependent Perturbation Theory

In the time-dependent perturbation theory [58], a time-dependent perturbation $V(t)$ is included to the unperturbed Hamiltonian H_0, which does not contain time explicitly or not time-dependent, such that the system is influenced by the external perturbation. As a result of the time-dependent perturbation, there is probability as a function of time for the system to be found in $|n\rangle$ with the initial state $|i\rangle$ $(n \neq i)$.

$$H = H_0 + V(t) \tag{2.61}$$

If $V(t) = 0$, one can derive the eigenstate $|n\rangle$ and eigenenergy E_n of H_0

$$H_0(t)\,|n(t)\rangle = E_n e^{-iE_n t/\hbar}\,|n\rangle \tag{2.62}$$

If $V(t) \neq 0$, H will evolve with time, and the time-evolution operator will be no longer as simple as $e^{-iHt/\hbar}$.

Let $|\alpha, t_0; t_0\rangle$ be a linear combination of all the pure state kets at t_0, and $|\alpha, t_0; t\rangle$ be the time-evolved state ket in Schrödinger picture at t of a physical system whose state ket at t_0 was found to be $|\alpha\rangle$

$$|\alpha\rangle = |\alpha, t_0; t_0\rangle = \sum_n c_n(t_0)\,|n\rangle \tag{2.63}$$

$$|\alpha, t_0; t\rangle_S = e^{-iHt/\hbar}\,|\alpha, t_0; t_0\rangle = e^{-i(H_0+V(t))t/\hbar}\,|\alpha, t_0; t_0\rangle = \sum_n c_n(t)e^{-iE_nt/\hbar}\,|n\rangle \tag{2.64}$$

It can be seen that $c_n(t)$ evolves with time due to the time-dependent perturbation $V(t)$, and the probability of finding $|n\rangle$ at t is

$$P_n(t) = |\,\langle n|\alpha, t_0; t\rangle\,|^2 = |c_n(t)|^2 \tag{2.65}$$

Starting from here, the goal is derive $c_n(t)$, which is more convenient in the interaction picture (Dirac picture), where states evolve slowly with the perturbation $V(t)$ and operators evolves as in Heisenberge picture $\frac{dA_I}{dt} = \frac{1}{i\hbar}[A_I, H_0]$. In this picture, both state and perturbation operator are time dependent, which are written as,

$$|\alpha, t_0; t\rangle_I = e^{iH_0t/\hbar}\,|\alpha, t_0; t\rangle_S = \sum_n c_n(t)\,|n\rangle \tag{2.66}$$

$$V_I(t) = e^{iH_0t/\hbar}V(t)e^{-iH_0t/\hbar} \tag{2.67}$$

and the time-evolution of a state in the interaction picture is described by the Schrödinger-like equation,

$$i\frac{\partial}{\partial t}\,|\alpha, t_0; t\rangle_I = V_I(t)\,|\alpha, t_0; t\rangle_I \tag{2.68}$$

Therefore, in the interaction picture, we can obtain $c_n(t)$ for the transition probability,

$$\begin{aligned} i\hbar\frac{\partial}{\partial t}c_n(t) &= \sum_m e^{i(E_n-E_m)t/\hbar}\langle n|V(t)|m\rangle\, c_m(t) \\ &= \sum_m e^{i(E_n-E_m)t/\hbar}V_{nm}(t)c_m(t)\ . \end{aligned} \tag{2.69}$$

When a system has many states (more than two), Eq. (2.69) becomes a large set of linear equations, and an exact solution of $c_n(t)$ is hardly available. In order to get solutions of $c_n(t)$, Eq. (2.69) is approximated with the initial condition $c_n^{(0)} = \delta_{ni}$, with expansion of $c_n^{(t)}$, and with the application of the time-evolution operator $U_I(t,t_0)$ which is defined as,

$$c_n(t) = c_n^{(0)} + c_n^{(1)} + c_n^{(2)} + \ldots \tag{2.70}$$

$$|\alpha, t_0; t\rangle_I = U_I(t,t_0)\,|\alpha, t_0; t_0\rangle_I \tag{2.71}$$

By plugging Eq. (2.71) into Eq. (2.68), we can find the following integral equation, which can be written into Dyson series, allowing $U_I(t,t_0)$ to be computed to any finite order of perturbation theory, regardless of convergence issues,

$$\begin{aligned} U_I(t,t_0) &= 1 - \frac{i}{\hbar}\int_{t_0}^{t} V_I(t')U_I(t',t_0)dt' \\ &= 1 - \frac{i}{\hbar}\int_{t_0}^{t} V_I(t')\left[1 - \frac{i}{\hbar}\int_{t_0}^{t'} V_I(t'')U_I(t'',t_0)dt''\right]dt' \\ &= 1 - \frac{i}{\hbar}\int_{t_0}^{t} dt' V_I(t') + \left(\frac{-i}{\hbar}\right)^2\int_{t_0}^{t}dt'\int_{t_0}^{t'}dt'' V_I(t')V_I(t'') + \ldots \end{aligned} \tag{2.72}$$

$c_n(t)$ can be found connected with $U_I(t,t_0)$ by Eq. (2.66) and Eq. (2.71),

$$\langle n|\alpha, t_0; t\rangle_I = \langle n|U_I(t,t_0)|i\rangle = c_n(t) \tag{2.73}$$

The above gives rise to the probabilty amplitude which can be expanded as below,

$$c_n = \langle n|U_I(t,t_0)|i\rangle = e^{i(E_n-E_i)t/\hbar}\langle n|U(t,t_0)|i\rangle \tag{2.74}$$

$$c_n^{(0)} = \langle n|U_I^{(0)}(t,t_0)|i\rangle = \delta_{ni} \tag{2.75}$$

$$\begin{aligned} c_n^{(1)} &= \langle n|U_I^{(1)}(t,t_0)|i\rangle \\ &= -\frac{i}{\hbar}\int_{t_0}^{t} dt' e^{i(E_n-E_i)t'/\hbar}\langle n|U(t',t_0)|i\rangle \end{aligned} \tag{2.76}$$

$$\begin{aligned} c_n^{(2)} &= \langle n|U_I^{(2)}(t,t_0)|i\rangle \\ &= \left(\frac{-i}{\hbar}\right)^2 \int_{t_0}^{t} dt' \int_{t_0}^{t'} dt'' \sum_m e^{i(E_n-E_m)t'/\hbar}\langle n|U(t',t'')|m\rangle\, e^{i(E_m-E_i)t''/\hbar}\langle m|U(t'',t_0)|i\rangle \end{aligned} \tag{2.77}$$

Finally, the Fermi's golden rule that describes the rate of transition can be derived from the time-derivative of the transition probability. The first- and second-order transitions are expressed as below,

$$\begin{aligned} k_{i\to[n]} &= \frac{2\pi}{\hbar}\overline{\left|V_{ni} + \sum_m \frac{V_{nm}V_{mi}}{E_i - E_m}\right|^2}\rho(E_n)|_{E_n\simeq E_i} \\ &= \frac{2\pi}{\hbar}\overline{\left|V_{ni} + \sum_m \frac{V_{nm}V_{mi}}{E_i - E_m + i\varepsilon}\right|^2}\rho(E_n)|_{E_n\simeq E_i} \end{aligned} \tag{2.78}$$

which is also written as

$$k_{i\to[n]} = \frac{2\pi}{\hbar}\left|V_{ni} + \sum_m \frac{V_{nm}V_{mi}}{E_i - E_m + i\varepsilon}\right|^2 \delta(E_n - E_i) \tag{2.79}$$

with the density of states being integrated $\int dE_n\rho(E_n)$ to a delta function $\delta(E_n - E_i)$.

2.3.2 Radiative Recombination

The radiative recombination is a result of electron-photon interaction. The rate of electronic transition with the emission of a photon can be described by the

following formula [59, 60],

$$k_{\mathrm{R}}(\mathbf{Q},\mathbf{q},\epsilon_{\mathbf{q},\lambda}) = \frac{2\pi}{\hbar}\left|\langle G, 1_{\mathbf{q},\lambda}|H_{\mathrm{int}}|S(\mathbf{Q},0)\rangle\right|^2 \delta(\hbar\Omega(\mathbf{Q}) - \hbar cq) \tag{2.80}$$

where H_{int} is the electron-photon interaction Hamiltonian, $|S(\mathbf{Q},0)\rangle$ represents the state of exciton in the absence of photon, $|G, 1_{\mathbf{q},\lambda}\rangle$ represents the ground state in the presence of a photon, and $\delta(\hbar\Omega(\mathbf{Q}) - \hbar cq)$ ensures the energy conservation during the radiative recombination process. Within each part of the equation, $\mathbf{Q}$ is the exciton wavevector, $\mathbf{q}$ is the photon wavevector, λ is for the two perpendicular traverse polarization modes of photon, $\hbar$ is the Planck's constant, and c is the speed of light.

Because of the zero dimension (0D) of point defects, the exciton wavevector is zero. This results in no temperature dependence and the reduced radiative recombination rate equation as below in the SI unit [59],

$$k_{\mathrm{R}} = \frac{1}{\tau_{\mathrm{R}}} = \frac{nE_0^3\mu_{e-h}^2}{3\pi\varepsilon_0 c^3\hbar^4} \tag{2.81}$$

where n is the refractive index of host solid (1 for 2D material and 2.4 for diamond), ε_0 is the vacuum permittivity, E_0 is excitation energy and μ_{e-h}^2 is the modulus square of exciton dipole moment. The excitation energy and oscillator strength of defects can be obtained from the many-body perturbation theory($\mathrm{G_0W_0}$ − BSE) [59]. We have employed similar method to calculate the radiative rates of defects in two dimensional (2D) and three dimensional (3D) materials [59, 61, 62, 49], which have shown good agreement with experiments.

2.3.3 Nonradiative Recombination: Intersystem Crossing

Using the Fermi's golden rule for the first-order transition, the ISC rate between electronic states with different spin multiplicities can be calculated as

$$k_{\mathrm{ISC}} = \frac{2\pi}{\hbar} g \sum_{n,m} p_{in} |\langle fm|H_{\mathrm{soc}}|in\rangle|^2 \delta(E_{fm} - E_{in}). \tag{2.82}$$

where $|in\rangle$ and $|fm\rangle$ are the n-th vibrational level of the initial state $|i\rangle$ and the m-th vibrational level of the final state $|f\rangle$, respectively. $|in\rangle$ and $|fm\rangle$ implicitly contain the electron coordinate $\mathbf{r}$ and nuclear coordinate $\mathbf{R}$.

Under Born-Oppenheimer approximation, the vibronic state is separable and can be written as the direct product of the electronic part and the vibrational part,

$$\begin{aligned} |fm\rangle &= |f\rangle \otimes |m\rangle \\ |in\rangle &= |i\rangle \otimes |n\rangle \end{aligned} \tag{2.83}$$

Under static coupling approximation, we can write the matrix element by Tayler expansion in terms of the k-th phonon mode denoted by $q_k = \sqrt{\omega_k/\hbar} Q_k$ to the first order [63, 64],

$$\begin{aligned} \langle fm|H_{\mathrm{soc}}|in\rangle &= \left(\langle m| \otimes \langle f|\right) H_{\mathrm{soc}} \left(|i\rangle \otimes |n\rangle\right) \\ &= \underbrace{\langle f|H_{\mathrm{soc}}|i\rangle \langle m|n\rangle}_{\text{direct spin-orbit coupling}} + \underbrace{\sum_k \left[\left(\frac{\partial}{\partial q_k} \langle f|H_{\mathrm{soc}}|i\rangle \right) \Big|_{q_k=0} \langle m|q_k|n\rangle \right]}_{\text{vibronic spin-orbit coupling}} + o(q_k) \end{aligned} \tag{2.84}$$

The zero-order term named direct spin-orbit coupling is forbidden when it does not contain the totally symmetric component. However, electron-phonon coupling by pseudo

Jahn-Teller effect [65] can lead to mixed state and non-vanishing SOC, as can be seen in Sec. 3.8. In principle, by considering the non-vanishing SOC perturbatively to the first-order q derivative which is so-called vibronic spin-orbic coupling [64], we can obtain the SOC matrix element with full phonon interaction completely from first-principles.

Alternatively, the scattering matrix $\langle fm|H_{\mathrm{soc}}|in\rangle$ including electron-phonon interaction can be treated as the product of an effective SOC matrix element and an effective phonon overlap, which is discussed in Sec. 3.8. Therefore, the ISC rate equation is expressed as

$$k_{\mathrm{ISC}} = \frac{2\pi}{\hbar} g\lambda^2 \widetilde{X}_{if} \tag{2.85}$$

$$\lambda = \langle\psi_f|H_{\mathrm{soc}}|\psi_i\rangle \tag{2.86}$$

$$\widetilde{X}_{if} = \sum_{n,m} p_{in}(T)|\langle\phi_m|\phi_n\rangle|^2 \delta(m\hbar\omega_f - n\hbar\omega_i + \Delta E_{if}) \tag{2.87}$$

where g is the degree of degeneracy on equivalent structural configuration, λ is the effective SOC matrix element, and $\widetilde{X}_{if}$ is the temperature-dependent phonon term representing the phonon contribution. $|\psi\rangle$ is the linear combination of possible electronic states after considering pseudo JT effect, and $|\phi\rangle$ denotes the phonon wavefunction under the harmonic oscillator approximation.

In this expression, we make the 1D effective phonon approximation [66, 67, 48] for the ISC rate. Compared to the full-phonon method used in Ref. [52, 68], an advantage of this 1D effective phonon method is that it enables the use of different values for the phonon energy of initial state ($\hbar\omega_i$) and the one of final state ($\hbar\omega_f$), and enables finite temperature occupation for both states.

2.3.4 Nonradiative Recombination: Internal Conversion

The internal conversion is a spin-conserving nonradiative transition, which is generally expressed as

$$k_{\mathrm{IC}} = \frac{2\pi}{\hbar} g \sum_{n,m} p_{in} |\langle fm|H_{\mathrm{eph}}|in\rangle|^2 \delta(E_{fm} - E_{in}). \tag{2.88}$$

Under the static coupling approximation and one-dimensional effective phonon approximation, the equation of nonradiative transition rate is written as [66, 67]

$$k_{\mathrm{IC}} = \frac{2\pi}{\hbar} g |W_{if}|^2 X_{if}(T) \tag{2.89}$$

$$W_{if} = \langle \psi_i(\mathbf{r},\mathbf{R})| \frac{\partial H}{\partial Q} |\psi_f(\mathbf{r},\mathbf{R})\rangle \Big|_{\mathbf{R}=\mathbf{R_a}} \approx (\varepsilon_f - \varepsilon_i) \left\langle \psi_i(\mathbf{r},\mathbf{R}) \middle| \frac{\partial \psi_f(\mathbf{r},\mathbf{R})}{\partial Q} \right\rangle \Big|_{\mathbf{R}=\mathbf{R_a}} \tag{2.90}$$

$$X_{if} = \sum_{n,m} p_{in}(T) \Big| \langle \phi_{fm}(\mathbf{R})|Q - Q_a|\phi_{in}(\mathbf{R})\rangle \Big|^2 \delta(m\hbar\omega_f - n\hbar\omega_i + \Delta E_{if}). \tag{2.91}$$

Here the rate equation is expressed as a product of the electronic term W_{if} and the the one-dimensional (1D) phonon term X_{if} at static coupling approximation [67]. ψ and ϕ are the electronic wavefunction and phonon wavefunction, respectively. ε is the single-particle electron eigenvalue. The effective phonon energy $\hbar\omega$ can be obtained from fitting the potential energy surface of the electronic states along the configuration coordinate. i and f stands for the initial and final electronic states, respectively. m and n are the vibrational quantum numbers in the f state and i state, respectively.

2.4 Master Equation for Optically Detected Magnetic Resonance

Here, we show the full derivation of the ODMR model based on the master equation [4, 69], which integrates all transition rates and allows the simulation of the dynamics of states populations. First is the conventional definition of ODMR contrast,

$$C(\mathbf{B}) = 1 - \frac{\bar{I}(t, \mathbf{B}, k_{\mathrm{MW}})}{\bar{I}(t, \mathbf{B}, k_{\mathrm{MW}} = 0)} \tag{2.92}$$

where $\bar{I}(t, \mathbf{B}, k_{\mathrm{MW}})$ is magnetic-field dependent photoluminescence (PL) intensity at steady state in the presence of microwave field (MW) that drives the rotation of population between any two spin sublevels, and $\bar{I}(t, \mathbf{B}, k_{\mathrm{MW}} = 0)$ is PL intensity at steady state in the absence of the microwave field. As the microwave field directs the optical cycle to the nonradiatively preferred channel which intersystem crossing (ISC) is faster, the steady-state PL intensity is different between these two conditions. It is worth noting that $\bar{I}(t)$ is constant with time elapsing after it reaches the steady state. Here, k_{MW} is the Rabi frequency of a microwave field that is applied for rotating the populations of spin sublevels [70]. It is a parameter in the model as it scales with the square root of the laser intensity. For clarity, when $E = 0$, the spin sublevels are $|0\rangle$, $|-1\rangle$ and $|+1\rangle$. When $E \neq 0$, the spin sublevels are $|0\rangle$, $|-\rangle$ and $|+\rangle$. Refer to Eq. (2.102) and Eq. (2.103).

The steady-state PL intensity depends on the radiative recombination rate and the excited state populations at the steady-state,

$$\bar{I}(t, \mathbf{B}) = \eta \sum_{i \in \mathrm{ES}} \sum_{j \in \mathrm{GS}} k_{ij}(\mathbf{B}) \bar{n}_i(t, \mathbf{B}) \tag{2.93}$$

In general, the time-resolved PL intensity in non-equilibrium is written as

$$I(t,\mathbf{B}) = \eta \sum_{i\in \mathrm{ES}} \sum_{j\in \mathrm{GS}} k_{ij}(\mathbf{B}) n_i(t,\mathbf{B}) \tag{2.94}$$

where η is the collection coefficient dependent on experimental setup, $k_{ij}(\mathbf{B})$ is the magnetic-field dependent transition rate between electronic state $|i\rangle$ and $|j\rangle$. $n_i(t,\mathbf{B})$ is the population of state $|i\rangle$ at time t under magnetic field $\mathbf{B}$. During optical excitation, $n_i(t,\mathbf{B})$ can be numerically solved by using the Euler method as below,

$$n_i(t_{m+1},\mathbf{B}) = n_i(t_m,\mathbf{B}) + \frac{dn_i}{dt}(t_m,\mathbf{B})dt \tag{2.95}$$

$$\frac{dn_i(t,\mathbf{B})}{dt} = \sum_j \left[k_{ji}(\mathbf{B}) n_j(t,\mathbf{B}) - k_{ij}(\mathbf{B}) n_i(t,\mathbf{B})\right] \tag{2.96}$$

where m represents time step m. After optical excitation ($t = 0$), the populations of states $n_i(t,\mathbf{B})$ decay exponentially according to their lifetime $\tau_i(\mathbf{B}) = 1/\sum_j k_{ij}(\mathbf{B})$. Therefore, we can express the PL after optical excitation,

$$I(t,\mathbf{B}) = \sum_{i\in \mathrm{ES}} \sum_{j\in \mathrm{GS}} k_{ij}(\mathbf{B}) n_i(0,\mathbf{B}) e^{-t/\tau_i(\mathbf{B})} \tag{2.97}$$

After all, the PL intensity and continuous-wave ODMR are essentially dependent on the rates $k_{ij}(\mathbf{B})$. First, we can evaluate the transition rate k_{ij}^0 at zero magnetic field (denoted by the superscript 0) for the transition from the initial state $\left|i^0\right\rangle$ to the final state $\left|j^0\right\rangle$ using Fermi's golden rule except Rabi frequency,

$$k_{ij}^0 = \frac{2\pi}{\hbar} \left| \left\langle i^0 \right| H_{int} \left| j^0 \right\rangle \right|^2 \delta(\Delta E_{ij}^0 + n\hbar\omega) \tag{2.98}$$

where H_{int} is the interaction Hamiltonian that generally represents electron-photon coupling for radiative recombination, electron-phonon coupling for internal conversion,

and spin-orbit coupling for intersystem crossing. $\delta(\Delta E_{ij}^0 + n\hbar\omega)$ ensures the energy conservation in transition $\left|i^0\right\rangle \rightarrow \left|j^0\right\rangle$, with ΔE_{ij}^0 being the energy difference between states $\left|i^0\right\rangle$ and $\left|j^0\right\rangle$, and $\hbar\omega$ being the energy gain or loss of the system in the manner of either photon or phonon.

Second, we need to consider zero-field splitting (ZFS) and the Zeeman effect as the Hamiltonian in Eq. (2.99), which is the source of magnetic field dependency and the splitting of the spin sublevels.

$$H = D(S_z^2 - \frac{\mathbf{S}^2}{3}) + E(S_x^2 - S_y^2) + g\mu_B \mathbf{B} \cdot \mathbf{S} \tag{2.99}$$

where S_i is the spin-1 operator along i axis, D in the first term is the axial zero-field splitting (ZFS) parameter, E in the second term is the rhombic ZFS parameter, g is the electron g-factor whose value is $\sim$2 in the case of the NV center, μ_B is Bohr magneton, and $\mathbf{B}$ is the magnetic field vector. By expanding the Hamiltonian with using Kronecker product of Pauli's matrices, we can find

$$H = \begin{pmatrix} D/3 + g\mu_B B_z & g\mu_B(B_x - iB_y)/2 & g\mu_B(B_x - iB_y)/2 & E \\ g\mu_B(B_x + iB_y)/2 & -D/3 & -D/3 & g\mu_B(B_x - iB_y)/2 \\ g\mu_B(B_x + iB_y)/2 & -D/3 & -D/3 & g\mu_B(B_x - iB_y)/2 \\ E & g\mu_B(B_x + iB_y)/2 & g\mu_B(B_x + iB_y)/2 & D/3 - g\mu_B B_z \end{pmatrix} \tag{2.100}$$

When the magnetic field in along the z direction, we can find the eigenvalues and

eigenvectors as follows,

$$\lambda_1 = -2D/3 \quad \lambda_2 = D/3 - \sqrt{E^2 + (g\mu_B B_z)^2}\ \lambda_3 = D/3 + \sqrt{E^2 + (g\mu_B B_z)^2} \quad \lambda_4 = 0. \tag{2.101}$$

$$|\nu_1\rangle = \frac{1}{\sqrt{2}} \begin{pmatrix} 0 \\ 1 \\ 1 \\ 0 \end{pmatrix} \ |\nu_2\rangle = \frac{1}{\sqrt{E^2 + C'^2}} \begin{pmatrix} E \\ 0 \\ 0 \\ -C' \end{pmatrix} \ |\nu_3\rangle = \frac{1}{\sqrt{E^2 + C'^2}} \begin{pmatrix} C' \\ 0 \\ 0 \\ E \end{pmatrix} \ |\nu_4\rangle = \frac{1}{\sqrt{2}} \begin{pmatrix} 0 \\ 1 \\ -1 \\ 0 \end{pmatrix} \tag{2.102}$$

where $C' = g\mu_B B_z + \sqrt{E^2 + (g\mu_B B_z)^2}$. $|\nu_1\rangle$ is the zero spin projection $|0\rangle$ of triplet state, and $|\nu_4\rangle$ is a singlet state which can be dropped off as it does not have spin-spin interaction. The eigenvectors $|\nu_2\rangle$ and $|\nu_3\rangle$ are respectively $|-\rangle$ and $|+\rangle$ of triplet states, which are the linear combination of $|+1\rangle$ and $|-1\rangle$. Particularly, in the high magnetic field limit, we have

$$\begin{aligned} \lim_{B_z \to \infty} |\nu_2\rangle &= -\,|-1\rangle \\ \lim_{B_z \to \infty} |\nu_3\rangle &= |+1\rangle\,. \end{aligned} \tag{2.103}$$

In the case where the rhombic ZFS $E = 0$, then $|-1\rangle$ and $|+1\rangle$ are degenerate at zero magnetic field, and separated with no spin mixing in the presence of a nonzero magnetic field along z direction.

ZFS lifts the degeneracy of spin sublevels, and Zeeman effect specifically can lead to the mixing of the original spin sublevels at zero magnetic field. Thus, when

there is magnetic field, the eigenstates $|i\rangle$ of the Hamiltonian Eq. (2.99) are the linear combination of the eigenstates $\left|j^0\right\rangle$ at zero magnetic field, with mixing coefficient $\alpha_{ij}(\mathbf{B})$.

$$|i\rangle = \sum_j \alpha_{ij}(\mathbf{B}) \left|j^0\right\rangle \tag{2.104}$$

The spin mixing has direct effect on transition rates. While the energy change by the ZFS and Zeeman effect is negligible compared to the energy difference between the electronic energy levels, the condition of energy conservation remains nearly the same, i.e. $\Delta E_{ij} \approx \Delta E^0_{pq}$. As a result, the transition rates are magnetic field dependent and expressed as

$$\begin{aligned} k_{ij}(\mathbf{B}) &= \frac{2\pi}{\hbar} \left| \langle i|H^{int}|j\rangle \right|^2 \delta(\Delta E_{ij} + \hbar\omega) \\ &\approx \frac{2\pi}{\hbar} \sum_{p,q} \left| \left\langle p^0\right|\alpha^*_{ip}(\mathbf{B}) H^{int} \alpha(\mathbf{B})_{jq} \left|q^0\right\rangle \right|^2 \delta(\Delta E^0_{pq} + \hbar\omega) \\ &= \sum_{p,q} |\alpha_{ip}(\mathbf{B})|^2 |\alpha_{jq}(\mathbf{B})|^2 k^0_{pq}. \end{aligned} \tag{2.105}$$

As for the radiative recombination, we only consider the spin-conserving case. Then the mixing of the spin sublevels of the triplet states $|\alpha_{ip}(\mathbf{B})|^2|\alpha_{jq}(\mathbf{B})|^2$ will lead to decreased spin-conserving and enhanced spin-flip radiative recombination between triplet ground state and excited state. Thus, the radiative recombination rate between triplet states decreases with magnetic field. In terms of the radiative recombination between two singlet states, the rate is not changed by magnetic field because there is no spin mixing within singlet states. The same rule applies to internal conversion (IC). For ISC, the mixing of the spin sublevels reduces the contrast between the axial and nonaxial ISC rates, resulting in decrease of ODMR contrast.

2.5 First-Principles Density-Matrix Dynamics

The first-principles density-matrix dynamics (FPDM) is an advanced approach that allows long-time simulation for open quantum systems in non-equilibrium state. In the following sections, the basic of the FPDM approach is presented, and the derivation details can be found from Ref. [71, 72, 73, 74, 75].

This theory starts from the Liouville-von Neumann equation in the Schrödinger picture,

$$\frac{d\rho\left(t\right)}{dt} = -\frac{i}{\hbar}[H, \rho\left(t\right)], \tag{2.106}$$

$$H = H_0 + H', \tag{2.107}$$

where H, H_0, and H' are total, unperturbed and perturbation Hamiltonians, respectively. A few approxmiation are considered in this framework to allow pratical simultaions of ultrafast dynamics, including single-particle approximation for the density matrix [76], a proper truncated BBGKY (Bogolyubov-Born-Green-Kirkwood-Yvon) hierarchy [77, 78] and the Mar kov approximation. The whole density matrix can be decomposed into the coherent part and the scattering part as below,

$$\frac{d\rho}{dt} = \frac{d\rho}{dt}|_{\text{coh}} + \frac{d\rho}{dt}|_{\text{scatt}}, \tag{2.108}$$

where $\frac{d\rho}{dt}|_{\text{coh}}$ describes the coherent dynamics of electrons including the free-particle dynamics, the laser-induced dynamics, electric field-induced dynamics and magnetic field-induced dynamics. $\frac{d\rho}{dt}|_{\text{scatt}}$ includes all the decoherence processes, such as electron-electron interaction, electron-phonon interaction and electron-impurity interaction.

Some important findings by using this approach are presented in Chapter 6 and Chapter 7 for perovskites. The ongoing development of this approach includes incorporating a complete description of electron-electron interactions in coherent dynamics, which was previously missing, and addressing the band renormalization effect.

Chapter 3

Application of Group Theory

3.1 Group Theory for Spin Defects: the NV Center Example

The NV center in diamond, characterized by its robust and clear structure, bright emission, high contrast in optically-detected magnetic resonance (ODMR), and high sensitivity to external magnetic fields, is a prototypical example in the realm of spin defects. Understanding the NV center is, therefore, crucial for studying spin defects and discovering new defects to enhance their performance.

In this chapter, we focus on the symmetry of the NV center, derive the irreducible representations of the electronic states and spin-orbit coupling operators, understand whether an SOC matrix element is allowed or forbidden from the symmetry point of view, and finally estimate the result of the coupling between the Jahn-Teller effects and the SOC.

The full derivation, combined with the first-principles calculations presented in this thesis, will provide a comprehensive understanding of the NV center and allow to clarify many previously unclear experimental observations, including the allowed radiative recombination, intersystem crossing, internal conversion, and ODMR contrast.

3.2 Introduction to Group Theory

In this section, we introduce the basic concepts of group theory that are essential for the symmetry analysis of spin defects, following the approach in the book by Dresselhaus et al. [79]. Only the necessary derivations will be presented here, and the fundamental proofs can be found in the referenced book. The C_{3v} point group will be shown as an example.

3.2.1 Definition of a Group

A group is a collection $\{A, B, C, D...\}$ of elements that satisfy the following four conditions [79]:

- Closure: the product of any two elements of the group is also an element of the group. Mathematically, this is expressed as $AB = C$.
- Association: $A(BC) = (AB)C$.
- Identity element: there exists an element E such that for any element of the group, the relationship $EA = AE = A$ holds.

- Inverse element: for any element A in the group, there exists an element A^{-1} such that $AA^{-1} = A^{-1}A = E$.

3.2.2 Multiplication of Symmetry Operations

Table 3.1: Table of multiplication of symmetry operations of C_{3v} group. The result is the multiplication of row element by column element. In total there are six symmetry operations or six elements in the group.

C_{3v}	E	C_3	C_3^{-1}	σ_v	σ_v'	σ_v''
E	E	C_3	C_3^{-1}	σ_v	σ_v'	σ_v''
C_3	C_3	C_3^{-1}	E	σ_v'	σ_v''	σ_v
C_3^{-1}	C_3^{-1}	E	C_3	σ_v''	σ_v	σ_v'
σ_v	σ_v	σ_v''	σ_v'	E	C_3^{-1}	C_3
σ_v'	σ_v'	σ_v	σ_v''	C_3	E	C_3^{-1}
σ_v''	σ_v''	σ_v'	σ_v	C_3^{-1}	C_3	E

By the multiplication of all the elements in the C_{3v} set, we can demonstrate it to be a group because it satisfies the conditions of closure, association, identity element and inverse element. The details of the multiplication of the group elements can be seen in Sec. 3.4.

By definition, the order of a group is equivalent to the number of elements in the group. According to Table 3.1, the order of C_{3v} is $h = 6$.

3.2.3 Conjugation and Class

The definition of conjugation: an element B is conjugate to A if B is defined as $B \equiv XAX^{-1}$, where X is an arbitrary element of the group.

A class is defined as the set of all elements that can be obtained from a given element through conjugation.

These concepts of conjugation and class are always used in the character table for categorizing symmetry operations or elements that correspond to distinct kinds of symmetry operation. By these definitions, we can categorize the elements of C_{3v} group into three classes:

- E (identity symmetry element)
- C_3 and C_3^{-1} (rotation operations of $2\pi/3$ about the C_3 axis)
- σ_v, σ_v' and σ_v'' (reflection operations about the three equivalent planes)

3.3 Theory of Group Representation and Orthogonality Theorem

The concept of representation, especially irreducible representation, is important and useful in describing eigenstates or energy levels. By labeling eigenstates with the irreducible representation, to which it transforms, we can immediately understand the degeneracy of the eigenstates, and obtain the result of symmetry operations without knowing the explicit expressions of the eigenstates.

The subsequent orthogonality theorem serves as a key application of group theory in quantum mechanics.

3.3.1 Group Representation

The concept of representation is introduced with the definition of homomorphism. In general, a representation Γ of a group G in a vector space V is defined by a homomorphism,

$$\Gamma : G \to \mathrm{GL}(V) \tag{3.1}$$

where $\mathrm{GL}(V)$ is the group of invertible linear operators on V. This abstract group representation can be more intuitive when we take the form of the matrix representation $D^{(\Gamma)}$ of a group G with the homomorphism,

$$D^{(\Gamma)} : G \to \mathrm{GL}(n, \mathbb{F}) \tag{3.2}$$

where $\mathrm{GL}(n, \mathbb{F})$ is the general linear group of degree n over a field $\mathbb{F}$ ($\mathbb{F} = \mathbb{R}$ or $\mathbb{C}$), the set of $n \times n$ invertible matrices. The dimensionality of a representation is equal to the degree or dimensionality n of each of its matrices.

However, a matrix representation can be non-unique when it is equivalent to other matrices by a similarity transformation, and the non-uniqueness introduces ambiguity in its application, like labeling eigenstates. This kind of representations are so-called reducible representations, whose matrices can be written as the combination

of the blocks as below,

$$\begin{pmatrix} D^{(\Gamma_1)}(R) & \mathcal{O} \\ \mathcal{O} & D^{(\Gamma_2)}(R) \end{pmatrix} \tag{3.3}$$

where $\mathcal{O} = (m \times n)$ matrix of zeros, R is the symmetry operation, Γ_1 and Γ_2 are the irreducible representations, which can be either distinct or identical.

The irreducible representations and character in Sec. 3.4 are introduced and defined in order to eliminate such ambiguity. It can be clear by the example of Eq. (3.3), an irreducible representation cannot be decomposed or reduced into smaller, non-trivial representations. In other words, the dimensionality of an irreducible representation cannot be further reduced.

3.3.2 Orthogonality Theorem

For the purposes of applying group theory, we will omit the rigorous proof of the orthogonality theorem, which relies on Schur's lemma. The statement of the orthogonality theorem is given as below,

$$\sum_R D^{(\Gamma_j)}_{\mu\nu}(R) D^{(\Gamma_{j'})}_{\mu'\nu'}(R^{-1}) = \frac{h}{l_j} \delta_{\Gamma_j,\Gamma_{j'}} \delta_{\mu\mu'} \delta_{\nu\nu'} \tag{3.4}$$

where $D^{(\Gamma_j)}$ and $D^{(\Gamma_{j'})}$ represent the matrices of the representations Γ_j and $\Gamma_{j'}$ that has dimensionalities of l_j and $l_{j'}$, respectively. The summation over R includes all the h elements of the group. μ, ν, μ' and ν' are the row and column indices of the matrix representations.

3.4 C_{3v} Point Group and the Character Table

By definition, the character of the matrix representation $\chi^{(\Gamma_j)}(R)$ for a symmetry operation R in a representation $D^{(\Gamma_j)}(R)$ is given by the trace of the representation matrix,

$$\chi^{(\Gamma_j)}(R) = \mathrm{Tr}(D^{(\Gamma_j)}(R)) = \sum_{\mu\mu}^{l_j} D^{(\Gamma_j)}(R)_{\mu\mu} \tag{3.5}$$

where l_j is the dimensionality of the representation Γ_j, and j is a representation index. It can be proved that the character for each element in a class is the same.

With the definition of character in Eq. (3.5) and the orthogonality theorem in Eq. (3.4), we can prove the orthogonality theorem for character as follows,

$$\sum_R \chi^{(\Gamma_j)}(R)\chi^{(\Gamma_{j'})}(R^{-1}) = \sum_R \chi^{(\Gamma_j)}(R)\left[\chi^{(\Gamma_{j'})}(R)\right]^* = h\delta_{\Gamma_j,\Gamma_{j'}} \tag{3.6}$$

$$\sum_{\Gamma_j} \chi^{(\Gamma_j)}(\mathcal{C}_k)\left[\chi^{(\Gamma_j)}(\mathcal{C}_{k'})\right]^* = h\delta_{kk'} \tag{3.7}$$

where the summation are over the symmetry operation R and class $\mathcal{C}$, respectively, and the index k' is the k'-th component of a k-dimensional vector. Also, we can obtain the following very useful theorems for constructing a character table,

- Theorem: a reducible representation can be decomposed into a direct sum of the irreducible representations,

$$\chi(\mathcal{C}_k) = \sum_{\Gamma_j} a_j \chi^{(\Gamma_j)}(\mathcal{C}_k) \tag{3.8}$$

  where a_j is the number of the irreducible representation Γ_j that is contained in the reducible representation.

- Theorem: the number of irreducible representations is equal to the number of classes.

The above definitions and theorems allow us to perform the following derivation.

Table 3.2: C_{3v} character table. Each character is the trace of the irreducible matrix representation.

C_{3v}	E	$2C_3$	$3\sigma_v$	linear functions rotations	quadratic functions
A_1	1	1	1	z	$x^2+y^2,\ z^2$
A_2	1	1	-1	R_z	–
E	2	-1	0	$(x,y),\ (R_x,R_y)$	$(x2-y2,xy),\ (xz,yz)$

In the character table, E is the identical operation, $2C_3$ including C_3 and C_3^{-1} are the rotation symmetry operation, and $3\sigma_v$ including σ_v, σ_v' and σ_v'' are the reflection symmetry operations.

By the convention[1], the rotation operation is applied on the object rather than the coordinates. Because the counterclockwise rotation of the object corresponds to the clockwise rotation of the coordinate, the Cartesian representation of C_n, the rotation operation by $2\pi/n$ on the coordinate about the principle rotation axis (z-axis here), is

[1] see Sec. 2-2. on page 8 and Chap. 4 on page 64 of Ref. [80]

expressed as

$$C_n = \begin{pmatrix} cos(2\pi/n) & sin(2\pi/n) & 0 \\ -sin(2\pi/n) & cos(2\pi/n) & 0 \\ 0 & 0 & 1 \end{pmatrix}. \tag{3.9}$$

[2]

And σ_v denotes the reflection operation with respect to the xz-plane, equivalent to a rotation through π about y-axis followed by an inversion symmetry operation [81]. Therefore, σ_v keeps x-axis and z-axis unchanged meanwhile reflect y-axis with respect to the xz-plane. It should be noticed that the symmetry operation on the coordinates is the inverse of that on the object $P_R f(\mathbf{x}) = f(\mathbf{R}^{-1}\mathbf{x})$. Therefore, $\sigma_v' = \sigma_v C_3(\text{obj})$ on the object is equivalent to $\sigma_v' = C_3(\text{coord})\sigma_v$ on the coordinates.

Following Eq. (3.9), the irreducible matrix Cartesian representations of E' under each symmetry operation upon coordinates are as follows [82],

$$\begin{aligned} E &= \begin{pmatrix} 1 & 0 \\ 0 & 1 \end{pmatrix} \qquad C_3 = \begin{pmatrix} -\frac{1}{2} & \frac{\sqrt{3}}{2} \\ -\frac{\sqrt{3}}{2} & -\frac{1}{2} \end{pmatrix} \\ C_3^{-1} &= \begin{pmatrix} -\frac{1}{2} & -\frac{\sqrt{3}}{2} \\ \frac{\sqrt{3}}{2} & -\frac{1}{2} \end{pmatrix} \qquad \sigma_v = \begin{pmatrix} 1 & 0 \\ 0 & -1 \end{pmatrix} \\ \sigma_v' = C_3\sigma_v &= \begin{pmatrix} -\frac{1}{2} & -\frac{\sqrt{3}}{2} \\ -\frac{\sqrt{3}}{2} & \frac{1}{2} \end{pmatrix} \qquad \sigma_v'' = C_3^{-1}\sigma_v = \begin{pmatrix} -\frac{1}{2} & \frac{\sqrt{3}}{2} \\ \frac{\sqrt{3}}{2} & \frac{1}{2} \end{pmatrix} \end{aligned} \tag{3.11}$$

[2]The rotation matrix of C_n on the object counterclockwise

$$C_n(\text{obj}) = \begin{pmatrix} cos(2\pi/n) & -sin(2\pi/n) & 0 \\ sin(2\pi/n) & cos(2\pi/n) & 0 \\ 0 & 0 & 1 \end{pmatrix} \tag{3.10}$$

We summarize the irreducible representations of C_{3v} with symmetry operations on the coordinates in Table 3.3.

Table 3.3: Table of the irreducible matrix representations of C_{3v} for symmetry operations on the Cartesian coordinates (x, y) [17]. The coordinates transform under symmetry operation as $P_R(x, y)^T \rightarrow \mathbf{R}^{-1}(x, y)^T$, where $\mathbf{R}^{-1}$ is the representation matrix of symmetry operation P_R.

C_{3v}	E	C_3	C_3^{-1}
A_1	1	1	1
A_2	1	1	1
E	$\begin{pmatrix} 1 & 0 \\ 0 & 1 \end{pmatrix}$	$\begin{pmatrix} -\frac{1}{2} & \frac{\sqrt{3}}{2} \\ -\frac{\sqrt{3}}{2} & -\frac{1}{2} \end{pmatrix}$	$\begin{pmatrix} -\frac{1}{2} & -\frac{\sqrt{3}}{2} \\ \frac{\sqrt{3}}{2} & -\frac{1}{2} \end{pmatrix}$

C_{3v}	σ_v	σ_v'	σ_v''
A_1	1	1	1
A_2	-1	-1	-1
E	$\begin{pmatrix} 1 & 0 \\ 0 & -1 \end{pmatrix}$	$\begin{pmatrix} -\frac{1}{2} & -\frac{\sqrt{3}}{2} \\ -\frac{\sqrt{3}}{2} & \frac{1}{2} \end{pmatrix}$	$\begin{pmatrix} -\frac{1}{2} & \frac{\sqrt{3}}{2} \\ \frac{\sqrt{3}}{2} & \frac{1}{2} \end{pmatrix}$

Likewise, we can also write down the table of the matrix representations for the symmetry operation on an object.

Table 3.4: Table of the irreducible matrix representations of C_{3v} for symmetry operations on the object. The object transforms under symmetry operation as $P_R(x, y) \rightarrow (x, y)\mathbf{R}$, consistent with Eq. (3.12). $\mathbf{R}$ is the representation matrix of symmetry operation P_R.

C_{3v}	E	C_3	C_3^{-1}
A_1	1	1	1
A_2	1	1	1
E	$\begin{pmatrix} 1 & 0 \\ 0 & 1 \end{pmatrix}$	$\begin{pmatrix} -\frac{1}{2} & -\frac{\sqrt{3}}{2} \\ \frac{\sqrt{3}}{2} & -\frac{1}{2} \end{pmatrix}$	$\begin{pmatrix} -\frac{1}{2} & \frac{\sqrt{3}}{2} \\ -\frac{\sqrt{3}}{2} & -\frac{1}{2} \end{pmatrix}$

C_{3v}	σ_v	$\sigma_v' = \sigma_v C_3$	$\sigma_v'' = \sigma_v C_3^{-1}$
A_1	1	1	1
A_2	-1	-1	-1
E	$\begin{pmatrix} 1 & 0 \\ 0 & -1 \end{pmatrix}$	$\begin{pmatrix} -\frac{1}{2} & -\frac{\sqrt{3}}{2} \\ -\frac{\sqrt{3}}{2} & \frac{1}{2} \end{pmatrix}$	$\begin{pmatrix} -\frac{1}{2} & \frac{\sqrt{3}}{2} \\ \frac{\sqrt{3}}{2} & \frac{1}{2} \end{pmatrix}$

3.5 Projection Operator

If $\varphi_\kappa^{(j)}$ is a basis function of the κ-th column (κ is defined as row index conventionally [80]) of the j-th irreducible representation Γ_j, and $\varphi_\lambda^{(j)}$ is the basis function's partner completing the basis for $\varphi_\kappa^{(j)}$, then the symmetry operation P_R of any element

R on $\varphi_\kappa^{(j)}$ can be expressed as a linear combination of $\varphi_\kappa^{(j)}$ and its partners $\varphi_\lambda^{(j)}$ [80],

$$P_R\varphi_\kappa^{(j)} = \sum_{\lambda=1}^{l_j} \varphi_\lambda^{(j)} D^{(\Gamma_j)}(R)_{\lambda\kappa} \tag{3.12}$$

Projection operator $\mathcal{P}_{\lambda\kappa}^{(j)}$ can be derived from the above with the great orthogonality theorm,

$$\mathcal{P}_{\lambda\kappa}^{(j)} = \frac{l_j}{h} \sum_R D^{(\Gamma_j)}(R)^*_{\lambda\kappa} P_R \tag{3.13}$$

where l_j is the dimensionality of the matrix of the irreducible representation Γ_j, h is the number of elements in the group or the order of the group, $D^{(\Gamma_j)}(R)_{\lambda\kappa}$ is the character belonging to the λ-th row and κ-th column of the matrix reprentation of Γ_j for the element R [3], and P_R is the symmetry operator. The projection operator can be used to extract a function that transforms as $\Gamma_j(R)_{\lambda\kappa}$,

$$\varphi_\lambda^{(j)} = \mathcal{P}_{\lambda\kappa}^{(j)} \varphi_\kappa^{(j)} = \frac{l_j}{h} \sum_R D^{(\Gamma_j)}(R)^*_{\lambda\kappa} P_R \varphi_\kappa^{(j)} \tag{3.14}$$

Because of the orthogonality property of the projection operator, $\varphi_\lambda^{(j)}$ is expected to be either transforming as $D_\lambda^{(\Gamma_j)}$ or 0 after the projection $P_{\lambda\kappa}^{(j)}$ on the basis function $\varphi_\kappa^{(j)}$. The result of the projection on different basis functions $\varphi_\kappa^{(j)}$, which belong to κ-th column of the $D^{(\Gamma_j)}$, can differ by a factor of constant. The factor does not influence the symmetry and can be eliminated by normalizing the projection result. Therefore, a single projection onto a known or constructed basis $\varphi_\kappa^{(j)}$ will be sufficient to determine $\varphi_\lambda^{(j)}$ if the projection is nonzero.

If dealing with the direct product of multiple bases, we can perform the fol-

[3] It should be noticed that κ-th column is explained as κ-th row on page 40 of Ref. [80]

lowing,

$$
\begin{aligned}
P_R\varphi_\kappa^{(i)} \otimes P_R\varphi_\mu^{(j)} &= \sum_{\lambda=1}^{l_i} \varphi_\lambda^{(i)} D^{(\Gamma_i)}(R)_{\lambda\kappa} \otimes \sum_{\nu=1}^{l_j} \varphi_\nu^{(j)} D^{(\Gamma_j)}(R)_{\nu\mu} \\
&= \sum_{\lambda=1}^{l_i} \sum_{\nu=1}^{l_j} \varphi_\lambda^{(i)} \varphi_\nu^{(j)} D^{(\Gamma_i)}(R)_{\lambda\kappa} D^{(\Gamma_j)}(R)_{\nu\mu} \\
&= \sum_{\lambda=1}^{l_i} \sum_{\nu=1}^{l_j} \varphi_\lambda^{(i)} \varphi_\nu^{(j)} \Gamma(R)_{\lambda\nu,\kappa\mu} \\
&= P_R \otimes P_R \varphi_\kappa^{(i)} \varphi_\mu^{(j)}
\end{aligned}
\tag{3.15}
$$

3.6 Representations of Electronic States

The final electronic states contain both the orbital part and the spin part. The projection operator above allows us to construct an electronic state that satisfy a certain symmetry, in other words, determine the expression of an electronic state that transforms as a certain irreducible representation. Because the electronic states can be expressed as the linear combination of the atomic orbitals and spins, we need to first understand the number of orbitals and spins that can be significant and should be involved in an active space.

3.6.1 Representation of Single-Particle Wavefunction

The NV center is comprised of one N atom substituted for a C atom, one vacancy by removing a C atom, and one electron from the external that results in the negatively charged defect. As shown in Fig. 3.1, four dangling bonds are formed by removing a C atom, three of which form as the σ[4] bonds located at the nearest neighbor

[4]The σ notation for chemical bonds is only used in this sub section, and should be not confused with σ in the other sections for the Pauli's matrices.

C atoms, denoted as σ_1, σ_2 and σ_3. The other one forms as the σ bond located at the N atom, denoted as σ_N. Furthermore, one can notice the additional two electrons, one from the N atom and one from the external. These two electrons may form a lone pair that have less contribution to the active space. Therefore, the minimal active space that can give rise to meaningful result should contains at least four electrons, or equivalently two holes for the triplet NV center [1, 83].

Here, we show how the derivation of single-particle wavefunction with only the orbital part from the atomic orbitals in the chosen active space.

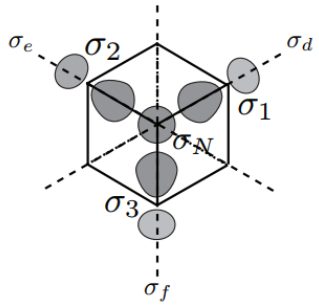

Figure 3.1: Schematic diagram of dangling bonds σ_1, σ_2, σ_3 and σ_N of NV centers with the symmetry axis pointing along the N-V axis, which is out-of-plane [1].

The irreducible matrix representations of the C_{3v} point group on the four-dimentional space formed by the four bases of orbitals are shown in Table 3.5.

Table 3.5: Table of the irreducible matrix representations of C_{3v} for symmetry operations on the coordinates σ_d, σ_e, σ_f and σ_n, or upon the bases of orbitals σ_1, σ_2, σ_3 and σ_N. If operating the coordinates, the bases vector transform under symmetry operation as $P_R(\sigma_d, \sigma_e, \sigma_f, \sigma_n) \rightarrow \mathbf{R}(\sigma_d, \sigma_e, \sigma_f, \sigma_n)^T$; if operating the the object, the bases vector transform under symmetry operation as $P_R(\sigma_1, \sigma_2, \sigma_3, \sigma_N) \rightarrow (\sigma_1, \sigma_2, \sigma_3, \sigma_N)\mathbf{R}$. Here $\mathbf{R}$ is the symmetry operation matrix.

E	C_3	C_3^{-1}
$\begin{pmatrix} 1 & 0 & 0 & 0 \\ 0 & 1 & 0 & 0 \\ 0 & 0 & 1 & 0 \\ 0 & 0 & 0 & 1 \end{pmatrix}$	$\begin{pmatrix} 0 & 0 & 1 & 0 \\ 1 & 0 & 0 & 0 \\ 0 & 1 & 0 & 0 \\ 0 & 0 & 0 & 1 \end{pmatrix}$	$\begin{pmatrix} 0 & 1 & 0 & 0 \\ 0 & 0 & 1 & 0 \\ 1 & 0 & 0 & 0 \\ 0 & 0 & 0 & 1 \end{pmatrix}$

σ_v	$\sigma_v' = \sigma_v C_3$	$\sigma_v'' = \sigma_v C_3^{-1}$
$\begin{pmatrix} 1 & 0 & 0 & 0 \\ 0 & 0 & 1 & 0 \\ 0 & 1 & 0 & 0 \\ 0 & 0 & 0 & 1 \end{pmatrix}$	$\begin{pmatrix} 0 & 0 & 1 & 0 \\ 0 & 1 & 0 & 0 \\ 1 & 0 & 0 & 0 \\ 0 & 0 & 0 & 1 \end{pmatrix}$	$\begin{pmatrix} 0 & 1 & 0 & 0 \\ 1 & 0 & 0 & 0 \\ 0 & 0 & 1 & 0 \\ 0 & 0 & 0 & 1 \end{pmatrix}$

Table 3.6: The transformation of dangling bonds of NV center under the symmetry operations of C_{3v} point group.

P_R	E	C_3	C_3^{-1}	σ_v	σ_v'	σ_v''
σ_1	σ_1	σ_2	σ_3	σ_1	σ_3	σ_2
σ_2	σ_2	σ_3	σ_1	σ_3	σ_2	σ_1
σ_3	σ_3	σ_1	σ_2	σ_2	σ_1	σ_3
σ_N	σ_N	σ_N	σ_N	σ_N	σ_N	σ_N

According to Figure 3.1 and Table 3.6, it is obvious that dangling bond σ_N transforms as totally symmetric representation A_1 ($\mathcal{P}^{A_2}\sigma_N = \mathcal{P}^{E_x}\sigma_N = \mathcal{P}^{E_y}\sigma_N = 0$). By using the projection operator technique Eq. (3.14), the single-particle wavefunction can be expressed as

$$\begin{aligned} a_1 = \varphi_1^{a_1} &= \mathcal{P}^{A_1}(\alpha'\sigma_1 + \beta'\sigma_N) \\ &= \frac{1}{6}\Big[\left(P_E + P_{C_3} + P_{C_3^{-1}} + P_{\sigma_v} + P_{\sigma_v'} + P_{\sigma_v''}\right)\alpha'\sigma_1 \\ &\quad + \left(P_E + P_{C_3} + P_{C_3^{-1}} + P_{\sigma_v} + P_{\sigma_v'} + P_{\sigma_v''}\right)\beta'\sigma_N\Big] \\ &= \frac{1}{6}\left(\alpha'\sigma_1 + \alpha'\sigma_2 + \alpha'\sigma_3 + \alpha'\sigma_1 + \alpha'\sigma_3 + \alpha'\sigma_2 + 6\beta'\sigma_N\right) \\ &= \frac{1}{3}\alpha'(\sigma_1 + \sigma_2 + \sigma_3) + \beta'\sigma_N \end{aligned} \tag{3.16}$$

where α' and β' are factors of weight.

$$
\begin{aligned}
e_x = \varphi_1^{e_x} &= \mathcal{P}^{E_x}\sigma_1 \\
&= \frac{2}{6}\Big\{\Big[E_{xx}(E)\sigma_1 + E_{yx}(E)\sigma_1\Big] + \Big[E_{xx}(C_3)\sigma_2 + E_{yx}(C_3)\sigma_2\Big] \\
&\quad + \Big[E_{xx}(C_3^{-1})\sigma_3 + E_{yx}(C_3^{-1})\sigma_3\Big] + \Big[E_{xx}(\sigma_v)\sigma_1 + E_{yx}(\sigma_v)\sigma_1\Big] \\
&\quad + \Big[E_{xx}(\sigma_v')\sigma_3 + E_{yx}(\sigma_v')\sigma_3\Big] + (E_{xx}(\sigma_v'')\sigma_2 + E_{yx}(\sigma_v'')\sigma_2)\Big\} \\
&= \frac{2}{6}\Big[(1+0)\sigma_1 + (-\frac{1}{2} - \frac{\sqrt{3}}{2})\sigma_2 + (-\frac{1}{2} + \frac{\sqrt{3}}{2})\sigma_3 \\
&\quad + (1+0)\sigma_1 + (-\frac{1}{2} - \frac{\sqrt{3}}{2})\sigma_3 + (-\frac{1}{2} + \frac{\sqrt{3}}{2})\sigma_2\Big] \\
&= \frac{1}{3}(2\sigma_1 - \sigma_2 - \sigma_3)
\end{aligned}
\tag{3.17}
$$

$$
\begin{aligned}
e_y = \varphi_1^{e_y} &= \mathcal{P}^{E_y}\sigma_1 \\
&= \frac{2}{6}\Big\{\Big[E_{xy}(E)\sigma_1 + E_{yy}(E)\sigma_1\Big] + \Big[E_{xy}(C_3)\sigma_2 + E_{yy}(C_3)\sigma_2\Big] \\
&\quad + \Big[E_{xy}(C_3^{-1})\sigma_3 + E_{yy}(C_3^{-1})\sigma_3\Big] + \Big[E_{xy}(\sigma_v)\sigma_1 + E_{yy}(\sigma_v)\sigma_1\Big] \\
&\quad + \Big[E_{xy}(\sigma_v')\sigma_3 + E_{yy}(\sigma_v')\sigma_3\Big] + \Big[E_{xy}(\sigma_v'')\sigma_2 + E_{yy}(\sigma_v'')\sigma_2\Big]\Big\} \\
&= \frac{2}{6}\Big[(0+1)\sigma_1 + (\frac{\sqrt{3}}{2} - \frac{1}{2})\sigma_2 + (-\frac{\sqrt{3}}{2} - \frac{1}{2})\sigma_3 \\
&\quad + (0-1)\sigma_1 + (-\frac{\sqrt{3}}{2} + \frac{1}{2})\sigma_3 + (\frac{\sqrt{3}}{2} + \frac{1}{2})\sigma_2\Big] \\
&= \frac{1}{\sqrt{3}}(\sigma_2 - \sigma_3)
\end{aligned}
\tag{3.18}
$$

The single-particle wavefunction can be renormalized. Similarly, one can use the projection operator technique Eq. (3.14) to extract the multi-electron configuration and spin-orbit wavefunctions.

3.6.2 Representation of Two-Particle Wavefunction

For simplicity, we consider to use the hole representations to extract the orbital part of the total electronic wavefunction. We apply symmetry operations on the coordinate to find the irreducible representations of the single-particle states.

Let e_x and e_y be the vectors along x-axis and y-axis, respectively.

$$e_x = \begin{pmatrix} 1 \\ \\ 0 \end{pmatrix} \qquad e_y = \begin{pmatrix} 0 \\ \\ 1 \end{pmatrix}. \tag{3.19}$$

By doing symmetry operations on the coordinates as Table 3.3, we can find that e_x and e_y transform as follows

$$P_{C_3}e_x = C_3e_x = -\frac{1}{2}e_x + \frac{\sqrt{3}}{2}e_y \qquad P_{C_3}e_y = C_3e_y = -\frac{\sqrt{3}}{2}e_x - \frac{1}{2}e_y \tag{3.20}$$

$$P_{C_3^{-1}}e_x = C_3^{-1}e_x = -\frac{1}{2}e_x - \frac{\sqrt{3}}{2}e_y \qquad P_{C_3^{-1}}e_y = C_3^{-1}e_y = \frac{\sqrt{3}}{2}e_x - \frac{1}{2}e_y \tag{3.21}$$

$$P_{\sigma_v}e_x = \sigma_v e_x = e_x \qquad P_{\sigma_v}e_y = \sigma_v e_y = -e_y \tag{3.22}$$

$$P_{\sigma_v'}e_x = \sigma_v' e_x = -\frac{1}{2}e_x - \frac{\sqrt{3}}{2}e_y \qquad P_{\sigma_v'}e_y = \sigma_v' e_y = -\frac{\sqrt{3}}{2}e_x + \frac{1}{2}e_y \tag{3.23}$$

$$P_{\sigma_v''}e_x = \sigma_v'' e_x = -\frac{1}{2}e_x + \frac{\sqrt{3}}{2}e_y \qquad P_{\sigma_v''}e_y = \sigma_v'' e_y = \frac{\sqrt{3}}{2}e_x + \frac{1}{2}e_y \tag{3.24}$$

Table 3.7: C_{3v} symmetry operations on the single-particle wavefunction based on Eq. (3.11) and Table 3.4.

P_R	E	C_3	C_3^{-1}	σ_v	σ_v'	σ_v''
a_1	a_1	a_1	a_1	a_1	a_1	a_1
e_x	e_x	$-\frac{1}{2}e_x + \frac{\sqrt{3}}{2}e_y$	$-\frac{1}{2}e_x - \frac{\sqrt{3}}{2}e_y$	e_x	$-\frac{1}{2}e_x - \frac{\sqrt{3}}{2}e_y$	$-\frac{1}{2}e_x + \frac{\sqrt{3}}{2}e_y$
e_y	e_y	$-\frac{\sqrt{3}}{2}e_x - \frac{1}{2}e_y$	$\frac{\sqrt{3}}{2}e_x - \frac{1}{2}e_y$	$-e_y$	$-\frac{\sqrt{3}}{2}e_x + \frac{1}{2}e_y$	$\frac{\sqrt{3}}{2}e_x + \frac{1}{2}e_y$

Table 3.7 shows that single-particle wavefunction a_1 transforms as A_1, and that e_x has its partner e_y. e_x and e_y form the bases of orbitals that transform as the irreducible representation E and are doubly degenerate. Then, we adopt the notation φ_1 and φ_2 to denote the two particles. Next, we can derive the transformation of two-particle wavefunctions, which will be used to construct the orbital part of total wavefunctions. Below, the example of $\varphi_1^{e_x}\varphi_2^{e_x}$ is shown,

$$P_E\varphi_1^{e_x}\varphi_2^{e_x} = P_{\sigma_v}\varphi_1^{e_x}\varphi_2^{e_x} = \varphi_1^{e_x}\varphi_2^{e_x} \tag{3.25}$$

$$\begin{aligned} P_{C_3}\varphi_1^{e_x}\varphi_2^{e_x} &= P_{\sigma_v''}\varphi_1^{e_x}\varphi_2^{e_x} \\ &= \left(-\frac{1}{2}\varphi_1^{e_x} + \frac{\sqrt{3}}{2}\varphi_1^{e_y}\right)\left(-\frac{1}{2}\varphi_2^{e_x} + \frac{\sqrt{3}}{2}\varphi_2^{e_y}\right) \\ &= \frac{1}{4}\varphi_1^{e_x}\varphi_2^{e_x} - \frac{\sqrt{3}}{4}\left(\varphi_1^{e_x}\varphi_2^{e_y} + \varphi_1^{e_y}\varphi_2^{e_x}\right) + \frac{3}{4}\varphi_1^{e_y}\varphi_2^{e_y} \end{aligned} \tag{3.26}$$

$$
\begin{aligned}
P_{C_3^{-1}}\varphi_1^{e_x}\varphi_2^{e_x} &= P_{\sigma_v'}\varphi_1^{e_x}\varphi_2^{e_x} \\
&= \left(-\frac{1}{2}\varphi_1^{e_x} - \frac{\sqrt{3}}{2}\varphi_1^{e_y}\right)\left(-\frac{1}{2}\varphi_2^{e_x} - \frac{\sqrt{3}}{2}\varphi_2^{e_y}\right) \\
&= \frac{1}{4}\varphi_1^{e_x}\varphi_2^{e_x} + \frac{\sqrt{3}}{4}\left(\varphi_1^{e_x}\varphi_2^{e_y} + \varphi_1^{e_y}\varphi_2^{e_x}\right) + \frac{3}{4}\varphi_1^{e_y}\varphi_2^{e_y}
\end{aligned}
\tag{3.27}
$$

By using the projection operator technique Eq. (3.13), we are able to derive the following two-particle wavefunctions (spin eigenstates, only orbital part) as a linear combination of two-particle bases $\varphi_1\varphi_2$ in Table 3.8, transforming like the irreducible representations of C_{3v} point group in Table 3.2. Two examples of different projectors $\mathcal{P}^{A_1}$ and $\mathcal{P}^{E_x}$ are shown below for the details of derivation,

$$
\begin{aligned}
\mathcal{P}^{A_1}\varphi_1^{e_x}\varphi_2^{e_x} &= \frac{1}{6}\left(P_E + P_{C_3} + P_{C_3^{-1}} + P_{\sigma_v} + P_{\sigma_v'} + P_{\sigma_v''}\right)\varphi_1^{e_x}\varphi_2^{e_x} \\
&= \frac{1}{6}\Bigg[\varphi_1^{e_x}\varphi_2^{e_x} \\
&\quad + \frac{1}{4}\varphi_1^{e_x}\varphi_2^{e_x} - \frac{\sqrt{3}}{4}\left(\varphi_1^{e_x}\varphi_2^{e_y} + \varphi_1^{e_y}\varphi_2^{e_x}\right) + \frac{3}{4}\varphi_1^{e_y}\varphi_2^{e_y} \\
&\quad + \frac{1}{4}\varphi_1^{e_x}\varphi_2^{e_x} + \frac{\sqrt{3}}{4}\left(\varphi_1^{e_x}\varphi_2^{e_y} + \varphi_1^{e_y}\varphi_2^{e_x}\right) + \frac{3}{4}\varphi_1^{e_y}\varphi_2^{e_y} \\
&\quad + \varphi_1^{e_x}\varphi_2^{e_x} \\
&\quad + \frac{1}{4}\varphi_1^{e_x}\varphi_2^{e_x} + \frac{\sqrt{3}}{4}\left(\varphi_1^{e_x}\varphi_2^{e_y} + \varphi_1^{e_y}\varphi_2^{e_x}\right) + \frac{3}{4}\varphi_1^{e_y}\varphi_2^{e_y} \\
&\quad + \frac{1}{4}\varphi_1^{e_x}\varphi_2^{e_x} - \frac{\sqrt{3}}{4}\left(\varphi_1^{e_x}\varphi_2^{e_y} + \varphi_1^{e_y}\varphi_2^{e_x}\right) + \frac{3}{4}\varphi_1^{e_y}\varphi_2^{e_y}\Bigg] \\
&= \frac{1}{2}\left(\varphi_1^{e_x}\varphi_2^{e_x} + \varphi_1^{e_y}\varphi_2^{e_y}\right)
\end{aligned}
\tag{3.28}
$$

$$
\begin{aligned}
\mathcal{P}^{E_x}\varphi_1^{e_x}\varphi_2^{e_x} &= \frac{2}{6}\Big[E_{xx}(E)P_E + E_{xx}(C_3)P_{C_3} + E_{xx}(C_3^{-1})P_{C_3^{-1}} \\
&\quad + E_{xx}(\sigma_v)P_{\sigma_v} + E_{xx}(\sigma_v')P_{\sigma_v'} + E_{xx}(\sigma_v'')P_{\sigma_v''}\Big]\varphi_1^{e_x}\varphi_2^{e_x} \\
&= \frac{2}{6}\left(P_E - \frac{1}{2}P_{C_3} - \frac{1}{2}P_{C_3^{-1}} + P_{\sigma_v} - \frac{1}{2}P_{\sigma_v'} - \frac{1}{2}P_{\sigma_v''}\right)\varphi_1^{e_x}\varphi_2^{e_x} \\
&= \frac{1}{6}\Big[2\varphi_1^{e_x}\varphi_2^{e_x} \\
&\quad - \frac{1}{4}\varphi_1^{e_x}\varphi_2^{e_x} + \frac{\sqrt{3}}{4}\left(\varphi_1^{e_x}\varphi_2^{e_y} + \varphi_1^{e_y}\varphi_2^{e_x}\right) - \frac{3}{4}\varphi_1^{e_y}\varphi_2^{e_y} \\
&\quad - \frac{1}{4}\varphi_1^{e_x}\varphi_2^{e_x} - \frac{\sqrt{3}}{4}\left(\varphi_1^{e_x}\varphi_2^{e_y} + \varphi_1^{e_y}\varphi_2^{e_x}\right) - \frac{3}{4}\varphi_1^{e_y}\varphi_2^{e_y} \\
&\quad + 2\varphi_1^{e_x}\varphi_2^{e_x} \\
&\quad - \frac{1}{4}\varphi_1^{e_x}\varphi_2^{e_x} - \frac{\sqrt{3}}{4}\left(\varphi_1^{e_x}\varphi_2^{e_y} + \varphi_1^{e_y}\varphi_2^{e_x}\right) - \frac{3}{4}\varphi_1^{e_y}\varphi_2^{e_y} \\
&\quad - \frac{1}{4}\varphi_1^{e_x}\varphi_2^{e_x} + \frac{\sqrt{3}}{4}\left(\varphi_1^{e_x}\varphi_2^{e_y} + \varphi_1^{e_y}\varphi_2^{e_x}\right) - \frac{3}{4}\varphi_1^{e_y}\varphi_2^{e_y}\Big] \\
&= \frac{1}{2}\left(\varphi_1^{e_x}\varphi_2^{e_x} - \varphi_1^{e_y}\varphi_2^{e_y}\right)
\end{aligned}
\tag{3.29}
$$

Table 3.8: Irreducible representation of two-particle orbital wavefunctions. Here φ_1 and φ_2 are adopted to denote two particles.

Electronic configuration	Γ	Two-particle wavefunction
ee	A_1	$\frac{1}{2}\left(\varphi_1^{e_x}\varphi_2^{e_x}+\varphi_1^{e_y}\varphi_2^{e_y}\right)$
	A_2	$\frac{1}{2}\left(\varphi_1^{e_x}\varphi_2^{e_y}-\varphi_1^{e_y}\varphi_2^{e_x}\right)$
	E_x	$\frac{1}{2}\left(\varphi_1^{e_x}\varphi_2^{e_x}-\varphi_1^{e_y}\varphi_2^{e_y}\right)$
	E_y	$\frac{1}{2}\left(\varphi_1^{e_x}\varphi_2^{e_y}+\varphi_1^{e_y}\varphi_2^{e_x}\right)$
a_1e	A_1	–
	A_2	–
	E_x	$\varphi_1^{a_1}\varphi_2^{e_x}$
	E_y	$\varphi_1^{a_1}\varphi_2^{e_y}$

3.6.3 Spin Symmetry Operation and C_{3v} Double Group

Spin has SU(2) symmetry. Its rotation is generated by Pauli matrix $\hat{\sigma}$ about the norm direction $\hat{\mathbf{n}}$.

$$\begin{aligned} R_{\hat{n}}(\theta) &= \exp(-\frac{i}{2}\hat{\mathbf{n}}\cdot\hat{\sigma}\theta) \\ &= I\cos(\theta/2) - i(\hat{\mathbf{n}}\cdot\hat{\sigma})\sin(\theta/2) \end{aligned} \tag{3.30}$$

where θ is the counterclockwise (positive) rotational angle, and

$$\sigma_1 = \begin{pmatrix} 0 & 1 \\ 1 & 0 \end{pmatrix} \qquad \sigma_2 = \begin{pmatrix} 0 & -i \\ i & 0 \end{pmatrix} \qquad \sigma_3 = \begin{pmatrix} 1 & 0 \\ 0 & -1 \end{pmatrix} \tag{3.31}$$

The matrix of rotation on spin wavefunction in space is

$$
\begin{aligned}
R(\alpha,\beta,\gamma) &= R_{\hat{z}'}(\gamma)R_{\hat{y}'}(\beta)R_{\hat{z}}(\alpha) \\
&= [R_{\hat{y}'}(\beta)R_{\hat{z}}(\gamma)R^{-1}_{\hat{y}'}(\beta)]R_{\hat{y}'}(\beta)R_{\hat{z}}(\alpha) \\
&= R_{\hat{y}'}(\beta)R_{\hat{z}}(\gamma)R_{\hat{z}}(\alpha) \\
&= [R_{\hat{z}}(\alpha)R_{\hat{y}}(\beta)R^{-1}_{\hat{z}}(\alpha)]R_{\hat{z}}(\gamma)R_{\hat{z}}(\alpha) \\
&= R_{\hat{z}}(\alpha)R_{\hat{y}}(\beta)R_{\hat{z}}(\gamma) \\
&= \begin{pmatrix} \exp(-i\frac{\alpha+\gamma}{2})\cos(\frac{\beta}{2}) & -\exp(i\frac{\gamma-\alpha}{2})\sin(\frac{\beta}{2}) \\ \exp(i\frac{\alpha-\gamma}{2})\sin(\frac{\beta}{2}) & \exp(i\frac{\alpha+\gamma}{2})\cos(\frac{\beta}{2}) \end{pmatrix}
\end{aligned}
\tag{3.32}
$$

There are two ways of rotating spin. One is rotate the coordinates and fix the spin. If rotating the coordinates, $\hat{y}'$ will be the new y-axis after the first rotation by α about $\hat{z}$, $\hat{z}'$ will be the new z-axis following the second rotation by β about $\hat{y}'$, and γ will be the third rotation about $\hat{z}'$. The other is rotate the spin and fix the coordinates, which is shown by Eq. (3.32) that it is equivalent to the rotation on the Cartesian coordinates. Because the rotation on the object is the inverse of that on the coordinates [80], γ, β and α become the first, second and third rotations about $\hat{z}$, $\hat{y}$ and $\hat{z}$, respectively [58, 81]. Here we follow the convention that symmetry operations act on the object in a space-fixed coordinates for convenience[5].

Because the rotation period of a fermion is 4π, twice as that of spatial wavefunction, the ordinary point group like Table 3.2 is insufficient to describe the symmetry of a fermion. One need to use a double group, which contains double number of elements as the ordinary group, to describe wavefunctions when there is half-integral spin.

[5]See page 101 and Table 5-1 on page 112 of Ref. [80]

A double group contains the additional irreducible representations that half-integral spin wavefunctions transform as. The characters of the irreducible representation of the spin 1/2 wavefunction can be evaluated using Eq. (3.32). For the irreducible representation $D_{1/2}$ of spin 1/2 wavefunction of C_{3v} symmetry, the matrix representations are,

$$E = R_{\hat{z}}(0)R_{\hat{y}}(0)R_{\hat{z}}(0) = \begin{pmatrix} 1 & 0 \\ 0 & 1 \end{pmatrix} \tag{3.33}$$

$$C_3 = R_{\hat{z}}(0)R_{\hat{y}}(0)R_{\hat{z}}(\frac{2\pi}{3}) = \begin{pmatrix} e^{-i\pi/3} & 0 \\ 0 & e^{i\pi/3} \end{pmatrix} \tag{3.34}$$

$$C_3^{-1} = R_{\hat{z}}(0)R_{\hat{y}}(0)R_{\hat{z}}(-\frac{2\pi}{3}) = \begin{pmatrix} e^{i\pi/3} & 0 \\ 0 & e^{-i\pi/3} \end{pmatrix} \tag{3.35}$$

$$\sigma_v = R_{\hat{z}}(0)R_{\hat{y}}(\pi)R_{\hat{z}}(0) = \begin{pmatrix} 0 & -1 \\ 1 & 0 \end{pmatrix} = i\sigma_y = -i \begin{pmatrix} 0 & -i \\ i & 0 \end{pmatrix} \tag{3.36}$$

$$\sigma_v' = \sigma_v C_3 = \begin{pmatrix} 0 & -e^{i\pi/3} \\ e^{-i\pi/3} & 0 \end{pmatrix} = \begin{pmatrix} 0 & e^{-i2\pi/3} \\ e^{-i\pi/3} & 0 \end{pmatrix} \tag{3.37}$$

$$\sigma_v'' = \sigma_v C_3^{-1} = \begin{pmatrix} 0 & -e^{-i\pi/3} \\ e^{i\pi/3} & 0 \end{pmatrix} = \begin{pmatrix} 0 & e^{i2\pi/3} \\ e^{i\pi/3} & 0 \end{pmatrix} \tag{3.38}$$

$$\bar{E} = R_{\hat{z}}(0)R_{\hat{y}}(0)R_{\hat{z}}(2\pi) = \begin{pmatrix} -1 & 0 \\ 0 & -1 \end{pmatrix} \tag{3.39}$$

$$\bar{C}_3 = R_{\hat{z}}(0)R_{\hat{y}}(0)R_{\hat{z}}(\frac{2\pi}{3} + 2\pi) = \bar{E}C_3 = \begin{pmatrix} -e^{-i\pi/3} & 0 \\ 0 & -e^{i\pi/3} \end{pmatrix} = \begin{pmatrix} e^{i2\pi/3} & 0 \\ 0 & e^{-i2\pi/3} \end{pmatrix} \tag{3.40}$$

$$\bar{C}_3^{-1} = R_{\hat{z}}(0)R_{\hat{y}}(0)R_{\hat{z}}(-\frac{2\pi}{3} + 2\pi) = \bar{E}C_3^{-1} = \begin{pmatrix} -e^{i\pi/3} & 0 \\ 0 & -e^{-i\pi/3} \end{pmatrix} = \begin{pmatrix} e^{-i2\pi/3} & 0 \\ 0 & e^{i2\pi/3} \end{pmatrix} \tag{3.41}$$

$$\bar{\sigma}_v = R_{\hat{z}}(0)R_{\hat{y}}(\pi)R_{\hat{z}}(2\pi) = \bar{E}\sigma_v = \begin{pmatrix} 0 & 1 \\ -1 & 0 \end{pmatrix} \tag{3.42}$$

$$\bar{\sigma}'_v = \bar{E}\sigma'_v = \begin{pmatrix} 0 & e^{i\pi/3} \\ -e^{-i\pi/3} & 0 \end{pmatrix} = \begin{pmatrix} 0 & e^{i\pi/3} \\ e^{i2\pi/3} & 0 \end{pmatrix} \tag{3.43}$$

$$\bar{\sigma}''_v = \bar{E}\sigma''_v = \begin{pmatrix} 0 & e^{-i\pi/3} \\ -e^{i\pi/3} & 0 \end{pmatrix} = \begin{pmatrix} 0 & e^{-i\pi/3} \\ e^{-i2\pi/3} & 0 \end{pmatrix} \tag{3.44}$$

The characters of $D_{1/2}$ can be obtained from the above representation matrices.

A two-electron wavefunction transforms as the direct product $D_{1/2} \otimes D_{1/2}$ [79]. Because $D_{1/2} \otimes D_{1/2} = A_1 \oplus A_2 \oplus E$, we expect to find two non-degenerate spin-orbit

states A_1 and A_2, and the degenerate spin-orbit states E' in the ground state manifold, which can consist of triplet and singlet states.

Table 3.9: The character table of C_{3v} double group.

C_{3v}	E	$2C_3$	$3\sigma_v$	$\bar{E}$	$2\bar{C}_3$	$3\bar{\sigma}_v$
A_1	+1	+1	+1	+1	+1	+1
A_2	+1	+1	-1	+1	+1	-1
E	+2	-1	0	+2	-1	0
${}^1D_{3/2}$	+1	-1	i	-1	+1	-i
${}^2D_{3/2}$	+1	-1	-i	-1	+1	i
$D_{1/2}$	+2	1	0	-2	-1	0

3.6.4 Symmetry Operation on One Spin Wavefunction

Let α denote spin up and β denote spin down. With the matrix representations, we find how the spin transforms under the symmetry operations in Table 3.10.

Table 3.10: C_{3v} symmetry operations on the one spin wavefunction based on Eq. (3.32).

P_R	E	C_3	C_3^{-1}	σ_v	σ_v'	σ_v''
α	α	$e^{-i\pi/3}\alpha$	$e^{i\pi/3}\alpha$	β	$e^{-i\pi/3}\beta$	$e^{i\pi/3}\beta$
β	β	$e^{i\pi/3}\beta$	$e^{-i\pi/3}\beta$	$-\alpha$	$e^{-i2\pi/3}\alpha$	$e^{i2\pi/3}\alpha$

P_R	$\bar{E}$	$\bar{C}_3$	$\bar{C}_3^{-1}$	$\bar{\sigma}_v$	$\bar{\sigma}_v'$	$\bar{\sigma}_v''$
α	$-\alpha$	$e^{i2\pi/3}\alpha$	$e^{-i2\pi/3}\alpha$	$-\beta$	$e^{i2\pi/3}\beta$	$e^{-i2\pi/3}\beta$
β	$-\beta$	$e^{-i2\pi/3}\beta$	$e^{i2\pi/3}\beta$	α	$e^{i\pi/3}\alpha$	$e^{-i\pi/3}\alpha$

3.6.5 Representation of Two-Spin Wavefunction

Subsequently, we can derive the transformation of the two-spin wavefunctions using the matrix reprentations in Sec. A.1. The result is summarized in Table 3.11.

Table 3.11: C_{3v} symmetry operations on the two-spin wavefunction based on Eq. (3.32) and Table 3.10.

P_R	E	C_3	C_3^{-1}	σ_v	σ_v'	σ_v''
$\alpha\alpha$	$\alpha\alpha$	$e^{-i2\pi/3}\alpha\alpha$	$e^{i2\pi/3}\alpha\alpha$	$\beta\beta$	$e^{-i2\pi/3}\beta\beta$	$e^{i2\pi/3}\beta\beta$
$\alpha\beta$	$\alpha\beta$	$\alpha\beta$	$\alpha\beta$	$-\beta\alpha$	$-\beta\alpha$	$-\beta\alpha$
$\beta\beta$	$\beta\beta$	$e^{i2\pi/3}\beta\beta$	$e^{-i2\pi/3}\beta\beta$	$\alpha\alpha$	$e^{i2\pi/3}\alpha\alpha$	$e^{-i2\pi/3}\alpha\alpha$

P_R	$\bar{E}$	$\bar{C}_3$	$\bar{C}_3^{-1}$	$\bar{\sigma}_v$	$\bar{\sigma}_v'$	$\bar{\sigma}_v''$
$\alpha\alpha$	$\alpha\alpha$	$e^{-i2\pi/3}\alpha\alpha$	$e^{i2\pi/3}\alpha\alpha$	$\beta\beta$	$e^{-i2\pi/3}\beta\beta$	$e^{i2\pi/3}\beta\beta$
$\alpha\beta$	$\alpha\beta$	$\alpha\beta$	$\alpha\beta$	$-\beta\alpha$	$-\beta\alpha$	$-\beta\alpha$
$\beta\beta$	$\beta\beta$	$e^{i2\pi/3}\beta\beta$	$e^{-i2\pi/3}\beta\beta$	$\alpha\alpha$	$e^{i2\pi/3}\alpha\alpha$	$e^{-i2\pi/3}\alpha\alpha$

Furthermore, by using the projection operator, we can derive the representation that a spin wavefunction transforms to, as shown in Table 3.12. Below is one

example,

$$
\begin{aligned}
P^{A_1}(\alpha\alpha,\alpha\beta,\beta\alpha,\beta\beta) &= \frac{1}{12}\begin{bmatrix} P_E + P_{C_3} + P_{C_3^{-1}} + P_{\sigma_v} + P_{\sigma_v'} + P_{\sigma_v''} \\ +P_{\bar{E}} + P_{\bar{C}_3} + P_{\bar{C}_3^{-1}} + P_{\bar{\sigma}_v} + P_{\bar{\sigma}_v'} + P_{\bar{\sigma}_v''} \end{bmatrix}(\alpha\alpha,\alpha\beta,\beta\alpha,\beta\beta) \\
&= \frac{1}{6}\left(P_E + P_{C_3} + P_{C_3^{-1}} + P_{\sigma_v} + P_{\sigma_v'} + P_{\sigma_v''}\right)(\alpha\alpha,\alpha\beta,\beta\alpha,\beta\beta) \\
&= \frac{1}{6}(\alpha\alpha,\alpha\beta,\beta\alpha,\beta\beta) \\
&\quad \times \begin{pmatrix} 1+e^{-i2\pi/3}+e^{i2\pi/3} & 0 & 0 & 1+e^{i2\pi/3}+e^{-i2\pi/3} \\ 0 & 2 & -2 & 0 \\ 0 & -2 & 2 & 0 \\ 1+e^{-i2\pi/3}+e^{i2\pi/3} & 0 & 0 & 1+e^{i2\pi/3}+e^{-i2\pi/3} \end{pmatrix} \\
&= \frac{1}{6}(\alpha\alpha,\alpha\beta,\beta\alpha,\beta\beta)\begin{pmatrix} 0 & 0 & 0 & 0 \\ 0 & 2 & -2 & 0 \\ 0 & -2 & 2 & 0 \\ 0 & 0 & 0 & 0 \end{pmatrix} \\
&= \frac{1}{3}(0,\alpha\beta-\beta\alpha,-\alpha\beta+\beta\alpha,0) \\
&= \frac{1}{\sqrt{2}}(0,\alpha\beta-\beta\alpha,-\alpha\beta+\beta\alpha,0)
\end{aligned}
\tag{3.45}
$$

This example indicates that only $\pm(\alpha\beta-\beta\alpha)$ transforms as A_1.

Table 3.12: Irreducible representation of two-spin wavefunctions.

Γ	Two-particle wavefunction
A_1	$1/\sqrt{2}(\alpha\beta - \beta\alpha)$
A_2	$1/\sqrt{2}(\alpha\beta + \beta\alpha)$
E_x	$1/\sqrt{2}(\alpha\alpha + \beta\beta)$
E_y	$-i/\sqrt{2}(\alpha\alpha - \beta\beta)$

3.6.6 Representation of Total Wavefunction

After deriving all the irreducible representations of the orbital and spin parts, we are ready to write the total wavefunctions, which are useful for understanding the spin-orbit interaction matrix elements. The derivation procedure is similar but the

projection operator works on the orbital part and spin part simultaneously.

$$\begin{aligned}
\mathcal{P}^{A_1}(\varphi_1^{e_x}\varphi_2^{e_x}\otimes\alpha\alpha) &= \frac{1}{12}\Big[P_E + P_{C_3} + P_{C_3^{-1}} + P_{\sigma_v} + P_{\sigma_v'} + P_{\sigma_v''} \\
&\quad + P_{\bar{E}} + P_{\bar{C}_3} + P_{\bar{C}_3^{-1}} + P_{\bar{\sigma}_v} + P_{\bar{\sigma}_v'} + P_{\bar{\sigma}_v''}\Big](\varphi_1^{e_x}\varphi_2^{e_x}\otimes\alpha\alpha) \\
&= \frac{1}{6}\Big[\frac{3}{4}(\varphi_1^{e_x}\varphi_2^{e_x} - \varphi_1^{e_y}\varphi_2^{e_y})\otimes\alpha\alpha + i\frac{3}{4}(\varphi_1^{e_x}\varphi_2^{e_y} + \varphi_1^{e_y}\varphi_2^{e_x})\otimes\alpha\alpha \\
&\quad + \frac{3}{4}(\varphi_1^{e_x}\varphi_2^{e_x} - \varphi_1^{e_y}\varphi_2^{e_y})\otimes\beta\beta - i\frac{3}{4}(\varphi_1^{e_x}\varphi_2^{e_y} + \varphi_1^{e_y}\varphi_2^{e_x})\otimes\beta\beta\Big] \\
&= \frac{1}{8}\Big[(\varphi_1^{e_x}\varphi_2^{e_x} - \varphi_1^{e_y}\varphi_2^{e_y})\otimes(\alpha\alpha+\beta\beta) \\
&\quad + i(\varphi_1^{e_x}\varphi_2^{e_y} + \varphi_1^{e_y}\varphi_2^{e_x})\otimes(\alpha\alpha-\beta\beta)\Big] \\
&= 0
\end{aligned} \tag{3.46}$$

The zero result of the projection on $\varphi_1^{e_x}\varphi_2^{e_x}\otimes\alpha\alpha$ cannot be a basis function of total wavefunction that transform as A_1. In contrast, $\varphi_1^{e_x}\varphi_2^{e_y}\otimes\alpha\beta$ is a basis function which can be used to generate its partner functions, and the linear combination of the basis and its partner forms as total wavefunction that transforms as A_1.

$$\begin{aligned}
\mathcal{P}^{A_1}(\varphi_1^{e_x}\varphi_2^{e_y}\otimes\alpha\beta) &= \frac{1}{12}\Big[P_E + P_{C_3} + P_{C_3^{-1}} + P_{\sigma_v} + P_{\sigma_v'} + P_{\sigma_v''} \\
&\quad + P_{\bar{E}} + P_{\bar{C}_3} + P_{\bar{C}_3^{-1}} + P_{\bar{\sigma}_v} + P_{\bar{\sigma}_v'} + P_{\bar{\sigma}_v''}\Big](\varphi_1^{e_x}\varphi_2^{e_x}\otimes\alpha\beta) \\
&= \frac{1}{6}\Big[\frac{3}{2}(\varphi_1^{e_x}\varphi_2^{e_y} - \varphi_1^{e_y}\varphi_2^{e_x})\otimes\alpha\beta \\
&\quad + \frac{3}{2}(\varphi_1^{e_x}\varphi_2^{e_y} - \varphi_1^{e_y}\varphi_2^{e_x})\otimes\beta\alpha\Big] \\
&= \frac{1}{4}(\varphi_1^{e_x}\varphi_2^{e_y} - \varphi_1^{e_y}\varphi_2^{e_x})\otimes(\alpha\beta+\beta\alpha)
\end{aligned} \tag{3.47}$$

It is important to notice that while group theory provides information about

symmetry and degeneracy, doesn't ensure the antisymmetry that is required by Pauli's principle for fermions. Therefore, the total wavefunction must be verified for antisymmetry after performing the projection. Likewise, we can perform A_2, E_x and E_y projections, and the results are summarized in Table 3.13 and Table 3.14.

Table 3.13: Irreducible representation of ground state two-particle total wavefunctions. The wavefunctions are normalized. For conciseness, the following notations are adopted in this table, $xy \pm yx \equiv \varphi_1^{e_x}\varphi_2^{e_y} \pm \varphi_1^{e_y}\varphi_2^{e_x}$ and $xx \pm yy \equiv \varphi_1^{e_x}\varphi_2^{e_x} \pm \varphi_1^{e_y}\varphi_2^{e_y}$. The symmetry of orbital part and spin part can be found in Table 3.8 and Table 3.12, respectively. This table is consistent with that in Ref. [18, 1].

Electronic configuration	Total wavefunction	Symmetry $\Gamma^{\text{tot}} = \Gamma^{\text{orb}} \otimes \Gamma^{\text{spin}}$	Label ${}^S\Gamma_{m_s}$
	$\frac{1}{2}(xy - yx) \otimes (\alpha\beta + \beta\alpha)$	$A_1 = A_2 \otimes A_2$	${}^3A_2^0$
	$\frac{1}{2}(xy - yx) \otimes (\alpha\alpha - \beta\beta)$	$E_x = A_2 \otimes E_y$	${}^3A_2^1 - {}^3A_2^{-1}$
	$\frac{1}{2}(xy - yx) \otimes (\alpha\alpha + \beta\beta)$	$E_y = A_2 \otimes E_x$	${}^3A_2^1 + {}^3A_2^{-1}$
ee	–	A_2	–
	$\frac{1}{2}(xx - yy) \otimes (\alpha\beta - \beta\alpha)$	$E_x = E_x \otimes A_1$	${}^1E_x$
	$\frac{1}{2}(xy + yx) \otimes (\alpha\beta - \beta\alpha)$	$E_y = E_y \otimes A_1$	${}^1E_y$
	$\frac{1}{2}(xx + yy) \otimes (\alpha\beta - \beta\alpha)$	$A_1 = A_1 \otimes A_1$	${}^1A_1$

Table 3.14: Irreducible representation of excited state two-particle total wavefunctions. The wavefunctions are normalized. For conciseness, the following notations are adopted in this table, $a_1x \pm xa_1 \equiv \varphi_1^{a_1}\varphi_2^{e_x} \pm \varphi_1^{e_x}\varphi_2^{a_1}$ and $a_1y \pm ya_1 \equiv \varphi_1^{a_1}\varphi_2^{e_y} \pm \varphi_1^{e_y}\varphi_2^{a_1}$. The symmetry of orbital part and spin part can be found in Table 3.8 and Table 3.12, respectively. This table is consistent with that in Ref. [18, 1].

Electronic configuration	Total wavefunction	Symmetry $\Gamma^{\text{tot}} = \Gamma^{\text{orb}} \otimes \Gamma^{\text{spin}}$	Label ${}^S\Gamma_{m_s}$
a_1e	$\frac{1}{2\sqrt{2}}\Big[(a_1x - xa_1)\otimes(\alpha\alpha+\beta\beta) + i(a_1y - ya_1)\otimes(\alpha\alpha-\beta\beta)\Big]$	$E_x = E_x\otimes E_x - E_y\otimes E_y$	${}^3E_x^{\pm1}$
	$\frac{1}{2\sqrt{2}}\Big[(a_1x - xa_1)\otimes(\alpha\alpha-\beta\beta) + i(a_1y - ya_1)\otimes(\alpha\alpha+\beta\beta)\Big]$	$E_y = E_x\otimes E_y + E_y\otimes E_x$	${}^3E_y^{\pm1}$
	$\frac{1}{2}(a_1y - ya_1)\otimes(\alpha\beta+\beta\alpha)$	$E_x = E_y\otimes A_2$	${}^3E_x^{0}$
	$\frac{1}{2}(a_1y - ya_1)\otimes(\alpha\beta+\beta\alpha)$	$E_y = E_x\otimes A_2$	${}^3E_y^{0}$
	$\frac{1}{2\sqrt{2}}\Big[(a_1x - xa_1)\otimes(\alpha\alpha+\beta\beta) - i(a_1y - ya_1)\otimes(\alpha\alpha-\beta\beta)\Big]$	$A_1 = E_x\otimes E_x + E_y\otimes E_y$	${}^3A_1^{\pm1}$
	$\frac{1}{2\sqrt{2}}\Big[(a_1x - xa_1)\otimes(\alpha\alpha-\beta\beta) - i(a_1y - ya_1)\otimes(\alpha\alpha+\beta\beta)\Big]$	$A_2 = E_x\otimes E_y - E_y\otimes E_x$	${}^3A_2^{\pm1}$
	$\frac{1}{2}(a_1x + xa_1)\otimes(\alpha\beta-\beta\alpha)$	$E_x = E_x\otimes A_1$	${}^1E_x'$
	$\frac{1}{2}(a_1y + ya_1)\otimes(\alpha\beta-\beta\alpha)$	$E_y = E_y\otimes A_1$	${}^1E_y'$

3.7 Spin-Orbit Coupling

Spin-orbit coupling (SOC) is important because it not only splits degenerate states by energy splitting, but also couples electronic states of different spins and enables intersystem crossing transition. We perform the symmetry analysis in order to

understand the two points below,

- whether an SOC matrix element is allowed or forbidden
- what the SOC strength is based on the spin-orbit Hamiltonian and the total wavefunctions.

The SOC arises from the interaction between the magnetic moment of an electron's spin and the magnetic field induced by its motion within the electric field of a nucleus [84],

$$\begin{aligned} H_{\text{soc}} &= \frac{1}{2m_e^2c^2}(\nabla V \times \mathbf{p}) \cdot \mathbf{S} \\ &= \frac{e}{2m_e^2c^2}(\nabla \phi_{\text{pot}} \times \mathbf{p}) \cdot \mathbf{S} \end{aligned} \tag{3.48}$$

where $\hbar$ is the Planck constant, m_e is the mass of electron, c is the speed of light, $V = e\phi_{\text{pot}}$ is an electric potential, $\mathbf{p} = -i\hbar\nabla$ is momentum, $\mathbf{S}$ is the spin angular momentum. H_{soc} can be rewritten in terms of $\mathbf{L} \cdot \mathbf{S}$ with $\mathbf{L}$ standing for the orbital angular momentum,

$$H_{\text{soc}} = \frac{e\hbar}{2m_e^2c^2}\mathbf{L} \cdot \mathbf{S} \tag{3.49}$$

The orbital part $\mathbf{L}$ resembles $(e_y a_1 - a_1 e_y, -e_x a_1 + a_1 e_x, e_x e_y - e_y e_x)$ of the orbital wavefunctions in Table 3.8. Also, by using the projection operator with an example as below, we can label each component of $\mathbf{L}$ by the irreducible representations to which it transforms

$$\mathcal{P}^{A_2}\partial_x\phi_{\text{pot}}p_y = \frac{1}{6}\left(P_E + P_{C_3} + P_{C_3^{-1}} - P_{\sigma_v} - P_{\sigma_v'} - P_{\sigma_v''}\right)\partial_x\phi_{\text{pot}}p_y \tag{3.50}$$

$$= (\partial_x\phi_{\text{pot}}p_y - \partial_y\phi_{\text{pot}}p_x) \tag{3.51}$$

The same as for the spin angular momentum with $S_z = \frac{1}{2}(|\alpha\rangle\langle\alpha| - |\beta\rangle\langle\beta|)$ as an example,

$$\mathcal{P}^{A_2} S_z = \frac{1}{6}\left(P_E + P_{C_3} + P_{C_3^{-1}} - P_{\sigma_v} - P_{\sigma_v'} - P_{\sigma_v''}\right) S_z \tag{3.52}$$

$$= \frac{1}{2}(|\alpha\rangle\langle\alpha| - |\beta\rangle\langle\beta|) \tag{3.53}$$

Then, we can write down the expression of the H_{soc} in terms of the irreducible representations as follows,

$$\begin{aligned} H_{\text{soc}} &= \frac{e\hbar}{2m_e^2c^2}(L^{E_y}, -L^{E_x}, L^{A_2}) \cdot (S^{E_y}, -S^{E_x}, S^{A_2}) \\ &= \frac{e\hbar}{2m_e^2c^2}(L^{E_y}S^{E_y} + L^{E_x}S^{E_x} + L^{A_2}S^{A_2}) \end{aligned} \tag{3.54}$$

$$\begin{aligned} H_{\text{soc}} &= \frac{\lambda_\perp}{2}(L_+S_- + L_-S_+) + \lambda_z L_z S_z \\ &= \lambda_\perp(L^{E_y}S^{E_y} + L^{E_x}S^{E_x}) + \lambda_z L^{A_2}S^{A_2} \end{aligned} \tag{3.55}$$

Here, $L_\pm$ and $S_\pm$ are the ladder operators for orbital angular momentum and spin angular momentum, respectively. They are associated with the nonaxial part $\lambda_\perp$ of SOC, while L_z and S_z are associated with the axial part λ_z of the SOC.

Then we use the selection rule to determine if an SOC matrix element is vanishing or not. Because only the matrix element that is invariant under all symmetry operations can survive, a matrix element can be nonvanishing if and only if the direct product of the matrix element includes the total symmetry irreducible representation A_1, i.e. the result of direct product $A_1 \in \{\Gamma_\alpha^{(f)} \otimes \Gamma^{\text{int}} \otimes \Gamma_\beta^{(i)}\}$, where Γ^{int} denotes the representation of the interaction Hamiltonian [6] [79].

The following procedures help understand whether an SOC matrix element is nonvanishing:

[6] See details on page 359 of Ref. [79]

1. If H_{soc} transforms as A_1 [85], then it will require $A_1 \in \Gamma_\alpha^{(f)} \otimes \Gamma_\beta^{(i)}$

2. If step 1 is satisfied, it will need to check the representation of the orbital matrix element and spin matrix element by using theWigner-Echkart theorem

The SOC hamiltonian above is general and contains the contribution from both the one-particle SOC and two-particle SOC [86]. For the defects like the NV center whose SOC interaction is weak, we consider the spin of electron mainly interacts with its own orbital. Therefore, we can write

$$LS = L_1 S_1 + L_2 S_2 \tag{3.56}$$

Then we can use the Wigner-Eckart theorem with the Clebsch–Gordan coefficients (CGC) to estimate the SOC strength [85]. The Wigner-Eckart theorem enables the decomposition of a total wavefunction into the product of the orbital part and the spin part, which can be further decomposed into the product of CGC, a unitary matrix, and the part that is independent of angular momentum orientation.

$$\begin{aligned}
\left\langle \Psi^{(\Gamma_r)_\alpha} \middle| H_{\text{soc}} \middle| \Psi^{(\Gamma_s)_\alpha} \right\rangle &= \sum_{j=1}^{2} \sum_{p,\beta} \left\langle \Psi^{(\Gamma_r)_\alpha} \middle| L_j^{(\Gamma_p)_\beta} S_j^{(\Gamma_p)_\beta} \middle| \Psi^{(\Gamma_s)_\alpha} \right\rangle \\
&= \sum_{j=1}^{2} \sum_{p,\beta} \sum_{\gamma,\lambda,\gamma',\lambda'} \left(\begin{array}{cc|c} \Gamma_k & \Gamma_l & \Gamma_r \\ \gamma & \lambda & \alpha \end{array} \right)^* \left(\begin{array}{cc|c} \Gamma_{k'} & \Gamma_{l'} & \Gamma_s \\ \gamma' & \lambda' & \alpha \end{array} \right) \\
&\quad \times \left\langle \phi^{(\Gamma_k)_\gamma} \middle| L_j^{(\Gamma_p)_\beta} \middle| \phi^{(\Gamma_{k'})_{\gamma'}} \right\rangle \left\langle \nu^{(\Gamma_l)_\lambda} \middle| S_j^{(\Gamma_p)_\beta} \middle| \nu^{(\Gamma_{l'})_{\lambda'}} \right\rangle
\end{aligned} \tag{3.57}$$

where α, r and s indicate that the total wavefunctions belong to the α-th row of the r-th and s-th representations, j denotes the particle index, p and β indicate that the orbital angular momentum L and spin angular momentum S belong to the β-th row of

p-th representation, k and γ denote the γ-th row of k-th representation that the orbital wavefunction transforms, and l and λ denote the λ-th row of l-th representation that the spin wavefunction transforms.

The Clebsch–Gordan coefficient is obtained by decomposed the total wavefunction as the product of the orbital part and the spin part,

$$\left|\Psi_{\alpha}^{(\Gamma_r)}\right\rangle = \sum_{\gamma,\lambda} \left(\begin{array}{cc|c} k & l & \Gamma_r \\ & & \\ \gamma & \lambda & \alpha \end{array}\right) \left|\phi_{\gamma}^{k}\right\rangle \left|\nu_{\lambda}^{l}\right\rangle \tag{3.58}$$

In Sec. 3.7.1, the analytic expression of Clebsch–Gordan coefficient is presented, along with the explicit CGC for C_{3v} symmetry. Similar table of CGC can be found in Ref. [85, 82].

3.7.1 Clebsch–Gordan Coefficients

The formulas of CGC can be drived by the orthogonality and completeness,

$$\left(\begin{array}{cc|c} \Gamma_j & \Gamma_{j'} & \Gamma \\ & & \\ \alpha_0 & \beta_0 & \gamma_0 \end{array}\right) = \sqrt{\frac{l_\Gamma}{h} \sum_{g\in G} D_{\alpha_0\alpha_0}^{(\Gamma_j)}(g) D_{\beta_0\beta_0}^{(\Gamma_{j'})}(g) D_{\gamma_0\gamma_0}^{(\Gamma^*)}(g)} \tag{3.59}$$

$$\left(\begin{array}{cc|c} \Gamma_j & \Gamma_{j'} & \Gamma \\ & & \\ \alpha & \beta & \gamma \end{array}\right) = \frac{1}{\left(\begin{array}{cc|c} \Gamma_j & \Gamma_{j'} & \Gamma \\ & & \\ \alpha_0 & \beta_0 & \gamma_0 \end{array}\right)} \frac{l_\Gamma}{h} \sum_{g\in G} D_{\alpha\alpha_0}^{(\Gamma_j)}(g) D_{\beta\beta_0}^{(\Gamma_{j'})}(g) D_{\gamma\gamma_0}^{(\Gamma^*)}(g) \tag{3.60}$$

The CG coefficients of C_{3v} group can be derived as follows,

$$\left(\begin{array}{cc|c} A_1 & A_1 & A_1 \\ & & \\ 1 & 1 & 1 \end{array}\right) = \left(\begin{array}{cc|c} A_1 & A_2 & A_2 \\ & & \\ 1 & 1 & 1 \end{array}\right) = 1 \tag{3.61}$$

$$\left(\begin{array}{cc|c} A_2 & A_1 & A_2 \\ 1 & 1 & 1 \end{array}\right) = \left(\begin{array}{cc|c} A_2 & A_2 & A_1 \\ 1 & 1 & 1 \end{array}\right) = 1 \tag{3.62}$$

$$\left(\begin{array}{cc|c} A_1 & E & E \\ 1 & \mu & \nu \end{array}\right) = \left(\begin{array}{cc|c} E & A_1 & E \\ \mu & 1 & \nu \end{array}\right) = \begin{pmatrix} 1 & 0 \\ 0 & 1 \end{pmatrix}_{\mu\nu} \tag{3.63}$$

$$\left(\begin{array}{cc|c} A_2 & E & E \\ 1 & \mu & \nu \end{array}\right) = \left(\begin{array}{cc|c} E & A_2 & E \\ \mu & 1 & \nu \end{array}\right) = \begin{pmatrix} 0 & 1 \\ -1 & 0 \end{pmatrix}_{\mu\nu} \tag{3.64}$$

$$\left(\begin{array}{cc|c} E & E & A_1 \\ \mu & \nu & 1 \end{array}\right) = \frac{1}{\sqrt{2}} \begin{pmatrix} 1 & 0 \\ 0 & 1 \end{pmatrix}_{\mu\nu} \tag{3.65}$$

$$\left(\begin{array}{cc|c} E & E & A_2 \\ \mu & \nu & 1 \end{array}\right) = \frac{1}{\sqrt{2}} \begin{pmatrix} 0 & 1 \\ -1 & 0 \end{pmatrix}_{\mu\nu} \tag{3.66}$$

$$\left(\begin{array}{cc|c} E & E & E \\ \mu & \nu & 1 \end{array}\right) = \frac{1}{\sqrt{2}} \begin{pmatrix} 1 & 0 \\ 0 & -1 \end{pmatrix}_{\mu\nu} \tag{3.67}$$

$$\left(\begin{array}{cc|c} E & E & E \\ \mu & \nu & 2 \end{array}\right) = \frac{1}{\sqrt{2}} \begin{pmatrix} 0 & 1 \\ 1 & 0 \end{pmatrix}_{\mu\nu} \tag{3.68}$$

3.7.2 SOC Matrix Elements $\langle {}^3A_2^0 | H_{\mathbf{soc}} | {}^1A_1 \rangle$

Here, we evaluate the $\left\langle {}^3A_2^0 \middle| H_{\mathrm{soc}} \middle| {}^1A_1 \right\rangle$ matrix element, which will be shown critical for the intersystem crossing ${}^1\widetilde{E} \nrightarrow {}^3\widetilde{A}_2$ [68, 65]. Let Φ be two-particle wavefunction and ν be two-spin wavefunction, we can write the SOC matrix element as

follows,

$$\begin{aligned}
\left\langle {}^3A_2^0 \middle| H_{\mathrm{soc}} \middle| {}^1A_1 \right\rangle &= \left\langle {}^3A_2^0 \middle| L^{E_y} S^{E_y} + L^{E_x} S^{E_x} + L^{A_2} S^{A_2} \middle| {}^1A_1 \right\rangle \\
&= \left(\begin{array}{cc|c} A_2 & A_2 & A_1 \\ & & \\ 1 & 1 & 1 \end{array} \right)^* \left(\begin{array}{cc|c} A_1 & A_1 & A_1 \\ & & \\ 1 & 1 & 1 \end{array} \right) \left\langle \Phi^{A_2} \middle| L^{A_2} \middle| \Phi^{A_1} \right\rangle \left\langle \nu^{A_2} \middle| S^{A_2} \middle| \nu^{A_1} \right\rangle \\
&= \left\langle \Phi^{A_2} \middle| L^{A_2} \middle| \Phi^{A_1} \right\rangle \left\langle \nu^{A_2} \middle| S^{A_2} \middle| \nu^{A_1} \right\rangle
\end{aligned} \tag{3.69}$$

Using Eq. (3.57), we can decompose the matrix element into two one-particle matrix element like Ref. [85],

$$\begin{aligned}
\left\langle \Phi^{A_2} \middle| L^{A_2} \middle| \Phi^{A_1} \right\rangle \left\langle \nu^{A_2} \middle| S^{A_2} \middle| \nu^{A_1} \right\rangle = \Big(& \left\langle \Phi^{A_2} \middle| L^{A_2}_{j=1} \middle| \Phi^{A_1} \right\rangle \left\langle \nu^{A_2} \middle| S^{A_2}_{j=1} \middle| \nu^{A_1} \right\rangle \\
& + \left\langle \Phi^{A_2} \middle| L^{A_2}_{j=2} \middle| \Phi^{A_1} \right\rangle \left\langle \nu^{A_2} \middle| S^{A_2}_{j=2} \middle| \nu^{A_1} \right\rangle \Big)
\end{aligned} \tag{3.70}$$

Explicitly,

$$\begin{aligned}
\left\langle \Phi^{A_2} \middle| L^{A_2}_{j=1} \middle| \Phi^{A_1} \right\rangle &= \left\langle \varphi_1^{e_x} \varphi_2^{e_y} - \varphi_1^{e_y} \varphi_2^{e_x} \middle| L^{A_2}_{j=1} \middle| \varphi_1^{e_x} \varphi_2^{e_x} + \varphi_1^{e_y} \varphi_2^{e_y} \right\rangle \\
&= \Big(\left\langle \varphi_1^{e_x} \varphi_2^{e_y} \middle| L^{A_2}_{j=1} \middle| \varphi_1^{e_x} \varphi_2^{e_x} \right\rangle + \left\langle \varphi_1^{e_x} \varphi_2^{e_y} \middle| L^{A_2}_{j=1} \middle| \varphi_1^{e_y} \varphi_2^{e_y} \right\rangle \\
&\quad - \left\langle \varphi_1^{e_y} \varphi_2^{e_x} \middle| L^{A_2}_{j=1} \middle| \varphi_1^{e_x} \varphi_2^{e_x} \right\rangle - \left\langle \varphi_1^{e_y} \varphi_2^{e_x} \middle| L^{A_2}_{j=1} \middle| \varphi_1^{e_y} \varphi_2^{e_y} \right\rangle \Big) \\
&= \Big(\left\langle \varphi_1^{e_x} \varphi_2^{e_y} \middle| L^{A_2}_{j=1} \middle| \varphi_1^{e_y} \varphi_2^{e_y} \right\rangle - \left\langle \varphi_1^{e_y} \varphi_2^{e_x} \middle| L^{A_2}_{j=1} \middle| \varphi_1^{e_x} \varphi_2^{e_x} \right\rangle \Big) \\
&= \Big(\left\langle \varphi_1^{e_x} \middle| L^{A_2}_{j=1} \middle| \varphi_1^{e_y} \right\rangle - \left\langle \varphi_1^{e_y} \middle| L^{A_2}_{j=1} \middle| \varphi_1^{e_x} \right\rangle \Big)
\end{aligned} \tag{3.71}$$

and

$$\begin{aligned}
\left\langle \Phi^{A_2} \middle| L_{j=2}^{A_2} \middle| \Phi^{A_1} \right\rangle &= \left\langle \varphi_1^{e_x}\varphi_2^{e_y} - \varphi_1^{e_y}\varphi_2^{e_x} \middle| L_{j=2}^{A_2} \middle| \varphi_1^{e_x}\varphi_2^{e_x} + \varphi_1^{e_y}\varphi_2^{e_y} \right\rangle \\
&= \Big(\left\langle \varphi_1^{e_x}\varphi_2^{e_y} \middle| L_{j=2}^{A_2} \middle| \varphi_1^{e_x}\varphi_2^{e_x} \right\rangle + \left\langle \varphi_1^{e_x}\varphi_2^{e_y} \middle| L_{j=2}^{A_2} \middle| \varphi_1^{e_y}\varphi_2^{e_y} \right\rangle \\
&\quad - \left\langle \varphi_1^{e_y}\varphi_2^{e_x} \middle| L_{j=2}^{A_2} \middle| \varphi_1^{e_x}\varphi_2^{e_x} \right\rangle - \left\langle \varphi_1^{e_y}\varphi_2^{e_x} \middle| L_{j=2}^{A_2} \middle| \varphi_1^{e_y}\varphi_2^{e_y} \right\rangle \Big) \\
&= \Big(\left\langle \varphi_1^{e_x}\varphi_2^{e_y} \middle| L_{j=2}^{A_2} \middle| \varphi_1^{e_y}\varphi_2^{e_y} \right\rangle - \left\langle \varphi_1^{e_y}\varphi_2^{e_x} \middle| L_{j=2}^{A_2} \middle| \varphi_1^{e_x}\varphi_2^{e_x} \right\rangle \Big) \\
&= \Big(\left\langle \varphi_2^{e_y} \middle| L_{j=2}^{A_2} \middle| \varphi_2^{e_x} \right\rangle - \left\langle \varphi_2^{e_x} \middle| L_{j=2}^{A_2} \middle| \varphi_2^{e_y} \right\rangle \Big)
\end{aligned} \tag{3.72}$$

Here $L_{j=1}^{A_2}$ and $L_{j=2}^{A_2}$ are the orbital angular momentum operators acting on particle 1 and 2, respectively. Using particle 1 as an example, it can be seen that $\left\langle \varphi_1^{e_x}\varphi_2^{e_y} \middle| L_{j=1}^{A_2} \middle| \varphi_1^{e_x}\varphi_2^{e_x} \right\rangle$ and $\left\langle \varphi_1^{e_y}\varphi_2^{e_x} \middle| L_{j=1}^{A_2} \middle| \varphi_1^{e_y}\varphi_2^{e_y} \right\rangle$ vanish because $E_x \otimes A_2 \otimes E_x = E_y \otimes A_2 \otimes E_y = 0$. The nonzero matrix elements in one-particle format can be further reduced by using the CG coefficients,

$$\left\langle \varphi_1^{e_x} \middle| L_{j=1}^{A_2} \middle| \varphi_1^{e_y} \right\rangle = \left(\begin{array}{cc|c} E & A_2 & E \\ & & \\ 2 & 1 & 1 \end{array} \right) \langle \psi^e | L_{j=1}^{A_2} | \psi^e \rangle = - \langle e || L^{A_2} || e \rangle \tag{3.73}$$

$$\left\langle \varphi_1^{e_y} \middle| L_{j=1}^{A_2} \middle| \varphi_1^{e_x} \right\rangle = \left(\begin{array}{cc|c} E & A_2 & E \\ & & \\ 1 & 1 & 2 \end{array} \right) \langle \psi^e | L_{j=1}^{A_2} | \psi^e \rangle = \langle e || L^{A_2} || e \rangle \tag{3.74}$$

Therefore, the orbital angular momenta of particle 1 and 2 between states $\left|{}^3A_2\right\rangle^0$ and $\left|{}^1A_1\right\rangle$ are

$$\left\langle \Phi^{A_2} \middle| L_{j=1}^{A_2} \middle| \Phi^{A_1} \right\rangle = -2 \langle e || L^{A_2} || e \rangle \tag{3.75}$$

$$\left\langle \Phi^{A_2} \middle| L_{j=2}^{A_2} \middle| \Phi^{A_1} \right\rangle = 2 \langle e || L^{A_2} || e \rangle \tag{3.76}$$

Next we evaluate the spin matrix element in the same way as for the orbital part by using the spin wavefunctions in Table 3.12 and Table 3.13,

$$\begin{aligned}
\left\langle \nu^{A_2} \middle| S_{j=1}^{A_2} \middle| \nu^{A_1} \right\rangle &= \hbar \left\langle \alpha\beta + \beta\alpha | S_{j=1}^{A_2} | \alpha\beta - \beta\alpha \right\rangle \\
&= \langle \alpha\beta | S_{j=1}^{A_2} | \alpha\beta \rangle - \langle \alpha\beta | S_{j=1}^{A_2} | \beta\alpha \rangle + \langle \beta\alpha | S_{j=1}^{A_2} | \alpha\beta \rangle - \langle \beta\alpha | S_{j=1}^{A_2} | \beta\alpha \rangle \\
&= \langle \alpha\beta | \frac{\hbar}{2} (|\alpha\rangle\langle\alpha| - |\beta\rangle\langle\beta|)_{j=1} | \alpha\beta \rangle - \langle \beta\alpha | \frac{\hbar}{2} (|\alpha\rangle\langle\alpha| - |\beta\rangle\langle\beta|)_{j=1} | \beta\alpha \rangle \\
&= \frac{\hbar}{2} (\langle\alpha|\alpha\rangle \langle\alpha|\alpha\rangle + \langle\beta|\beta\rangle \langle\beta|\beta\rangle) \\
&= \hbar
\end{aligned} \tag{3.77}$$

and

$$\begin{aligned}
\left\langle \nu^{A_2} \middle| S_{j=2}^{A_2} \middle| \nu^{A_1} \right\rangle &= \hbar \left\langle \alpha\beta + \beta\alpha | S_{j=2}^{A_2} | \alpha\beta - \beta\alpha \right\rangle \\
&= \langle \alpha\beta | S_{j=2}^{A_2} | \alpha\beta \rangle - \langle \alpha\beta | S_{j=2}^{A_2} | \beta\alpha \rangle + \langle \beta\alpha | S_{j=2}^{A_2} | \alpha\beta \rangle - \langle \beta\alpha | S_{j=2}^{A_2} | \beta\alpha \rangle \\
&= \langle \alpha\beta | \frac{\hbar}{2} (|\alpha\rangle\langle\alpha| - |\beta\rangle\langle\beta|)_{j=2} | \alpha\beta \rangle - \langle \beta\alpha | \frac{\hbar}{2} (|\alpha\rangle\langle\alpha| - |\beta\rangle\langle\beta|)_{j=2} | \beta\alpha \rangle \\
&= \frac{\hbar}{2} (- \langle\beta|\beta\rangle \langle\beta|\beta\rangle - \langle\alpha|\alpha\rangle \langle\alpha|\alpha\rangle) \\
&= -\hbar
\end{aligned} \tag{3.78}$$

Finally, by summing over the product of the orbital part and the spin part of particles 1 and 2, and taking the CGC (the value is 1) and the normalization factor ($|\Psi\rangle = 1/\sqrt{N_\lambda!} a_\lambda^\dagger |0\rangle$, N_λ denotes the number of creator $a_\lambda^\dagger$, so the value is 1/2) of the wavefunction into consideration, we can find

$$\left\langle {}^3A_2^0 \middle| H_{\text{soc}} \middle| {}^1A_1 \right\rangle = -2\hbar \langle e || L^{A_2} || e \rangle \tag{3.79}$$

The value $-2\hbar \langle e || L^{A_2} || e \rangle$ is the same as that in Tabel 2 and Table 4 of Ref. [18].

3.7.3 SOC Matrix Elements $\left\langle {}^3A_2^1 - {}^3A_2^{-1}\middle|H_{\mathbf{soc}}\middle|{}^1E_x'\right\rangle$

This $\left\langle {}^3A_2^1 - {}^3A_2^{-1}\middle|H_{\rm soc}\middle|{}^1E_x'\right\rangle$ SOC matrix element is found critical for the ${}^1\widetilde{E} \rightarrow {}^3\widetilde{A}_2$ ISC transition when $\left\langle {}^3A_2^1 - {}^3A_2^{-1}\middle|H_{\rm soc}\middle|{}^1E_x\right\rangle$ is forbidden. Below is the evaluation.

$$\begin{aligned}
\left\langle {}^3A_2^1 - {}^3A_2^{-1}\middle|H_{\rm soc}\middle|{}^1E_x'\right\rangle &= \left\langle {}^3A_2^1 - {}^3A_2^{-1}\middle|L^{E_y}S^{E_y} + L^{E_x}S^{E_x} + L^{A_2}S^{A_2}\middle|{}^1E_x'\right\rangle \\
&= \left(\begin{array}{cc|c} A_2 & E & E \\ & & \\ 1 & 2 & 1 \end{array}\right)^* \left(\begin{array}{cc|c} E & A_1 & E \\ & & \\ 1 & 1 & 1 \end{array}\right) \\
&\quad \times \left\langle \Phi^{A_2}\middle|L^{E_y}\middle|\Phi^{E_x}\right\rangle \left\langle \nu^{E_y}\middle|S^{E_y}\middle|\nu^{A_1}\right\rangle \\
&= -\left\langle \Phi^{A_2}\middle|L^{E_y}\middle|\Phi^{E_x}\right\rangle \left\langle \nu^{E_y}\middle|S^{E_y}\middle|\nu^{A_1}\right\rangle \\
&= -\left(\begin{array}{cc|c} E & E & A_2 \\ & & \\ 2 & 1 & 1 \end{array}\right) \left(\begin{array}{cc|c} E & A_1 & E \\ & & \\ 2 & 1 & 2 \end{array}\right) \\
&\quad \times \left\langle \Phi^{A_2}\middle|\middle|L^E\middle|\middle|\Phi^E\right\rangle \left\langle \nu^E\middle|\middle|S^E\middle|\middle|\nu^{A_1}\right\rangle \\
&= \frac{1}{\sqrt{2}} \left\langle \Phi^{A_2}\middle|\middle|L^E\middle|\middle|\Phi^E\right\rangle \left\langle \nu^E\middle|\middle|S^E\middle|\middle|\nu^{A_1}\right\rangle
\end{aligned} \tag{3.80}$$

where the matrix element can be further reduced as below,

$$\begin{aligned}
\left\langle \Phi^{A_2}\middle|L^{E_y}\middle|\Phi^{E_x}\right\rangle &= \left(\begin{array}{cc|c} E & E & A_2 \\ & & \\ 2 & 1 & 1 \end{array}\right) \left\langle \Phi^{A_2}\middle|\middle|L^E\middle|\middle|\Phi^E\right\rangle \\
&= -\frac{1}{\sqrt{2}} \left\langle \Phi^{A_2}\middle|\middle|L^E\middle|\middle|\Phi^E\right\rangle
\end{aligned} \tag{3.81}$$

Using Eq. (3.57), we can decompose the matrix element into two one-particle matrix element like Ref. [85],

$$\begin{aligned}
\left\langle \Phi^{A_2}\middle|L^{E_y}\middle|\Phi^{E_x}\right\rangle \left\langle \nu^{E_y}\middle|S^{E_y}\middle|\nu^{A_1}\right\rangle = \Big(&\left\langle \Phi^{A_2}\middle|L^{E_y}_{j=1}\middle|\Phi^{E_x}\right\rangle \left\langle \nu^{E_y}\middle|S^{E_y}_{j=1}\middle|\nu^{A_1}\right\rangle \\
&+ \left\langle \Phi^{A_2}\middle|L^{E_y}_{j=2}\middle|\Phi^{E_x}\right\rangle \left\langle \nu^{E_y}\middle|S^{E_y}_{j=2}\middle|\nu^{A_1}\right\rangle \Big)
\end{aligned} \tag{3.82}$$

$$
\begin{aligned}
\left\langle \Phi^{A_2} \middle| L_{j=1}^{E_y} \middle| \Phi^{E_x} \right\rangle &= \left\langle \varphi_1^{e_x}\varphi_2^{e_y} - \varphi_1^{e_y}\varphi_2^{e_x} \middle| L_{j=1}^{E_y} \middle| \varphi_1^{a_1}\varphi_2^{e_x} + \varphi_1^{e_x}\varphi_2^{a_1} \right\rangle \\
&= -\left\langle \varphi_1^{e_y}\varphi_2^{e_x} \middle| L_{j=1}^{E_y} \middle| \varphi_1^{a_1}\varphi_2^{e_x} \right\rangle \\
&= -\left\langle \varphi_1^{e_y} \middle| L_{j=1}^{E_y} \middle| \varphi_1^{a_1} \right\rangle \\
&= -\begin{pmatrix} E & A_1 \\ 2 & 1 \end{pmatrix} \begin{vmatrix} E \\ 2 \end{vmatrix} \langle \psi^e | L_{j=1}^{E} | \varphi_1^{a_1} \rangle \\
&= -\langle e || L^E || a_1 \rangle
\end{aligned}
\tag{3.83}
$$

$$
\begin{aligned}
\left\langle \Phi^{A_2} \middle| L_{j=2}^{E_y} \middle| \Phi^{E_x} \right\rangle &= \left\langle \varphi_1^{e_x}\varphi_2^{e_y} - \varphi_1^{e_y}\varphi_2^{e_x} \middle| L_{j=2}^{E_y} \middle| \varphi_1^{a_1}\varphi_2^{e_x} + \varphi_1^{e_x}\varphi_2^{a_1} \right\rangle \\
&= \left\langle \varphi_1^{e_x}\varphi_2^{e_y} \middle| L_{j=2}^{E_y} \middle| \varphi_1^{e_x}\varphi_2^{a_1} \right\rangle \\
&= \left\langle \varphi_2^{e_y} \middle| L_{j=2}^{E_y} \middle| \varphi_2^{a_1} \right\rangle \\
&= \begin{pmatrix} E & A_1 \\ 2 & 1 \end{pmatrix} \begin{vmatrix} E \\ 2 \end{vmatrix} \langle \varphi_2^{e} | L_{j=2}^{E} | \varphi_2^{a_1} \rangle \\
&= \langle e || L^E || a_1 \rangle
\end{aligned}
\tag{3.84}
$$

On the other hand, the spin matrix elements evaluated in the same way as for the orbital part by using the spin wavefunctions in Table 3.12, Table 3.13 and Table 3.14 are as

follows,

$$\begin{aligned}
\left\langle \nu^{E_y} \middle| S_{j=1}^{E_y} \middle| \nu^{A_1} \right\rangle &= \langle \alpha\alpha - \beta\beta | S_{j=1}^{E_y} | \alpha\beta - \beta\alpha \rangle \\
&= \langle \alpha\alpha | S_{j=1}^{E_y} | \alpha\beta \rangle - \langle \alpha\alpha | S_{j=1}^{E_y} | \beta\alpha \rangle - \langle \beta\beta | S_{j=1}^{E_y} | \alpha\beta \rangle + \langle \beta\beta | S_{j=1}^{E_y} | \beta\alpha \rangle \\
&= - \langle \alpha\alpha | \frac{\hbar}{2} (|\alpha\rangle\langle\beta| + |\beta\rangle\langle\alpha|)_{j=1} | \beta\alpha \rangle - \langle \beta\beta | \frac{\hbar}{2} (|\alpha\rangle\langle\beta| + |\beta\rangle\langle\alpha|)_{j=1} | \alpha\beta \rangle \\
&= - \langle \alpha | \frac{\hbar}{2} (|\alpha\rangle\langle\beta| + |\beta\rangle\langle\alpha|)_{j=1} | \beta \rangle - \langle \beta | \frac{\hbar}{2} (|\alpha\rangle\langle\beta| + |\beta\rangle\langle\alpha|)_{j=1} | \alpha \rangle \\
&= -\frac{\hbar}{2} (\langle\alpha|\alpha\rangle \langle\beta|\beta\rangle + \langle\beta|\beta\rangle \langle\alpha|\alpha\rangle) \\
&= -\hbar
\end{aligned} \tag{3.85}$$

and

$$\begin{aligned}
\left\langle \nu^{E_y} \middle| S_{j=2}^{E_y} \middle| \nu^{A_1} \right\rangle &= \langle \alpha\alpha - \beta\beta | S_{j=2}^{E_y} | \alpha\beta - \beta\alpha \rangle \\
&= \langle \alpha\alpha | S_{j=2}^{E_y} | \alpha\beta \rangle - \langle \alpha\alpha | S_{j=2}^{E_y} | \beta\alpha \rangle - \langle \beta\beta | S_{j=2}^{E_y} | \alpha\beta \rangle + \langle \beta\beta | S_{j=2}^{E_y} | \beta\alpha \rangle \\
&= \langle \alpha\alpha | \frac{\hbar}{2} (|\alpha\rangle\langle\beta| + |\beta\rangle\langle\alpha|)_{j=2} | \alpha\beta \rangle + \langle \beta\beta | \frac{\hbar}{2} (|\alpha\rangle\langle\beta| + |\beta\rangle\langle\alpha|)_{j=2} | \beta\alpha \rangle \\
&= \langle \alpha | \frac{\hbar}{2} (|\alpha\rangle\langle\beta| + |\beta\rangle\langle\alpha|)_{j=2} | \beta \rangle + \langle \beta | \frac{\hbar}{2} (|\alpha\rangle\langle\beta| + |\beta\rangle\langle\alpha|)_{j=2} | \alpha \rangle \\
&= \frac{\hbar}{2} (\langle\alpha|\alpha\rangle \langle\beta|\beta\rangle + \langle\beta|\beta\rangle \langle\alpha|\alpha\rangle) \\
&= \hbar
\end{aligned} \tag{3.86}$$

By summing up the SOC of the two particles and taking the CGC (the value is $1/\sqrt{2}$) and normalization factor (the value is $1/2$) of the wavefunctions into consideration, the total SOC matrix element is

$$\left\langle {}^3A_2^1 - {}^3A_2^{-1} \middle| H_{\text{soc}} \middle| {}^1E_x' \right\rangle = \frac{1}{\sqrt{2}} \hbar \langle e || L^E || a_1 \rangle \tag{3.87}$$

The value $1/\sqrt{2}\hbar\langle e||L^E||a_1\rangle$ is the same as that $(1/\sqrt{2}\hbar\langle e||\lambda_E||a_1\rangle)$ in Tabel 2 and Table 4 of Ref. [18].

3.7.4 $\langle {}^3A_2^0|H_{\mathbf{soc}}|{}^1A_1\rangle$ vs $\langle {}^3A_2^1\,{}^3A_2^{-1}|H_{\mathbf{soc}}|{}^1E_x'\rangle$

We obtain the SOC matrix element $\langle {}^3A_2^0|H_{\rm soc}|{}^1A_1\rangle$ in Eq. (3.79), and SOC matrix element $\langle {}^3A_2^1\,{}^3A_2^{-1}|H_{\rm soc}|{}^1E_x'\rangle$ in Eq. (3.87). They are expressed in terms of the reduced one-particle matrix elements. Ignoring the factor of $1/\sqrt{2}$ from CGC for $\langle {}^3A_2^1\,{}^3A_2^{-1}|H_{\rm soc}|{}^1E_x'\rangle$, they differ by a factor of 1/2, which is simply due to the different number of reduced matrix elements. Specifically, $\langle {}^3A_2^0|H_{\rm soc}|{}^1A_1\rangle$ has four reduced one-particle matrix elements being nonzero, and $\langle {}^3A_2^1\,{}^3A_2^{-1}|H_{\rm soc}|{}^1E_x'\rangle$ only has two out of four being nonzero.

In Ref. [18], the unit SOC strengths for the axial and nonaxial components are defined based on the reduced one-particle matrix elements, i.e.

$$\lambda_z = -i\hbar\langle e||L^{A_2}||e\rangle \tag{3.88}$$

$$\lambda_\perp = -\frac{i}{\sqrt{2}}\hbar\langle e||L^E||a_1\rangle \tag{3.89}$$

With these unit SOC, we can find

$$\langle {}^3A_2^0|H_{\rm soc}|{}^1A_1\rangle = -2i\lambda_z \tag{3.90}$$

$$\langle {}^3A_2^1\,{}^3A_2^{-1}|H_{\rm soc}|{}^1E_x'\rangle = i\lambda_\perp \tag{3.91}$$

According to the SOC matrix elements are evaluated with one-particle wavefunctions, we can understand the factor of 2 for $\langle {}^3A_2^0|H_{\rm soc}|{}^1A_1\rangle$, as well as the factor of 1 for $\langle {}^3A_2^1\,{}^3A_2^{-1}|H_{\rm soc}|{}^1E_x'\rangle$ that are adopted for ISC rate calculations in Ref. [68].

However, we directly evaluate the SOC matrix elements with wavefunctions that already include multi-reference character in our calculation, instead of using the one-particle wavefunctions. Therefore, we do not need to consider the number of reduced matrix elements and the CGC but only focus on whether an SOC matrix element is allowed or forbidden.

3.7.5 Axial SOC $\left\langle {}^1A_1 \middle| H_{\mathbf{soc}} \middle| {}^3E_x^0/{}^3E_y^0 \right\rangle$

Here we show that the $\left\langle {}^1A_1 \middle| H_{\mathrm{soc}} \middle| {}^3E_x^0/{}^3E_y^0 \right\rangle$ SOC matrix element is zero. By using the Wigner-Eckart Theorem and wavefunctions in Table 3.13 and Table 3.14, the matrix element is written as

$$\begin{aligned}\left\langle {}^1A_1 \middle| H_{\mathrm{soc}} \middle| {}^3E_x^0/{}^3E_y^0 \right\rangle &= \sum_{j=1}^{2} \left\langle {}^1A_1 \middle| L_j^{A_2} S_j^{A_2} \middle| {}^3E_x^0/{}^3E_y^0 \right\rangle \\ &= \sum_{j=1}^{2}\sum_{i=1}^{2} \left(\begin{array}{cc|c} A_1 & A_1 & A_1 \\ 1 & 1 & 1 \end{array}\right)^* \left(\begin{array}{cc|c} E & A_2 & E \\ i & 1 & k \end{array}\right) \\ &\quad \times \left\langle \varphi_1^{a_1} \middle| L_j^{A_2} \middle| \psi^{E_i} \right\rangle \left\langle \nu^{A_1} \middle| S_j^{A_2} \middle| \nu^{A_2} \right\rangle \end{aligned} \tag{3.92}$$

i and k in the equation can take values 1 or 2 which corresponds to x or y, respectively. The above Clebsch–Gordan coefficients can be found in Sec. 3.7.1. Because the orbital matrix element transforms as $\{A_1 \otimes A_2 \otimes E\} = \{E\}$ which does not include the total symmetry A_1, the matrix element vanishes.

3.7.6 Axial SOC in the Excited Triplet Manifold

All the SOC matrix elements of interest are estimated and summarized in Table 5.2. One thing we can notice is that the following SOC splits the excited triplet

manifold $\{{}^3E_x^{\pm1}, {}^3E_y^{\pm1}, {}^3E_x^0, {}^3E_y^0, {}^3A_1^{\pm1}, {}^3A_2^{\pm1}, {}^1E_x', {}^1E_y'\}$,

$$\left\langle {}^3E_x^{\pm1}\middle|H_{\rm soc}\middle|{}^3E_x^{\pm1}\right\rangle \neq 0 \tag{3.93}$$

$$\left\langle {}^3E_y^{\pm1}\middle|H_{\rm soc}\middle|{}^3E_y^{\pm1}\right\rangle \neq 0 \tag{3.94}$$

$$\left\langle {}^3A_1^{\pm1}\middle|H_{\rm soc}\middle|{}^3A_1^{\pm1}\right\rangle \neq 0 \tag{3.95}$$

$$\left\langle {}^3A_2^{\pm1}\middle|H_{\rm soc}\middle|{}^3A_2^{\pm1}\right\rangle \neq 0 \tag{3.96}$$

$$\left\langle {}^3E_x^{0}\middle|H_{\rm soc}\middle|{}^3E_x^{0}\right\rangle = 0 \tag{3.97}$$

$$\left\langle {}^3E_y^{0}\middle|H_{\rm soc}\middle|{}^3E_y^{0}\right\rangle = 0 \tag{3.98}$$

Below is the reason that some are nonzero but the others are zero. In terms of the reduced one-particle format, we can write

$$\begin{aligned}
&\left\langle {}^3E_x^{\pm1}\middle|H_{\rm soc}\middle|{}^3E_x^{\pm1}\right\rangle \\
=&\left\langle {}^3E_x^{\pm1}\middle|L^{E_y}S^{E_y}+L^{E_x}S^{E_x}+L^{A_2}S^{A_2}\middle|{}^3E_x^{\pm1}\right\rangle \\
=&\left\langle \Phi^{E_x}\otimes\nu^{E_x}-\Phi^{E_y}\otimes\nu^{E_y}\middle|L^{E_y}S^{E_y}+L^{E_x}S^{E_x}+L^{A_2}S^{A_2}\middle|\Phi^{E_x}\otimes\nu^{E_x}-\Phi^{E_y}\otimes\nu^{E_y}\right\rangle \\
=&\Big(\left\langle\Phi^{E_x}\middle|L^{A_2}\middle|\Phi^{E_x}\right\rangle\left\langle\nu^{E_x}\middle|S^{A_2}\middle|\nu^{E_x}\right\rangle+\left\langle\Phi^{E_y}\middle|L^{A_2}\middle|\Phi^{E_y}\right\rangle\left\langle\nu^{E_y}\middle|S^{A_2}\middle|\nu^{E_y}\right\rangle\Big) \\
&-\Big(\left\langle\Phi^{E_x}\middle|L^{A_2}\middle|\Phi^{E_y}\right\rangle\left\langle\nu^{E_x}\middle|S^{A_2}\middle|\nu^{E_y}\right\rangle+\left\langle\Phi^{E_y}\middle|L^{A_2}\middle|\Phi^{E_x}\right\rangle\left\langle\nu^{E_y}\middle|S^{A_2}\middle|\nu^{E_x}\right\rangle\Big) \\
=&-\left\langle\Phi^{E_x}\middle|L^{A_2}\middle|\Phi^{E_y}\right\rangle\left\langle\nu^{E_x}\middle|S^{A_2}\middle|\nu^{E_y}\right\rangle-\left\langle\Phi^{E_y}\middle|L^{A_2}\middle|\Phi^{E_x}\right\rangle\left\langle\nu^{E_y}\middle|S^{A_2}\middle|\nu^{E_x}\right\rangle
\end{aligned} \tag{3.99}$$

Because $\left\langle \Phi^{E_x} \middle| L^{A_2} \middle| \Phi^{E_x} \right\rangle = \left\langle \Phi^{E_y} \middle| L^{A_2} \middle| \Phi^{E_y} \right\rangle = 0$, the first two terms are zero. Applying the same method for the orbital part, we can have

$$\begin{aligned}
\left\langle \Phi^{E_x} \middle| L^{A_2}_{j=1} \middle| \Phi^{E_y} \right\rangle &= \left\langle \varphi_1^{a_1}\varphi_2^{e_x} - \varphi_1^{e_x}\varphi_2^{a_1} \middle| L^{A_2}_{j=1} \middle| \varphi_1^{a_1}\varphi_2^{e_y} - \varphi_1^{e_y}\varphi_2^{a_1} \right\rangle \\
&= \left\langle \varphi_1^{e_x}\varphi_2^{a_1} \middle| L^{A_2}_{j=1} \middle| \varphi_1^{e_y}\varphi_2^{a_1} \right\rangle \\
&= \left\langle \varphi_1^{e_x} \middle| L^{A_2} \middle| \varphi_1^{e_y} \right\rangle \\
&= \begin{pmatrix} A_2 & E & \Big| & E \\ 1 & 2 & \Big| & 1 \end{pmatrix} \langle e||L^{A_2}||e\rangle \\
&= -\langle e||L^{A_2}||e\rangle
\end{aligned} \tag{3.100}$$

$$\begin{aligned}
\left\langle \Phi^{E_x} \middle| L^{A_2}_{j=2} \middle| \Phi^{E_y} \right\rangle &= \left\langle \varphi_1^{a_1}\varphi_2^{e_x} - \varphi_1^{e_x}\varphi_2^{a_1} \middle| L^{A_2}_{j=2} \middle| \varphi_1^{a_1}\varphi_2^{e_y} - \varphi_1^{e_y}\varphi_2^{a_1} \right\rangle \\
&= \left\langle \varphi_1^{a_1}\varphi_2^{e_x} \middle| L^{A_2}_{j=2} \middle| \varphi_1^{a_1}\varphi_2^{e_y} \right\rangle \\
&= \left\langle \varphi_1^{e_x} \middle| L^{A_2} \middle| \varphi_1^{e_y} \right\rangle \\
&= \begin{pmatrix} A_2 & E & \Big| & E \\ 1 & 2 & \Big| & 1 \end{pmatrix} \langle e||L^{A_2}||e\rangle \\
&= -\langle e||L^{A_2}||e\rangle
\end{aligned} \tag{3.101}$$

and the spin part is as follows,

$$\begin{aligned}
\left\langle \nu^{E_x} \middle| S^{A_2}_{j=1} \middle| \nu^{E_y} \right\rangle &= \frac{\hbar}{2} \langle \alpha\alpha + \beta\beta | (|\alpha\rangle\langle\alpha| - |\beta\rangle\langle\beta|)_{j=1} | i(\alpha\alpha - \beta\beta)\rangle \\
&= i\frac{\hbar}{2}(\langle \alpha\alpha | (|\alpha\rangle\langle\alpha|)_{j=1} | \alpha\alpha\rangle + \langle \beta\beta | (|\beta\rangle\langle\beta|)_{j=1} | \beta\beta\rangle) \\
&= i\hbar
\end{aligned} \tag{3.102}$$

$$\begin{aligned}\left\langle \nu^{E_x}\middle|S^{A_2}_{j=2}\middle|\nu^{E_y}\right\rangle &= \frac{\hbar}{2}\left\langle \alpha\alpha+\beta\beta\middle|(|\alpha\rangle\langle\alpha|-|\beta\rangle\langle\beta|)_{j=2}\middle|i(\alpha\alpha-\beta\beta)\right\rangle \\ &= i\frac{\hbar}{2}(\left\langle \alpha\alpha|(|\alpha\rangle\langle\alpha|)_{j=2}|\alpha\alpha\right\rangle+\left\langle \beta\beta|(|\beta\rangle\langle\beta|)_{j=2}|\beta\beta\right\rangle) \\ &= i\hbar\end{aligned} \tag{3.103}$$

Finally. by considering the two-particle wavefunction normalization factor (1/2) and the number of reduced one-particle matrix elements (in total 4), the SOC strength that splits the triplet states is

$$\left\langle {}^3E_x^{\pm1}\middle|H_{\rm soc}\middle|{}^3E_x^{\pm1}\right\rangle = i\hbar\left\langle e||L^{A_2}||e\right\rangle = -\lambda_z \tag{3.104}$$

which is same as the result in Ref. [85, 18]. It should be noticed that here is the hole representation of the wavefunctions used for the evaluation of SOC matrix elements, there is sign reversed for the value[7]. The other axial SOC matrix elements that split the triplet excited states can be evaluated likewise.

The nonaxial component is claimed to vanish because the orbital part of $H_{\rm soc}$ is Hermitian and purely imaginary, and the wavefunctions are real [85]. Mate et al. state that the wavefunctions are numerically proven to be real [87], but the numerical result is not found anywhere. The SOC matrix element for the states ${}^3E_x^0/{}^3E_y^0$ is shown to be zero because the spin part does not transform as A_1,

$$\begin{aligned}\left\langle {}^3E_x^0\middle|H_{\rm soc}\middle|{}^3E_x^0\right\rangle &= \left\langle {}^3E_x^0\middle|L^{E_y}S^{E_y}+L^{E_x}S^{E_x}+L^{A_2}S^{A_2}\middle|{}^3E_x^0\right\rangle \\ &= \left\langle E_y\otimes A_2|L^{E_y}S^{E_y}+L^{E_x}S^{E_x}+L^{A_2}S^{A_2}|E_y\otimes A_2\right\rangle \\ &= \left\langle E_y|L^{E_y}-L^{E_x}+L^{A_2}|E_y\right\rangle\left\langle A_2|S^{E_y}-S^{E_x}+S^{A_2}|A_2\right\rangle \\ &= 0\end{aligned} \tag{3.105}$$

[7]Mentioned in Ref. [1, 83] as "If a hole representation is chosen, some care must be taken, as some interactions reverse their sign, such as the spin–orbit interaction."

This explains why the SOC Hamiltonian that describes splitting the triplet excited states [1] can be written as

$$H_{\text{soc}} = \lambda_z \left(\left| {}^3A_1^{\pm 1} \right\rangle\!\!\left\langle {}^3A_1^{\pm 1} \right| + \left| {}^3A_2^{\pm 1} \right\rangle\!\!\left\langle {}^3A_2^{\pm 1} \right| - \left| {}^3E_x^{\pm 1} \right\rangle\!\!\left\langle {}^3E_x^{\pm 1} \right| - \left| {}^3E_y^{\pm 1} \right\rangle\!\!\left\langle {}^3E_y^{\pm 1} \right| \right) \quad (3.106)$$

Finally, the SOC matrix elements of interest are derived and tabulated in Table 3.15.

Table 3.15: SOC matrix element of NV center from group theory. Because H_{soc} is Hermitian, the upper half of the matrix element is sufficient. The result is consistent with Table 2 in Ref. [18]. $\lambda_z(\lambda_\perp)$ denotes the nonzero matrix element due to axial (nonaxial) SOC. The matrix elements here are expressed in terms of the reduced one-particle matrix elements, $\lambda_z = -i\hbar\langle e||L^{A_2}||e\rangle$ and $\lambda_\perp = -(i/\sqrt{2})\hbar\langle e||L^{E}||a_1\rangle$. See the derivation details in Sec. 3.7.2 and 3.7.3.

	$^3A_2^0$	$^3A_2^{-1}$	$^3A_2^1$	^1E_x	^1E_y	$^1A_1$	$^3E_x^{\pm1}$	$^3E_y^{\pm1}$	$^3E_x^0$	$^3E_y^0$	$^3A_1^{\pm1}$	$^3A_2^{\pm1}$	$^1E'_x$	$^1E'_y$
$^3A_2^0$	0	0	0	0	0	$-2i\lambda_z$	0	0	0	0	$\sqrt{2}\lambda_\perp$	0	0	0
$^3A_2^{-1}$		0	0	0	0	0	0	0	$-\lambda_\perp$	$-\lambda_\perp$	0	0	$i\lambda_\perp$	$i\lambda_\perp$
$^3A_2^1$			0	0	0	0	0	0	$-\lambda_\perp$	$-\lambda_\perp$	0	0	$i\lambda_\perp$	$i\lambda_\perp$
^1E_x				0	0	0	$-\sqrt{2}i\lambda_\perp$	0	0	0	0	0	0	0
^1E_y					0	0	0	$-\sqrt{2}i\lambda_\perp$	0	0	0	0	0	0
$^1A_1$						0	0	0	0	0	$\sqrt{2}i\lambda_\perp$	0	0	0
$^3E_x^{\pm1}$							$-\lambda_z$	0	0	0	0	0	0	0
$^3E_y^{\pm1}$								$-\lambda_z$	0	0	0	0	0	0
$^3E_x^0$									0	0	0	0	$-i\lambda_z$	0
$^3E_y^0$										0	0	0	0	$-i\lambda_z$
$^3A_1^{\pm1}$											λ_z	0	0	0
$^3A_2^{\pm1}$												λ_z	0	0
$^1E'_x$													0	0
$^1E'_y$														0

3.8 Configuration Interaction, Pseudo Jahn-Teller Effect and Dynamical Jahn-Teller Effect on SOC

3.8.1 Configuration Interaction and Pseudo Jahn-Teller Effect on SOC

It can be noticed that all intersystem crossing transitions of interest turn out to have finite values from experiments [88, 89, 4]. This implies that the axial $\langle {}^3E|H_{\text{soc}}|{}^1A_1\rangle$, nonaxial $\langle {}^1E|H_{\text{soc}}|{}^3A_2\rangle$ and axial $\langle {}^1E|H_{\text{soc}}|{}^3A_2\rangle$ SOC matrix elements can be allowed. The discrepancy observed between experimental findings and the current predictions of group theory highlights the need for finding underlying mechanisms governing SOC. It implies that there might be transformative processes altering the symmetries of these relevant electronic states, ultimately triggering significant changes in the strength of the SOC.

Previous studies suggest that the mechanisms are configuration interaction [20] and pseudo Jahn-Teller (JT) effect [68]. First, the configuration interaction leads to electron-electron correlation in the singlet ground state $|{}^1E\rangle$ and singlet excited state $|{}^1E'\rangle$ (singlet state of $a_1^1e^3$ configuration), and causes mixing between $|{}^1E\rangle$ and $|{}^1E'\rangle$ [18, 1, 20]. In addition, $|{}^1A_1\rangle$ and $|{}^1A_1'\rangle$ (singlet state of e^4 configuration) were also claimed to be coupled by configuration interaction, which could explain the blueshift of the phonon side bands of $|{}^1A_1\rangle \rightarrow |{}^1E\rangle$ with respect to those of $|{}^3A_2\rangle \rightarrow |{}^3E\rangle$ [20]. This

mixing of states results in the following linear combinations

$$\left|{}^1\bar{E}\right\rangle = C_1 \left|{}^1E\right\rangle + \sqrt{1-C_1^2}\left|{}^1E'\right\rangle \tag{3.107}$$

$$\left|{}^1\bar{A}_1\right\rangle = C_2 \left|{}^1A_1\right\rangle + \sqrt{1-C_2^2}\left|{}^1A'\right\rangle \tag{3.108}$$

where C_1 and C_2 are the mixing coefficients. Our CASSCF calculation shows the configuration interaction by the mixing coefficients, which can be seen in Table 3.16. The effect of the configuration interaction on SOC is turning the originally symmetry-forbidden $\lambda_\perp({}^1E,{}^3A_2)$ and $\lambda_\perp({}^1E,{}^3E)$ into allowed, as can be seen in Table 3.17.

Table 3.16: Electronic configurations of the multi-particle states from SA(6)-CASSCF(6,6) calculation using the $C_{33}H_{36}N^{-1}$ cluster model. The composition of the electronic configurations includes orbitals a_{1N}, a_{1C}, e_x, e_y, e'_x and e'_y. a_{1N} is the a_1 type orbital around the N atom, and a_{1C} is the a_1 type orbital around the C atom.

State	Configuration						Weight (%)	Note
	a_{1N}	a_{1C}	e_y	e_x	e'_x	e'_y		
${}^3A_2$	↑↓	↑↓	↑	↑			94	Group theory prediction
	↑↓	↓	↑	↑	↑		1	–
${}^3E$	↑↓	↑	↑↓	↑			87	Group theory prediction
	↑↓	↑	↓	↑	↑		3	–
	↑↓	↑	↑	↑↓			87	Group theory prediction
	↑↓	↑	↓	↑		↑	3	–

State	Configuration						Weight (%)	Note
	a_{1N}	a_{1C}	e_y	e_x	e'_x	e'_y		
^1E	↑↓	↑↓	↑	↓			77	Group theory prediction
	↑↓	↑	↑↓	↓			17	$^1E - {}^1E'$ coupling due to configuration interaction
	↑↓	↑↓	↑↓				38	Group theory prediction
	↑↓	↑↓		↑↓			39	Group theory prediction
	↑↓	↑	↓	↑↓			16	$^1E - {}^1E'$ coupling due to configuration interaction
$^1A_1$	↑↓	↑↓	↑↓				33	Group theory prediction
	↑↓	↑↓		↑↓			33	Group theory prediction
	↑↓		↑↓	↑↓			21	$^1A_1 - {}^1A'_1$ coupling due to configuration interaction and double excitation
	↑↓	↑	↓	↑		↓	3	Double excitation

The current theory with configuration interaction, however, does not fully explain experiments which show finite values for all the intersystem crossing between triplet and singlet electronic states. In order to account for experimental observed SOC, as suggested by Ref. [68], we can take pseudo JT effect to account for the experimental observation. Let the vibronic wave funciton expressed as below under the Born–Oppenheimer approximation,

$$\left|\widetilde{\Psi}\right\rangle = \sum_{i,j,\Gamma} C^{\Gamma}_{i,j} \left|\psi_i\right\rangle \otimes \left|\chi^{\Gamma}_{i,j}\right\rangle \tag{3.109}$$

$$\left|\chi^{\Gamma}_{i,j}\right\rangle = \sum_{n+m=0}^{j-1} \left|nm\right\rangle^{\Gamma} \tag{3.110}$$

where $\left|\chi^{\Gamma}_{i,j}\right\rangle$ represents the vibrational wave functions that compose n active e_x phonons

Table 3.17: Summary of SOC matrix elements predicted by group theory, calculated at the theory levels of CASSCF and TDDFT in this work, calculated in previous work at DFT with HSE functional, and from experiments. The unit is GHz. "CI" stands for configuration interaction that mixes $\left|^1E\right\rangle$ and $\left|^1E'\right\rangle$. Pseudo JT effect mixes $\left|^1A_1\right\rangle$ and $\left|^1E\right\rangle$ through electron-phonon coupling, leading to nonzero SOCs. "–" denotes value that does not exist or that is not found.

	$\lambda_z(^3E,^3E)$	$\lambda_\perp(^1A_1,^3E)$	$\lambda_z(^1A_1,^3E)$	$\lambda_\perp(^1E,^3E)$	$\lambda_z(^1E,^3E)$
Group Theory [1]	$\pm\lambda_z$	$i\sqrt{2}\lambda_\perp$	0	$-i\sqrt{2}\lambda_\perp$	nonzero by CI
SA(10)-CASSCF(4,6)	7.56	2.04	0	7.95	1.56[2]
SA(6)-CASSCF(6,6)	14.21	3.96	0.06	11.66	3.33[2]
TDDFT	–	6.12	0.001	9.38	8.90
(w/ pseudo JT)	$\lambda_z(^3\widetilde{E},^3\widetilde{E})$	$\lambda_\perp(^1\widetilde{A}_1,^3\widetilde{E})$	$\lambda_z(^1\widetilde{A}_1,^3\widetilde{E})$	$\lambda_\perp(^1\widetilde{E},^3\widetilde{E})$	$\lambda_z(^1\widetilde{E},^3\widetilde{E})$
Group Theory[1]	$\pm\lambda_z$	nonzero	nonzero by pseudo JT	nonzero	nonzero by CI
Effective SOC SA(10)-CASSCF(4,6)	7.56	3.96	0.39	8.20	1.51
Effective SOC SA(6)-CASSCF(6,6)	14.21	6.75	0.83	12.28	3.22
HSE [52, 68]	15.8[3]	56.3[4]	–	–	–
Expt. [88, 90]	5.33	6.4[7]	– (nonzero)	–	–

	$\lambda_\perp(^3A_2,^1A_1)$	$\lambda_z(^3A_2,^1A_1)$	$\lambda_\perp(^3A_2,^1E)$	$\lambda_z(^3A_2,^1E)$
Group Theory [1]	0	$-i2\lambda_z$	nonzero by CI	0
SA(10)-CASSCF(4,6)	0	31.78	4.29[2]	0
SA(6)-CASSCF(6,6)	0	31.09	5.22[2]	0.03
TDDFT	1.87	0.001	8.18	50.37
(w/ pseudo JT)	$\lambda_\perp(^3\widetilde{A}_2,^1\widetilde{A}_1)$	$\lambda_z(^3\widetilde{A}_2,^1\widetilde{A}_1)$	$\lambda_\perp(^3\widetilde{A}_2,^1\widetilde{E})$	$\lambda_z(^3\widetilde{A}_2,^1\widetilde{E})$
Group Theory[1]	nonzero by pseudo JT	nonzero	nonzero by CI	nonzero by pseudo JT
Effective SOC SA(10)-CASSCF(4,6)	1.07	30.76	4.15	7.94
Effective SOC SA(6)-CASSCF(6,6)	1.31	30.10	5.05	7.77
HSE [52, 68]	–	–	18.96[5]	15.8[6]
Expt. [88, 90]	–	–	– (nonzero)	– (nonzero)

1. The matrix elements here are expressed in terms of the reduced one-particle matrix elements, $\lambda_z = -i\hbar\langle e||L^{A_2}||e\rangle$ and $\lambda_\perp = -(i/\sqrt{2})\hbar\langle e||L^E||a_1\rangle$.

2. The matrix element is nonzero because ^1E coupled with singlet excited state $^1E'$ through configuration interaction, and $\lambda_z(^3E,^1E')$ is allowed. This coupling exists in CASSCF solutions, as can be seen in Table 3.16.

3. $\lambda_z(^3E,^3E)$ was calculated by $\langle e_+|H_{\rm soc}|e_+\rangle$ (with $|e_+\rangle = \frac{1}{\sqrt{2}}(|e_x\rangle + i\,|e_y\rangle)$) at HSE [52]. The matrix element reduced to 4.8 by a reduction factor.

4. $\lambda_\perp(^1A_1,^3E)$ was calculated by $\langle e_+|H_{\rm soc}|a_1\rangle$ (with $|e_+\rangle = \frac{1}{\sqrt{2}}(|e_x\rangle + i\,|e_y\rangle)$) at HSE [52], assuming single-particle picture and that KS wavefunctions constructed ^3E and $^1A_1$ did not differ [26].

5. $\lambda_\perp(^3\widetilde{A}_2,^1\widetilde{E})$ was a parameter estimated by taking $\lambda_\perp(^3\widetilde{A}_2,^1\widetilde{E})/\lambda_z(^3\widetilde{A}_2,^1\widetilde{E}) = 1.2$ for matching it with experiment [68].

6. $\lambda_z(^3\widetilde{A}_2,^1\widetilde{E})$ was calculated according to $\langle ^3E|H_{soc}|^3E\rangle = \langle e_+|H_{\rm soc}|e_+\rangle$ [52, 68].

7. The matrix element is estimated by using the ratio $\lambda_\perp(\to {}^1A_1)/\lambda_z(\to {}^1A_1) = 1.2$ [26].

and m active e_y phonons belonging to the i-th electronic state. The corresponding structure distortion has Γ symmetry. $C_{i,j}^{\Gamma}$ is the amplitude or coefficient that weights the vibronic state, and will be specifically replaced by c_j, d_j, f_j, g_j for electron-phonon coupling from strong to weak. As only e phonons essentially break the symmetry by geometry distortion, we only consider the JT-active e phonon modes in the phonon configuration. For simplicity, electron coordinate and nuclear coordinate are included implicitly. The vibronic wave function of $\left|{}^3A_2\right\rangle$ is the direct product of the electronic wave function and the vibrational wave functions since it is nondegenerate. As for $\left|{}^3E\right\rangle$, even though there is dynamical JT effect on ${}^3E$, the mixing degenerate electronic states does not influence the SOC matrix elements other than $\lambda_z({}^3E,{}^3E)$ which is discussed in Sec. 3.8.2. Therefore, we also write its vibronic wave function as the direct product of the electronic wave function and vibrational wave function. In addition, the pseudo JT effect can be weak when the bandgap between the electronic states of interest are large [65, 68]. Because $\left|{}^3A_2\right\rangle$ and $\left|{}^3E\right\rangle$ are separated by a large energy 1.945 eV, the pseudo JT effect for these states be minuscule. Here, we write the vibronic states for ${}^3A_2$ and ${}^3E$ as,

$$\left|{}^3\widetilde{A}_2\right\rangle = \left|{}^3A_2\right\rangle \otimes \sum_{i=1}^{\infty}\left[c_i'''\left|\chi_i^{A_1}\right\rangle + d_i'''\left|\chi_i^{E_+}\right\rangle + f_i'''\left|\chi_i^{E_-}\right\rangle + g_i'''\left|\chi_i^{A_2}\right\rangle\right] \tag{3.111}$$

$$\left|{}^3\widetilde{E}\right\rangle = \left|{}^3E\right\rangle \otimes \sum_{i=1}^{\infty}\left[c_i''\left|\chi_i^{A_1}\right\rangle + d_i''\left|\chi_i^{E_+}\right\rangle + f_i''\left|\chi_i^{E_-}\right\rangle + g_i''\left|\chi_i^{A_2}\right\rangle\right] \tag{3.112}$$

The singlet states ${}^1\bar{A}_1$ and ${}^1\bar{E}$ are actually coupled by the electron-phonon

coupling due to pseudo JT effect [68, 7]. The pseudo JT Hamiltonian is

$$H = \underbrace{\begin{pmatrix} \Lambda & 0 & 0 \\ 0 & 0 & 0 \\ 0 & 0 & 0 \end{pmatrix}}_{H_{\mathrm{e}}} + \underbrace{\frac{K}{2}(Q_x^2 + Q_y^2)}_{H_{\mathrm{osc}}} + \underbrace{\begin{pmatrix} 0 & FQ_x & FQ_y \\ FQ_x & 0 & 0 \\ FQ_y & 0 & 0 \end{pmatrix}}_{H_{\mathrm{PJT}}} \tag{3.113}$$

$$F = \left\langle {}^1A_1 \middle| \frac{\partial V}{\partial Q_x} \middle| {}^1E_x \right\rangle = \left\langle {}^1A_1 \middle| \frac{\partial V}{\partial Q_y} \middle| {}^1E_y \right\rangle \tag{3.114}$$

Here, Λ is the energy gap between ${}^1A_1$ and ${}^1E$. ${}^1A_1$, ${}^1E_x$ and ${}^1E_y$ form the bases of the Hamiltonian. F is the linear vibronic coupling constant. Due to the pseudo JT effect, the eigenstates become the linear combination of the bases. By retaining the symmetry, we can write the vibronic wave functions as below,

$$\begin{aligned} \left| {}^1\widetilde{E}_x \right\rangle = \sum_{i=1}^{\infty} \Bigg[& c_i \left| {}^1\bar{E}_x \right\rangle \otimes \left| \chi_i^{A_1} \right\rangle + d_i \left| {}^1A_1 \right\rangle \otimes \left| \chi_i^{E_x} \right\rangle \\ & + \frac{f_i}{\sqrt{2}} \left(\left| {}^1\bar{E}_x \right\rangle \otimes \left| \chi_i^{E_x} \right\rangle - \left| {}^1\bar{E}_y \right\rangle \otimes \left| \chi_i^{E_y} \right\rangle \right) + g_i \left| {}^1\bar{E}_y \right\rangle \otimes \left| \chi_i^{A_2} \right\rangle \Bigg] \end{aligned} \tag{3.115}$$

$$\begin{aligned} \left| {}^1\widetilde{E}_y \right\rangle = \sum_{i=1}^{\infty} \Bigg[& c_i \left| {}^1\bar{E}_y \right\rangle \otimes \left| \chi_i^{A_1} \right\rangle + d_i \left| {}^1A_1 \right\rangle \otimes \left| \chi_i^{E_y} \right\rangle \\ & + \frac{f_i}{\sqrt{2}} \left(\left| {}^1\bar{E}_x \right\rangle \otimes \left| \chi_i^{E_y} \right\rangle + \left| {}^1\bar{E}_y \right\rangle \otimes \left| \chi_i^{E_x} \right\rangle \right) + g_i \left| {}^1\bar{E}_x \right\rangle \otimes \left| \chi_i^{A_2} \right\rangle \Bigg] \end{aligned} \tag{3.116}$$

$$\left| {}^1\widetilde{A}_1 \right\rangle = \sum_{i=1}^{\infty} \left[c_i' \left| {}^1A_1 \right\rangle \otimes \left| \chi_i^{A_1} \right\rangle + \frac{d_i'}{\sqrt{2}} \left(\left| {}^1\bar{E}_x \right\rangle \otimes \left| \chi_i^{E_x} \right\rangle + \left| {}^1\bar{E}_y \right\rangle \otimes \left| \chi_i^{E_y} \right\rangle \right) \right] \tag{3.117}$$

These functions are written according to the quadratic functions in C_{3v} point group that $x^2 - y^2$ and xz transform as E_x, that xy and yz transform as E_y, and that $x^2 + y^2$ and z^2 transform as A_1. Because the vibronic wave function $\left| {}^1\widetilde{E}_x \right\rangle$ and $\left| {}^1\widetilde{E}_y \right\rangle$ are

degenerate, each term of $\left|{}^1\widetilde{E}_x\right\rangle$ has the same amplitude as that of $\left|{}^1\widetilde{E}_y\right\rangle$. Alternatively, we can rewrite these vibronic wave functions according to the other notation $|E_\pm\rangle = \big(\,|E_x\rangle \pm i\,|E_y\rangle\,\big)/\sqrt{2}$. Since

$$\begin{aligned}
|E_\pm\rangle \otimes |E_\mp\rangle &= \frac{1}{2}\big(\,|E_x\rangle \pm i\,|E_y\rangle\,\big) \otimes \big(\,|E_x\rangle \mp i\,|E_y\rangle\,\big) \\
&= \frac{1}{2}\big(\,|E_x\rangle \otimes |E_x\rangle + |E_y\rangle \otimes |E_y\rangle\,\big)
\end{aligned} \tag{3.118}$$

$$\begin{aligned}
|E_\pm\rangle \otimes |E_\pm\rangle &= \frac{1}{2}\big(\,|E_x\rangle \pm i\,|E_y\rangle\,\big) \otimes \big(\,|E_x\rangle \pm i\,|E_y\rangle\,\big) \\
&= \frac{1}{2}\Big[\,|E_x\rangle \otimes |E_x\rangle - |E_y\rangle \otimes |E_y\rangle \pm i\big(\,|E_x\rangle \otimes |E_y\rangle + |E_y\rangle \otimes |E_x\rangle\,\big)\Big]
\end{aligned} \tag{3.119}$$

we can find

$$\begin{aligned}
\left|{}^1\widetilde{E}_\pm\right\rangle &= \frac{1}{\sqrt{2}}\left(\left|{}^1\widetilde{E}_x\right\rangle \pm i\left|{}^1\widetilde{E}_y\right\rangle\right) \\
&= \sum_{i=1}^{\infty}\Bigg[c_i\left|{}^1\bar{E}_\pm\right\rangle \otimes \left|\chi_i^{A_1}\right\rangle + d_i\left|{}^1A_1\right\rangle \otimes \left|\chi_i^{E_\pm}\right\rangle \\
&\quad + f_i\left|{}^1\bar{E}_\pm\right\rangle \otimes \left|\chi_i^{E_\pm}\right\rangle \pm i g_i\left|{}^1\bar{E}_\mp\right\rangle \otimes \left|\chi_i^{A_2}\right\rangle\Bigg] \\
&= \sum_{i=1}^{\infty}\Bigg[c_i\left|{}^1\bar{E}_\pm\right\rangle \otimes \left|\chi_i^{A_1}\right\rangle + d_i\left|{}^1A_1\right\rangle \otimes \left|\chi_i^{E_\pm}\right\rangle \\
&\quad + f_i\left|{}^1\bar{E}_\pm\right\rangle \otimes \left|\chi_i^{E_\pm}\right\rangle + g_i\left|{}^1\bar{E}_\mp\right\rangle \otimes \left|\chi_i^{A_2}\right\rangle\Bigg]
\end{aligned} \tag{3.120}$$

$$\left|{}^1\widetilde{A}_1\right\rangle = \sum_{i=1}^{\infty}\left[c_i'\left|{}^1A_1\right\rangle \otimes \left|\chi_i^{A_1}\right\rangle + \frac{d_i'}{\sqrt{2}}\left(\left|{}^1\bar{E}_+\right\rangle \otimes \left|\chi_i^{E_-}\right\rangle + \left|{}^1\bar{E}_-\right\rangle \otimes \left|\chi_i^{E_+}\right\rangle\right)\right] \tag{3.121}$$

Here, a factor of $\pm i$ is implicitly contained in the amplitude g_i in Eq. (3.120) when using the $E_\pm$ notation. The normalization factor of $1/\sqrt{2}$ is implicitly contained in all the coefficients.

The states mixing due to the configuration interaction and pseudo JT effect turn the originally forbidden SOC matrix elements into nonzero by the sum of multiple

SOC components. Here, we write down the nonzero matrix elements which contain the totally symmetric component than transforms as A_1,

$$\begin{aligned}\left\langle {}^1\widetilde{A}_1\middle|H_{\rm soc}\middle|{}^3\widetilde{E}\right\rangle = \sum_{i,j=1}^{\infty}\Bigg[& c_i' c_j'' \left\langle {}^1A_1\middle|H_{\rm soc}\middle|{}^3E\right\rangle \otimes \left\langle \chi_i^{A_1}\middle|\chi_j^{A_1}\right\rangle \\ & + \frac{d_i' f_j''}{\sqrt{2}} \left\langle {}^1\bar{E}_+\middle|H_{\rm soc}\middle|{}^3E\right\rangle \otimes \left\langle \chi_i^{E_-}\middle|\chi_j^{E_-}\right\rangle \\ & + \frac{d_i' d_j''}{\sqrt{2}} \left\langle {}^1\bar{E}_-\middle|H_{\rm soc}\middle|{}^3E\right\rangle \otimes \left\langle \chi_i^{E_+}\middle|\chi_j^{E_+}\right\rangle \Bigg]\end{aligned} \tag{3.122}$$

$$\begin{aligned}\left\langle {}^3\widetilde{A}_2\middle|H_{\rm soc}\middle|{}^1\widetilde{E}_\pm\right\rangle = \sum_{i,j=1}^{\infty}\Bigg[& c_j c_i''' \left\langle {}^3A_2\middle|H_{\rm soc}\middle|{}^1\widetilde{E}_\pm\right\rangle \otimes \left\langle \chi_i^{A_1}\middle|\chi_j^{A_1}\right\rangle \\ & + d_j \left\langle {}^3A_2\middle|H_{\rm soc}\middle|{}^1A_1\right\rangle \otimes \left(d_i''' \left\langle \chi_i^{E_+}\middle|\chi_j^{E_\pm}\right\rangle + f_i''' \left\langle \chi_i^{E_-}\middle|\chi_j^{E_\pm}\right\rangle \right) \\ & + f_j \left\langle {}^3A_2\middle|H_{\rm soc}\middle|{}^1\bar{E}_\pm\right\rangle \otimes \left(d_i''' \left\langle \chi_i^{E_+}\middle|\chi_j^{E_\pm}\right\rangle + f_i''' \left\langle \chi_i^{E_-}\middle|\chi_j^{E_\pm}\right\rangle \right) \\ & + g_j g_i''' \left\langle {}^3A_2\middle|H_{\rm soc}\middle|{}^1\bar{E}_\mp\right\rangle \otimes \left\langle \chi_i^{A_2}\middle|\chi_j^{A_2}\right\rangle \Bigg]\end{aligned} \tag{3.123}$$

$$\begin{aligned}\left\langle {}^1\widetilde{E}_\pm\middle|H_{\rm soc}\middle|{}^3\widetilde{E}\right\rangle = \sum_{i,j=1}^{\infty}\Bigg[& c_i c_j'' \left\langle {}^1\bar{E}_\pm\middle|H_{\rm soc}\middle|{}^3E\right\rangle \otimes \left\langle \chi_i^{A_1}\middle|\chi_j^{A_1}\right\rangle \\ & + d_i \left\langle {}^1A_1\middle|H_{\rm soc}\middle|{}^3E\right\rangle \otimes \left(d_j'' \left\langle \chi_i^{E_\pm}\middle|\chi_j^{E_+}\right\rangle + f_j'' \left\langle \chi_i^{E_\pm}\middle|\chi_j^{E_-}\right\rangle \right) \\ & + f_i \left\langle {}^1\bar{E}_\pm\middle|H_{\rm soc}\middle|{}^3E\right\rangle \otimes \left(d_j'' \left\langle \chi_i^{E_\pm}\middle|\chi_j^{E_+}\right\rangle + f_i'' \left\langle \chi_i^{E_\pm}\middle|\chi_j^{E_+}\right\rangle \right) \\ & + g_j g_i'' \left\langle {}^1\bar{E}_\mp\middle|H_{\rm soc}\middle|{}^3E\right\rangle \otimes \left\langle \chi_i^{A_2}\middle|\chi_j^{A_2}\right\rangle \Bigg]\end{aligned} \tag{3.124}$$

$$\begin{aligned}\left\langle {}^3\widetilde{A}_2\middle|H_{\rm soc}\middle|{}^1\widetilde{A}_1\right\rangle = \sum_{i,j=1}^{\infty}\Bigg[& c_j' c_i''' \left\langle {}^3A_2\middle|H_{\rm soc}\middle|{}^1A_1\right\rangle \otimes \left\langle \chi_i^{A_1}\middle|\chi_j^{A_1}\right\rangle \\ & + \frac{d_j' f_i'''}{\sqrt{2}} \left\langle {}^3A_2\middle|H_{\rm soc}\middle|{}^1\bar{E}_+\right\rangle \otimes \left\langle \chi_i^{E_-}\middle|\chi_j^{E_-}\right\rangle \\ & + \frac{d_j' d_i'''}{\sqrt{2}} \left\langle {}^3A_2\middle|H_{\rm soc}\middle|{}^1\bar{E}_-\right\rangle \otimes \left\langle \chi_i^{E_+}\middle|\chi_j^{E_+}\right\rangle \Bigg]\end{aligned} \tag{3.125}$$

Separating the parallel and perpendicular parts of the SOC matrix element according to symmetry analysis by group theory, it can be found that

$$\begin{aligned}\left\langle {}^1\widetilde{A}_1\middle|H_{\mathrm{soc}}\middle|{}^3\widetilde{E}\right\rangle_z = \sum_{i,j=1}^{\infty}\Bigg[&\frac{d_i' f_j''}{\sqrt{2}}\left\langle {}^1\bar{E}_+\middle|H_{\mathrm{soc}}\middle|{}^3E\right\rangle_z \otimes \left\langle \chi_i^{E_-}\middle|\chi_j^{E_-}\right\rangle \\ &+ \frac{d_i' d_j''}{\sqrt{2}}\left\langle {}^1\bar{E}_-\middle|H_{\mathrm{soc}}\middle|{}^3E\right\rangle_z \otimes \left\langle \chi_i^{E_+}\middle|\chi_j^{E_+}\right\rangle\Bigg]\end{aligned} \tag{3.126}$$

$$\begin{aligned}\left\langle {}^1\widetilde{A}_1\middle|H_{\mathrm{soc}}\middle|{}^3\widetilde{E}\right\rangle_\perp = \sum_{i,j=1}^{\infty}\Bigg[&c_i' c_j''\left\langle {}^1A_1\middle|H_{\mathrm{soc}}\middle|{}^3E\right\rangle_\perp \otimes \left\langle \chi_i^{A_1}\middle|\chi_j^{A_1}\right\rangle \\ &+ \frac{d_i' f_j''}{\sqrt{2}}\left\langle {}^1\bar{E}_+\middle|H_{\mathrm{soc}}\middle|{}^3E\right\rangle_\perp \otimes \left\langle \chi_i^{E_-}\middle|\chi_j^{E_-}\right\rangle \\ &+ \frac{d_i' d_j''}{\sqrt{2}}\left\langle {}^1\bar{E}_-\middle|H_{\mathrm{soc}}\middle|{}^3E\right\rangle_\perp \otimes \left\langle \chi_i^{E_+}\middle|\chi_j^{E_+}\right\rangle\Bigg]\end{aligned} \tag{3.127}$$

$$\left\langle {}^3\widetilde{A}_2\middle|H_{\mathrm{soc}}\middle|{}^1\widetilde{E}_\pm\right\rangle_z = \sum_{i,j=1}^{\infty} d_j\left\langle {}^3A_2\middle|H_{\mathrm{soc}}\middle|{}^1A_1\right\rangle_z \otimes \left(d_i'''\left\langle \chi_i^{E_+}\middle|\chi_j^{E_\pm}\right\rangle + f_i'''\left\langle \chi_i^{E_-}\middle|\chi_j^{E_\pm}\right\rangle\right) \tag{3.128}$$

$$\begin{aligned}\left\langle {}^3\widetilde{A}_2\middle|H_{\mathrm{soc}}\middle|{}^1\widetilde{E}_\pm\right\rangle_\perp = \sum_{i,j=1}^{\infty}\Bigg[&c_j c_i'''\left\langle {}^3A_2\middle|H_{\mathrm{soc}}\middle|{}^1\bar{E}_\pm\right\rangle_\perp \otimes \left\langle \chi_i^{A_1}\middle|\chi_j^{A_1}\right\rangle \\ &+ f_j\left\langle {}^3A_2\middle|H_{\mathrm{soc}}\middle|{}^1\bar{E}_\pm\right\rangle_\perp \otimes \left(d_i'''\left\langle \chi_i^{E_+}\middle|\chi_j^{E_\pm}\right\rangle + f_i'''\left\langle \chi_i^{E_-}\middle|\chi_j^{E_\pm}\right\rangle\right) \\ &+ g_j g_i'''\left\langle {}^3A_2\middle|H_{\mathrm{soc}}\middle|{}^1\bar{E}_\mp\right\rangle_\perp \otimes \left\langle \chi_i^{A_2}\middle|\chi_j^{A_2}\right\rangle\Bigg]\end{aligned} \tag{3.129}$$

$$\left\langle {}^1\widetilde{E}_\pm \middle| H_{\rm soc} \middle| {}^3\widetilde{E} \right\rangle_z = \sum_{i,j=1}^{\infty} \Bigg[c_i c_j'' \left\langle {}^1\bar{E}_\pm \middle| H_{\rm soc} \middle| {}^3E \right\rangle_z \otimes \left\langle \chi_i^{A_1} \middle| \chi_j^{A_1} \right\rangle + f_i \left\langle {}^1\bar{E}_\pm \middle| H_{\rm soc} \middle| {}^3E \right\rangle_z \otimes \left(d_j'' \left\langle \chi_i^{E_\pm} \middle| \chi_j^{E_+} \right\rangle + f_i'' \left\langle \chi_i^{E_\pm} \middle| \chi_j^{E_+} \right\rangle \right) + g_j g_i'' \left\langle {}^1\bar{E}_\mp \middle| H_{\rm soc} \middle| {}^3E \right\rangle_z \otimes \left\langle \chi_i^{A_2} \middle| \chi_j^{A_2} \right\rangle \Bigg] \tag{3.130}$$

$$\left\langle {}^1\widetilde{E}_\pm \middle| H_{\rm soc} \middle| {}^3\widetilde{E} \right\rangle_\perp = \sum_{i,j=1}^{\infty} \Bigg[c_i c_j'' \left\langle {}^1\bar{E}_\pm \middle| H_{\rm soc} \middle| {}^3E \right\rangle_\perp \otimes \left\langle \chi_i^{A_1} \middle| \chi_j^{A_1} \right\rangle + d_i \left\langle {}^1A_1 \middle| H_{\rm soc} \middle| {}^3E \right\rangle_\perp \otimes \left(d_j'' \left\langle \chi_i^{E_\pm} \middle| \chi_j^{E_+} \right\rangle + f_j'' \left\langle \chi_i^{E_\pm} \middle| \chi_j^{E_-} \right\rangle \right) + f_i \left\langle {}^1\bar{E}_\pm \middle| H_{\rm soc} \middle| {}^3E \right\rangle_\perp \otimes \left(d_j'' \left\langle \chi_i^{E_\pm} \middle| \chi_j^{E_+} \right\rangle + f_i'' \left\langle \chi_i^{E_\pm} \middle| \chi_j^{E_+} \right\rangle \right) + g_j g_i'' \left\langle {}^1\bar{E}_\mp \middle| H_{\rm soc} \middle| {}^3E \right\rangle_\perp \otimes \left\langle \chi_i^{A_2} \middle| \chi_j^{A_2} \right\rangle \Bigg] \tag{3.131}$$

$$\left\langle {}^3\widetilde{A}_2 \middle| H_{\rm soc} \middle| {}^1\widetilde{A}_1 \right\rangle_z = \sum_{i,j=1}^{\infty} c_j' c_i''' \left\langle {}^3A_2 \middle| H_{\rm soc} \middle| {}^1A_1 \right\rangle_z \otimes \left\langle \chi_i^{A_1} \middle| \chi_j^{A_1} \right\rangle \tag{3.132}$$

$$\left\langle {}^3\widetilde{A}_2 \middle| H_{\rm soc} \middle| {}^1\widetilde{A}_1 \right\rangle_\perp = \sum_{i,j=1}^{\infty} \Bigg[\frac{d_j' f_i'''}{\sqrt{2}} \left\langle {}^3A_2 \middle| H_{\rm soc} \middle| {}^1\bar{E}_+ \right\rangle_\perp \otimes \left\langle \chi_i^{E_-} \middle| \chi_j^{E_-} \right\rangle + \frac{d_j' d_i'''}{\sqrt{2}} \left\langle {}^3A_2 \middle| H_{\rm soc} \middle| {}^1\bar{E}_- \right\rangle_\perp \otimes \left\langle \chi_i^{E_+} \middle| \chi_j^{E_+} \right\rangle \Bigg] \tag{3.133}$$

The exact evaluation of the matrix elements requires all the state-mixing coefficients and all phonons of the electronic states ${}^3A_2$, ${}^1E$, ${}^1A_1$ and ${}^3E$. This is highly computation-intensive even though it is possible with the optimized geometry of the singlet states ${}^1\bar{E}$ and ${}^1A_1$ by spin-flip TDDFT [7]. Alternatively, we can take the effective one-dimensional (1D) phonon approximation, which greatly simplifies the evaluation of

spin-mixing coefficients. The approximation is valid when the electron-phonon coupling is not weak or moderate [66, 91]. A comparison between the 1D Huang-Rhys (HR) factor and the full-phonon HR factor is shown for validation of this approximation in Table 3.18.

Table 3.18: Comparison between one-dimensional Huang-Rhys factor (S_{1D}) and full-phonon Huang-Rhys factor (S_{full}). For these HR factors, the optimized geometries at HSE are used. The phonon modes are calculated at PBE since phonon modes at PBE and HSE are similar [19].

Cell size	HR factor	$^3E \rightarrow ^1A_1$	$^1E \rightarrow ^3A_2$
$3 \times 3 \times 3$	S_{1D}	0.45	3.38
	S_{full}	0.42	3.12

Under this approximation, we can separate the spin-orbit-phonon entangled SOC matrix elements into the effective SOC matrix elements and the effective phonon

wavefunction overlap $\langle \chi^{\Gamma_f} | \chi^{\Gamma_i} \rangle$. With the effective SOC matrix elements,

$$\lambda_z({}^1\widetilde{A}_1, {}^3\widetilde{E}) = d'_{eff} \langle {}^1\bar{E}_\pm | H_{\rm soc} | {}^3E \rangle_z \tag{3.134}$$

$$\lambda_\perp({}^1\widetilde{A}_1, {}^3\widetilde{E}) = c'_{eff} \langle {}^1A_1 | H_{\rm soc} | {}^3E \rangle_\perp + d'_{eff} \langle {}^1\bar{E}_\pm | H_{\rm soc} | {}^3E \rangle_\perp \tag{3.135}$$

$$\lambda_z({}^3\widetilde{A}_2, {}^1\widetilde{E}_\pm) = d_{eff} \langle {}^3A_2 | H_{\rm soc} | {}^1A_1 \rangle_z \tag{3.136}$$

$$\begin{aligned}\lambda_\perp({}^3\widetilde{A}_2, {}^1\widetilde{E}_\pm) = {} & c_{eff} \langle {}^3A_2 | H_{\rm soc} | {}^1\bar{E}_\pm \rangle_\perp + f_{eff} \langle {}^3A_2 | H_{\rm soc} | {}^1\bar{E}_\pm \rangle_\perp \\ & + g_{eff} \langle {}^3A_2 | H_{\rm soc} | {}^1\bar{E}_\mp \rangle_\perp\end{aligned} \tag{3.137}$$

$$\lambda_z({}^1\widetilde{E}_\pm, {}^3\widetilde{E}) = c_{eff} \langle {}^1\bar{E}_\pm | H_{\rm soc} | {}^3E \rangle_z + f_{eff} \langle {}^1\bar{E}_\pm | H_{\rm soc} | {}^3E \rangle_z + g_{eff} \langle {}^1\bar{E}_\mp | H_{\rm soc} | {}^3E \rangle_z \tag{3.138}$$

$$\begin{aligned}\lambda_\perp({}^1\widetilde{E}_\pm, {}^3\widetilde{E}) = {} & c_{eff} \langle {}^1\bar{E}_\pm | H_{\rm soc} | {}^3E \rangle_\perp + d_{eff} \langle {}^1A_1 | H_{\rm soc} | {}^3E \rangle_\perp \\ & + f_{eff} \langle {}^1\bar{E}_\pm | H_{\rm soc} | {}^3E \rangle_\perp + g_{eff} \langle {}^1\bar{E}_\mp | H_{\rm soc} | {}^3E \rangle_\perp\end{aligned} \tag{3.139}$$

$$\lambda_z({}^3\widetilde{A}_2, {}^1\widetilde{A}_1) = c'_{eff} \langle {}^3A_2 | H_{\rm soc} | {}^1A_1 \rangle_z \tag{3.140}$$

$$\lambda_\perp({}^3\widetilde{A}_2, {}^1\widetilde{A}_1) = d'_{eff} \langle {}^3A_2 | H_{\rm soc} | {}^1\bar{E}_\pm \rangle_\perp \tag{3.141}$$

where c_{eff} and d_{eff} are the effective state-mixing coefficients, which have been normalized and satisfy $|c_{eff}|^2 + |d_{eff}|^2 = 1$. And the same for d'_{eff}, c'_{eff}, f'_{eff}, g'_{eff}, with $|c'_{eff}|^2 + |d_{eff}|^2 + |f'_{eff}|^2 + |g'_{eff}|^2 = 1$. Because g_i, g'_i, g''_i and g'''_i coefficients are usually small, the terms consisted of these coefficients are negligible [68]. Then Eq. (3.137) is simplified to

$$\lambda_\perp({}^3\widetilde{A}_2, {}^1\widetilde{E}_\pm) \approx c'_{eff} \langle {}^3A_2 | H_{\rm soc} | {}^1\bar{E}_\pm \rangle_\perp + f'_{eff} \langle {}^3A_2 | H_{\rm soc} | {}^1\bar{E}_\pm \rangle_\perp \tag{3.142}$$

where $|c'_{eff}|^2 + |g'_{eff}|^2 + |f'_{eff}|^2 = 1$.

3.8.2 Dynamical Jahn-Teller Reducing $\lambda_z(^3E,^3E)$

The SOC matrix element $\lambda_z(^3E,^3E)$ does not contribute to any ISC involed in the excitation and relaxation processes of optically detected magnetic resonance (ODMR). As a consequence, $\lambda_z(^3E,^3E)$ is not a key factor to consider for ODMR. At low temperature, the ^3E state manifests the character of orbital doublet and spin triplet [90, 92, 93]. However, the orbital doublet can be smeared out at room temperature, and only spin triplet retains. At room temperature, the electron spin-spin interactation induced zero-field splitting (ZFS) becomes significant and $\lambda_z(^3E,^3E)$ can be ignored.

In Eq. (3.112) we don't consider the mixing of ^3E_x and ^3E_y due to the electon-phonon coupling described by the dynamical JT effect because it does not affect the SOC $\lambda_{z/\perp}(^3\widetilde{E},^1\widetilde{A}_1)$. If we care about $\lambda_z(^3E,^3E)$, the dynamical JT effect can reduce the magnitude and needs to be taken into account. To do that, we rewrite the vibronic

triplet excited state ${}^3\widetilde{E}$ as the linear combination of ${}^3\widetilde{E}_x$ and ${}^3\widetilde{E}_y$,

$$\begin{aligned}\left|{}^3\widetilde{E}_x\right\rangle = \sum_{i=1}^{\infty}\Bigg[&c_i''\left|{}^3E_x\right\rangle\otimes\left|\chi_i^{A_1}\right\rangle + \frac{f_i''}{\sqrt{2}}\Bigg(\left|{}^3E_x\right\rangle\otimes\left|\chi_i^{E_x}\right\rangle - \left|{}^3E_y\right\rangle\otimes\left|\chi_i^{E_y}\right\rangle\Bigg)\\ &+ g_i''\left|{}^3E_y\right\rangle\otimes\left|\chi_i^{A_2}\right\rangle\Bigg]\end{aligned} \tag{3.143}$$

$$\begin{aligned}\left|{}^3\widetilde{E}_y\right\rangle = \sum_{i=1}^{\infty}\Bigg[&c_i''\left|{}^3E_y\right\rangle\otimes\left|\chi_i^{A_1}\right\rangle + \frac{f_i''}{\sqrt{2}}\Bigg(\left|{}^3E_x\right\rangle\otimes\left|\chi_i^{E_y}\right\rangle + \left|{}^3E_y\right\rangle\otimes\left|\chi_i^{E_x}\right\rangle\Bigg)\\ &+ g_i''\left|{}^3E_x\right\rangle\otimes\left|\chi_i^{A_2}\right\rangle\Bigg]\end{aligned} \tag{3.144}$$

$$\begin{aligned}\left|{}^3\widetilde{E}_\pm\right\rangle &= \frac{1}{\sqrt{2}}(\left|{}^3\widetilde{E}_x\right\rangle \pm i\left|{}^3\widetilde{E}_y\right\rangle)\\ &= \frac{1}{\sqrt{2}}\sum_{i=1}^{\infty}\Bigg[c_i''\Big(\left|{}^3E_x\right\rangle \pm i\left|{}^3E_y\right\rangle\Big)\otimes\left|\chi_i^{A_1}\right\rangle\\ &\quad + \frac{f_i''}{\sqrt{2}}\Bigg(\left|{}^3E_x\right\rangle\otimes\left|\chi_i^{E_x}\right\rangle - \left|{}^3E_y\right\rangle\otimes\left|\chi_i^{E_y}\right\rangle \pm i\left|{}^3E_x\right\rangle\otimes\left|\chi_i^{E_y}\right\rangle \pm i\left|{}^3E_y\right\rangle\otimes\left|\chi_i^{E_x}\right\rangle\Bigg)\\ &\quad + g_i''\Big(\left|{}^3E_y\right\rangle \pm i\left|{}^3E_x\right\rangle\Big)\otimes\left|\chi_i^{A_2}\right\rangle\Bigg]\\ &= \frac{c_i''}{\sqrt{2}}\left|{}^3E_\pm\right\rangle\otimes\left|\chi_i^{A_1}\right\rangle + \frac{f_i''}{2}\left|{}^3E_\pm\right\rangle\otimes\left|\chi_i^{E_\pm}\right\rangle \pm i\frac{g_i''}{\sqrt{2}}\left|{}^3E_\mp\right\rangle\otimes\left|\chi_i^{A_2}\right\rangle\\ &= c_i''\left|{}^3E_\pm\right\rangle\otimes\left|\chi_i^{A_1}\right\rangle + \frac{f_i''}{\sqrt{2}}\left|{}^3E_\pm\right\rangle\otimes\left|\chi_i^{E_\pm}\right\rangle + g_i''\left|{}^3E_\mp\right\rangle\otimes\left|\chi_i^{A_2}\right\rangle\end{aligned} \tag{3.145}$$

In the last step, we merge the imaginary i into the coefficient g_i'' as it won't affect any conclusion of symmetry, and implicitly consider $1/\sqrt{2}$ in all the coefficients. By using Eq. (3.145) and Eq. (3.121), we can derive the following equation,

$$\begin{aligned}\left\langle{}^1\widetilde{A}_1\middle|H_{\text{soc}}\middle|{}^3\widetilde{E}\right\rangle = \sum_{i,j=0}^{\infty}\Bigg[&c_i'c_j''\left\langle{}^1A_1\middle|H_{\text{soc}}\middle|{}^3E_\pm\right\rangle\otimes\left\langle\chi_i^{A_1}\middle|\chi_j^{A_1}\right\rangle\\ &+ \frac{d_i'f_j''}{\sqrt{2}}\Bigg(\left\langle{}^1\bar{E}_+\middle|H_{\text{soc}}\middle|{}^3E_\pm\right\rangle\otimes\left\langle\chi_i^{E_-}\middle|\chi_j^{E_\pm}\right\rangle\\ &+ \left\langle{}^1\bar{E}_-\middle|H_{\text{soc}}\middle|{}^3E_\pm\right\rangle\otimes\left\langle\chi_i^{E_+}\middle|\chi_j^{E_\pm}\right\rangle\Bigg)\Bigg]\end{aligned} \tag{3.146}$$

This can be seen essentially no difference from Eq. (3.122) if tracing off the f_i'' coefficient, demonstrating that dynamical JT in ^3E does not affect the SOC that couples ^3E and $^1A_1$.

Then we can look at how this dynamical JT reduces the SOC that breaks the degeneracy of ^3E.

$$
\begin{aligned}
\left\langle {}^3\widetilde{E}_\pm \middle| H_{\mathrm{soc}} \middle| {}^3\widetilde{E}_\pm \right\rangle = \sum_{i,j=0}^{\infty} \Bigg(& c_i'' c_j'' \left\langle {}^3E_\pm \middle| H_{\mathrm{soc}} \middle| {}^3E_\pm \right\rangle \otimes \left\langle \chi_i^{A_1} \middle| \chi_j^{A_1} \right\rangle \\
& + \frac{f_i'' f_j''}{2} \left\langle {}^3E_\pm \middle| H_{\mathrm{soc}} \middle| {}^3E_\pm \right\rangle \otimes \left\langle \chi_i^{E_\pm} \middle| \chi_j^{E_\pm} \right\rangle \\
& + g_i'' g_j'' \left\langle {}^3E_\mp \middle| H_{\mathrm{soc}} \middle| {}^3E_\mp \right\rangle \otimes \left\langle \chi_i^{A_2} \middle| \chi_j^{A_2} \right\rangle \Bigg) \\
= \sum_{i=0}^{\infty} & \left[\left(|c_i''|^2 + \frac{|f_i''|^2}{2} \right) \left\langle {}^3E_\pm \middle| H_{\mathrm{soc}} \middle| {}^3E_\pm \right\rangle + |g_i''|^2 \left\langle {}^3E_\mp \middle| H_{\mathrm{soc}} \middle| {}^3E_\mp \right\rangle \right] \\
= \sum_{i=0}^{\infty} & \left[\left(|c_i''|^2 + \frac{|f_i''|^2}{2} \right) \left\langle {}^3E_x \mp i\,{}^3E_y \middle| H_{\mathrm{soc}} \middle| {}^3E_x \pm i\,{}^3E_y \right\rangle \right. \\
& \left. + |g_i''|^2 \left\langle {}^3E_x \pm i\,{}^3E_y \middle| H_{\mathrm{soc}} \middle| {}^3E_x \mp i\,{}^3E_y \right\rangle \right] \\
= \sum_{i=0}^{\infty} & \left[\left(|c_i''|^2 + \frac{|f_i''|^2}{2} \right) \Big(\left\langle {}^3E_x \middle| H_{\mathrm{soc}} \middle| {}^3E_x \right\rangle + \left\langle {}^3E_y \middle| H_{\mathrm{soc}} \middle| {}^3E_y \right\rangle \right. \\
& \left. \pm i \left\langle {}^3E_x \middle| H_{\mathrm{soc}} \middle| {}^3E_y \right\rangle \mp i \left\langle {}^3E_y \middle| H_{\mathrm{soc}} \middle| {}^3E_x \right\rangle \Big) \right. \\
& \left. + |g_i''|^2 \Big(\left\langle {}^3E_x \middle| H_{\mathrm{soc}} \middle| {}^3E_x \right\rangle + \left\langle {}^3E_y \middle| H_{\mathrm{soc}} \middle| {}^3E_y \right\rangle \right. \\
& \left. \left. \mp i \left\langle {}^3E_x \middle| H_{\mathrm{soc}} \middle| {}^3E_y \right\rangle \pm i \left\langle {}^3E_y \middle| H_{\mathrm{soc}} \middle| {}^3E_x \right\rangle \Big) \right] \\
= \sum_{i=0}^{\infty} & \left[\left(|c_i''|^2 + \frac{|f_i''|^2}{2} + |g_i''|^2 \right) \Big(\left\langle {}^3E_x \middle| H_{\mathrm{soc}} \middle| {}^3E_x \right\rangle + \left\langle {}^3E_y \middle| H_{\mathrm{soc}} \middle| {}^3E_y \right\rangle \Big) \right. \\
& \left. \pm i \left(|c_i''|^2 + \frac{|f_i''|^2}{2} - |g_i''|^2 \right) \Big(\left\langle {}^3E_x \middle| H_{\mathrm{soc}} \middle| {}^3E_y \right\rangle - \left\langle {}^3E_y \middle| H_{\mathrm{soc}} \middle| {}^3E_x \right\rangle \Big) \right]
\end{aligned}
\tag{3.147}
$$

For the SOC matrix elements within ${}^3E$, they are all axial. As a consqeunce, the first two terms are zero. Then based on the CGC of C_{3v} in Eq. (3.60), $\left\langle {}^3E_x \middle| H_{\text{soc}} \middle| {}^3E_y \right\rangle = -\left\langle {}^3E_y \middle| H_{\text{soc}} \middle| {}^3E_x \right\rangle$, and this results in a factor of 2 which will cancels out with the wavefunction normalization factor in Eq. (3.145). Finally, the SOC matrix elements within ${}^3E$ is expressed as

$$\left\langle {}^3\widetilde{E}_{\pm} \middle| H_{\text{soc}} \middle| {}^3\widetilde{E}_{\pm} \right\rangle = \pm i \sum_i^{\infty} \left(|c_i''|^2 + \frac{|f_i''|^2}{2} - |g_i''|^2 \right) \left\langle {}^3E_x \middle| H_{\text{soc}} \middle| {}^3E_y \right\rangle \tag{3.148}$$

$\sum_i^{\infty} \left(|c_i''|^2 + \frac{|f_i''|^2}{2} - |g_i''|^2 \right)$ is the same as the reduction factor that is discussed in Ref. [52]. In this expression, only the orbital part of wavefunction is considered for simplicity, and the spin part needs to be taken into account for a full derivation.

3.8.3 Pseudo Jahn-Teller Effect Between ${}^3E$ and ${}^3A_2$

It is possible that ${}^3E$ couples with ${}^3A_2$ by the pseudo JT effect.

$$H = \underbrace{\begin{pmatrix} \Lambda & 0 & 0 \\ 0 & 0 & 0 \\ 0 & 0 & 0 \end{pmatrix}}_{H_{\text{e}}} + \underbrace{\frac{K}{2}(Q_x^2 + Q_y^2)}_{H_{\text{osc}}} + \underbrace{\begin{pmatrix} 0 & FQ_x & FQ_y \\ FQ_x & 0 & 0 \\ FQ_y & 0 & 0 \end{pmatrix}}_{H_{\text{PJT}}} \tag{3.149}$$

$$F = \left\langle {}^3A_2 \middle| \frac{\partial V}{\partial Q_x} \middle| {}^3E_x \right\rangle = \left\langle {}^3A_2 \middle| \frac{\partial V}{\partial Q_y} \middle| {}^3E_y \right\rangle \tag{3.150}$$

Let's write the vibronic wavefunctions of ${}^3\widetilde{E}$ and ${}^3\widetilde{A}_2$ with retaining the overall symmetry.

$$\begin{aligned}
\left|{}^3\widetilde{E}_\pm\right\rangle &= \sum_{i=0}^{\infty} c_i'' \left|{}^3E_\pm\right\rangle \otimes \left|\chi_i^{A_1}\right\rangle \mp i d_i'' \left|{}^3A_2\right\rangle \otimes \left|\chi_i^{E_\mp}\right\rangle + \frac{f_i''}{\sqrt{2}} \left|{}^3E_\pm\right\rangle \otimes \left|\chi_i^{E_\pm}\right\rangle \\
&\quad \pm i g_i'' \left|{}^3E_\mp\right\rangle \otimes \left|\chi_i^{A_2}\right\rangle \\
&= c_i'' \left|{}^3E_\pm\right\rangle \otimes \left|\chi_i^{A_1}\right\rangle + d_i'' \left|{}^3A_2\right\rangle \otimes \left|\chi_i^{E_\mp}\right\rangle + \frac{f_i''}{\sqrt{2}} \left|{}^3E_\pm\right\rangle \otimes \left|\chi_i^{E_\pm}\right\rangle \\
&\quad + g_i'' \left|{}^3E_\mp\right\rangle \otimes \left|\chi_i^{A_2}\right\rangle
\end{aligned} \tag{3.151}$$

$$\begin{aligned}
\left|{}^3\widetilde{A}_2\right\rangle &= \sum_{i=0}^{\infty} c_i''' \left|{}^3A_2\right\rangle \otimes \left|\chi_i^{A_1}\right\rangle + \frac{d_i'''}{\sqrt{2}} \left(\left|{}^3E_x\right\rangle \otimes \left|\chi_i^{E_y}\right\rangle - \left|{}^3E_y\right\rangle \otimes \left|\chi_i^{E_x}\right\rangle \right) \\
&= c_i''' \left|{}^3A_2\right\rangle \otimes \left|\chi_i^{A_1}\right\rangle + \frac{d_i'''}{\sqrt{2}i} \left(\left|{}^3E_-\right\rangle \otimes \left|\chi_i^{E_+}\right\rangle - \left|{}^3E_+\right\rangle \otimes \left|\chi_i^{E_-}\right\rangle \right)
\end{aligned} \tag{3.152}$$

This pseudo JT effect that couples ${}^3E$ and ${}^3A_2$ will give rise to additional SOC component $c'_{\text{eff}} d'''_{\text{eff}} \left\langle {}^1A_1 \middle| H_{\text{soc}} \middle| {}^3A_2 \right\rangle_z$ to $\lambda_z({}^1\widetilde{A}_1, {}^3\widetilde{E})$ besides Eq. (3.134), and SOC component $d'_{\text{eff}} d'''_{\text{eff}} \left\langle {}^1A_1 \middle| H_{\text{soc}} \middle| {}^1\bar{E} \right\rangle_\perp$ to $\lambda_\perp({}^1\widetilde{A}_1, {}^3\widetilde{E})$ besides Eq. (3.135). Similarly, one can find the additional SOC components that contribute to $\lambda_{z/\perp}({}^3\widetilde{A}_2, {}^1\widetilde{E})$ due to the pseudo JT effect. Furthermore, the pseudo JT effect can lead to some correction to the internal conversion because of the mixing of states. However, this pseudo JT effect should be very small because the pseudo JT effect can disappear when the energy splitting is too large and $\Delta E({}^3E - {}^3A_2) \approx 2\Delta E({}^1A_1 - {}^1E)$ [65]. In conclusion, we don't need to consider the pseudo JT effect that couples ${}^3E$ and ${}^3A_2$.

3.9 Conclution

We evaluate SOC using group theory to comprehensively understand the allowed and forbidden SOC matrix elements from a symmetry perspective. This helps determine the validity of first-principles calculations and clarify experimental observations by considering underlying mechanisms that might have been overlooked.

1. We have evaluated all the SOC matrix elements of interest, including the SOC matrix elements that couples the singlet ground state ^1E and triplet ground state $^3A_2$, $\langle {}^3A_2^0 | H_{\text{soc}} | {}^1A_1 \rangle$ for λ_z and $\langle {}^3A_2^1 - {}^3A_2^{-1} | H_{\text{soc}} | {}^1E_x' \rangle$ for $\lambda_\perp$. We reproduce the SOC matrix elements in previous literature Ref. [18], and further derive all the effective SOC with considering the Jahn-Teller effects.

2. Because the SOC module implemented in ORCA already includes the multi-reference character, normalization factor and CGC of electronic states [94, 95], there should be no need to consider additional factor to enter into the scattering matrix of the intersystem crossing formula, Eq. 2.82.

3. For calculating SOC, the previous studies [52, 68] use single-particle wavefunction for the SOC matrix elements so only one-particle SOC is included. However, ORCA evaluates SOC by using the spin-orbit mean-field (SOFM) operator [94] approximates to the Breit-Pauli operator and takes into account both both one-particle and two-particle SOC [8]. Therefore, our evaluation of the SOC matrix elements are believed more complete and accurate.

[8] See Eq. (11) on page 2 and "The SOFM operator used in this study was developed as an approximation to the Breit-Pauli operator" on page 5 of Ref. [94]

Chapter 4

Identifying Solid-State Spin Defects

This chapter focuses on the identification of solid-state spin defects. In particular, spin defects in the 2D hBN. The problem is critical for the application of spin defects for quantum information technology and nanoscale measurement. The unknown chemical structures of spin defects hinder the in-depth study, deterministic generation and precise control for their piratical use.

First-principles methodologies enable to provide comprehensive profiles of defect candidates from many aspects, the ease of defect formation, the static properties including possible charge states, excitation energies and PL spectrum, the dynamical properties including transitions due to radiative recombination and nonradiative recombination. The theoretical study identifies the carbon trimer defect C_2C_N to be the most likely defect candidate responsible for the experimentally observed 2 eV single-photon emitter, out of many possible defect candidates.

4.1 Introduction

A single-photon emitter (SPE) is a crucial building block in quantum information technologies, such as linear-optical quantum information processing [96], quantum simulation [97], and quantum communication [98]. Hexagonal boron nitride (hBN) is a two-dimensional (2D) material with a wide band gap (∼6 eV) [99, 100], and can host stable and bright color centers which possess single-photon emission [22]. Meanwhile, the manipulation of the optoelectronic properties of singe-photon emitters has garnered special interest [101, 102]. These properties imply a great potential of hBN in developing quantum applications. Being able to select and purify single-photon emitters is critical for generating controllable and narrow line width single-photon emission. Hence, the identification of the atomic origin of the single-photon emitters is crucial to the development of this field.

Since 2016 [103], numerous experimental results have been reported on the photoluminescent properties of the single-photon emitters at ∼2 eV in hBN [104, 105, 106, 103, 3, 107, 101, 108, 109, 110, 111, 112, 113, 114, 115, 116, 117, 118, 119, 120, 111]. In Table 4.1, we summarize the range and averaged values of photoluminescent properties observed in experiments, including the zero-phonon line (ZPL), phonon-sideband energy (PSE), Huang-Rhys factor (HR factor), and the photoluminescence lifetime (τ^{PL}). Typically, a ∼2 eV single-photon emitter in hBN exhibits a photoluminescence (PL) spectrum comprised of a sharp ZPL and one or two moderate phonon sidebands (PSB) at room temperature. The PSE is the energy separation between the ZPL and the first PSB peak. The electron-phonon coupling is estimated by either the HR factor (S) or

Debye-Waller (DW) factor ($DW = e^{-S}$) [121]. The HR factor is typically ∼1, which indicates weak electron-phonon coupling. Furthermore, the PL lifetime is of the order of a few ns, and quantum yield (QY, η) is reported to be 6∼12% [102]. The PL lifetime (τ^{PL}) reflects the lifetime of an excited state, determined by radiative (τ^{R}) and nonradiative recombination together [τ^{NR}, $\tau^{PL} = 1/(1/\tau^{R} + 1/\tau^{NR})$]. On the other hand, QY (η) reflects the proportion of radiative recombination rates with respect to the total recombination rates, and is related to the PL lifetime through $\tau^{PL} = \tau^{R} * \eta$. PL lifetime and QY underscore the importance of studying both radiative and nonradiative recombination lifetimes.

Table 4.1: Summary of the zero-phonon line (ZPL), phonon sideband (PSE), Huang-Rhys (HR) factor, and photoluminescence (PL) lifetime (τ^{PL}) for ∼2 eV single-photon emitters in h-BN from experimental measurements and our calculated two carbon defects.

	ZPL (eV)	PSE (meV)	HR factor	τ^{PL} (ns)
Range(exp.)	1.56-2.24[1]	30-200[2]	0.63-1.93[3]	0.38-19.7[4]
Mean(exp.)	2.00 ± 0.19[1]	156 ± 33[2]	1.19 ± 0.43[3]	2.6 ± 1.5[4]
C_2C_N(calc.)	2.13[5]	180	1.35	2.19
C_2C_B(calc.)	1.42[5]	175	1.25	$3.83 * 10^2$

1. From Ref. [104, 105, 106, 122, 103, 3, 107, 101, 108, 109, 110, 123, 111, 112, 113, 114, 124, 115, 116, 117, 118, 119, 120, 111].

2. From Ref. [105, 106, 122, 3, 107, 101, 108, 110, 123, 112, 113, 114, 115, 116, 117, 118, 119].

3. From Ref. [104, 123, 116].

4. From Ref. [104, 105, 106, 103, 101, 108, 109, 110, 113, 114, 124, 116, 117]. As 19.7 ns in Ref. [124] is far from the other data points, it is removed when evaluating the mean.

5. From the excitation energy at G_0W_0 − BSE@PBE and taking into account the Franck-Condon shift.

Finally, many of the reported single-photon emitters ∼ 2 eV possess linearly polarized excitation and emission [122, 103, 3, 108, 109, 110, 111, 112, 124, 125, 116], indicating the anisotropic structural symmetry of the corresponding defects [59, 126],

i.e., possibly belonging to the C_{2v}, C_2, or C_s groups.

In terms of the atomic origin of these single-photon emitters, annular dark-field images have shown that carbon substitutions are abundant in hBN [127]. Recently, Mendelson *et al.* [3] identified that various techniques of incorporating carbon into hBN yield ∼2 eV single-photon emitters. Moreover, x-ray photoelectron spectroscopy measurements show that more C-B bonds exist than that of C-N bonds [3]. This is an evidence that carbon substitution of nitrogen is more likely than carbon substitution of boron.

Theoretically, several defects have been proposed to be possibly responsible for single-photon emission, such as C_BV_N [128, 22], boron dangling bonds [129], N_BV_N [67], and carbon trimers [28]. Based on experimental observations [3], we focus on carbon defects in this work. Among the carbon defects, C_BV_N has high formation energy that is 3∼6 eV higher than other carbon defects such as carbon dimer and trimers [27]. Carbon trimers including C_2C_N and C_2C_B, theoretically proposed by Jara *et al.* [28], were found to be energetically favorable and in good agreement with experimental PSE and PL [28]. However, some important information is still missing to confirm carbon trimers as a SPE candidate theoretically. For example, only the ZPL for the lowest transition was calculated, about 0.4 eV smaller than the mean of ZPL in Table 4.1. And other important properties such as HR factor, PL lifetime, and QY, as the experimental characteristics of ∼2 eV single-photon emitters, were not calculated. Therefore, further study of these properties is desired to unveil the role of carbon trimers as experimentally observed SPEs.

In this Letter, electronic and optical properties of the carbon trimers C_2C_N and C_2C_B are calculated from both first-principles many-body perturbation theory and density functional theory (DFT) levels. We evaluate both the static and dynamical properties of radiative and phonon-assisted nonradiative recombination, including exciton-defect and electron-phonon interactions. Our results demonstrate that C_2C_N has remarkable agreement with experimental observations of 2 eV single-photon emitters, including ZPL, PL lifetime, PSE, HR factor, and PL spectrum. We emphasize the importance of comparing all key signatures between theory and experiments for defect identification and validations.

4.2 Computational Methods

We employ the open-source plane-wave code Quantum ESPRESSO [130] for structural relaxation and phonon calculations of carbon defects in monolayer hBN. We note that experimentally multilayer or bulk hBN are often used instead of monolayer hBN. However, increasing the number of layers will decrease both the quasiparticle (electronic) gap and exciton binding energy, which result in optical gaps or ZPL with minimum changes, as discussed in Refs. [131, 132]. Additionally, prior theoretical [51, 133] and experimental [134] works have shown negligible changes when comparing the ZPL of point defects such as boron dangling bonds in monolayer and multilayer hBN. More detailed studies of the layer dependence of carbon defects and its effects on optical spectra and excited-state lifetime are needed.

We use the optimized norm-conserving Vanderbilt (ONCV) pseudopotentials [135]

and a 55 Ry wave-function energy cutoff. We choose a supercell size of 6×6 which shows good convergence, as tested in Refs. [67, 136, 137]. Charged defect correction is included to eliminate the spurious electrostatic interaction by using the techniques developed in Refs. [138, 139] and implemented in the JDFTx code [140]. Total energy, defect formation energy, and geometry are obtained with the Perdew-Burke-Ernzerhof (PBE) exchange-correlation functional [39]. The charged defect formation energy $E_f^q(d)$ with the charge state q is calculated by

$$E_f^q(d) = E_{\rm tot}^q(d) - E_{\rm tot}(p) - \sum_i N_i\mu_i + qE_{\rm Fermi} + E_{\rm corr}, \tag{4.1}$$

where $E_{\rm tot}^q(d)$ is the total energy of the charged defect, $E_{\rm tot}(p)$ is the total energy of the pristine system, N_i is the number of atoms of atomic species i that is added ($N_i > 0$) or removed ($N_i < 0$), μ_i is the chemical potential of the atomic species i, $E_{\rm Fermi}$ is the electron chemical potential, and $E_{\rm corr}$ is the charged defect correction. The chemical potentials of B, N, and C are obtained as follows. In the N-rich condition, $\mu_{\rm N}^{\rm N-rich} = 1/2E_{\rm tot}({\rm N_2})$ where $E_{\rm tot}({\rm N_2})$ is the total energy of the N_2 molecule. In the N-poor condition, $\mu_{\rm B}^{\rm N-poor} = E_{\rm tot}({\rm B})$ where $E_{\rm tot}({\rm B})$ is one atom's total energy in a boron crystal. $\mu_{\rm N}^{\rm N-poor}$ and $\mu_{\rm B}^{\rm N-rich}$ are calculated according to the constraint $\mu_{\rm N} + \mu_{\rm B} = \mu_{\rm BN}$, where $\mu_{\rm BN}$ is the total energy of BN with one unit cell. $\mu_{\rm C}$, on the other hand, is one atom's total energy in graphene.

We evaluate the electronic structures under the GW approximation with the PBE eigenvalues and wave functions as the starting point by using the Yambo code [141]. The starting wavefunctions at PBE are sufficient for accurate descriptions of current *sp* defect wavefunctions by comparing with the ones at hybrid functionals (see the Supple-

mental Material (SM) Fig. S1 [142] for the wave-function comparison [143, 144, 137]). Prior studies of hBN by the GW plus Bethe-Salpeter equation method (GW-BSE) have been mostly started from single-particle states at local and semilocal functionals, and have shown excellent agreement with experimental electronic and optical properties [132, 131, 145, 146, 147, 148, 149]. In the single-shot GW (G_0W_0) calculations in this work, the Godby-Needs plasmon-pole approximation (PPA) [150, 151] is used to calculate the dielectric matrices with the plasmon frequency $\omega_p = 27.2$ eV. Then, the Bethe-Salpeter Equation (BSE) is further solved on top of the GW approximation to include the electron-hole interaction in the absorption spectra. Coulomb truncation for 2D systems [152] is applied to the out-of-plane direction, and k-point sampling is set to $3 \times 3 \times 1$ for $6 \times 6 \times 1$ supercells in all of the G_0W_0 and BSE calculations. More details on convergence tests can be found in Sec. II of the SM [142].

The method in Ref. [59] based on Fermi's golden rule and solving BSE is applied to calculate the radiative lifetime of intradefect transitions that include exciton-defect coupling. The nonradiative recombination lifetime is also calculated with electron-phonon matrix elements in the static coupling approximation. The method of fixing bulk atoms [136] is used to speed up the supercell convergence of the nonradiative lifetime. The details of the nonradiative recombination can be found in Refs. [66, 67]. The generating function approach, which is detailed and introduced in Ref. [19], is applied to the calculation of the PL line shape.

4.3 Charged Defect Formation Energy

When nitrogen and boron atoms are unevenly substituted by atomic impurities, the formation energy of the defects depends on the elemental chemical potentials, i.e., different at the N-rich (B-poor) and N-poor (B-rich) conditions. In the N-rich condition, C_2C_B is more likely to form than C_2C_N because of the smaller formation energy of C_2C_B, as shown in Fig. 4.1(b). On the other hand, C_2C_N is more likely to form in the N-poor condition. It is also found that both defects can be stable in charge states of $q = 0, \pm 1$ at a range of electron chemical potentials within the electronic band gap. Without losing generality, we investigate both C_2C_N and C_2C_B in all possible charge states of $q = 0, \pm 1$, and we find that the $q = \pm 1$ charge states have ZPL either too large or too small, away from the experimental range (details found in the SM, Table S1 [142]). Thus, we focus on the neutral state of the defects. In particular, we find that the neutral C_2C_N have good agreement with experiments on all properties of ~ 2 eV single-photon emitter, so we mainly discuss the neutral C_2C_N in the following. The results of C_2C_B can be found in Sec. III of the SM [142] and summarized in Table 4.1. We find that the major discrepancy of C_2C_B to experiments is in the ZPL and PL lifetime.

4.4 Electronic Structure and Optical Properties

The single-particle diagram in Fig. 4.2(a) shows the defect-related electronic energy levels with their wave functions, and the host monolayer hBN band edges at

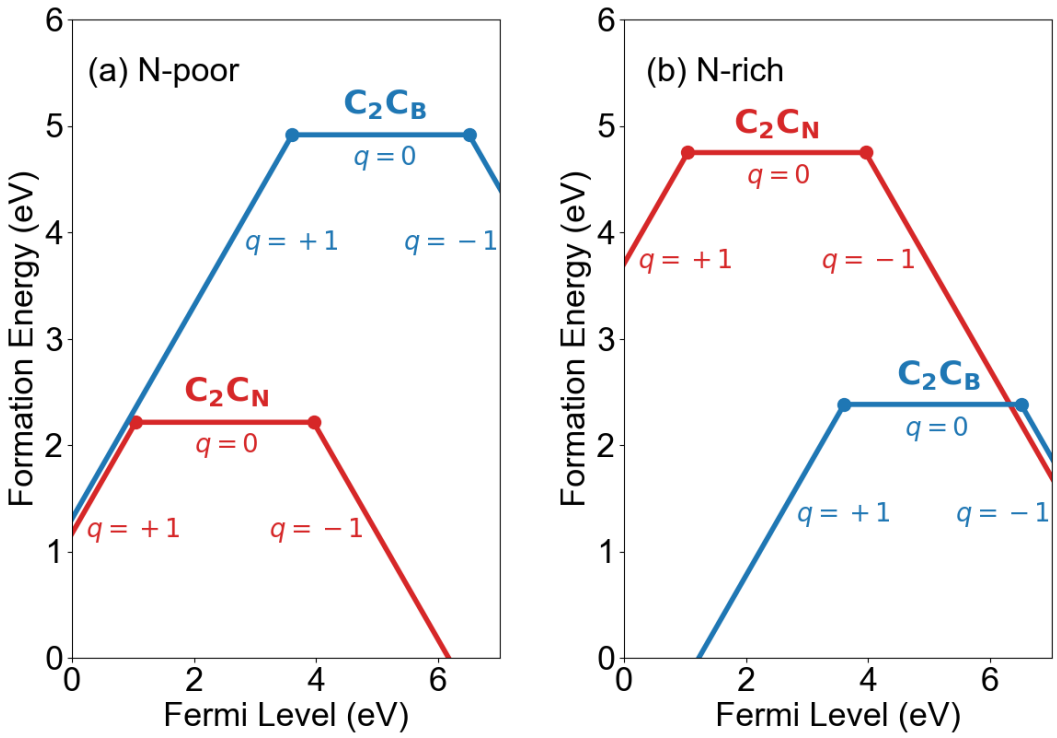

Figure 4.1: Charged defect formation energy of defects C_2C_N and C_2C_B as a function of Fermi level at (a) N-poor and (b) N-rich conditions.

the GW approximation, referenced to the vacuum level. One unoccupied defect state ($2a_2$) and three occupied defect states ($2b_1$, $1a_2$, $1b_1$) in the spin-down channel can lead to intradefect transitions via radiative recombination or nonradiative recombination. To obtain optical transitions (or two-particle excitations), we calculate the absorption spectra by solving the BSE, which uses GW quasiparticle energies as inputs and includes the excitonic effect. Details of numerical convergence tests can be found in Sec. II of the SM [142]. Here, only spin-conserved transitions are considered. We then calculate the radiative lifetimes of the intradefect recombination via Fermi's golden rule by Eq. (4.2) (with dielectric constant equal to unity for monolayer 2D systems),

$$\tau^R = \frac{3c^3}{4E_0^3\mu_{e-h}^2}, \tag{4.2}$$

where E_0 is the excitation energy, and μ_{e-h}^2 is the modulus square of the exciton dipole moment in atomic units. The derivation detail of this equation can be found in Refs. [60, 59]. We find two strong absorption peaks due to the optically allowed intradefect transitions in Fig. 4.2(b) and summarize the optical properties in Table 4.2. In particular, only the transition $2a_{2\downarrow} \rightarrow 1a_{2\downarrow}$ shows a relatively short radiative lifetime that possibly falls into the range of experimental values. The other transition has an order-of-magnitude-longer radiative lifetime. Therefore, we mainly focus on the former transition. Its shorter lifetime (i.e., 51.9 ns) is because of stronger oscillator strength and higher excitation energy (shown in Table 4.2). Note that the excitonic effect at the defect is comparable or stronger than its host materials [132, 153], e.g., over one eV exciton binding energy E_b for both transitions in Table II. The exciton wave function in the SM, Fig. S3 [142], shows that the exciton is localized and bound to the carbon

defect C_2C_N and a few neighboring BN atoms, consistent with its large exciton binding energy. In order to compare with the experimental PL lifetimes in Table 4.1, we also need to compute the nonradiative lifetime as follows.

Table 4.2: Radiative recombination of C_2C_N. Excitation energy (E_0), square modulus of dipole moment (μ^2_{e-h}), radiative lifetime (τ^R), and exciton binding energy (E_b) of the C_2C_N defect for the two transitions that are prominent in the optical excitations below the optical gap.

Transition	E_0 (eV)	μ^2_{e-h} (a.u.)	τ^R (ns)	E_b (eV)
$2a_{2\downarrow} \rightarrow 2b_{1\downarrow}$	1.34	$4.90 * 10^{-1}$	$7.95 * 10^2$	2.08
$2a_{2\downarrow} \rightarrow 1a_{2\downarrow}$	2.33	1.43	$5.19 * 10^1$	1.58

4.5 Nonradiative Recombination

The nonradiative lifetime (τ^{NR}) is a measure of how fast the nonradiative recombination happens between the final state $|f\rangle$ and initial state $|i\rangle$. The phonon-assisted nonradiative recombination is influenced by several factors and also evaluated via Fermi's golden rule as below,

$$\frac{1}{\tau^{NR}_{if}} = \frac{2\pi}{\hbar} g \sum_{n,m} p_{in} |\langle fm|H^{e-ph}|in\rangle|^2 \delta(E_{fm} - E_{in}) \tag{4.3}$$

where H^{e-ph} is the electron-phonon coupling Hamiltonian, g is the degeneracy factor of the final state that depends on the number of equivalent atomic configurations, and p_{in}

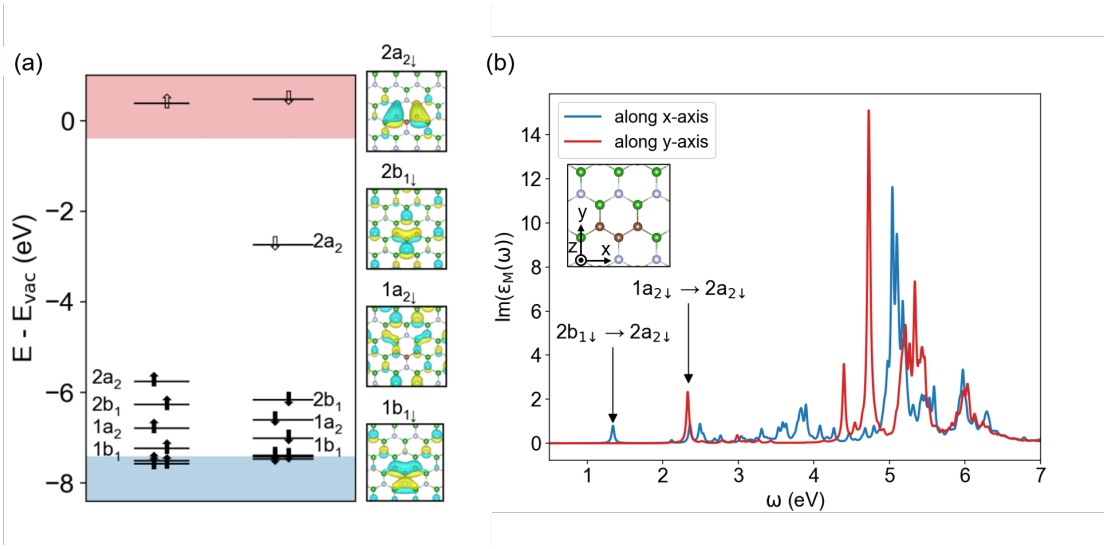

Figure 4.2: (a) Single-particle diagram of the ground state ${}^2_0A_2$ at the level of G_0W_0@PBE, and (b) $G_0W_0 - BSE$@PBE of C_2C_N. VBM and CBM are -7.431 and -0.400 eV, respectively [2]. The defect states in the band gap are denoted by the irreducible representations of the C_{2v} symmetry group based on the corresponding wavefunction symmetry. The isosurface of the wavefunctions (PBE) is 3% of the maximum. In the $G_0W_0 - BSE$@PBE spectra, the absorption peaks are labeled by the corresponding intradefect transitions. x and y are the in-plane directions that are perpendicular and parallel to the C_2 axis, respectively, and z is the out-of-plane direction. The spectral broadening is 0.02 eV.

is the occupation number of the vibronic state $|in\rangle$ following the Boltzmann distribution.

Under the static coupling approximation with one-dimensional (1D) phonon approximation [66, 67], we can rewrite Eq. (4.3) as

$$\frac{1}{\tau_{if}^{NR}} = \frac{2\pi}{\hbar} g |W_{if}|^2 X_{if}(T) \tag{4.4}$$

$$W_{if} = \langle \psi_i(\mathbf{r}, \mathbf{R}) | \frac{\partial H}{\partial Q} | \psi_f(\mathbf{r}, \mathbf{R}) \rangle \, |_{\mathbf{R}=\mathbf{R_a}} \tag{4.5}$$

$$X_{if} = \sum_{n,m} p_{in} | \langle \phi_{fm}(\mathbf{R}) | Q - Q_a | \phi_{in}(\mathbf{R}) \rangle |^2 \times \delta(m\hbar\omega_f - n\hbar\omega_i + \Delta E_{if}). \tag{4.6}$$

Equation (4.4) is separated into the electronic term (W_{if}), which depends on the electronic wave function (ψ) overlap, and the phonon term (X_{if}), which describes the strength of the phonon contribution. The phonon term includes the energy conservation between the initial and final vibronic states with vibrational frequencies of ω_i and ω_f, and ϕ is the phonon wave function. The detailed derivation can be found in Refs. [66, 67].

We summarize the nonradiative recombination lifetime of the intradefect transitions, along with ZPL, HR factor of the final state [$S_f(1D)$] in Table 4.3. Note that the HR factor from the nonradiative recombination calculation is with 1D effective phonon approximation. Its comparison with the full-phonon HR factor (S, including all phonon eigenmodes) can be found in Sec. VI of the SM [142]. The calculated 1D HR factor, is close to the full-phonon HR factor as can be seen by comparing Table 4.3 (1D) with Fig. 4.3 (full phonon). ZPL is evaluated by two methods: one is using the vertical neutral excitation energy obtained from BSE with subtracting the Frank-Condon shift

in the excited state [ZPL(BSE)], and another is from constrained DFT (CDFT) at the PBE level with geometry optimization [ZPL(CDFT)]. The ZPL from two methods has 0.1 and 0.4 eV energy difference for the first two transitions, respectively. We used the CDFT in the nonradiative lifetime calculation to be consistent with other quantities in the equation. The nonradiative recombination of ${}^2_2A_2 \rightarrow {}^2_0A_2$ is fast due to the following reason. The electronic term W_{if} of ${}^2_2A_2 \rightarrow {}^2_0A_2$ is large because it is symmetry allowed, about four orders of magnitude larger than the other two transitions. Since τ^{NR} is inversely proportional to the square of W_{if} according to Eq. (4.4), the difference of W_{if} dominates over the phonon contribution in X_{if}. The nonradiative lifetime of ${}^2_2A_2 \rightarrow {}^2_0A_2$ (2.29 ns) is several orders shorter than the other two transitions.

We note that different from Jara *et al.* [28], which focuses on the first transition, we focus on the second transition at 2.13 eV (BSE) in Table 4.3, which gives much better agreement with experiments for several parameters. A more detailed comparison with Ref. [28] with hybrid functionals can be found in the SM, Table S4 [142].

4.6 PL Lifetime and Quantum Yield

Next we will compute the PL lifetime and quantum yield [129] using the radiative and nonradiative recombination lifetime from Table 4.2 and Table 4.3, respectively. We list them along with the full-phonon HR factors calculated with the method in Ref. [19], and quantum yield (η) computed by Eq. (4.7) [154] in the multiplet diagram

Table 4.3: Properties of nonradiative recombination of the intradefect transitions. The transitions are denoted using the multielectron wavefunction notations. The ZPL(BSE) are evaluated by subtracting the Franck-Condon shift (E_{FC}) from the excitation energies from $\mathrm{G_0W_0}$ − BSE calculations. The ZPL(CDFT) are obtained by constrained DFT calculations at the PBE level, which are used as the energy input for the nonradiative lifetime. ΔQ is the nuclear coordinate change between the initial and final states. $\hbar\omega_f$ is the phonon energy of the final state. $S_f(1D)$ is the HR factor with 1D effective phonon approximation. W_{if} and X_{if} are the electronic and phonon terms, respectively. The nonradiative lifetimes are calculated with a 6×6 supercell at 300 K at the PBE level. Here, ${}^2_1B_1 \rightarrow {}^2_0A_2$ is related to the transition $2\mathrm{a}_{2\downarrow} \rightarrow 2\mathrm{b}_{1\downarrow}$ in the single particle picture; transition ${}^2_2A_2 \rightarrow {}^2_0A_2$ is related to the transition $2\mathrm{a}_{2\downarrow} \rightarrow 1\mathrm{a}_{2\downarrow}$; transition ${}^2_2A_2 \rightarrow {}^2_1B_1$ is related to the transition $2\mathrm{b}_{1\downarrow} \rightarrow 1\mathrm{a}_{2\downarrow}$.

Transition	E_{FC} (eV)	ZPL(BSE) (eV)	ZPL(CDFT) (eV)	ΔQ ($\mathrm{amu}^{1/2}$Å)	$\hbar\omega_f$ (meV)
${}^2_1B_1 \rightarrow {}^2_0A_2$	0.13	1.21	1.16	0.26	122
${}^2_2A_2 \rightarrow {}^2_0A_2$	0.20	2.13	1.70	0.27	145
${}^2_2A_2 \rightarrow {}^2_1B_1$	0.01	–	0.55	0.19	128

Transition	$S_f(1D)$	W_{if}	X_{if}	τ^{NR}
		(eV/(amu$^{1/2}$Å))	(amu·Å^2/eV)	
${}^2_1B_1 \rightarrow {}^2_0A_2$	0.95	$1.34 * 10^{-4}$	$7.17 * 10^{-6}$	∼1 ms
${}^2_2A_2 \rightarrow {}^2_0A_2$	1.26	$3.13 * 10^{-1}$	$4.69 * 10^{-7}$	2.29 ns
${}^2_2A_2 \rightarrow {}^2_1B_1$	0.67	$5.58 * 10^{-5}$	$1.05 * 10^{-2}$	3.20 μs

Fig. 4.3,

$$\eta = \frac{1}{\tau^{\mathrm{R}}} / (\frac{1}{\tau^{\mathrm{R}}} + \sum_i \frac{1}{\tau_i^{\mathrm{NR}}}), \tag{4.7}$$

where i denotes the i^{th} nonradiative pathway for the transition from the initial state. In addition, we calculate the PL lifetime which is the inverse of the total recombination rate by Eq. (4.8),

$$\tau^{\mathrm{PL}} = 1/(\frac{1}{\tau^{\mathrm{R}}} + \sum_i \frac{1}{\tau_i^{\mathrm{NR}}}) = \tau^{\mathrm{R}} * \eta. \tag{4.8}$$

For transition ${}^2_2A_2 \rightarrow {}^2_0A_2$, the nonradiative lifetime is nearly 10 times shorter than the radiative lifetime. By including the nonradiative recombination ${}^2_2A_2 \rightarrow {}^2_1B_1$, the overall recombination leads to the quantum yield of 4.23%, about 2% lower than the experimental quantum yield range 6∼12% [102]. More importantly, the PL lifetime of transition ${}^2_2A_2 \rightarrow {}^2_0A_2$ from Eq. (4.8) is calculated to be 2.19 ns, exactly within the experimental range of the PL lifetimes [Table 4.1 and Fig. 4.5(a)]. In addition, the calculated full-phonon HR factor of this transition is 1.35, indicating weak electron-phonon interaction and good agreement with the experimental HR factor in Table 4.1 and Fig. 4.5(b).

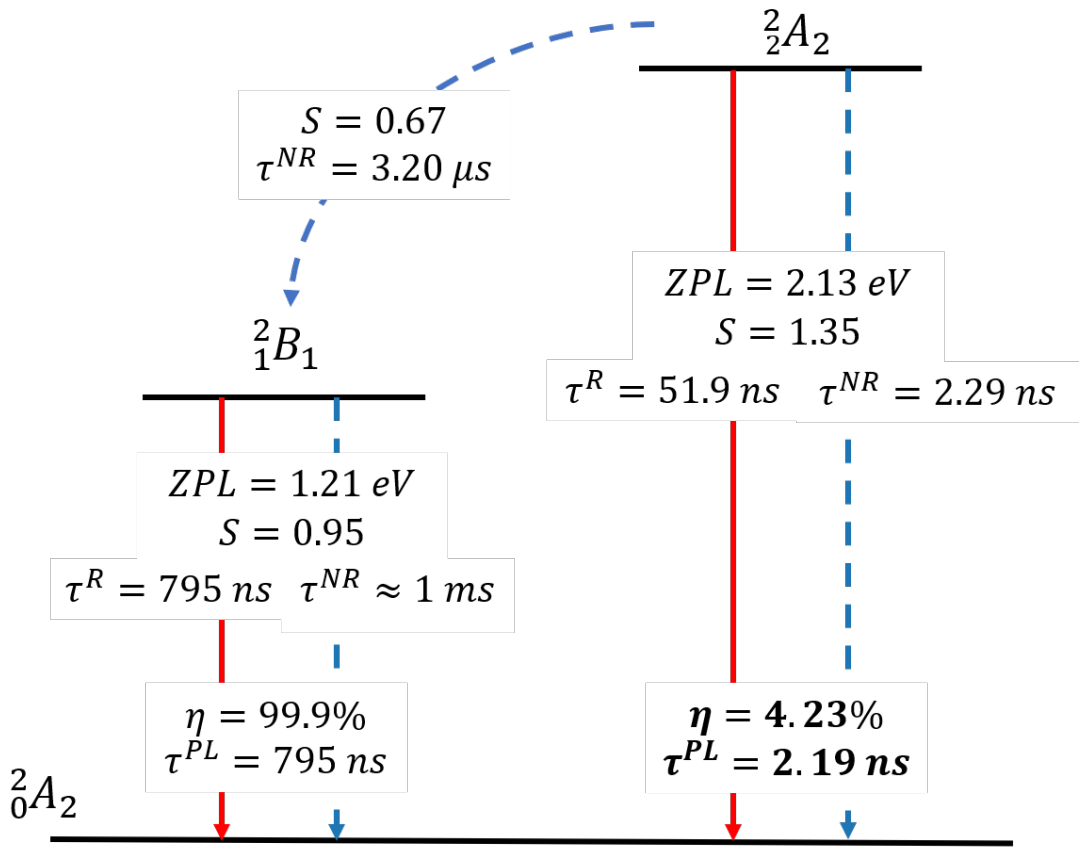

Figure 4.3: Multiplet structure and important physical parameters of C_2C_N in hBN. $^2_0A_2$ is the ground state, and $^2_1B_1$ and $^2_2A_2$ are the excited states. The red solid lines denote radiative recombination and the blue dashed lines denote nonradiative recombination. S is the HR factor with full-phonon calculations. τ^R and τ^{NR} are the radiative lifetime and nonradiative lifetime, respectively. η and τ^{PL} are the QY and PL lifetime, respectively.

4.7 Phonon Modes of C_2C_N in hBN

To get more insight into the electron-phonon coupling of C_2C_N in hBN, we calculate the spectral function $[S(\hbar\omega)]$ of ${}^2_2A_2 \rightarrow {}^2_0A_2$ with the partial HR factor (S_k) of phonon mode k, as shown in Fig. 4.4. The phonon modes spread over the range 0∼190 meV, and the phonon modes around 180 meV have the largest contribution to the spectral function. In particular, the 187 meV phonon mode has the largest partial HR factor among these modes. By visualizing this phonon mode shown by the inset in Fig. 4.4, we find it to be an out-of-phase phonon mode. The atoms involved in this phonon mode include not only defect-related atoms, but also many B and N atoms around and away from the defect. Hence, the 187 meV phonon mode is quasilocal. To quantitatively characterize the localization of dominant phonon modes, we estimate the number of atoms involved in the vibration of a phonon mode, by projection of the inverse participation ratio (IPR) on this phonon mode k [19],

$$\mathrm{IPR_k} = \frac{1}{\sum_\alpha (\sum_i \Delta r^2_{k;\alpha,i})^2}, \tag{4.9}$$

where $\Delta r_{k;\alpha,i}$ is a normalized vector that describes the displacement of the atom α along the direction i in the phonon mode k between the initial and final states. We then estimate the localization of the phonon mode by the localization ratio β,

$$\beta_k = \mathrm{NAT}/\mathrm{IPR_k}, \tag{4.10}$$

where NAT stands for the total number of atoms in the supercell. The larger the localization ratio is, the more localized the phonon mode is. We find that the IPR of the 187 meV phonon mode is 46 for the 6x6 supercell calculation, and the localization

ratio β is $\sim$2. The IPR of this mode increases as a function of supercell sizes, but the localization ratio keeps constant, as can be seen in the SM, Table S4 [142]. This again reflects the nature of this mode being a mixture of defect and bulk phonons or a "quasilocal" mode. Besides the 187 meV phonon, the 60 meV phonon is pronounced in the low-energy range of the spectral function, as an in-phase phonon mode (see the inset in Fig. 4.4). It also has a large IPR of 48 and β of $\sim$2. Comparing the calculated phonon mode energies with the experimental ones for 2eV single-photon emitters [101, 155], the 187 meV phonon mode is in good agreement with the $\sim$180 meV longitudinal optical phonon that leads to the pronounced PSB.

4.8 Comparison between C_2C_N Defect and Experiments

To further validate that C_2C_N is a possible candidate of experimentally observed single-photon emitters, we calculate the PL of C_2C_N for transition ${}^2_2A_2 \rightarrow {}^2_0A_2$ and compare it with the PL spectra of $\sim$2 eV SPEs [3] in Fig. 4.5. The details of the PL calculation can be found in Sec. V of the SM [142, 156, 157, 158]. The calculated PL shows similar PSB peaks to the experimental PL [3], as can be seen in Fig. 4.5(d). A weak PSB peak next to the first PSB peak can be seen in both the calculated and experimental PL spectra. This peak has been found to be more visible when the brightness is enhanced in an as-prepared array [155]. In addition, phonon-sideband energy can be a measure of the averaged phonon energy, found to be 180 meV, within the experimental range in Table 4.1 and Fig. 4.5(c). The excellent agreement between the calculated and experimental physical parameters including ZPL, PL lifetime, HR factor, PSE, and

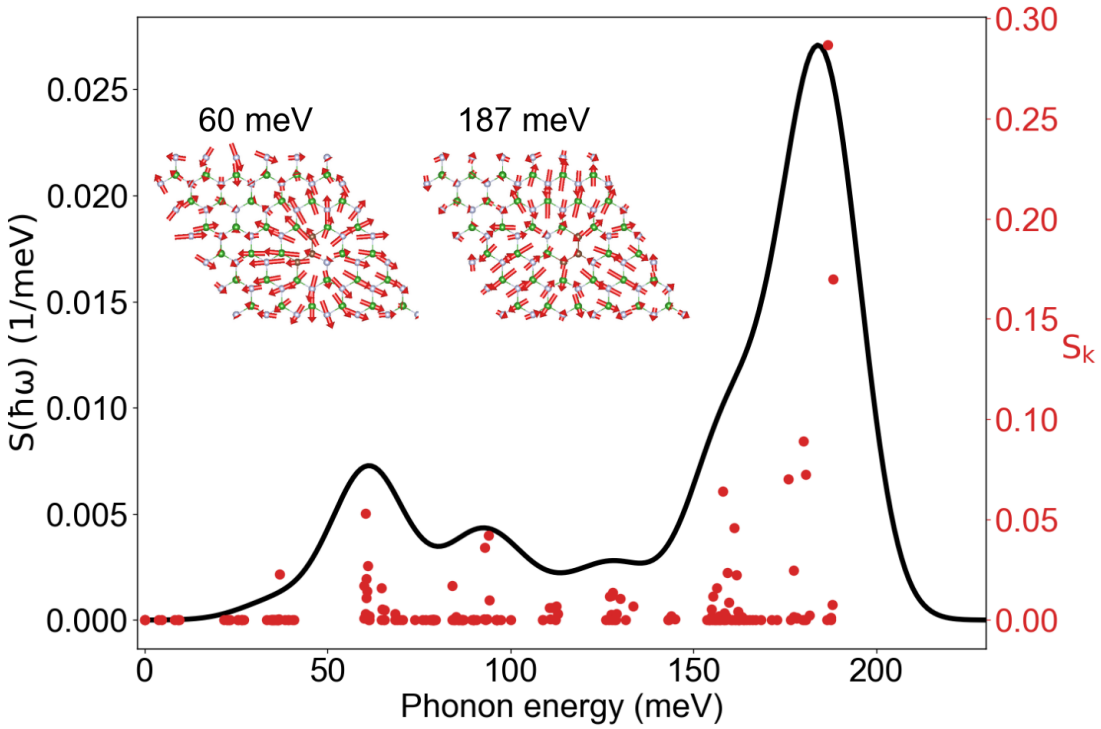

Figure 4.4: Spectral function that shows the distribution of phonon modes and the contribution of phonon modes to the electron-phonon interaction of the C_2C_N defect in hBN. The left vertical axis and black solid line are for the spectral function, and the right vertical axis and red dots are for the partial HR factor as a function of phonon energy. The inset figures are the low-energy phonon mode (60 meV) and dominant phonon mode (187 meV) of C_2C_N for transition ${}^2_2A_2 \rightarrow {}^2_0A_2$. The red arrows show the atom displacement of the corresponding phonon modes.

PL spectrum strongly suggests that the C_2C_N defect is one possible source of ∼2 eV single-photon emission.

According to our theoretical calculations, as shown in Fig. 4.3, besides the emission around 2 eV , there is a near-infrared (near-IR) emission which can be another identifier of the C_2C_N defect. Note that besides the PL lifetime, photon detection rate I can be another experimentally measurable quantity,

$$I = \alpha\Gamma^{R} \tag{4.11}$$

where α is the photon collection coefficient, and Γ^{R} is the radiative rate or emission rate [159, 160].

To estimate the photon detection rate of the near-IR emission, we first calculate the emission rate, which is 1.26×10^6 counts/s based on the radiative lifetime 795 ns in Table 4.2. Second, we estimate the photon collection coefficient from existing experiments [101], which is 0.31, by taking the ratio of the experimental photon detection rate (6×10^6 counts/s) of the 2 eV emission [101] to the theoretical emission rate (1.93×10^7 counts/s) of C_2C_N at 2.13 eV (radiative lifetime 51.9 ns in Table 4.2). Assuming the photon collection coefficient is the same between the 2 eV and the near-IR emission, the photon detection rate estimates to be 3.92×10^5 counts/s for the near-IR emission. This is experimentally measurable with sufficiently long acquisition time.

Finally, we note that the variation in experimental results shown in Table 4.1 can be from several sources of single-phonon emitters and possible internal strains due to material preparation. Further defect identification including spin-related properties can be through calculations of optically detected magnetic resonance (ODMR), which

measures the spin-dependent optical contrast and is directly related to the information readout of spin qubits [161].

4.9 Conclusions

In conclusion, we investigated the possibilities of carbon defects for 2 eV single-photon emission in hBN, by comparing key physical properties from first-principles calculations with experiments, including ZPL, PL lifetime, and line shape, as well as HR factor. We showcase the importance of considering multiple key signatures including both static and dynamical properties when identifying defects through theory and experimental comparison. We found that C_2C_N has the best agreement with experiments for all concerned properties. In particular, we show that the radiative lifetime can be an order longer than the experimentally observed PL lifetime; but after including non-radiative processes, the agreement with the experimental PL lifetime is much better. We show the electron-phonon coupling in C_2C_N is moderate with small HR factor and the dominant phonon mode at $\sim$180 meV is quasilocal with significant participation of bulk atoms. The near-infrared emission can be another identifier of C_2C_N, which can be used for experimental verification of the nature of SPEs. Our work provides insight into the $\sim$2 eV single-photon emission from the theoretical perspective, which is important for unraveling the unknown chemical nature of defects in hBN, manipulating defects, and developing quantum applications.

Besides hBN, other 2D materials such as black phosphorus and graphene have shown highly tunable light emission properties [162, 163, 164], which may be promising

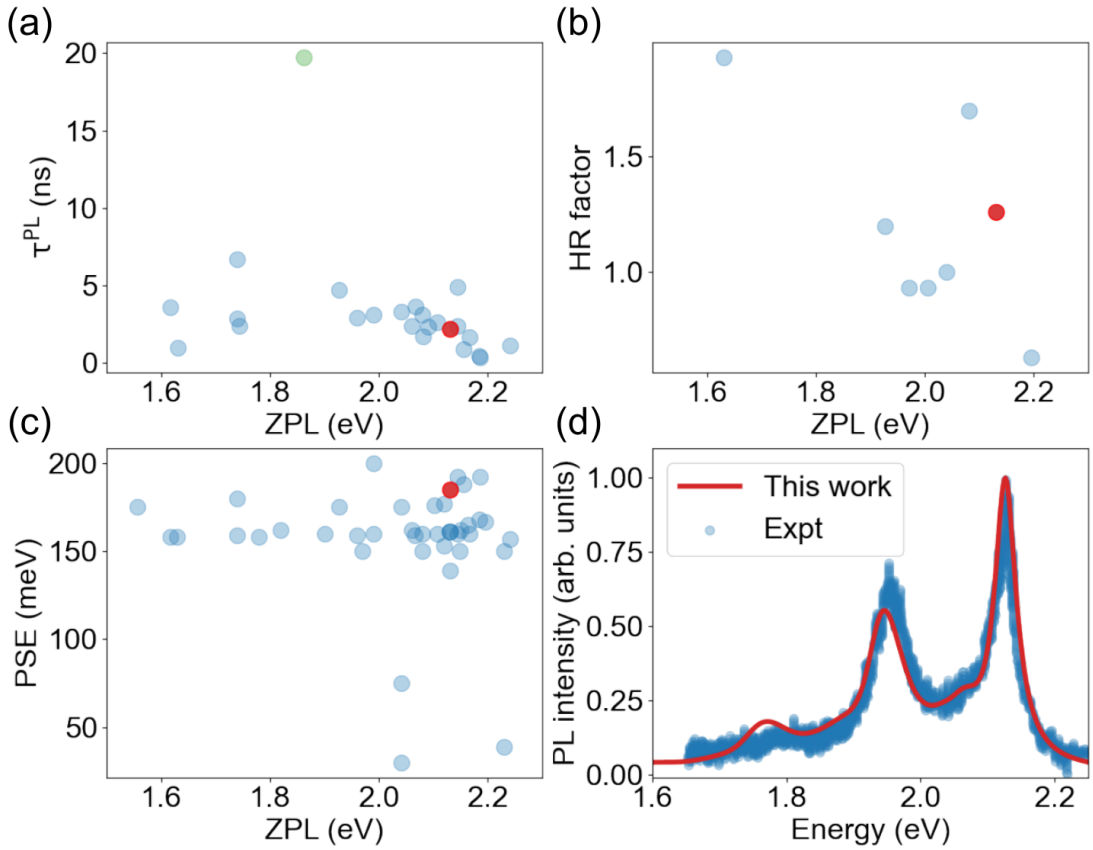

Figure 4.5: The calculated properties of C_2C_N along with the experimental values which are summarized in Table. 4.1. (a) PL lifetime vs ZPL; (b) HR factor vs ZPL; (c) PSE vs ZPL; (d) comparison between the theoretical PL spectrum (this work) and the experimental PL spectrum (Expt) [3]. In (a), (b), and (c), the blue dots are for the experimental values of ∼2 eV single-photon emitters, the green dot is for the experimental PL lifetime of ∼20 ns, and the red dots are for the calculated values. The calculated ZPL here is from the G_0W_0 – BSE@PBE calculation. The comparison shows that ZPL, PL lifetime, HR factor, and PSE are all in the experimental range. The calculated PL spectrum also matches well with the experimental PL of the ∼2 eV single-photon emission [3].

for single-photon emission and spin qubit applications as well. For better spatial control and emission tunability of quantum defects in 2D materials, promising pathways have been suggested by interfacing quantum emitters with metasurfaces [165, 166], coupling with microcavities [167] and far-field patterns [168].

Chapter 5

Excited-State Dynamics of Solid-State Spin Defects

In Chapter 4, the first-principles methodologies and their application to defect identification are presented. This chapter focuses on the advanced development of first-principles method and simulation model for characterizing spin polarization of spin defects via the spin-photon interface. Many important questions related the excited-state dynamics of the NV center in diamond are unambiguously answered. Deeper insight into the excited-state dynamics from the theoretical point of view is provided for many spin defects that share common characteristics with the NV center. Chapter 3 presents the details of symmetry study of spin defects.

5.1 Introduction

Point defects in solids as spin qubits offer multiple avenues to quantum technologies, in particular quantum sensing and quantum networking [169]. The promising candidates exhibit long quantum coherence times [170, 171, 172], essential for performing multi-step quantum operations with high fidelity. They are relatively scalable and easy to integrate into existing technologies due to their solid-state nature [173]. Furthermore, they can be optically initialized and reliably read out in a wide temperature range [174, 175, 176], through the spin-photon entanglement [177]. While discovering and exploring new spin defects beyond the extensively-studied negatively-charged nitrogen-vacancy (NV) center in diamond [82] has been a key interest in recent years, reliable theoretical predictions of optical readout properties remain challenging, which hinder rapid progress.

The first outstanding issue is the missing link between experimental observable and first-principles simulations for the spin polarization processes. The experimental tool to study spin polarization is through optically detected magnetic resonance (ODMR) [4, 92, 93, 178], by recording photoluminescence contrast with and without microwave radiation as a function of magnetic field. This requires to solve the kinetic equations for excited-state populations of different spin sublevels. The excited-state population is determined by kinetic processes in the polarization cycle, including radiative and nonradiative recombination between different spin states. Previously, only model simulations with experimental rates and energy levels to describe ODMR have been reported [4, 92, 93, 178]. A first-principles formalism and computational tool is

yet to be developed in order to interpret experiments or predict ODMR of new spin defect systems.

To perform first-principles ODMR, predictions of optical excitation energies, zero-field splitting, radiative and nonradiative recombination rates are required. Various first-principles electronic structure methods have been proposed to calculate excitation energies of spin defects. The key consideration is to accurately capture the electron correlation of defect states. For instance, mean-field theory such as constrained DFT (CDFT) [68] could provide reasonable structural and ground state information, but GW and solving the Bethe-Salpeter Equation (GW-BSE) can provide more accurate quasi-particle energies and optical properties including electron-hole interactions [48, 139]. On the other hand, if the defect states have strong multi-reference nature, such as open-shell singlet excited state of the NV center, theories like quantum-defect-embedding theory (QDET) for solids [179, 180] or multi-reference wavefunction methods [181] may be more appropriate. Note that such theory still requires substantial development in order to study dynamical and spin-orbit properties.

The first-principles theory for excited-state kinetic properties of spin defects has recent advancement as well. For example, the radiative recombination rates have been calculated at finite temperature with inputs from many-body perturbation theory for a better description of excitons [179, 59]. The nonradiative recombination transitions, in particular intersystem crossing (ISC) that requires spin-flip transition and phonon-assisted internal conversion (IC), can be obtained from phonon perturbation to electronic states [67, 48, 52, 68]. However, these calculations have not considered

the multi-reference nature of the electronic states and complex Jahn-Teller (JT) effects coupled in the kinetic processes.

In this work, we have developed the first-principles ODMR theory and computational tool to directly predict ODMR contrast without *prior* input parameters as shown in Fig. 5.1(a). We note that such tool is fully general to all solid-state defect systems, although we first use the NV center as a prototypical example. By combining advanced electronic structure methods and group theory analysis, we provide a complete set of SOC constants for ISC processes which has not been shown before, and a comprehensive picture of excitation and relaxation dynamics of the NV center. We discuss the significance of configuration interaction, pseudo JT and dynamical JT effects to the SOC, ISC and IC. The consideration of these effects facilitates the interpretation of the experimentally observed ISC rates that essentially contribute to spin polarization. Particularly, we provide a definitive answer to the longstanding question regarding the axial ISC of $^3E \rightarrow ^1 A_1$: why symmetry predicts it to be forbidden in the first order [182, 1, 18], experiments show it to be nonzero [88, 4, 89]. Our work demonstrates a tight connection between theoretical predictions and experimental observations for various experimental observables, including excitation energy, radiative recombination rate, SOC, ISC, IC and ODMR. Our theoretical results show qualitative or quantitative agreement with experimental data, depending on properties. We note that, for the quantities related to the open-shell excited states, a proper treatment of possible multireference character is necessary. Additionally, our calculated SOC values complement those difficult to measure experimentally. Importantly, we explain why the transition

$^1A_1 \rightarrow ^1E$ is predominantly nonradiative by estimating the IC rates between two singlet states. We predict the ODMR contrast as a function of an external magnetic field fully from first-principles, in good agreement with experimental results. We demonstrate that these simulations are invaluable for predicting spin-polarization mechanism and provide control strategy on high fidelity optical initialization and readout.

5.2 Computational Methods

We carry out first-principles calculations of structural and ground-state properties using the open-source plane-wave code Quantum Espresso [130]. The NV center defect is introduced into a simple cubic diamond crystal with $3 \times 3 \times 3$ supercell size, containing 216 atoms. Only Gamma point is sampled in the Brillouin zone of the defect supercells for all calculations, except for the $G_0W_0 - BSE$ calculations for the radiative lifetime, where a k-point sampling of $2 \times 2 \times 2$ is used. We use the optimized norm-conserving Vanderbilt (ONCV) pseudopotentials [135] with the wavefunction energy cutoff of 70Ry. The lattice constant is optimized by using the exchange-correlation functional with the Perdew-Burke-Ernzerhof (PBE) generalized gradient approximation [39]. For geometry optimization and excitation energies, we mainly use the range-separated hybrid function proposed by Heyd, Scuseria, and Ernzerhof (HSE) [47, 46], and part of the results using PBE functional are for comparison with HSE, presented in the supplementary material (SM). The HSE functional has been shown to better describe the electronic structure of the NV center in diamond compared to the PBE functional [183, 184, 91]. We calculate the excitation energies using three different

methods, constrained DFT (CDFT), single-shot GW plus the Bethe-Salpeter Equation (G_0W_0-BSE), and complete active space self-consistent field method with second order perturbation theory (CASSCF-CASPT2) [185].

The many-body perturbation theory calculations are performed by using the WEST code [186, 187], which takes the advantage of various techniques [188, 189] and GPU parallelization to enable large-scale computaions. The Bethe-Salpeter Equation (BSE) is solved within the density matrix perturbation theory (DMPT) formalism, and the projective dielectric eigenpotentials (PDEP) technique is utilized to compute the screened exchange integral, avoiding the need for empty bands. The number of PDEP is converged to 2000 (about 2 times the number of electrons) as determined from our test with GW. The details of the G_0W_0-BSE calculations can be found in Sec. II.

Due to the multi-reference character of the ^3E, ^1E, and $^1A_1$ excited states of the NV center, a single Slater determinant description in DFT is incomplete. To overcome this problem, we use the CASSCF method [185] to construct the state wave-functions as linear combinations of multiple Slater determinants. Each determinant describes a particular occupation of single-electron orbitals. We use the $C_{33}H_{36}N^{-1}$ cluster model, which is considered in Ref. [181]. The cluster model is cut from the $^3A_2$ ground state geometry of $3\times3\times3$ supercell, and the C atoms that have dangling bonds are terminated H atoms with standard C-H bond length of 1.09 Å. In the CASSCF method, the orbital space is partitioned into subspaces of the inactive, active, and virtual orbitals. The occupation of the active orbitals is allowed to change to generate all possible spin- and symmetry-allowed determinants for a particular electronic state.

A choice of a partition of the orbital space, that is the choice of a number of active orbitals and active electrons, determines the CASSCF active space. The active space of (6e, 6o) is chosen to include two molecular orbitals of the a_1 (a_{1N} and a_{1C}) symmetry and two orbitals of the e symmetry (e_x, e_y, e'_x, and e'_y), all localized near the vacancy defect. Inclusion of the e'_x and e'_y orbitals in the active space is necessary for accurate description of the correlation between electrons near the defect [181]. We use the state-average (SA) version of the CASSCF method as implemented in ORCA [190, 191] to obtain state wavefunctions for calculations of SOC matrix elements. The $^3A_2$, ^3E, $^1A_1$, and ^1E electronic states, involved in the spin polarization cycle [52, 68], are included in state-averaging. Accurate prediction of the excitation energies requires correction of the CASSCF energies for the dynamic electron correlation. In this work, we use the fully internally contracted (FIC) version of the complete active space second order perturbation theory (CASPT2) [192] and *N*-electron valence state second order perturbation theory (NEVPT2) [193] as implemented in the ORCA 5.0 program package. The second order Douglas-Kroll-Hess (DKH2) Hamiltonian [194] and the cc-pVDZ-DK basis set [195, 196] were used to account for the scalar relativistic effects. The spin-orbit mean-field operator was used [197].

5.3 ODMR Theory, Implementation, and Benchmark

The basic mechanism of ODMR is related to the excited-state populations of spin sublevels. Therefore, we begin with the Hamiltonian that describes the spin

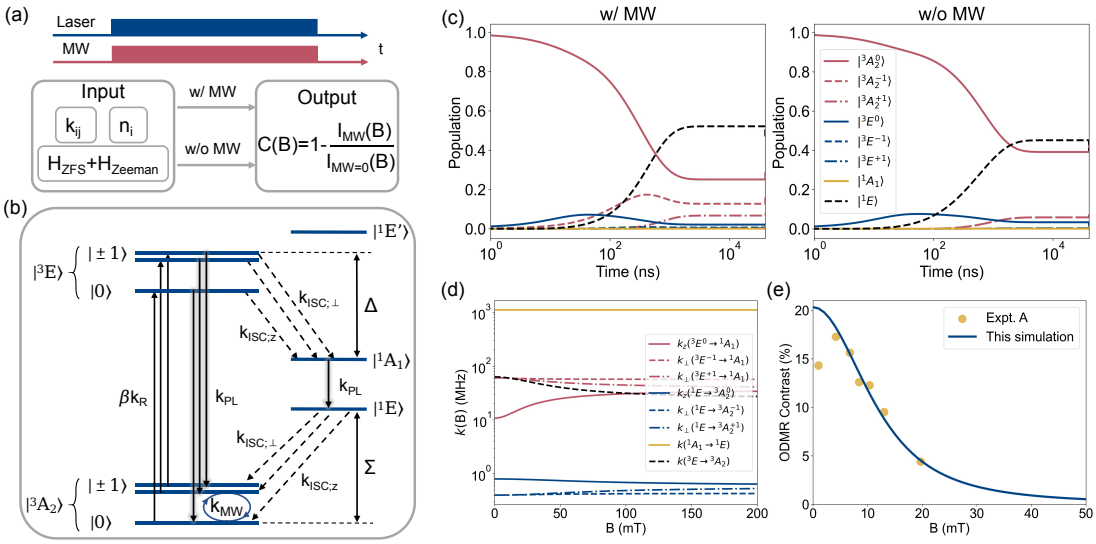

Figure 5.1: Numerical implementation of ODMR contrast and its benchmark with the NV center in diamond regarding the experiment [4], where the magnetic field is applied at an angle of 74° with respect to the NV axis. (a) The continuous-wave (cw) ODMR and its simulation workflow with first-principles inputs. (b) Schematic diagram depicting the energy levels and excited-state kinetic processes of the NV center in diamond. $|0\rangle$, $|-1\rangle$ and $|+1\rangle$ denote the spin sublevels in the triplet states. The spin sublevels $|+1\rangle$ and $|-1\rangle$ are degenerate under zero magnetic field. (c) The time-evolved populations of the states reach a steady-state plateau with sufficiently long time, in the presence (w/MW, left panel) or absence (w/o MW, right panel) of microwave field. (d) Transition rates (k) for different processes vary differently with magnetic field B. (e) Simulated ODMR contrast as a function of magnetic field (solid line) and compared with the experiment (dots) [4]. The experimental data is extracted from a figure by using WebPlotDigitizer tool [5].

sublevels of triplet states as in Fig. 5.1(b),

$$H_{\mathrm{s}} = D(S_z^2 - \frac{\mathbf{S}^2}{3}) + E(S_x^2 - S_y^2) + g_e \mu_B \mathbf{B} \cdot \mathbf{S} \tag{5.1}$$

$$\mathbf{B} \cdot \mathbf{S} = S_z B \cos\theta_B + S_x B \sin\theta_B \cos\phi_B + S_y B \sin\theta_B \sin\phi_B \tag{5.2}$$

where S_i is the spin-1 operator along i axis, D in the first term is the axial zero-field splitting (ZFS) parameter, E in the second term is the rhombic ZFS parameter, g_e is the electron g-factor or gyromagnetic ratio whose value is $\sim$2 in the NV center, μ_B is Bohr magneton, and $\mathbf{B}$ is the external magnetic field. The ZFS lifts the spin degeneracy. The third term describes the Zeeman effect occuring under magnetic field ($\mathbf{B}$) and further leading to the mixing of the original spin sublevels. θ_B and ϕ_B denote the misaligned angle of the magnetic field regarding the NV axis and the azimuthal angle in the x-y plane, respectively. Since in this work, we consider the symmetry retained in the x-y plane for ZFS, the ODMR does not depend on ϕ_B. Let α_{ij} be the mixing coefficient of original spin sublevels $|i\rangle$ and $|j\rangle$, then we can write the transition rates under magnetic field $k_{ij}(\mathbf{B})$ to be a function of mixing coefficients and the rates at zero magnetic field (k_{pq}^0),

$$k_{ij}(\mathbf{B}) = \sum_{p,q} |\alpha_{ip}(\mathbf{B})|^2 |\alpha_{jq}(\mathbf{B})|^2 k_{pq}^0. \tag{5.3}$$

The spin mixing will be shown below to be the source of the magnetic field-dependent ODMR.

We then numerically implement the ODMR contrast based on the kinetic master equation [4, 69], which integrates all transition rates and allows to simulate the dynamics of states populations, photoluminescence (PL) intensity, as well as continuous

wave (cw) or time-resolved ODMR. The model starts with the conventional definition of ODMR contrast,

$$C(\mathbf{B}) = 1 - \frac{\bar{I}(t, \mathbf{B}, k_{\mathrm{MW}})}{\bar{I}(t, \mathbf{B}, k_{\mathrm{MW}} = 0)} \tag{5.4}$$

$$\bar{I}(t, \mathbf{B}) = \eta \sum_{i \in \mathrm{ES}} \sum_{j \in \mathrm{GS}} k_{ij}(\mathbf{B}) \bar{n}_i(t, \mathbf{B}) \tag{5.5}$$

where $\bar{I}(t, \mathbf{B}, k_{\mathrm{MW}})$ is the magnetic-field dependent PL intensity at the steady state in the presence of microwave resonance (MW), which is different from the case in the absence of microwave resonance ($k_{\mathrm{MW}} = 0$). Here, k_{MW} is the Rabi frequency of a microwave field that is applied for rotating the populations of spin sublevels, and is a parameter in the model as it scales with the amplitude of the microwave field [70]. η is the collection coefficient parameter for PL intensity which depends on experimental setup but does not affect ODMR. The optical saturation parameter β seen in Fig. 5.1(b) and SM Sec. I plays a role in the optical excitation. Both k_{MW} and β are determined according to the experimental range [4]. The PL intensity evolves with time depending on $n_i(t, \mathbf{B})$, the population of spin level $|i\rangle$ at time t, and can be solved numerically using the Euler method.

To validate the ODMR contrast implementation for triplet systems, we firstly simulate the ODMR of the prototypical system NV center, as shown in Fig. 5.1(b), using the experimental values of ZFS and rates [4, 20, 69]. The purpose of this benchmark is to confirm the numerical implementation of ODMR contrast from Eq. (5.1) to Eq. (5.5), independent of the accuracy of electronic structure and kinetic rates, which will be discussed in detail in the next sections. Values for the ODMR simulation parameters

are tabulated in SM Table S1, and the microwave resonance is applied to drive the rotation between $|^3A_2^0\rangle$ and $|^3A_2^{-1}\rangle$. Since the simulated cw-ODMR is observed at steady state, arbitrary initial populations of the spin sublevels can be used.

The system reaches the steady state after $\sim 10^4$ ns, as shown in Fig. 5.1(c). From the steady-state populations, we can find that $|^3A_2^{-1}\rangle$ has larger population due to the Rabi oscillation in the presence of the microwave field compared to the absence of the microwave field. Because the optical excitation is mostly spin-conserving [89], the population of $|^3E^{-1}\rangle$ is subsequently larger. Because the nonaxial ISC $^3E \rightarrow^1 A_1$ is symmetrically allowed and fast, as can be seen in Fig. 5.1(d), it competes with the radiative recombination $^3E \rightarrow^3 A_2$, leading to overall smaller excited-state population. Therefore, the PL intensity in the presence of the microwave field becomes smaller, and the ODMR contrast is positive as shown in Fig. 5.1(e).

The ODMR contrast is a result of the difference between the axial and nonaxial ISCs, which are the transitions between spin sublevel $|0\rangle$ and $|\pm 1\rangle$ to singlet, and vice versa, eventually leading to spin polarization. The decrease of ODMR contrast with the magnetic field is a consequence of the smaller difference between axial ISC rates and nonaxial ISC rates, compared Fig. 5.1(d) to Fig. 5.1(e). The fundamental reason is the mixing of spin sublevels, which will be discussed in details in Sec. 5.8. To understand the magnetic field effect, first, when the magnetic field is misaligned with the NV axis, there is mixing between spin sublevels $m_s = 0$ and $m_s = \pm 1$. Second, the spin mixing will further mix ISC rates between different transitions as Eq. (5.3). For the NV center, the spin polarization is mainly a result of $k_\perp(^3E \rightarrow^1 A_1) \gg k_z(^3E \rightarrow^1 A_1)$. When

$k_\perp(^3E \rightarrow^1 A_1)$ is similar to $k_z(^3E \rightarrow^1 A_1)$ due to spin mixing, spin polarization is weaker, ODMR contrast is smaller. In the extreme case, where the axial ISC is equal to the nonaxial ISC, there will be no ODMR contrast because no spin polarization among m_s spin sublevels.

The excellent agreement of our simulation with experiment in Fig. 5.1(e) validates the numerical implementation of ODMR. In SM Fig. S2 and Fig. S3, we present additional results of the benchmark regarding ODMR frequency and time-resolved PL intensity of the NV center. More importantly, we determine that the dip of ODMR at $B = 0$ is a result of nonzero rhombic ZFS E in Eq. 5.1, which is induced by symmetry-breaking. Detailed discussion can be found in SM Sec. I, Fig. S4 and Fig. S5.

Besides triplet spin defects, singlet defects that have a triplet metastable state can also show ODMR signal, like ST1 defect in diamond [198, 199]. In SM Table S2 and Fig. S6, we additionally include the detailed benchmark of the ODMR model for singlet spin defects. The benchmark for both triplet and singlet spin defects demonstrates the generality of the ODMR model.

Next, we will discuss in detail the first-principles calculations of electronic structure and excited-state kinetic rates at solid-state spin defects, specifically the NV center here.

Table 5.1: The excitation energies of the NV center from various theories along with experiments. The energy of $^3A_2$ is aligned to 0 eV, and the energies of the other states are entered with respect to $^3A_2$. Σ is the excitation energy of ^1E with respect to $^3A_2$, and Δ is the energy difference between ^3E and $^1A_1$, as illustrated in Fig. 5.1(b).

Method	^1E or Σ (eV)	$^1A_1$ (eV)	^3E (eV)	Δ (eV)
Expt. (ZPL)	0.325-0.411[1]	1.515-1.601 [200, 201, 20]	1.945 [202, 88, 26]	0.344-0.430[2] [88, 26]
Expt. (absorption)	–	1.76[3] [20]	2.180 [202]	–
CDFT (HSE, ZPL)	0.37	–	1.95	–
GW-BSE@PBE (absorption)	-	-	2.40	-
SA(6)-CASSCF(6,6) (absorption)	0.66	1.96	2.30	0.34
CASPT2 (absorption)	0.55	1.57	2.22	0.65
CASSCF [181]	0.25	1.60	2.14	0.54
QDET [180]	0.46	1.27	2.15	0.88
NEVPT2-DMET [203]	0.50	1.52	2.31	0.79
CI-CRPA [204]	0.49	1.41	1.75[4]	0.34

1. The range of ^1E or Σ was determined according to the triplet ZPL $^3E \rightarrow^3 A_2$, the singlet ZPL $^1A_1 \rightarrow^1 E$, and Δ.

2. The range of Δ was extracted from the ISC rate equation in Ref. [88, 26]. It is simply for reference.

3. This energy is obtained by adding the approximate energy (0.40 eV) of ^1E to the absorption energy $^1E \rightarrow^1 A_1$ 1.36 eV (912 nm).

4. ZPL

5.4 Electronic Structure, Excitation Energies and Radiative Recombination of NV Center

The NV center comprises a substitutional nitrogen atom and a vacancy with one extra electron in the faced-center cubic diamond, with its local structure described by the C_{3v} symmetry point group. The three-fold symmetry axis is the nitrogen-vacancy axis along the [111] direction. The ground and low-lying excited electronic states of the NV center can be determined from two one-electron orbitals, a_1 and e (e_x, e_y), which transform as the A_1 and E irreducible representations of the C_{3v} point group, respectively. These one-electron orbitals are formed by the carbon and nitrogen dangling bonds near the vacancy defect. The $a_1^2e^2$ configuration gives rise to the $^3A_2$, ^1E and $^1A_1$ states, and a_1e^3 to the ^3E state. The states above are listed in the ascending energy order determined experimentally and from the group theory [201, 20, 88, 68]. The total spin-orbit irreducible representations of these states are given in SM Table S3. The derivation of the representations can be found in literature [80, 1, 18].

Excitation energies play an important role in energy conservation in radiative (electron-photon interaction) and nonradiative (electron-phonon interaction) recombination rates. As we discussed earlier, the excited states of defects can have multi-reference character which is difficult to describe by conventional DFT. Therefore we show the calculated excitation energies from several different electronic structure methods, CDFT, G_0W_0 − BSE@PBE, CASSCF, and CASPT2 as listed in Table 5.1. The CASPT2 method predicts the excitation energies of the $^1A_1$ and ^3E states in the good

agreement with the experimental values and with energies obtained using the superclusters of different sizes [180, 203]. The experimental absorption energy of the ^1E state is unknown. The CASPT2 method consistently predicts the energy of the ^1E state in the range of 0.55 to 0.60 eV, see SM Table S4. This energy is in close agreement with the value of 0.50 (0.46) eV obtained with the embedding theories [180, 203] and with the value of 0.49 eV obtained using the configuration interaction method [204]. Therefore, the CASPT2 excitation energies are in good agreement with those obtained using larger cluster models, and their use in the ODMR simulations is well-justified. We find that the NEVPT2 theory systematically overestimates energies of the ^1E and ^3E states, see SM Table S4. More discussion about the excitation energies can be found in SM Sec. IIA.

With the excitation energies, we employ the Fermi's golden rule to calculate radiative recombination rate. The details of calculation methods can be found in our past work [59, 67, 48] and results can be found in SM Sec. IIC. For the convenience of comparing our calculated results with previous experiment and calculations, here we adopt lifetime (τ), which is the inverse of rate ($\tau = 1/k$). Using the optical dipole moments and excitation energy from $G_0W_0 - BSE@PBE$ calculations which includes excitonic effect accurately, we obtain τ_R =12.44 ns for the $^3E \rightarrow^3 A_2$ transition and 237 ns for the $^1A_1 \rightarrow^1 E$ transition. Our calculated radiative lifetime of the $^3E \rightarrow^3 A_2$ transition is consistent with experiment 12 ns for $^3E \rightarrow^3 A_2$ [88]. The radiative lifetime of the $^1A_1 \rightarrow^1 E$ transition has not been determined experimentally and is found to be dominated by nonradiative processes [201]. Thus, we will mostly focus on the IC

transition for $^1A_1 \rightarrow ^1E$ as discussed in Sec. 5.7.

5.5 Spin-Orbit Coupling and Pseudo Jahn-Teller Effect

Spin-orbit coupling Hamiltonian can be separated into the axial/nonaxial SOC components ($\lambda_{z/\perp}$) with the angular momentum ladder operators ($L_\pm$ and $S_\pm$) and z components (L_z and S_z),

$$H_{\text{soc}} = \frac{\lambda_\perp}{2}(L_+S_- + L_-S_+) + \lambda_z L_z S_z. \tag{5.6}$$

Group theory provides important information of whether a SOC matrix element is allowed or forbidden, from the symmetry point of view. And the multi-particle representation of the SOC matrix elements can be reduced to the single-particle representation by using the Wigner-Eckark theorem [18]. Some SOC matrix elements were previously evaluated at the single-particle level at HSE, as shown in Table 5.2. However, because of their multi-reference character, the excited states cannot be properly described with a single Slater determinant [181], as can be seen in SM Table S9 and Fig. S11. Therefore, we perform CASSCF for the evaluation of SOC to take into account the multi-reference nature of the states, in comparison with TDDFT [95] and previous DFT results [52, 68].

As shown in Table 5.2, the SOC matrix elements from CASSCF are in accordance with the group theory prediction. Specifically, within the important SOC matrix elements listed, only $\lambda_z(^3E,^3E)$ and $\lambda_\perp(^3E,^1A_1)$ are symmetry-allowed. Accordingly we obtain finite values for these SOC matrix elements at CASSCF. We note that the

Table 5.2: Summary of SOC matrix elements predicted by group theory, calculated at the theory level of CASSCF and from experiment. The unit is GHz. CASSCF (C_{3v}) SOC constants are consistent with prediction. "CI" stands for configuration interaction that mixes ^1E and $^1E'$. Pseudo JT effect mixes $^1A_1$ and ^1E through electron-phonon coupling, leading to nonzero SOCs. "–" denotes values that do not exist or are not found.

	$\lambda_z(^3E,^3E)$	$\lambda_\perp(^1A_1,^3E)$	$\lambda_z(^1A_1,^3E)$	$\lambda_\perp(^3A_2,^1\bar{E})$	$\lambda_z(^3A_2,^1\bar{E})$
Group Theory (C_{3v})[1]	$\pm\lambda_z$	$i\lambda_\perp$	0	nonzero by CI	0
SA(6)-CASSCF(6,6) (C_{3v})	14.21	3.96	0.06	5.22[2]	0.03
(w/ pseudo JT)	$\lambda_z(^3\widetilde{E},^3\widetilde{E})$	$\lambda_\perp(^1\widetilde{A}_1,^3\widetilde{E})$	$\lambda_z(^1\widetilde{A}_1,^3\widetilde{E})$	$\lambda_\perp(^3\widetilde{A}_2,^1\widetilde{E})$	$\lambda_z(^3\widetilde{A}_2,^1\widetilde{E})$
Group Theory	$\pm\lambda_z$	nonzero	nonzero by pseudo JT	nonzero by CI	nonzero by pseudo JT
Effective SOC SA(6)-CASSCF(6,6)	14.21	6.75	0.83	5.05	7.72
HSE [52, 68]	15.8[3]	56.3[4]	–	18.96[5]	15.8[6]
Expt. [88, 90, 26]	5.33	6.4[7]	– (nonzero)	– (nonzero)	– (nonzero)

1. The matrix elements here are expressed in terms of the reduced one-particle matrix elements, $\lambda_z = -i\hbar\langle e||L^{A_2}||e\rangle$ and $\lambda_\perp = -(i/\sqrt{2})\hbar\langle e||L^E||a_1\rangle$.

2. The matrix element is nonzero because ^1E coupled with singlet excited state $^1E'$ through configuration interaction, and $\lambda_z(^3A_2,^1E')$ is symmetry-allowed. This coupling exists in CASSCF solutions, as can be seen in SM Table S9.

3. $\lambda_z(^3E,^3E)$ was calculated by $\langle e_+|H_{\rm soc}|e_+\rangle$ with $|e_+\rangle = \frac{1}{\sqrt{2}}(|e_x\rangle + i\,|e_y\rangle)$ at HSE [52]. The matrix element reduced to 4.8 by a reduction factor.

4. $\lambda_\perp(^1A_1,^3E)$ was calculated by $\langle e_+|H_{\rm soc}|a_1\rangle$ with $|e_+\rangle = \frac{1}{\sqrt{2}}(|e_x\rangle + i\,|e_y\rangle)$ at HSE [52], assuming single-particle picture and that KS wavefunctions constructed ^3E and $^1A_1$ did not differ [26].

5. $\lambda_\perp(^3\widetilde{A}_2,^1\widetilde{E})$ was a parameter estimated by taking $\lambda_\perp(^3\widetilde{A}_2,^1\widetilde{E})/\lambda_z(^3\widetilde{A}_2,^1\widetilde{E}) = 1.2$ for matching with experiment [68].

6. $\lambda_z(^3\widetilde{A}_2,^1\widetilde{E})$ was calculated according to $\langle ^3E|H_{soc}|^3E\rangle = \langle e_+|H_{\rm soc}|e_+\rangle$ [52, 68].

7. The matrix element is estimated by using the ratio $\lambda_\perp(^1A_1,^3E)/\lambda_z(^1A_1,^3E) = 1.2$ [26].

nonzero $\lambda_\perp(^3A_2,^1E)$ at CASSCF does not contradict to the zero value from the group theory prediction. This is because ^1E couples with the higher singlet excited state $^1E'$ under configuration interaction, as also discussed in Refs [20, 18, 1], resulting in $^1\bar{E} = C^1E + (1-C)^1E'$ (C the mixing coefficient). This leads to symmetry-allowed $\lambda_\perp(^3A_2,^1\bar{E})$. In comparison, the SOC matrix elements from TDDFT do not agree with the group theory prediction. The issue is that TDDFT does not describe the multi-reference state correctly, as can be seen in SM Table S10. An apparent error is that the symmetry of the wavefunction is not preserved, as can be seen in SM Fig. S12.

However, experiments show allowed axial ISC for $^3E \rightarrow^1 A_1$ and $^1E \rightarrow^3 A_2$ [88, 4, 205, 89]. This is contradictory to the current group theory prediction that these axial ISC transitions are forbidden by zero $\lambda_z(^3E,^1A_1)$ and $\lambda_z(^3A_2,^1E)$. It implies that an additional mechanism may have modified the symmetry of wavefunctions. Previous studies attribute it to the pseudo JT effect, which particularly couples nondegenerate electronic states through electron-phonon coupling [206, 65, 68, 7, 91],

$$H = \underbrace{\begin{pmatrix} \Lambda & 0 & 0 \\ 0 & 0 & 0 \\ 0 & 0 & 0 \end{pmatrix}}_{H_\mathrm{e}} + \underbrace{\frac{K}{2}(Q_x^2+Q_y^2)}_{H_\mathrm{osc}} + \underbrace{\begin{pmatrix} 0 & FQ_x & FQ_y \\ FQ_x & 0 & 0 \\ FQ_y & 0 & 0 \end{pmatrix}}_{H_\mathrm{PJT}} \tag{5.7}$$

$$F = \langle {}^1A_1 | \frac{\partial V}{\partial Q_x} | {}^1E_x \rangle = \langle {}^1A_1 | \frac{\partial V}{\partial Q_y} | {}^1E_y \rangle \tag{5.8}$$

Here, Λ is the energy gap between $|{}^1A_1\rangle$ and $|{}^1E\rangle$ in the electronic Hamiltonian H_e . K is the elastic vibronic constant in the harmonic oscillator Hamiltonian H_osc. F is the linear vibronic coupling constant in the pseudo JT Hamiltonian H_PJT. $|{}^1A_1\rangle$, $|{}^1E_x\rangle$

and $\left|{}^1E_y\right\rangle$ form the basis of the Hamiltonian H. Q_x and Q_y are the nuclear coordinate transform as x and y, respectively. Under the pseudo JT distortion, ${}^1A_1$ is coupled with ${}^1E$ with the assistance of the JT-active e phonon, denoted as $(A_1+E)\otimes e$. The coupling of electronic states results in the vibronic states ${}^1\widetilde{E}$ and ${}^1\widetilde{A}_1$ as the linear combination of ${}^1E$ and ${}^1A_1$,

$$\begin{aligned}\left|{}^1\widetilde{E}_\pm\right\rangle = \sum_{i=1}^{\infty}\Bigg[& c_i\left|{}^1\bar{E}_\pm\right\rangle\otimes\left|\chi_i^{A_1}\right\rangle + d_i\left|{}^1A_1\right\rangle\otimes\left|\chi_i^{E_\pm}\right\rangle \\ & + f_i\left|{}^1\bar{E}_\pm\right\rangle\otimes\left|\chi_i^{E_\pm}\right\rangle + g_i\left|{}^1\bar{E}_\mp\right\rangle\otimes\left|\chi_i^{A_2}\right\rangle\Bigg]\end{aligned} \tag{5.9}$$

$$\begin{aligned}\left|{}^1\widetilde{A}_1\right\rangle = \sum_{i=1}^{\infty}\Bigg[& c_i'\left|{}^1A_1\right\rangle\otimes\left|\chi_i^{A_1}\right\rangle \\ & + \frac{d_i'}{\sqrt{2}}\Big(\left|{}^1\bar{E}_+\right\rangle\otimes\left|\chi_i^{E_-}\right\rangle + \left|{}^1\bar{E}_-\right\rangle\otimes\left|\chi_i^{E_+}\right\rangle\Big)\Bigg]\end{aligned} \tag{5.10}$$

where $\left|\chi_i^{\Gamma}\right\rangle$ is the i-th phonon wavefunction transforming as irreducible representation Γ, and c_i, d_i, f_i, g_i, c_i' and d_i' are the amplitude of vibronic states. The states coupling give rise to a significant change in the SOC matrix elements as listed below:

$$\lambda_z({}^1\widetilde{A}_1,{}^3\widetilde{E}) = d'_{eff}\left\langle{}^1\bar{E}\middle|H_{\rm soc}\middle|{}^3E\right\rangle_z \tag{5.11}$$

$$\lambda_\perp({}^1\widetilde{A}_1,{}^3\widetilde{E}) = c'_{eff}\left\langle{}^1A_1\middle|H_{\rm soc}\middle|{}^3E\right\rangle_\perp + d'_{eff}\left\langle{}^1\bar{E}\middle|H_{\rm soc}\middle|{}^3E\right\rangle_\perp \tag{5.12}$$

$$\lambda_z({}^3\widetilde{A}_2,{}^1\widetilde{E}) = d_{eff}\left\langle{}^3A_2\middle|H_{\rm soc}\middle|{}^1A_1\right\rangle_z \tag{5.13}$$

$$\lambda_\perp({}^3\widetilde{A}_2,{}^1\widetilde{E}) = (c_{eff}+f_{eff})\left\langle{}^3A_2\middle|H_{\rm soc}\middle|{}^1\bar{E}\right\rangle_\perp \tag{5.14}$$

where c'_{eff}, d'_{eff}, c_{eff}, d_{eff}, f_{eff} are the normalized effective state mixing coefficients, e.g. $|c'_{eff}|^2+|d'_{eff}|^2=1$.

We complete the derivation for all effective SOC matrix elements of the NV center, in complement to Ref. [68] which only provides $\lambda_{\perp/z}({}^3\widetilde{A}_2,{}^1\widetilde{E})$. The derivation

details can be found in SM Sec. IVA. The pseudo JT effect results in the finite values of $\lambda_z(^1\widetilde{A}_1,^3\widetilde{E})$ and $\lambda_z(^3\widetilde{A}_2,^1\widetilde{E})$, and a modification to $\lambda_\perp(^1\widetilde{A}_1,^3\widetilde{E})$ and $\lambda_\perp(^3\widetilde{A}_2,^1\widetilde{E})$, as can be seen in Table 5.2. The resulting effective SOC shows much better agreement with experiments, in contrast to other calculations by DFT or TDDFT. As will be shown in Sec. 5.6, the nonzero SOC matrix elements lead to allowed ISC, consistent with experimental observations.

Finally, another approach based on the Taylor expansion of SOC matrix element in terms of coupling with phonon vibration is commonly used for the study of ISC in molecules [63, 64]. We examine this approach by computing its first-order derivative of SOC with respect to nuclear coordinate change. The result indicates that this approach does not apply to the NV center under the 1D effective phonon approximation. More details can be seen in the SM Sec. IVC.

5.6 Electron-Phonon Coupling and ISC

The ISC rate between electronic states with different spin multiplicities can be calculated as

$$k_{\mathrm{ISC}} = \frac{2\pi}{\hbar} g \sum_{n,m} p_{in} |\langle fm|H_{\mathrm{soc}}|in\rangle|^2 \delta(E_{fm} - E_{in}). \tag{5.15}$$

Here, we make the 1D effective phonon approximation [66, 67, 48] for the ISC rate. Compared to the full-phonon method used in Ref. [52, 68], an advantage of this 1D effective phonon method is that it enables the use of different values for the phonon energy of initial state ($\hbar\omega_i$) and the one of final state ($\hbar\omega_f$), and enables finite temper-

Table 5.3: Electron-phonon coupling and rates of ISC ${}^3\widetilde{E} \rightarrow {}^1\widetilde{A}_1$ and ${}^1\widetilde{E} \rightarrow {}^3\widetilde{A}_2$ at 300 K. The degree of geometry degeneracy g is specified as 3. ΔQ is the nuclear coordinate change between the initial and final states. $\hbar\omega_i$ and $\hbar\omega_f$ represent the phonon energy of the initial and final states, respectively. S_f denotes the 1D Huang-Rhys (HR) factor of the final state, which is a measure of e-ph coupling strength. $\widetilde{X}_{if}$ is the phonon term. In these calculations, the JT-distorted geometries of C_s symmetry are used for the initial states ${}^3\widetilde{E}$ and ${}^1\widetilde{E}$, and the geometry of C_{3v} symmetry of ${}^3\widetilde{A}_2$ is used for the final states ${}^1\widetilde{A}_1$ and ${}^3\widetilde{A}_2$, considering the fact that the geometry and phonon modes of ${}^1\widetilde{A}_1$ are similar to those of ${}^3\widetilde{A}_2$ [7, 20].

	Transition	ΔQ (amu$^{1/2}$Å)	$\hbar\omega_i$ (meV)	$\hbar\omega_f$ (meV)
Expt.	${}^3\widetilde{E} \rightarrow {}^1\widetilde{A}_1$	0.64[1]	–	71 [20]
Calc.		0.65	73.74	67.75
Calc. [52, 68]		–	77.6	66 – 91.8
Expt.	${}^1\widetilde{E} \rightarrow {}^3\widetilde{A}_2$	0.34[1]	–	64 [20]
Calc. ($\widetilde{X}_{if}$ at HSE)		0.23	75.85	71.04
Calc. ($\widetilde{X}_{if}$ at spin-flip TDDFT)		0.41 [7]	48.81	69.88
Calc. [68]		–	–	66

	Transition	S_f (eV^{-1})	$\widetilde{X}_{if}$ (MHz)	$k_\perp$ (MHz)	k_z
Expt.		3.49 [20]	–	24.3 [88]	< 0.62 [88]
Calc.	$^3\widetilde{E} \rightarrow ^1\widetilde{A}_1$	3.38	1.34	29.86	0.46
Calc. [52, 68]		2.61[2]	–	243	–
Expt.		0.9[3] [20]	–	2.61 [89]	3.0 [89]
Calc. ($\widetilde{X}_{if}$ at HSE)	$^1\widetilde{E} \rightarrow ^3\widetilde{A}_2$	0.45	1.17×10^{-4}	1.47×10^{-3}	3.47×10^{-3}
Calc. ($\widetilde{X}_{if}$ at spin-flip TDDFT)		1.46	0.20	2.49	5.89
Calc. [68]		–	0.90[4]	4.95[4]	

1. ΔQ is estimated by the Huang-Rhys factor and phonon energy, $S = \omega \Delta Q^2 / 2\hbar$, under one-dimensional effective phonon approximation. 2. $S = 2.61$ when approximating $e_x e_x$ singlet determinant for $^1\widetilde{A}_1$, and $S = 3.11$ when using $^3A_2$ geometry for $^1\widetilde{A}_1$.

3. This HR factor is for $^1\widetilde{A}_1 \rightarrow ^1\widetilde{E}$. Considering the similarity of geometry and potential surfaces between $^3\widetilde{A}_2$ and $^1\widetilde{A}_1$, we put it here for comparison with our calculations.

4. The corresponding SOC can be found in Table 5.2.

ature occupation for both states. As already discussed in Sec. 5.5 and SM Sec. IVA, the SOC matrix element $\langle fm|H_{\text{soc}}|in\rangle$ that couples the initial vibronic state $|in\rangle$ and final vibronic state $|fm\rangle$ can be separated into the effective SOC and effective phonon overlap. Therefore, the ISC rate equation is expressed as

$$k_{\text{ISC}} = \frac{2\pi}{\hbar} g\lambda^2 \widetilde{X}_{if} \tag{5.16}$$

$$\lambda = \langle \psi_f | H_{\text{soc}} | \psi_i \rangle \tag{5.17}$$

$$\widetilde{X}_{if} = \sum_{n,m} p_{in}(T) |\langle \phi_m | \phi_n \rangle|^2 \delta(m\hbar\omega_f - n\hbar\omega_i + \Delta E_{if}) \tag{5.18}$$

where g is the degree of degeneracy on equivalent structural configuration, λ is the effective SOC matrix element, and $\widetilde{X}_{if}$ is the temperature-dependent phonon term representing the phonon contribution. $|\psi\rangle$ is the linear combination of possible electronic states after considering pseudo JT effect, and $|\phi\rangle$ denotes the phonon wavefunction under the harmonic oscillator approximation. λ has been discussed in detail in Sec. 5.5. Therefore, our primary focus in this section will be on the phonon term $\widetilde{X}_{if}$. We will show that dynamical JT effect is important to include for electron-phonon coupling in the nonradiative intersystem-crossing transitions. Otherwise the transition rates can be order of magnitude smaller.

In Fig. 5.2(a), we show the lower branch adiabatic potential energy surface (APES) of ^1E by fitting the Hamiltonian in Eq. (5.19) [65] to the calculated potential

energy curves,

$$H = \underbrace{\frac{K}{2}(Q_x^2 + Q_y^2)}_{H_{\mathrm{osc}}} + \underbrace{F(Q_x\sigma_z - Q_y\sigma_x) + G[(Q_x^2 - Q_y^2)\sigma_z + 2Q_xQ_y\sigma_x]}_{H_{\mathrm{DJT}}}. \tag{5.19}$$

Here K, F and G are elastic, linear and quadratic vibronic constants, respectively. σ_z and σ_x are Pauli's matrices. Q_x and Q_y denote nuclear coordinate transform as x and y, respectively. The APES appears as a tricorn Mexican hat under the $E \otimes e$ JT distortion, which splits the doubly degenerate electronic states via the coupling with e phonon. The symmetry of the geometry is C_{3v} at the conical intersection, and C_s at the three equivalent geometries of energy minima. The three-fold degeneracy of the geometry indicates that g should be 3 in the ISC calculation. We find that the three energy minima are separated by a minor energy barrier ($\delta = 2F^2|G|/(K^2 - 4G^2)$) at $\sim$30 meV. Because of the small energy barrier, the system of the vibronic ground state may be delocalized and tend to undergo a hindered internal rotation among the energy minima like ^3E [207], which is the so-called "dynamical JT effect".

The dynamical JT effect distorts the geometries from C_{3v} to lower symmetry. Then the geometries of C_s symmetry become the starting points for the system to relax from the initial states $^1\widetilde{E}$ ($^3\widetilde{E}$) to the final state $^3\widetilde{A}_2$ ($^1\widetilde{A}_1$) through ISC. The nonradiative process is depicted in Fig. 5.2(b), the configuration coordinate diagram of $^1\widetilde{E} \rightarrow^3 \widetilde{A}_2$ as an example. In the nonradiative process, the JT-active e phonon breaks the symmetry of ^1E and alters the potential energy curve of ^1E. This results in a small energy barrier between the initial and final electronic states, which is easy

to overcome. Finally, the small energy barrier consequences in the fast nonradiative relaxation [208, 67]. In contrast, if not considering the dynamical JT effect, only the totally symmetric a_1 type phonon would participate in the ISC, and the transition rate would be orders of magnitude smaller due to the large energy barrier between the initial and final electronic states. The dramatic difference between C_{3v}-symmetry geometry and C_s-symmetry geometry as starting point indicates that dynamical JT effect plays an essential role in the nonradiative processes.

By listing the ISC calculation details in Table 5.3, we first find $k_{\perp}(^3\widetilde{E} \rightarrow^1 \widetilde{A}_1)$ shows good agreement with experimental values. And $k_z(^3\widetilde{E} \rightarrow^1 \widetilde{A}_1)$ becomes allowed in the first order due to the finite SOC by the pseudo JT effect, consistent with the nonzero ISC in experiment [88, 4, 205, 89]. On the other hand, the $k_{\perp/z}(^1\widetilde{E} \rightarrow^3 \widetilde{A}_2)$ ISC rates are three orders of magnitude smaller than experiment, but the ratio $k_z(^1\widetilde{E} \rightarrow^3 \widetilde{A}_2)/k_{\perp}(^1\widetilde{E} \rightarrow^3 \widetilde{A}_2) = 2.37$ is similar to the experimental value 1.15±0.05 or 1.6±0.4 [89] (the ratio between k_z and $k_{\perp}$ is more critical for spin polarization). The underestimation of the rates can be originated from the underestimated electron-phonon coupling related to $\widetilde{X}_{if}$, the phonon contribution to ISC. Recent spin-flip TDDFT calculation [7] predicts accurate PL lineshape for the $^1E \rightarrow^1 A_1$ transition, which indicates accurate electron-phonon coupling description despite the lack of double excitation. We therefore use spin-flip TDDFT calculation to correct the phonon term $\widetilde{X}_{if}$ of this transition. It can be found that the phonon term is underestimated by orders of magnitude at HSE compared to spin-flip TDDFT.

In fact, the underestimation of electron-phonon coupling can be traced back

to the JT effects, including the dynamical JT effect and pseudo JT effect. Our HSE calculation captures the dynamical JT effect, giving $\Delta Q = 0.23$ amu$^{1/2}$Å. This value is similar to the value 0.26 amu$^{1/2}$Å obtained with spin-flip TDDFT [7]. However, due to the mean-field approximation and the absence of spin-flip process in HSE, the pseudo JT effect is relatively weak in the ^1E state. This results in the lack of the additional distortion of ^1E by the pseudo JT effect in our HSE calculation. If using spin-flip TDDFT, ΔQ is enhanced to 0.42 amu$^{1/2}$Å, which is closer to the experiment 0.34 amu$^{1/2}$Å that is estimated by the experiment phonon energy and Huang-Rhys factor. With the spin-flip TDDFT data, we obtain $k_{\perp/z}(^1\widetilde{E} \rightarrow^3 \widetilde{A}_2)$ in good agreement with the experimental observation, as listed in Table 5.3.

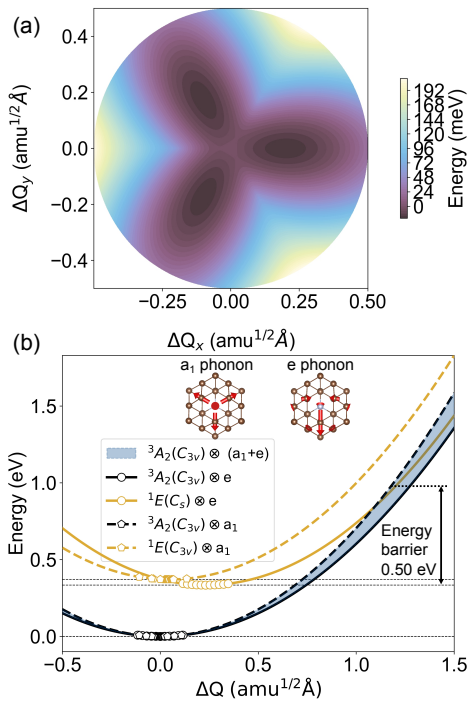

Figure 5.2: (a) Adiabatic potential energy surface (APES) of ^1E of the NV center with the dynamical JT effect. ΔQ denotes the nuclear coordinate change, the mass weighted total nuclear displacement. x and y represent the displacement directions due to the degenerate e_x and e_y phonons, respectively. (b) The configuration coordinate diagram for the $^1\widetilde{E} \rightarrow ^3\widetilde{A}_2$ ISC. The ISC starts from $^1\widetilde{E}$, whose geometry at local energy minima can have C_{3v} and C_s symmetries, and ends at $^3\widetilde{A}_2$ of C_{3v} symmetry. The solid line represents the potential energy curve created by electron coupling with e phonon, and the dashed line represents that due to electron coupling with a_1 phonon. The shaded area between the solid and dashed lines includes electron coupling with the mix of a_1 and e phonons. The energy barrier is 0.50 eV. The inset is the visualization of effective a_1 and e phonons, whose arrows represent the vibration amplitude larger than the threshold 0.005 amu$^{1/2}$Å and 0.03 amu$^{1/2}$Å, respectively.

5.7 Internal Conversion

The IC represents spin-conserving phonon-assisted nonradiative transition. Under the static coupling approximation and one-dimensional effective phonon approximation, the equation of nonradiative transition rates is expressed as [66, 67]

$$k_{\mathrm{IC}} = \frac{2\pi}{\hbar} g |W_{if}|^2 X_{if}(T) \tag{5.20}$$

$$W_{if} = (\varepsilon_f - \varepsilon_i) \left\langle \psi_i(\mathbf{r}, \mathbf{R}) \middle| \frac{\partial \psi_f(\mathbf{r}, \mathbf{R})}{\partial Q} \right\rangle \Big|_{\mathbf{R}=\mathbf{R_a}} \tag{5.21}$$

$$\begin{aligned} X_{if} = \sum_{n,m} p_{in}(T) \Big| \langle \phi_{fm}(\mathbf{R}) | Q - Q_a | \phi_{in}(\mathbf{R}) \rangle \Big|^2 \\ \times \delta(m\hbar\omega_f - n\hbar\omega_i + \Delta E_{if}). \end{aligned} \tag{5.22}$$

This equation is similar to that of ISC except that the electronic term W_{if} replaces SOC λ with single particle wavefunctions ψ_i to approximate many-electron wavefunctions, and that the phonon term becomes X_{if} with additional expectation values of nuclear coordinate change $(Q - Q_a)$.

From our calculations reported in Table 5.4, $^3E \rightarrow ^3A_2$ shows long IC lifetime (1.20 s) because a great number of emitted phonons is needed to fulfill the energy conservation between ^3E and $^3A_2$. Therefore, this spin-conserving transition process is dominated by the radiative recombination. On the other hand, the $^1A_1 \rightarrow ^1E$ transition is likely to be nonradiative-dominant according to past experiments [201], but does not appear in the HSE calculation where we obtain long IC lifetime. This can be a consequence of inaccurate description of the electron-phonon coupling of multi-reference states $^1A_1$ and ^1E, currently calculated at DFT.

Similar to ISC, we also correct the phonon term X_{if} of ${}^1E \rightarrow {}^1A_1$ transition, which is the primarily underestimated component, by using the potential energy surfaces of ${}^1A_1$ and ${}^1E$ at spin-flip TDDFT@DDH. The improved electron-phonon coupling enhances X_{if} and the IC rate by several orders of magnitude. The enhanced IC rate is in good agreement with the experimental observation [200]. More details can be found in SM Sec. VD.

Without correcting the IC rate, we find that the PL rate ($k_{\mathrm{PL}} = k_{\mathrm{R}} + k_{\mathrm{IC}}$) of ${}^1A_1 \rightarrow {}^1E$ is underestimated, but still allows us to obtain qualitatively correct ODMR contrast. When we consider the corrected $k_{\mathrm{IC}}({}^1\widetilde{A}_1 \rightarrow {}^1\widetilde{E})$ by using spin-flip TDDFT data, this transition becomes dominant by nonradiative recombination, and ODMR contrast is in better agreement with experiments. More details can be seen in Sec. 5.8.

5.8 Angle-Dependent and Magnetic-Field Dependent ODMR

The rates of radiative recombination, internal conversion and intersystem crossing obtained from the calculations above set the prerequisite for the simulation of ODMR contrast (spin-dependent PL contrast). Additionally, the ZFS of triplet ground state and excited state are entered to account for their spin sublevels. Our calculated ZFS of ${}^3A_2$ is $D = 3.03$ GHz by the first-principles method explained in SM Sec. VIA, similar to the experimental value $D = 2.87$ GHz [48, 4, 209]. We currently use the experimental value of $D = 1.42$ GHz for excited triplet state ${}^3E$ [209] given methods for accurate prediction of excited state ZFS remain to be developed. The optical saturation parameter β and Rabi frequency k_{MW} are entered as parameters into the model, and their

Table 5.4: Calculation details of internal conversion of the NV center at 300 K. The degree of geometry degeneracy g is specified as 3. The ZPL is the energy change in the complete nonradiative process. ΔQ denotes the nuclear coordinate change between the initial and final states. $S_f = \omega \Delta Q^2 / 2\hbar$ is the phonon energy of the final state. S_f denotes the Huang-Rhys factor under 1D effective phonon approximation. W_{if} and X_{if} are the electronic and phonon terms, respectively.

Transition	ZPL (eV)	ΔQ (amu$^{1/2}$Å)	$\hbar\omega_f$ (meV)	S_f
$^3E \rightarrow ^3A_2$	1.97	0.65	67.75	3.38
$^1A_1 \rightarrow ^1E$ (X_{if} at HSE)	1.13	0.24	75.69	
$^1\widetilde{A}_1 \rightarrow ^1\widetilde{E}$ (X_{if} at spin-flip TDDFT)	1.13	0.42 [7]	87.33	1.82
$^1A_1 \rightarrow ^1E$ (Expt.)	1.19	0.31-0.35	–	0.9 [20]

Transition	W_{if} (eV/(amu$^{1/2}$Å))	X_{if} (amu·Å^2/eV)	τ_{IC}	k_{IC} (MHz)
$^3E \rightarrow ^3A_2$	16.59	1.06×10^{-19}	1.20 s	8.35×10^{-7}
$^1A_1 \rightarrow ^1E$ (X_{if} at HSE)	1.05×10^{-2}	4.28×10^{-11}	7.35 ms	1.36×10^{-4}
$^1\widetilde{A}_1 \rightarrow ^1\widetilde{E}$ (X_{if} at spin-flip TDDFT)	1.05×10^{-2}	1.52×10^{-4}	2.07 ns	4.82×10^2
$^1A_1 \rightarrow ^1E$ (Expt.)	–	–	0.9 ns[2] [200]	1.11×10^3 [2] [200]

1. ΔQ is estimated by the Huang-Rhys factor and phonon energy in the range 63-76.4 meV, $S = \omega \Delta Q^2 / 2\hbar$, under one-dimensional effective phonon approximation.

2. These are the PL lifetime and rate of $^1A_1$. Since the transition is claimed to be dominated by nonradiative processes [201], they are approximately IC lifetime and rate.

values are selected within the experimental range [69]. cw-ODMR, which is evaluated at the steady state when the populations no longer change as a function of time, is independent on the initial spin state. We then apply an oscillatory microwave field to drive the population between $|-1\rangle$ and $|0\rangle$ spin sublevels in $^3A_2$.

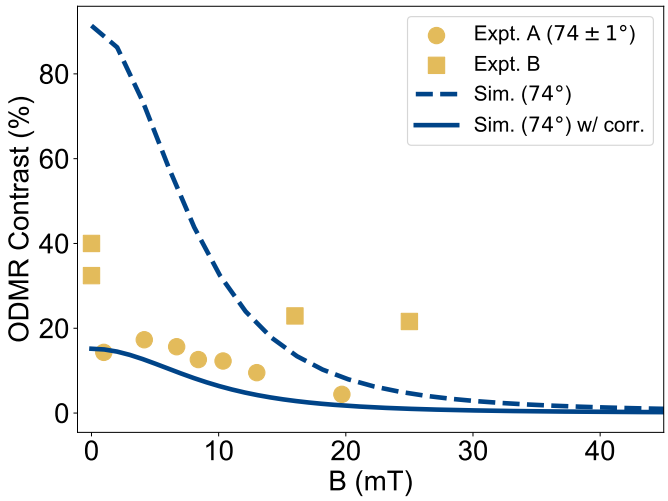

Figure 5.3: ODMR contrast from the simulation using the calculated rates compared with Expt. A [4] and Expt. B [6]. The angle refers to the angle of magnetic field with respect to the NV axis along [111]. Expt. A shows an angle of $74 \pm 1°$. The angle of magnetic field in Expt. B is unknown. The dashed blue curve is the ODMR simulation using all the rates from calculations using HSE phonon. The solid blue curve is the simulation with calculated rates using the phonon term calculated with spin-flip TDDFT as discussed in Sec. 5.6 and Sec. 5.7.

Using the input from our first-principles calculations, we plot the simulated ODMR contrast against magnetic field in comparison with the experiments [4, 6] in Fig. 5.3. The simulated ODMR contrast decreases with increasing the magnetic field,

consistent with the trend shown by the experiments (yellow dots and squares). Such decrease of ODMR contrast is originated from the mixing of the spin sublevels under magnetic field, as can be seen in SM Fig. S21. The mixing of the spin sublevels leads to smaller contrast of the axial and nonaxial ISC rates, especially $k_{\perp/z}({}^3\widetilde{E} \rightarrow^1 \widetilde{A}_1)$. Consequently, the spin polarization is less pronounced, manifesting as reduced ODMR contrast.

Our simulated ODMR contrast is overestimated compared to experiments. This is because of the underestimated ISC rates $k_{\perp/z}({}^1\widetilde{E} \rightarrow^3 \widetilde{A}_2)$ and IC rate $k_{\mathrm{IC}}({}^1\widetilde{A}_1 \rightarrow^1 \widetilde{E})$, with detailed explanation in earlier sections. Under continuous optical excitation, the system is easier to populate ${}^1\widetilde{E}$ and ${}^1\widetilde{A}_1$ through the channel ${}^3\widetilde{E}^{\pm 1} \rightarrow^1 \widetilde{A}_1 \rightarrow^1 \widetilde{E}$ when there is an applied microwave field driving populations from spin sublevel $|0\rangle$ to $|-1\rangle$. When $k_{\perp/z}({}^1\widetilde{E} \rightarrow^3 \widetilde{A}_2)$ and $k_{\mathrm{IC}}({}^1\widetilde{A}_1 \rightarrow^1 \widetilde{E})$ are underestimated, the population accumulates at the singlet states ${}^1\widetilde{A}_1$ and ${}^1\widetilde{E}$. This results in the enhanced PL intensity contrast between the two situations, namely in the presence and absence of a microwave field. With the calculated rates using spin-flip TDDFT data discussed in Sec. 5.7 and Sec. 5.6, we obtain ODMR contrast slightly underestimated but in better agreement with the experiments.

Finally, we study the ODMR contrast dependence on the magnetic field direction. How spin sublevels mix depends on the magnetic field direction with respect to the NV axis, which is quantified by polar angle θ_B. In Figs. 5.4(a) and 5.4(b), we show both the angle dependency and magnetic-field dependency of normalized PL intensity and ODMR contrast. The simulated normalized PL intensity at $\theta_B = 1^\circ$ exhibits sim-

ilar sharp reduction character as the experiment [8]. This reduction shares the same origin as the ODMR, as elaborated below. When the magnetic field is perfectly aligned with the NV axis, the ODMR contrast is maximal since there is no spin mixing. When magnetic field is slightly misaligned to the NV axis, we can see two positions of sharp reductions of the ODMR contrast at $B = \sim$50 mT and $\sim$100 mT, which are related to the ZFS in ^3E and the one in $^3A_2$, respectively. This is resulted from the excited state level-anticrossing (ESLAC) and the ground-state level-anticrossing (GSLAC). As can be seen in SM Fig. S21 that shows the extend to which the spin sublevels mix, there is strong spin mixing of $|0\rangle$ to $|-1\rangle$ at ESLAC and GSLAC. When the magnetic field is more misaligned with the NV axis, i.e. $10^\circ < \theta_B < 90^\circ$, the ODMR contrast becomes highly sensitive to the magnetic field, nearly vanishing after the ESLAC. In addition, we find that the GSLAC and ESLAC of the NV center gradually disappear with increasing magnetic field after $B > 25$ mT. The vanishing GSLAC and ESLAC can also be reflected by the ODMR frequency plots in SM Fig. S22. In general, this result suggests our theory can reliably predict the ODMR dependence on magnetic field direction, which is useful for setting up experiments. Considering the complexity of the computation process, it is beneficial to outline the procedures for ODMR simulation from first principles. Fig. 5.6 illustrates the overall workflow.

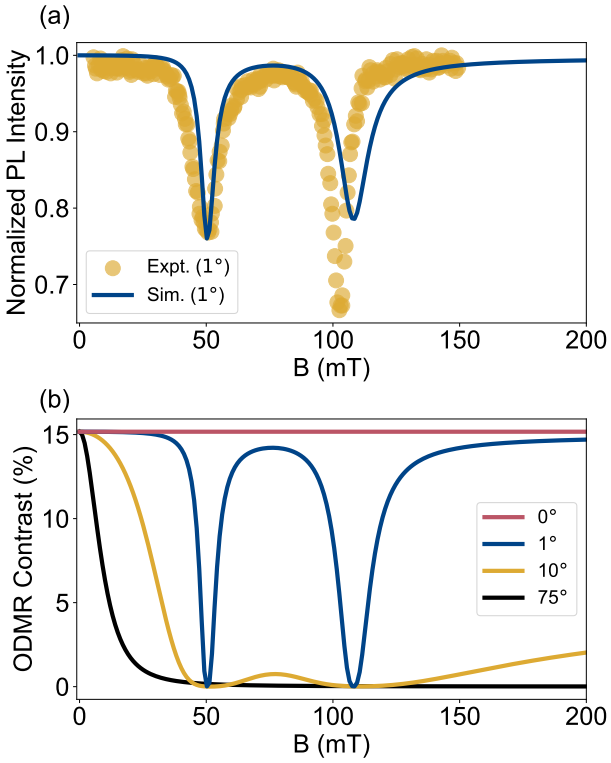

Figure 5.4: (a) Normalized PL intensity simulated using first-principles rates with spin-flip TDDFT data [7] against the applied magnetic field **B**, with a direction of 1° relative to the NV axis. The experiment for comparison is from Ref. [8]. (b) ODMR contrast as a function of magnetic field with an angle relative to the NV axis [111], which is the spin quantization axis at $B = 0$. The strong magnetic field dependency is originated from spin mixing. In both the normalized PL intensity and ODMR contrast, the sharp reduction at $B = \sim$50 and $\sim$100 mT corresponds to level-anticrossing (LAC) due to ZFS and Zeeman effect in the excited state ^3E and ground state $^3A_2$, respectively. At $\theta_B = 0°$, the ODMR contrast is optimized with no spin mixing.

5.9 Optimization for ODMR Contrast

The optimization of ODMR contrast is a critical step experimentally, as we show next can be realized through tuning optical saturation parameter β (related to excitation efficiency βk_R) and tuning Rabi frequency k_{MW} [69]. Such parameters are cumbersome to search for experimentally but our theory can be much more efficient.

Considering that the $k_{\perp/z}({}^1\widetilde{E} \rightarrow^3 \widetilde{A}_2)$ rates largely vary across different experiments [89, 4], and that the optimization behavior of the ODMR contrast is sensitive to these variations, it is essential to understand the relationship between the ISC rate and the optimization of ODMR. For clarity, we use the scale factor k/k_0 to represent the variations of $k_{\perp/z}({}^1\widetilde{E} \rightarrow^3 \widetilde{A}_2)$, and k_0 denotes the $k_{\perp/z}({}^1\widetilde{E} \rightarrow^3 \widetilde{A}_2)$ rates from our calculation in Table 5.3.

Fig. 5.5(a) shows that the ODMR is optimized at $\beta < 0.01$ when the $k_{\perp/z}({}^1\widetilde{E} \rightarrow^3 \widetilde{A}_2)$ rates are overestimated compared to the experimental observation. If the $k_{\perp/z}({}^1\widetilde{E} \rightarrow^3 \widetilde{A}_2)$ rates are close to or below experimental values, the ODMR is optimized when the optical excitation power is ~ 0.1 of the saturation. Despite variations in the $k_{\perp/z}({}^1\widetilde{E} \rightarrow^3 \widetilde{A}_2)$ rates, the part in $\beta > 0.1$ is consistent with the experiment [69]. However, the high sensitivity of the ODMR optimization to β underscores the importance of obtaining accurate rates for the correct prediction.

Fig. 5.5(b) indicates that the ODMR contrast can reach its maximum at $k_{\mathrm{MW}} \approx 5$ MHz. The variations in the $k_{\perp/z}({}^1\widetilde{E} \rightarrow^3 \widetilde{A}_2)$ rates primarily affect the magnitude of the ODMR contrast with respect to k_{MW}. When the populations of the spin sublevels are driven by the Rabi oscillation, the nonaxial ISC ${}^3\widetilde{E} \rightarrow^1 \widetilde{A}_1$ becomes the

preferential path for the relaxation from ${}^3\widetilde{E}$. Thus, the upper bound of the ODMR contrast in this case is limited by the contrast between $k_\perp({}^3\widetilde{E} \rightarrow {}^1\widetilde{A}_1)$ and $k_z({}^3\widetilde{E} \rightarrow {}^1\widetilde{A}_1)$.

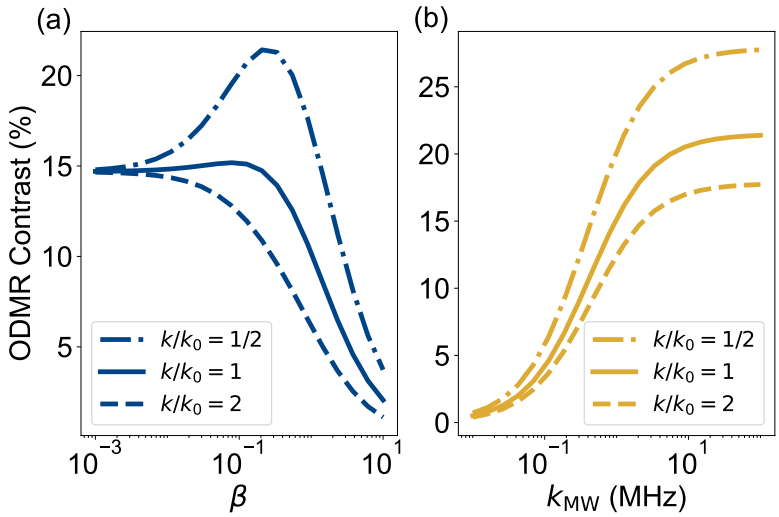

Figure 5.5: ODMR contrast can be optimized by tuning (a) optical saturation parameter β and (b) Rabi frequency k_{MW}. The ODMR is simulated at $B = 0$ and $\theta_B = 0$. The corrected rates by using the spin-flip TDDFT data are used for the ODMR simulation to show the optimization of ODMR contrast. k_0 denotes the $k_{\perp/z}({}^1\widetilde{E} \rightarrow {}^3\widetilde{A}_2)$ rates from our calculation. With maintaining the ratio of $k_\perp({}^1\widetilde{E} \rightarrow {}^3\widetilde{A}_2)/k_z({}^1\widetilde{E} \rightarrow {}^3\widetilde{A}_2)$, the scaled version, k, is used to illustrate how the optimization behavior of ODMR contrast changes with the variation in the $k_{\perp/z}({}^1\widetilde{E} \rightarrow {}^3\widetilde{A}_2)$ rates.

5.10 Conclusion

In conclusion, we have developed general first-principles computational platform for spin-dependent PL contrast and cw-ODMR, for triplet and singlet spin defects

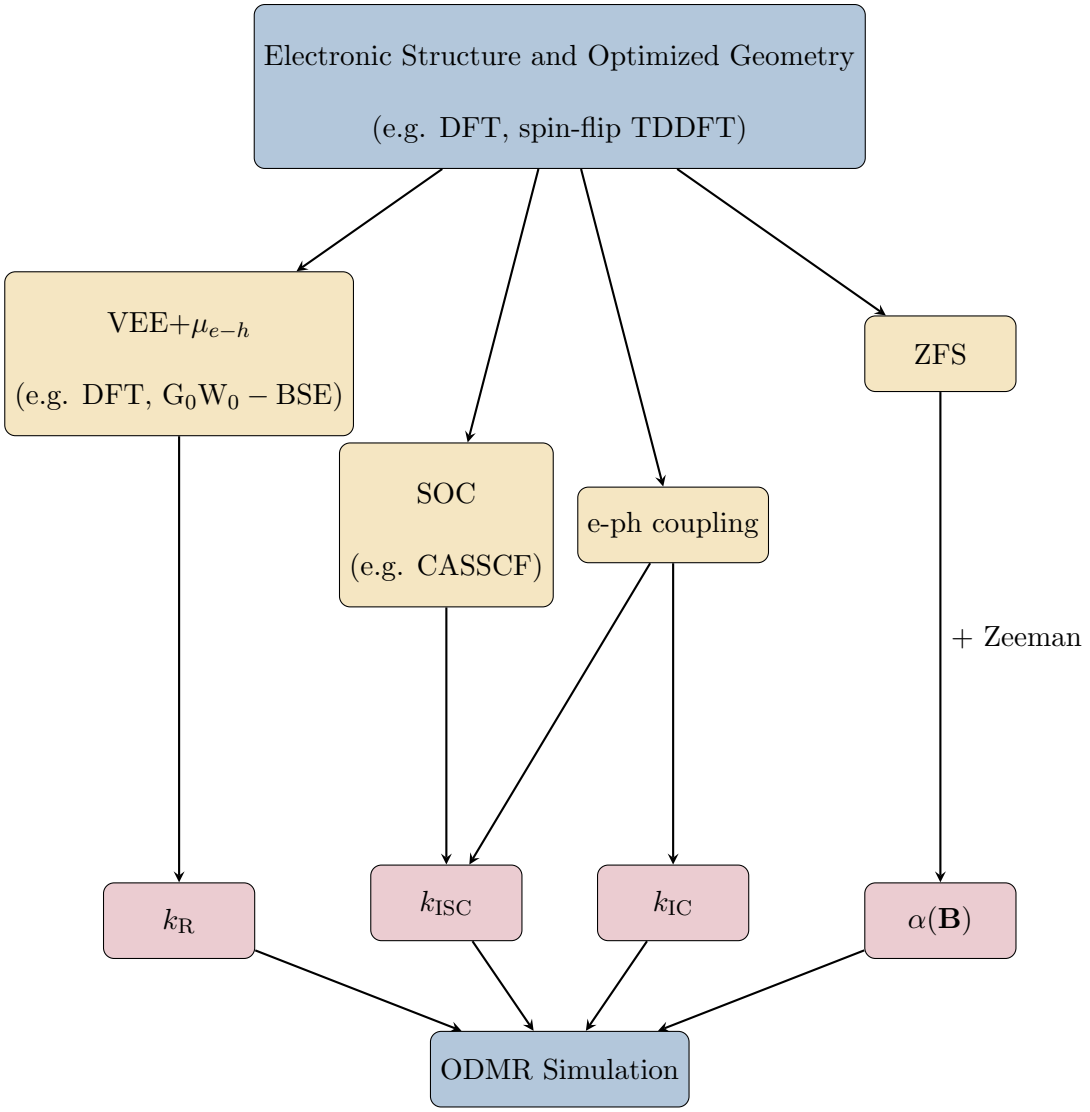

Figure 5.6: Workflow of ODMR simulation from first-principles. VEE stands for vertical excitation energy. μ_{e-h} represents optical dipole moment. e-ph coupling represents electron-phonon coupling. k represents the rates which can be obtained using the Fermi's golden rule. $\alpha(\mathbf{B})$ represents the mixing coefficient in Eq. (5.3).

in solids. We solved the kinetic master equation to obtain steady-state excited-state occupations. These occupations are determined by excited-state kinetic rates, which

we implemented fully from first-principles. We then validated our implementation by comparing with the experimental data on NV center in diamond. We show our first-principles computational platform for ODMR is fully general and accurate, as long as we have reliable electronic structure as inputs (including state energies, wavefunction, and defect geometry).

The ODMR simulation from first principles requires calculations of spin sublevels due to ZFS, and the rates of all possible transitions i.e. radiative recombination, ISC (spin-flip nonradiative recombination) and IC (spin-conserving nonradiative recombination). In this work we examined the theory and implementation of ISC in great detail, emphasizing accurate description of both spin-orbit coupling and electron-phonon coupling. In particular, by using NV center in diamond as prototypical example, we identify the coupling of ^1E and $^1E'$ due to the configuration interaction from CASSCF calculation and group theory, and show the corresponding effect on SOC matrix elements. We complete the derivation and calculation for the effective SOC matrix elements of the NV center considering the pseudo JT effect. As a result, we unequivocally clarify the experimental observation of the axial ISC $^3\widetilde{E} \rightarrow^1 \widetilde{A}_1$, which was thought to be forbidden in the first order by symmetry. Importantly, we show the dynamical JT effect in the degenerate states ^3E and ^1E significantly enhances the nonradiative recombination by reducing the potential energy barrier. The results showcase the rich physics underlying the entire excitation and relaxation cycle.

Finally, we simulate cw-ODMR of the NV center from first-principles calculations. Through our calculations, we attribute the dip in ODMR contrast at $B = 0$

to the non-zero rhombic ZFS parameter E, indicating symmetry breaking of the NV center in the experiment. We provide the optimization strategies for ODMR contrast with respect to magnetic field, optical saturation parameter and Rabi frequency. These are found to be informative especially for the range of conditions difficult to reach experimentally. This shows the critical role of our computational technique can play in guiding experiments, which also enables deeper understanding to the spin polarization of spin defects.

The study emphasizes the importance of accounting for the multi-reference character of the electronic states, SOC and electron-phonon coupling for spin defects. It unveils the challenge that there is a need of developing advanced first-principles theory for accurate prediction of SOC and electron-phonon coupling in solid-state spin defects. On the other hand, the atomic structure of many spin defects has not been determined yet, such as ST1 defect in diamond and quantum defects in two-dimensional wide-band gap semiconductors. Our developed computational platform can be essential for identifying existing spin defects, and potentially applied to the design of new solid-state spin defect important for nanophotonics and quantum information science.

Chapter 6

Spin Relaxation and Dephasing in Perovskites

This chapter starts to present the spin of carriers in solids, in particular perovskites. In contrast to spin of solid-state defects in Chapter 4 and Chapter 5, the spin of carriers is delocalized, the spin dynamics can be related to the properties of carrier transport, and is momentum-dependent under magnetic field. To understand how spin relax and dephase in perovskites, a group of materials possessing strong SOC and highly tunable symmetry, the first-principles study is performed with the application of the advanced approach of first-principle density-matrix dynamics. The upper bound of intrinsic spin lifetime is provided by this study. Important mechanisms are clarified for spin dynamics in various perovskites across a temperature range from 4 K to 300 K and a range of external magnetic fields.

6.1 Introduction

The field of semiconductor spintronics aims to achieve the next generation of low-power electronics by making use of the spin degree of freedom. Several classes of materials for spintronic applications have been discovered, investigated and engineered in the past decade [210, 30, 211, 212, 213]. Efficient spin generation and manipulation require a large spin-orbit coupling (SOC), with GaAs a prototypical system, whereas long spin lifetimes (τ_s) is mostly found in weak SOC materials, such as graphene and diamond. Materials with large SOC as well as long τ_s are ideal for spintronic applications but rare, presenting a unique opportunity for the discovery of new materials.

Halide perovskites, known as prominent photovoltaic [214] and light-emitting materials [215] with remarkable optoelectronic properties, have recently attracted interests also for spin-optoelectronic properties [33, 10, 216, 9, 34, 217], since these materials exhibit both long lifetimes and large SOC (due to heavy elements). Compared to conventional spintronic materials, the optical accessibility for spin generation and detection of halide perovskites opens up a new avenue for spin-optoelectronics applications. Additionally, with highly tunable symmetry through the organic-inorganic framework, large Rashba splitting and high spin polarization have been realized at room temperature, critical for device applications. For example, extremely high spin polarization was produced through charge current in chiral nonmagnetic halide perovskites at room temperature in the absence of external magnetic fields [33] ($\mathbf{B}^{\text{ext}}$), which is a hallmark in semiconductor spintronics. Persistent spin helix states that preserve SU(2) symmetry and that can potentially provide exceptionally long τ_s were recently discovered in

two-dimensional halide perovskites [34].

Several recent experimental studies have sought to identify the dominant spin relaxation and dephasing mechanisms to further control and elongate τ_s of halide perovskites, [10, 216, 33, 9] e.g. via time-resolved Kerr/Faraday rotations. In particular, the bulk halide perovskite such as $CsPbBr_3$, which possesses one of the simplest halide perovskite structures, is a good benchmark system to understand the fundamental physical mechanisms but already presents several outstanding questions. First, what is the intrinsic τ_s of $CsPbBr_3$? Experimentally this is not possible to isolate due to the unavoidable contributions from defects and nuclear spins. However, the intrinsic τ_s are essential as the upper limits to guide the experimental optimization of materials. Next, what scattering processes and phonon modes dominate spin relaxation when varying the temperature, carrier density, etc.? This has been extensively studied for carrier relaxation dynamics, but not yet for spin relaxation dynamics. As we show here, the role of electron-phonon (e-ph) coupling, and especially the Fröhlich interaction known to be important for carrier relaxation in halide perovskites [218], can be dramatically different in spin relaxation. Lastly, how do electron and hole τ_s respond to $\mathbf{B}^{\text{ext}}$, and what are the roles of their respective g-factor inhomogeneity [10, 216]?

To answer these questions, we need theoretical studies of spin relaxation and dephasing due to various scattering processes and SOC, free of experimental or empirical parameters. Previous theoretical work on spin properties of halide perovskites have largely focused on band structure and spin texture [219, 220, 34], and have not yet addressed spin relaxation and dephasing directly. Here, we apply our recently-developed

first-principles real-time density-matrix dynamics (FPDM) approach [71, 72, 73, 221, 222], to simulate spin relaxation and dephasing times of free electrons and holes in bulk $CsPbBr_3$. FPDM approach was applied to disparate materials including silicon, (bcc) iron, transition metal dichalcogenides (TMDs), graphene-hBN, GaAs, in good agreement with experiments [71, 72, 221]. We account for *ab initio* Landé g-factor and magnetic momenta, self-consistent SOC, and quantum descriptions of e-ph, electron-impurity (e-i) and electron-electron (e-e) scatterings. We can therefore reliably predict τ_s with and without impurities, as a function of temperature, carrier density, and $\mathbf{B}^{\text{ext}}$.

6.2 Theory of First-Principles Real-Time Density-Matrix Dyanmics

We simulate spin and carrier dynamics based on the FPDM approach [71, 72]. We solve the quantum master equation of density matrix $\rho(t)$ in the Schrödinger picture as the following:[72]

$$\frac{d\rho_{12}(t)}{dt} = -\frac{i}{\hbar}\left[H\left(\mathbf{B}^{\text{ext}}\right), \rho(t)\right]_{12} + \left(\begin{array}{c} \frac{1}{2}\sum_{345} \left\{ \begin{array}{c} \left[I-\rho(t)\right]_{13} P_{32,45}\rho_{45}(t) \\ -\left[I-\rho(t)\right]_{45} P^{*}_{45,13}\rho_{32}(t) \end{array} \right\} \\ +H.C. \end{array} \right), \tag{6.1}$$

where the first and second terms on the right side of Eq. 7.12 relate to Larmor precession and scattering processes respectively. The scattering processes induce spin relaxation via the SOC. $H\left(\mathbf{B}^{\text{ext}}\right)$ is the electronic Hamiltonian at an external magnetic field $\mathbf{B}^{\text{ext}}$.

$[H, \rho] = H\rho - \rho H$. H.C. is Hermitian conjugate. The subindex, e.g., "1" is the combined index of $\mathbf{k}$-point and band. P is the generalized scattering-rate matrix considering e-ph, e-i and e-e scattering processes, computed from the corresponding scattering matrix elements and energies of electrons and phonons.

Starting from an initial density matrix $\rho(t_0)$ prepared with a net spin, we evolve $\rho(t)$ through Eq. 7.12 for a long enough time, typically from hundreds of ps to a few μs. We then obtain the excess spin observable vector $\delta\mathbf{S}^{\text{tot}}(t)$ from $\rho(t)$ (Eq. S1-S2) and extract spin lifetime τ_s from $\delta\mathbf{S}^{\text{tot}}(t)$ using Eq. S3.

Historically, two types of τ_s - spin relaxation time (or longitudinal time) T_1 and ensemble spin dephasing time (or transverse time) T_2^* were used to characterize the decay of spin ensemble or $\delta\mathbf{S}^{\text{tot}}(t)$ [223, 224]. Suppose the spins are initially polarized along $\mathbf{B}^{\text{ext}} \neq 0$, if $\delta\mathbf{S}^{\text{tot}}(t)$ is measured in the parallel direction of $\mathbf{B}^{\text{ext}}$, τ_s is called T_1; if along $\perp \mathbf{B}^{\text{ext}}$, it is called T_2^*. Note that without considering nuclear spins, magnetic impurities, and quantum interference effects[225], theoretical $\tau_s\left(\mathbf{B}^{\text{ext}} = 0\right)$ should be regarded as T_1. See more discussions about spin relaxation/dephasing in Supporting Information Sec. SI.

Below we first show theoretical results of T_1 and T_2^* of bulk (itinerant or delocalized) carriers. For bulk carriers of halide perovskites, T_1 are mainly limited by Elliott-Yafet (EY) and D'yakonov-Perel' (DP) mechanisms [226, 227]. EY represents the spin relaxation pathway due to mostly spin-flip scattering (activated by SOC). DP is caused by randomized spin precession between adjacent scattering events and is activated by the fluctuation of the SOC fields induced by inversion symmetry broken (ISB).

Different from T_1, T_2^* is additionally affected by the Landé-g-factor fluctuation at transverse $\mathbf{B}^{\text{ext}}$. We later generalize our results for other halide perovskites by considering the ISB and composition effects. We at the end discuss T_2^* of localized carriers due to interacting with nuclear spins. By simulating T_1 and T_2^*, and determining the dominant spin relaxation/dephasing mechanism, we provide answers of critical questions raised earlier and pave the way for optimizing and controlling spin relaxation and dephasing in halide perovskites.

6.3 Spin Lifetimes at Zero Magnetic Field

Intrinsic τ_s, free from crystal imperfections and nuclear spin fluctuation, is investigated first, which sets up the ideal limit for experiments. At $\mathbf{B}^{\text{ext}} = 0$, bulk $CsPbBr_3$ possesses both time-reversal (nonmagnetic) and spatial inversion symmetries, resulting in Kramers degeneracy of a pair of bands between (pseudo-) up and down spins. Spin relaxation in such systems is conventionally characterized by EY mechanism [227]. To confirm if such mechanism dominates in $CsPbBr_3$, the proportionality between τ_s and carrier lifetime (τ_p, $\tau_s \propto \tau_p$) is a characteristic signature, as is discussed below. Even for intrinsic τ_s, varying temperature (T) and carrier density (n_c) would lead to large change, and its trend is informative for mechanistic understanding.

Fig. 6.1a and 6.1b show theoretical τ_s at $\mathbf{B}^{\text{ext}} = 0$, including e-ph and e-e scatterings, as a function of T and n_c respectively, for free electrons and holes (SI Fig. S7). Note that although bulk $CsPbBr_3$ crystal symmetry is orthorhombic, the spin lifetime anisotropy along three principle directions is weak (see SI Fig. S8). Therefore

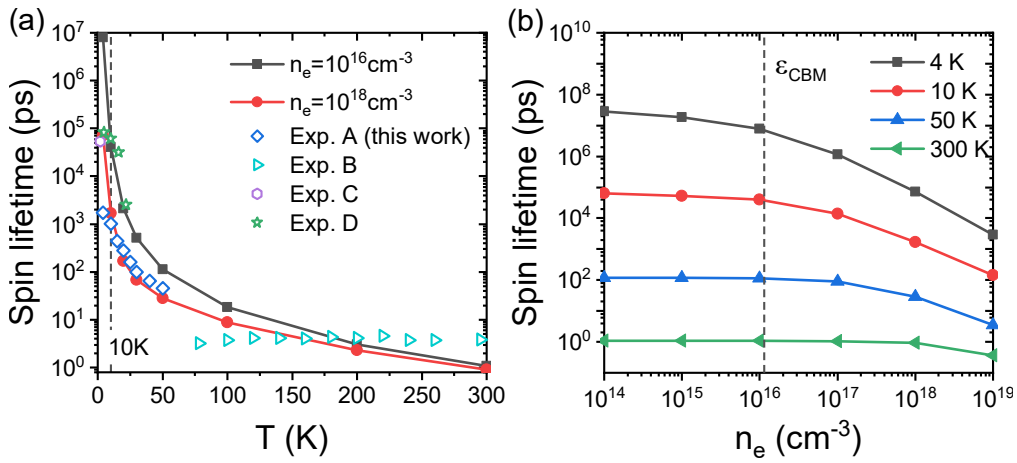

Figure 6.1: Spin lifetime τ_s of electrons of $CsPbBr_3$. We compare electron and hole τ_s in Supplementary information (SI) Fig. S7 and they have the same order of magnitude at all conditions we investigated. (a) τ_s due to both the electron-phonon (e-ph) and electron-electron (e-e) scatterings calculated as a function of T at different electron densities n_e compared with experimental data. In Fig. S6, we show τ_s versus T using log-scale for both y- and x-axes to highlight low-T region. Exp. A are our experimental data of T_2^* of free electrons in bulk $CsPbBr_3$ at a small external transverse magnetic field. For Exp. A, the density of photo-excited carriers is estimated to be about 10^{18} cm^{-3}. Exp. B are experimental data of exciton τ_s of $CsPbBr_3$ films from Ref. [9]. Exp. C and Exp. D are experimental data of spin relaxation time T_1 of bulk $CsPbBr_3$ and $CsPbBr_3$ nanocrystals measured by the spin inertia method from Ref. [10] and [11] respectively. In Ref. [11], it was declared that quantum confinement effects do not modify the spin relaxation/dephasing significantly (see its Table 1), so that their T_1 data can be compared with our theoretical results. For Exp. C and D, the measured lifetimes cannot be unambiguously ascribed to electrons or holes and can be considered as values between electron and hole T_1. The carrier densities are not reported for Exp. C and D. (b) τ_s due to both the e-ph and e-e scatterings as a function of n_e at different T. The vertical dashed line in panel (b) corresponding to n_e with chemical potential $\mu_{F,c}$ at the conduction band minimum (CBM).

only τ_s along the [001] direction is presented here. We have several major observations as summarized below.

First, a clear decay of τ_s as increasing T is observed. As τ_s with and without e-e scattering (SI Fig. S7) has little difference, this indicates e-ph scattering is the dominant spin relaxation mechanism (without impurities and $\mathbf{B}^{\text{ext}}$). Note that with increasing T, phonon occupations increase, which enhances the e-ph scattering and thus lowers both carrier (τ_p) and spin (τ_s) lifetime.

Next, τ_s steeply decreases with increasing n_c at low T but is less sensitive to n_c at high T, as shown in Fig. 6.1b. The trend of T_1 decreasing with n_c is consistent with the experimental observation of T_1 decreasing with pump power/fluence in halide perovskites [228, 229, 230, 231]. At 4 K, τ_s decreases steeply by three orders of magnitude with n_c increasing from 10^{16} cm^{-3} to 10^{19} cm^{-3}. Such phenomenon was reported previously for monolayer WSe_2 [232, 72], where spin relaxation is dominated by EY mechanism, the same as in $CsPbBr_3$. The cause of such strong n_c-dependence at low T is discussed below in more details, attributing to n_c effects on (averaged) spin-flip matrix elements. As a result, at low T and low n_c, τ_s of $CsPbBr_3$ can be rather long, e.g., $\sim$200 ns at 10 K and $\sim$8 μs at 4 K. This is in fact comparable to the ultralong hole τ_s of TMDs and their heterostructures [233, 234, 72], $\geq$2 μs at $\sim$5 K, again suggesting the advantageous character of halide perovskite in spintronic applications.

Importantly, good agreement between theoretical results and several independent experimental measurements is observed. Our theoretical results agree well with experimental T_1 of bulk $CsPbBr_3$ [10] (Exp. C) assuming $n_c \approx 10^{18}$ cm^{-3}, and $CsPbBr_3$

nanocrystal [11] (Exp. D) assuming $n_c \approx 10^{16}$ cm^{-3}, respectively. We further compare theoretical results with our own measured T_2^* (at B^{ext}=100 mT; Exp. A). Excellent agreement is observed at $T \geqslant$10 K with n_c around 10^{18} cm^{-3} (estimated from the experimental averaged pump power). The agreement however becomes worse at $T <$10 K. The discrepancy is possibly due to nuclear-spin-induced spin dephasing of carriers, as will be discussed in the last subsection.

We then study the effects of the e-i scattering on τ_s for various point defects. We find that at low T, e.g., $T<$20 K, the e-i scattering reduces τ_s, consistent with EY mechanism (which states increasing extrinsic scatterings reduces spin lifetime). With a high impurity density n_i, e.g., 10^{18} cm^{-3}, the e-i scattering may significantly reduce τ_s below 10 K, seemingly leading to better agreement between theoretical τ_s and experimental data from Exp. A, as shown in SI Fig. S9. However, as will be discussed below in the subsection of magnetic-field effects, a relatively high n_i predicts incorrect values of T_2^* and worse agreement with experimental data (Exp. A) on $\mathbf{B}^{\text{ext}}$-dependence. Therefore, the discrepancy between our theoretical τ_s and our measured T_2^* below 10 K is probably not explained by the impurity scattering effects.

In addition, the electron and hole τ_s have the same order of magnitude (Fig. S7), consistent with experiments, but in sharp contrast to conventional semiconductors (e.g., silicon and GaAs [235]), which have longer electron τ_s than hole owing to band structure difference between valence and conduction band edges.

Finally, we also predict the spin diffusion length (l_s) of pristine $CsPbBr_3$ in the low-density limit, which sets the upper bound of l_s at different T. We use the relation

$l_s = \sqrt{D\tau_s}$, where D is diffusion coefficient obtained using the Einstein relation, with carrier mobility μ from first-principles calculations [73] (more details in Sec. SVII). Excellent agreement between theoretical and experimental carrier mobility is found for $CsPbBr_3$ (SI Fig. S12a). We find l_s is longer than 10 nm at 300 K, and possibly reach tens of μm at $T \leq 10$ K (see details in Sec. SVII and Fig. S12 in SI).

6.4 Analysis of Spin-phonon Relaxation

To gain deep mechanistic insights, we next analyze different phonon modes and carrier density effects on spin relaxation through examining spin-resolved e-ph matrix elements.

In Fig. 6.2, we compare the contribution of different phonon modes to τ_s and τ_p. First, we find that at a very low T - 4 K, only acoustic modes (A1-A3) contribute to spin and carrier relaxation. This is simply because the optical phonons are not excited at such low T (corresponding k_BT ~0.34 meV much lower than optical energy $\gtrsim$ 2 meV). At $T \geqslant$10 K, optical modes are more important for both spin and carrier relaxation (green and blue dashed lines closer to black line (all phonons) in Fig. 6.2).

In particular, from Fig. 6.2b, we find that two special optical modes - 57th and 58th modes (O57-O58, modes ordered by phonon energy with their phonon vector plots in SI Fig. S3) dominate carrier relaxation at $T \geqslant$50 K, because τ_p due to O57-O58 (blue dashed line) nearly overlaps with τ_p due to all phonon modes (black line). These two optical modes are mixture of longitudinal and transverse vibration as shown in SI Fig. S3. In contrast, for spin relaxation in Fig. 6.2a, at $T \geqslant$10 K O57-O58 are

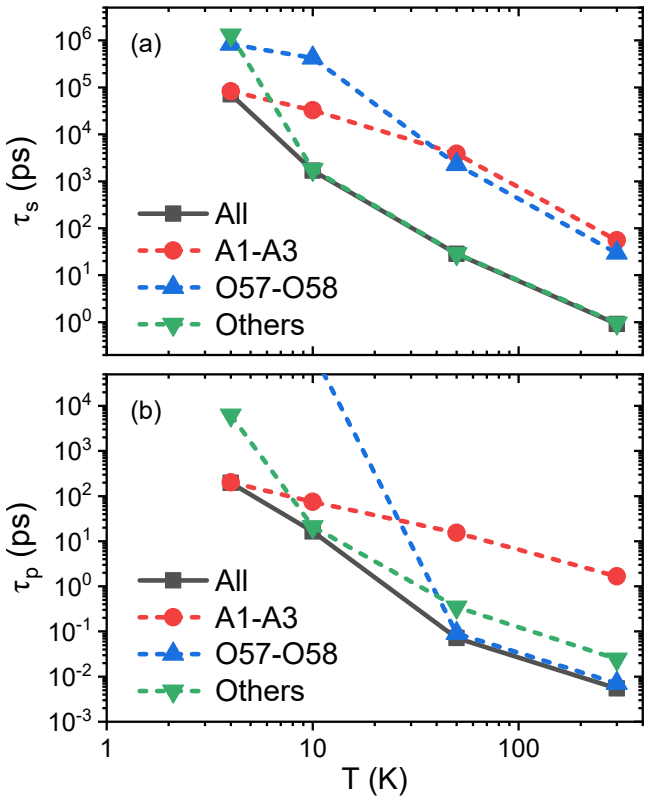

Figure 6.2: Phonon-mode contribution analysis. (a) Spin lifetime τ_s and (b) carrier lifetime τ_p due to different phonon modes. "A" and "O" denote acoustic and optical modes respectively. The number index is ordered by increasing phonon energies. The phonon dispersion is given in SI Fig. S2. Here carrier density n_c is set to be 10^{18} cm^{-3}. We note that special optical phonon modes O57 and O58 are dominant in carrier relaxation above 50 K (panel b), consistent with the usual Fröhlich interaction picture, but are not important in spin relaxation (panel a).

less important than other optical modes (green dashed line). More specifically, in this temperature range, there are tens of phonon modes (with energies ranging from 2 meV to 18 meV), contributing similarly to spin relaxation. This is contradictory to the simple assumption frequently employed in previous experimental studies [10, 12, 236] that a single longitudinal optical (LO) phonon with a relatively high energy (e.g. ∼18 meV for $CsPbBr_3$ in Ref. [10]) dominates spin relaxation over a wide T range, e.g., from 50 K to 300 K, through a Fröhlich type e-ph interaction.

In the simplified picture of Fermi's golden rule (FGR), τ_s^{-1} and τ_p^{-1} (due to e-ph scattering) are proportional to the modulus square of spin-flip ($|\widetilde{g}^{\uparrow\downarrow}|^2$) and spin-conserving ($|\widetilde{g}^{\uparrow\uparrow}|^2$) matrix elements (ME), respectively. From Fig. 6.3a, we find that spin-flip ME is dominated by "other optical modes" (blue line), opposite to the spin-conserving ME in Fig. 6.3b (i.e. instead, dominated by special optical phonon modes O57 and O58 (red line)). This well explains the different roles of optical O57-O58 modes in carrier and spin relaxation. Moreover, spin-conserving ME for O57-O58 in Fig. 6.3b diverges at $q \to 0$, which indicates its dominant long-range nature, consistent with the common long-range Fröhlich interaction picture [237], mostly driving carrier relaxation in polar materials at high T (e.g., 300 K). On the contrary, the small magnitude of spin-flip ME for O57-O58 modes indicates that Fröhlich interaction is unimportant for spin relaxation. This is because all spin-dependent parts of the e-ph interaction are short-ranged, while Fröhlich interaction is the only long-range part of the e-ph interaction but is spin-independent. This important conclusion again emphasizes the sharp difference between spin and carrier relaxations in polar materials.

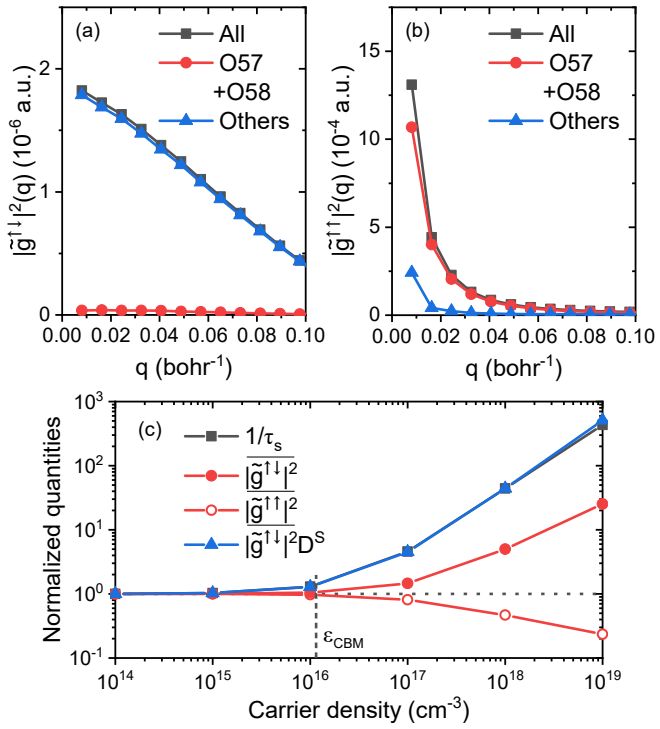

Figure 6.3: The analysis of the e-ph matrix elements (ME). (a) The q-resolved modulus square of spin-flip e-ph ME $|\widetilde{g}^{\uparrow\downarrow}|^2(q)$ at a high temperature - 300 K with a part of or all phonon modes. (b) The same as panel (a) but for spin-conserving e-ph ME $|\widetilde{g}^{\uparrow\uparrow}|^2(q)$. (c) $\overline{|\widetilde{g}^{\uparrow\downarrow}|^2}$, $\overline{|\widetilde{g}^{\uparrow\uparrow}|^2}$ and $\overline{|\widetilde{g}^{\uparrow\downarrow}|^2}D^{\mathrm{S}}$ of conduction electrons as a function of carrier density at a low T - 10 K compared with the spin relaxation rates $1/\tau_s$. $\overline{|\widetilde{g}^{\uparrow\downarrow}|^2}$ and $\overline{|\widetilde{g}^{\uparrow\uparrow}|^2}$ are the T and $\mu_{F,c}$ dependent effective (averaged around the band edge or $\mu_{F,c}$) modulus square of spin-flip and spin-conserving e-ph ME, respectively (see Eq. 6.12). D^{S} is the scattering density of states (Eq. 6.15). The vertical dashed line corresponding to $\mu_{F,c}$ at CBM.

To explain the strong n_c dependence of τ_s at low T, we further analyze the T and chemical potential ($\mu_{F,c}$) dependent effective spin-flip ME $\overline{|\widetilde{g}^{\uparrow\downarrow}|^2}$ (averaged around $\mu_{F,c}$, see Eq. 6.12) and scattering density of states D^{S} (Eq. 6.15). In FGR, we have the approximate relation in Eq. 6.17, i.e. $\tau_s^{-1} \propto \overline{|\widetilde{g}^{\uparrow\downarrow}|^2} D^{\mathrm{S}}$.

In Fig. 6.3c, we show the n_c dependence of τ_s^{-1}, compared with $\overline{|\widetilde{g}^{\uparrow\downarrow}|^2}$ and $\overline{|\widetilde{g}^{\uparrow\downarrow}|^2} D^{\mathrm{S}}$. Indeed we can see τ_s^{-1} and $\overline{|\widetilde{g}^{\uparrow\downarrow}|^2} D^{\mathrm{S}}$ nearly overlapped, as the result of Eq. 6.17. The strong increase of τ_s^{-1} at $n_c \geqslant 10^{16}$ cm^{-3} can be attributed to the fact that both spin-flip ME $\overline{|\widetilde{g}^{\uparrow\downarrow}|^2}$ and scattering density of states D^{S} increase with n_c. Interestingly, the effective spin-conserving ME $\overline{|\widetilde{g}^{\uparrow\uparrow}|^2}$, most important in carrier relaxation, decreases with n_c, opposite to spin-flip $\overline{|\widetilde{g}^{\uparrow\downarrow}|^2}$. This again emphasizes the e-ph scattering affects carrier and spin relaxation differently, given the opposite trends of spin-conserving and spin-flip scattering as a function of n_c. When $n_c < 10^{16}$ cm^{-3}, τ_s^{-1} is insensitive to n_c, which is because both $\overline{|\widetilde{g}^{\uparrow\downarrow}|^2}$ and D^{S} are determined by e-ph transitions around the band edge. In "Methods" section, we have proven that at the low density limit, since carrier occupation satisfies Boltzmann distribution, both $\overline{|\widetilde{g}^{\uparrow\downarrow}|^2}$ and D^{S} are $\mu_{F,c}$ and n_c independent.

6.5 Landé g-factor and Transverse-magnetic-field Effects

At $\mathbf{B}^{\mathrm{ext}}$, the electronic Hamiltonian reads

$$H_k\left(\mathbf{B}^{\mathrm{ext}}\right) = H_{0,k} + \mu_B \mathbf{B}^{\mathrm{ext}} \cdot \left(\mathbf{L}_k + g_0 \mathbf{S}_k\right), \tag{6.2}$$

where μ_B is Bohr magneton; g_0 is the free-electron g-factor; $\mathbf{S}$ and $\mathbf{L}$ are the spin and orbital angular momentum respectively. The simulation of $\mathbf{L}$ is nontrivial for periodic systems and the details are given in Method section and Ref. [238]. Having $H\left(\mathbf{B}^{\text{ext}}\right)$ at a transverse $\mathbf{B}^{\text{ext}}$ perpendicular to spin direction, T_2^* is obtained by solving the density-matrix master equation in Eq. 7.12.

The key parameters for the description of the magnetic-field effects are the Landé g-factors. Their values relate to $\mathbf{B}^{\text{ext}}$-induced energy splitting (Zeeman effect) $\Delta E_k\left(\mathbf{B}^{\text{ext}}\right)$ and Larmor precession frequency Ω_k, satisfying $\Omega_k \approx \Delta E_k = \mu_B B^{\text{ext}} \widetilde{g}_k$ with $\widetilde{g}_k$ the k-resolved Landé g-factor. More importantly, the g-factor fluctuation (near Fermi surface or $\mu_{F,c}$) leads to spin dephasing at transverse $\mathbf{B}^{\text{ext}}$, corresponding to T_2^*.

Fig. 6.4a shows $\widetilde{g}_k$ of electrons and holes at $\mathbf{k}$-points around the band edges. $\widetilde{g}_k$ are computed using $\Delta E_k\left(\mathbf{B}^{\text{ext}}\right)$ (Eq. 6.8 and 6.9) obtained from $H_k\left(\mathbf{B}^{\text{ext}}\right)$. Our calculated electron $\widetilde{g}_k$ are larger than hole $\widetilde{g}_k$, and the sum of electron and hole $\widetilde{g}_k$ range from 1.85 to 2.4, in agreement with experiments [10, 235]. Furthermore, $\widetilde{g}_k$ are found sensitive to state energies and wavevectors $\mathbf{k}$, and the fluctuation of $\widetilde{g}_k$ is enhanced with increasing the state energy. In Figs. 6.4b and 6.4c, we show the global g-factor g^{Ω} and the amplitude of the g-factor fluctuation (near the Fermi surface) $\Delta\widetilde{g}$ (Eq. 6.11) as a function of n_c. Both g^{Ω} and $\Delta\widetilde{g}$ are insensitive to n_c at $n_c < 10^{16}$ cm^{-3}, but sensitive to n_c at $n_c \geqslant 10^{16}$ cm^{-3}.

In Fig. 6.4, we show *ab initio* g-factors computed with the PBE functional[239]. We further compare g-factors computed using different exchange-correlation functionals (V_{xc}) in SI Sec. SV. It is found that the magnitude of $\Delta\widetilde{g}$ and the trend of g-factor

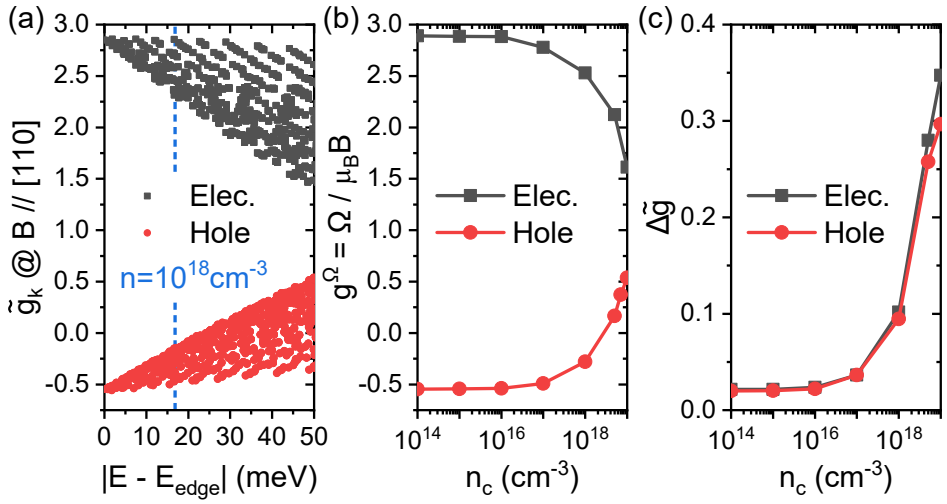

Figure 6.4: The Landé g-factors of electrons and holes calculated at the PBE functional. The external magnetic fields $\mathbf{B}^{\text{ext}}$ are along [110] direction. (a) The $\mathbf{k}$-dependent g-factor $\widetilde{g}_k$ (Eq. 6.8 and 6.9) at $\mathbf{k}$ points around the band edges. Each data-point corresponds to a $\mathbf{k}$ point. (b) The global g-factor $g^{\Omega} = \Omega/\mu_B B$ as a function of n_c, where Ω is Larmor precession frequency extracted from spin dynamics at $\mathbf{B}^{\text{ext}} \neq 0$. $g^{\Omega} = \pm|g^{\Omega}|$ if the excess/excited spin $\delta\mathbf{S}^{\text{tot}}(t)$ precesses along $\pm\delta\mathbf{S}^{\text{tot}}(t) \times \mathbf{B}^{\text{ext}}$. g^{Ω} is close to the averaged g-factor $\overline{\widetilde{g}}$ defined in Eq. 6.10. (c) The effective amplitude of the fluctuation of g factors - $\Delta\widetilde{g}$ defined in Eq. 6.11 as a function of carrier density at 10 K.

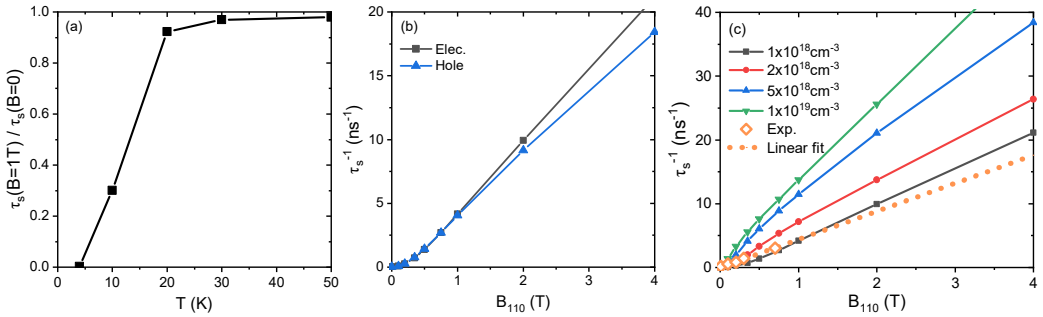

Figure 6.5: The effects of transverse $\mathbf{B}^{\text{ext}}$ (perpendicular to spin direction) on calculated τ_s of free carriers of $CsPbBr_3$. (a) The ratio of τ_s at B^{ext}=1 T and τ_s at B^{ext}=0 as a function of T. Here electron carrier density n_e=10^{18} cm^{-3}. (b) Spin decay rates (τ_s^{-1}) of electrons and holes as a function of B^{ext} at 4 K with $n_c = 10^{18}$ cm^{-3}. (c) τ_s^{-1} as a function of B^{ext} at 4 K at different n_e. "Exp." (orange open diamond) represent our experimental data (with $\mathbf{B}^{\text{ext}}$ along [010] direction), where the density of photo-excited carriers is estimated about 10^{18} cm^{-3}. The orange dashed line is the linear fit of experimental data. The linear relation between ensemble spin dephasing rate and B^{ext} was frequently found and used in previous experimental measurements[10, 12, 13, 14].

change with the state energy are both insensitive to V_{xc}. Since T_2^* only depends on $\Delta\widetilde{g}$, our predictions of T_2^* should be reliable.

Next, we discuss magnetic-field effects on τ_s in Fig. 6.5, calculated from our FPDM approach, and analyze them with phenomenological models. At transverse $\mathbf{B}^{\text{ext}}$, the total spin decay rate is approximately expressed by

$$\tau_s^{-1}\left(\mathbf{B}^{\text{ext}}\right) \approx \left(\tau_s^0\right)^{-1} + \left(\tau_s^{\Delta\Omega}\right)^{-1}\left(\mathbf{B}^{\text{ext}}\right), \tag{6.3}$$

where $\left(\tau_s^0\right)^{-1}$ is the zero-field spin relaxation rate due to EY mechanism;

$\left(\tau_s^{\Delta\Omega}\right)^{-1}$ is induced by the Larmor-precession-frequency fluctuation ($\Delta\Omega = \mu_B B^{\text{ext}} \Delta\widetilde{g}$), and can be described by different mechanisms depending on the magnitude of $\tau_p \Delta\Omega$ [223, 227]:

(i) Free induction decay (FID) mechanism if $\tau_p \Delta\Omega \gtrsim 1$ (weak scattering limit). We have

$$\left(\tau_s^{\Delta\Omega}\right)^{-1} \sim \left(\tau_s^{\text{FID}}\right)^{-1} \sim C^{\Delta g} \Delta\Omega = C^{\Delta g} \mu_B B^{\text{ext}} \Delta\widetilde{g}, \tag{6.4}$$

where $C^{\Delta g}$ is a constant and often taken as 1 or $1/\sqrt{2} \approx 0.71$ [240, 223, 10, 241, 12, 13, 14]. The latter assumes a Gaussian distribution of g-factors and the scattering being completely absent [223, 241, 14].

(ii) Dyakonov Perel (DP) mechanism if $\tau_p \Delta\Omega \ll 1$ (strong scattering limit). We have

$$\left(\tau_s^{\Delta\Omega}\right)^{-1} \sim \left(\tau_s^{\text{DP}}\right)^{-1} \sim \tau_p \left(\Delta\Omega\right)^2 = \tau_p \left(\mu_B B^{\text{ext}} \Delta\widetilde{g}\right)^2. \tag{6.5}$$

(iii) Between (i) and (ii) regimes, there isn't a good approximate relation for $\left(\tau_s^{\Delta\Omega}\right)^{-1}$, but we may expect that[223]

$$\left(\tau_s^{\text{DP}}\right)^{-1} < \left(\tau_s^{\Delta\Omega}\right)^{-1} < \left(\tau_s^{\text{FID}}\right)^{-1}. \tag{6.6}$$

From Fig. 6.5a, we find that magnetic-field effects are weak ($\tau_s\left(\mathbf{B}^{\text{ext}}\right)/\tau_s\left(0\right) \approx 1$) at $T \geqslant 20$ K. This is because at high T, e-ph scattering is strong which leads to short τ_p and short spin lifetime at zero field τ_s^0 (large $(\tau_s^0)^{-1}$). Then the spin relaxation falls into strong or intermediate scattering regimes ((ii) or (iii)), which give small $(\tau_s^{\Delta\Omega})^{-1}$. Finally, following $\left(\tau_s^{\Delta\Omega}\right)^{-1} \ll \left(\tau_s^0\right)^{-1}$ obtained above, we reach $\tau_s\left(\mathbf{B}^{\text{ext}}\right)/\tau_s\left(0\right) \approx 1$ from Eq. 6.3.

As a result, we only discuss τ_s at $\mathbf{B}^{\text{ext}} \neq 0$ below 20 K, specifically at 4K afterwards. From Fig. 6.5b, we can see that magnetic-field effects on electron and hole τ_s are quite similar, which is a result of their similar band curvatures, e-ph scattering, and $\Delta\widetilde{g}$ (Fig. 6.4c), although their absolute g-factors are quite different, as shown in Fig. 6.4a and 6.4b.

We further examine magnetic-field effects on τ_s at 4 K in Fig. 6.5c. As discussed above, $\tau_s^{-1}\left(\mathbf{B}^{\text{ext}}\right)$ increases with B^{ext}. More specifically, we find that the calculated $\tau_s^{-1}\left(\mathbf{B}^{\text{ext}}\right)$ is proportional to $\left(B^{\text{ext}}\right)^2$ at low B^{ext} (details in SI Fig. S13) following the DP mechanism (Eq. 6.5), but linear to B at higher B following the free induction decay mechanism(Eq. 6.4).

The comparison of calculated $\tau_s^{-1}\left(\mathbf{B}^{\text{ext}}\right)$ with experimental data (orange diamond in Fig. 6.5b) is reasonable with n_e around 10^{18} cm^{-3} (the experimental estimated average n_c). However, their $\mathbf{B}^{\text{ext}}$-dependence is not the same in the small $\mathbf{B}^{\text{ext}}$ range, e.g. at B^{ext}<0.4 Tesla, the calculated $\tau_s^{-1}\left(\mathbf{B}^{\text{ext}}\right)$ is proportional to $\left(B^{\text{ext}}\right)^2$ (as shown in SI Fig. S13), whereas the experimental $\tau_s^{-1}\left(\mathbf{B}^{\text{ext}}\right)$ is more likely linear to B^{ext}. In principles, extremely small B^{ext} will lead to $\Delta\Omega$ small enough falling in the DP regime ($(\tau_s^{\Delta\Omega})^{-1}$ proportional to $\left(B^{\text{ext}}\right)^2$). However, experimental results still keep in the FID regime ($(\tau_s^{\Delta\Omega})^{-1}$ linear dependent on B^{ext}) at small $\mathbf{B}^{\text{ext}}$. This inconsistency implies additional magnetic field fluctuation contributes to $\Delta\Omega$ and/or other faster spin dephasing processes exist at small external B^{ext}. It may originate from nuclear spin fluctuation, magnetic impurities, carrier localization, chemical potential fluctuation, etc. [10, 235] in samples, which are however rather complicated for a fully first-principles description.

In this work, we focus on spin dephasing of bulk carriers due to Zeeman effects and various scattering processes.

Moreover, in Fig. 6.5c, we find that at $\mathbf{B}^{\text{ext}} \neq 0$, τ_s decreases with n_c, similar to the case at $\mathbf{B}^{\text{ext}} = 0$. But the origin of the strong n_c dependence at high B^{ext} is very different from τ_s at $\mathbf{B}^{\text{ext}} = 0$. When $B^{\text{ext}} \geq$0.4 Tesla, τ_s is dominated by the FID mechanism (Eq. 6.4), thus its n_c dependence is mostly from $\Delta\widetilde{g}$'s strong n_c dependence shown in Fig. 6.4c.

Finally, we show $\tau_s^{-1}\left(\mathbf{B}^{\text{ext}}\right)$ as a function of $\mathbf{B}^{\text{ext}}$ at 4 K with the e-i scattering in Fig. S14. We find that with relatively strong impurity scattering (e.g, with 10^{17} cm^{-3} V_{Pb} neutral impurities), the $\mathbf{B}^{\text{ext}}$-dependence of τ_s becomes quite weak, in disagreement with experiments, indicating that impurity scattering is probably weaker in those experiments. See more discussions in Sec. SVIII.

6.6 Inversion Symmetry Broken (ISB), Composition Effects and Hyperfine Coupling

For halide perovskites, ISB may present due to ferroelectric polarization, strain, surface, applying electric fields, etc. One of the most important effects from ISB is inducing $\mathbf{k}$-dependent SOC fields (called $\mathbf{B}^{\text{in}}$). $\mathbf{B}^{\text{in}}$ can change the electronic energies and spin textures, which may significantly modify the spin relaxation/dephasing. To understand the ISB effects, we simulate τ_s with two important types of $\mathbf{B}^{\text{in}}$ - Rashba and PSH (persistent spin helix) ones. Rashba SOC presents in many 2D and 3D materials,

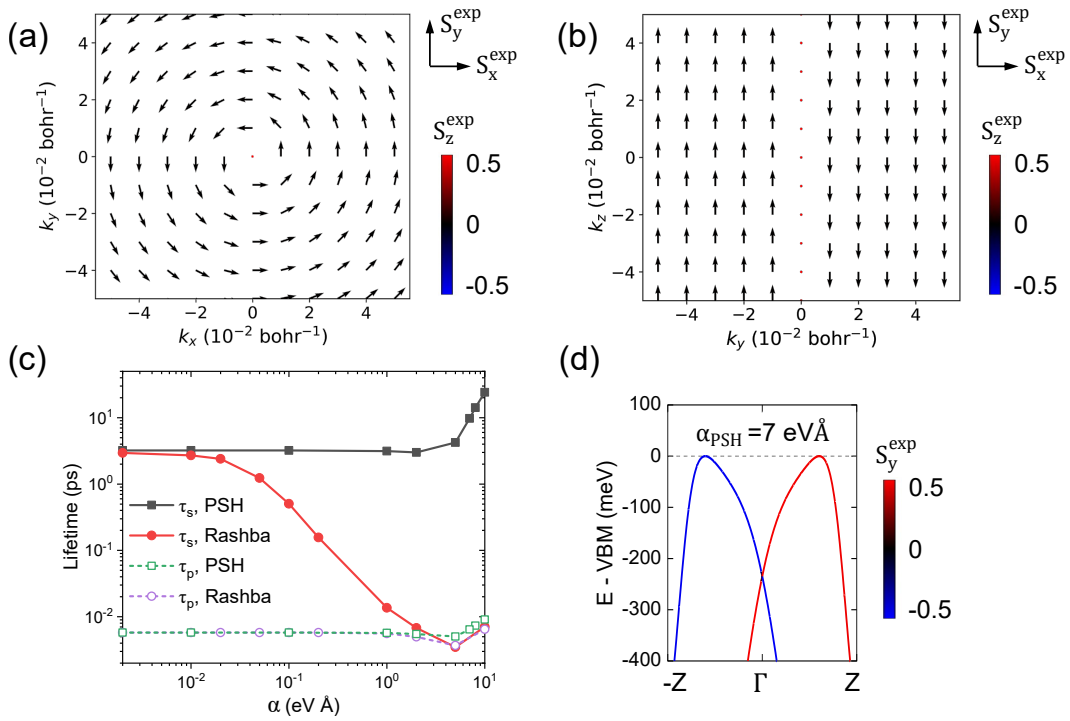

Figure 6.6: The effects of model SOC fields. (a) Spin textures in the $k_x - k_y$ plane of the $CsPbBr_3$ system with model Rashba SOC. $\mathbf{S}^{exp} \equiv (S_x^{exp}, S_y^{exp}, S_z^{exp})$ with S_i^{exp} being spin expectation value along direction i and is the diagonal element of spin matrix s_i in Bloch basis. The arrow represents the spin orientation in the $S_x^{exp} - S_y^{exp}$ plane. The color scales S_z^{exp}. (b) Spin textures in the $k_y - k_z$ plane of the $CsPbBr_3$ system with model PSH (persistent spin helix) SOC. (c) Spin lifetime τ_s and carrier lifetime τ_p of $CsPbBr_3$ holes at 300 K considering the effects of Rashba or PSH SOC. α is the Rashba/PSH SOC strength coefficient. Rashba fields have spin texture perpendicular to $\mathbf{k}$ direction, in the same plane (xy plane here) surrounding Γ point. PSH fields have spin texture parallel along the same axis (y axis here). The detailed forms of the model SOC fields and Hamiltonians are given in Eq. 6.19-6.23 in "Methods" section. τ_s is perpendicular to the SOC-field plane for Rashba SOC and is along the high-spin-polarization axis for PSH SOC respectively. (d) The band structure of valence bands considering PSH SOC with α=7 eVÅ. The color scales the S_y^{exp} in panel (d).

e.g., wurtzite GaN and graphene on SiO_2/hBN. PSH exhibits SU(2) symmetry [242, 243] which is robust against spin-conserving scattering, and was recently realized in 2D hybrid perovskites [34]. Their effects are considered by introducing an additional SOC term to the electronic Hamiltonian perturbatively. The specific forms of Rashba and PSH SOC Hamiltonians are given in Eq. 6.19-6.23 in "Methods" section.

From Fig. 6.6a, we find that τ_s is reduced by Rashba SOC and the reduction is significant when the SOC coefficient $\alpha \geq 0.5$ eVÅ. This is because Rashba SOC induces a nonzero $\Delta\Omega \propto \alpha$ and then induces an DP/FID spin decay channel additional to the EY one. Similar to Eq. 6.3, the total rate $\tau_s^{-1} \approx \tau_s^{-1}|_{\alpha=0} + \left(\tau_s^{-1}\right)^{\Delta\Omega}$. At $\alpha \geq 0.5$ eVÅ, $\left(\tau_s^{-1}\right)^{\Delta\Omega}$ becomes large, so that τ_s is significantly reduced from $\tau_s^{-1}|_{\alpha=0}$. τ_s keeps decreasing with α but its low limit is bound by τ_p. On the other hand, with PSH SOC, τ_s (along PSH $\mathbf{B}^{\text{in}}$ - $\mathbf{B}^{\text{PSH}}$, which is along y direction here) is unchanged at $\alpha \leq 2$ eVÅ, and increases at a larger α. The reason is: with PSH SOC, spins are highly polarized along $\mathbf{B}^{\text{PSH}}$, so that τ_s along $\mathbf{B}^{\text{PSH}}$ is still dominated by EY mechanism (no spin precession). One critical effect of $\mathbf{B}^{\text{PSH}}$ is then modifying the energies (spin split energies). At small α, the energy changes are not significant compared with k_BT, so that the e-ph scattering contribution to spin relaxation is not modified much; as a result, τ_s is close to $\tau_s|_{\alpha=0}$. From Fig. 6.6b, we can see that at large α (e.g., 7 eVÅ) the band structure is however significantly changed. The valence band maxima are now at two opposite k-points away from Γ and with opposite spins. Therefore, at large α, spin relaxation is dominated by the spin-flip scattering processes between two opposite valleys away from Γ. This can lead to longer τ_s since the spin-flip processes within one valley (intravalley scattering) are

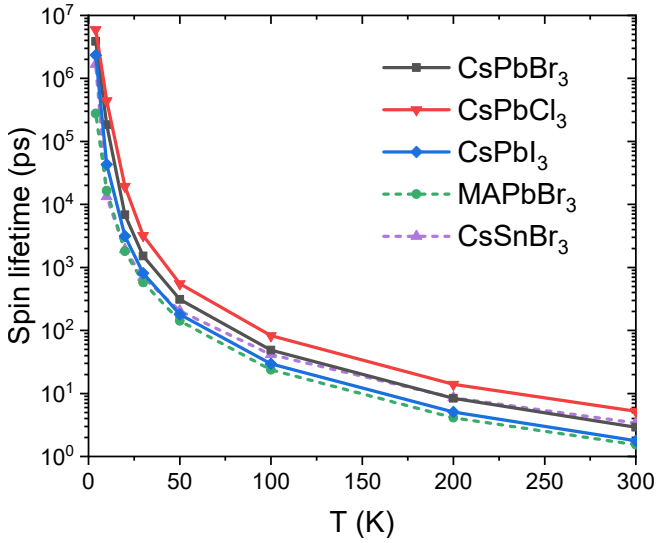

Figure 6.7: Spin lifetimes of holes of bulk $CsPbBr_3$, $CsPbCl_3$, $CsPbI_3$, $MAPbBr_3$ and $CsSnBr_3$ as a function of temperature with carrier density 10^{16} cm^{-3}.

suppressed, essentially a spin-valley locking condition is realized [73, 34]. Our FPDM simulations with model SOC suggest that Rashba SOC likely reduces τ_s while PSH SOC can enhance τ_s as anticipated in previous experimental study [243]. Note that in practical materials, the ISB effects may not be completely captured by model SOC fields as introduced here. Although in general, we include self-consistent SOC in our FPDM calculations instead of perturbatively, but since the studied equilibrium bulk structure has inversion symmetry, we therefore have to include model ISB SOC perturbatively to simulate such effects induced by various causes. Therefore, further FPDM simulations of materials with ISB structures are important for comprehensive understanding of the ISB effects.

Furthermore, it is crucial to understand the chemical composition effects to improve our understandings of spin dynamics and transport in many other kinds of halide

perovskites beside $CsPbBr_3$. As an initial study, we performed FPDM simulations of τ_s of holes of pristine bulk $CsPbCl_3$, $CsPbI_3$, $MAPbBr_3$ and $CsSnBr_3$ as a function of temperature, at the same carrier density. We consider the inversion-symmetric orthorhombic phase for all systems, the same as $CsPbBr_3$ here, in order to study chemical composition effect alone. From Fig. 6.7, our FPDM simulations show that the differences of τ_s of $CsPbBr_3$, $CsPbCl_3$, $CsPbI_3$, $MAPbBr_3$ and $CsSnBr_3$ are mostly tens of percent or a few times in the wide temperature range from 4 K to 300 K. Specifically, τ_s of $MAPbBr_3$ is found always shorter than $CsPbBr_3$. τ_s of $CsSnBr_3$ is found slightly longer than $CsPbBr_3$ at 300 K but becomes shorter than $CsPbBr_3$ at T<100 K. A trend of hole τ_s is found for $CsPbX_3$: $\tau_s(CsPbCl_3) > \tau_s(CsPbBr_3) > \tau_s(CsPbI_3)$, indicating that the lighter the halogen atom, the longer the spin lifetime. This trend may be partly due to two reasons: (i) For the band gap, we have $CsPbCl_3 > CsPbBr_3 > CsPbI_3$ (1.40, 1.03 and 0.75 eV respectively at PBE), so that spin mixing due to the conduction-valence band mixing is reduced at lighter halogen compound, which usually weakens the spin-phonon interaction; (ii) The lighter halogen atom reduces the SOC strength of the material (weaker SOC reduces the spin mixing between up and down states). Additionally, we find that for all these inversion-symmetric orthorhombic materials, the anisotropy of τ_s along different crystalline directions is rather weak (see SI Fig. S8). Overall, our results indicate that the chemical composition effects on τ_s are not very strong when comparing with the effects of the symmetry change (e.g. broken inversion symmetry resulting in Rashba or PSH discussed in Fig. 6.6). A more systematic study of the composition, symmetry, and dimensionality effects is of great importance and will

be our future work.

Above we focus on spin relaxation/dephasing of bulk (or itinerant or delocalized) electrons, for which hyperfine coupling is usually unimportant[244, 223]. In actual samples, due to polarons, ionized impurities, etc., a considerable portion of electron carriers are localized. It is known that hyperfine coupling can induce spin dephasing of localized electrons through spin precessions about randomly-distributed nuclear-spin (magnetic) fields $\mathbf{B}^{\text{Nuclear}}$. When nuclear spins are weakly polarized (because of weak $\mathbf{B}^{\text{ext}}$), T_2^* of localized electrons - $T_{2,\text{loc}}^*$ is often estimated based on FID mechanism $1/T_{2,\text{loc}}^* \sim \sigma_{\Omega_N}$ [245, 246, 247], where Ω_N is Larmor frequency of a localized electron due to $\mathbf{B}^{\text{Nuclear}}$ and σ_{Ω_N} is the parameter describing its fluctuation or determining its distribution (Eq. 6.29 for $\mathbf{B}^{\text{ext}}$=0). According to Refs. [245, 246, 247, 10], $\sigma_{\Omega_N}^2 \sim C^{\text{loc}}/V^{\text{loc}}$ (Eq. 6.31), where V^{loc} is the localization volume. At $\mathbf{B}^{\text{ext}}$=0, C^{loc} is determined by hyperfine constant A, nuclear spin I, isotope abundance and unitcell volume (Eq. 6.32). See detailed formulae and our estimates of the above quantities in "Methods" section. Our estimated C^{loc} is ∼180 and ∼530 nm^3 ns^{-2} for electrons and holes respectively. The estimated localization radii for halide perovskites are 2.5-14 nm [248, 249, 250, 251], which lead to $T_{2,\text{loc}}^*\left(\mathbf{B}^{\text{ext}}=0\right)$ ∼0.6-8.0 ns for electrons and ∼0.35-4.6 ns for holes. Since bulk and localized carriers coexist in materials, $T_{2,\text{loc}}^*$ roughly gives the lower bound of the effective carrier T_2^*.

In addition to the hyperfine coupling for spin dephasing of localized carriers above, the fluctuation of hyperfine coupling for bulk (delocalized) carriers at different k-points may lead to spin dephasing when nuclear spins are polarized along a non-

zero transverse $\mathbf{B}^{\text{ext}}$. This effect is however rather complicated (probably requiring the difficult $\mathbf{L}$ contribution[252] to hyperfine coupling), beyond the scope of this work.

In summary, through a combined *ab initio* theory and experimental study, we reveal the spin relaxation and dephasing mechanism of carriers in halide perovskites. Using our FPDM approach and implementing *ab initio* magnetic momenta and g-factor, we simulate free-carrier τ_s as a function of T and $\mathbf{B}^{\text{ext}}$, in excellent agreement with experiments. The transverse magnetic-field effects are found only significant at $T<20$ K. We predict ultralong T_1 of pristine $CsPbBr_3$ at low T, e.g., $\sim$200 ns at 10 K and $\sim$8 μs at 4 K. We find strong n_c dependence of both T_1 and T_2 at low T, e.g. τ_s can be tuned by three order of magnitude with n_c from the low density limit to 10^{19} cm^{-3}. The reasons are attributed to the strong electronic-energy-dependences of spin-flip e-ph matrix elements and $\Delta\widetilde{g}$ for T_1 and T_2^* respectively. From the analysis of e-ph matrix elements, we find that contrary to common belief, Fröhlich interaction is unimportant to spin relaxation, although critical for carrier relaxation. We further study ISB and composition effects on τ_s of halide perovskites. We find that ISB effects can significantly change τ_s, i.e. spin lifetime can increase with PSH SOC, but not with Rashba SOC. The composition effect is found not very strong and only changes τ_s by tens of percent or a few times in a wide temperature. Our work provides fundamental insights on how to control and manipulate spin relaxation in halide perovskites, which are vital for their spintronics and quantum information applications.

6.7 Methods

Spin dynamics and transport. Spin dynamics and spin lifetime τ_s are simulated by our recently developed first-principles density-matrix dynamics (FPDM) method [71, 72, 73, 221, 222]. Starting from an initial state with a spin imbalance, we evolve the time-dependent density matrix $\rho(t)$ through the quantum master equation with Lindblad dynamics for a long enough simulation time, typically from ns to μs, varying with systems. After obtaining the excess spin observable $\delta\mathbf{S}^{\text{tot}}(t)$ from $\rho(t)$ and fitting $\delta\mathbf{S}^{\text{tot}}(t)$ to an exponentially oscillating decay curve, the decay constant τ_s and the precession frequency Ω are then obtained (Eq. S3 and Fig. S1 in SI). All required quantities of FPDM simulations, including electron energies, phonon eigensystems, e-ph and e-i scattering matrix elements, are calculated on coarse k and q meshes using the DFT open source software JDFTx [253], and then interpolated to fine meshes in the basis of maximally localized Wannier functions [254, 255, 256]. The e-e scattering matrix is computed using the same method given in Ref. [72]. More theoretical background and technical details are given in Ref. [73] and [72], as well as the Supporting Information.

Using the same first-principles electron and phonon energies and matrix elements on fine meshes, we calculate the carrier mobility by solving the linearized Boltzmann equation using a full-band relaxation-time approximation [257] and further estimate spin diffusion length based on the drift-diffusion model (SI Sec. SVII).

Orbital angular momentum. With the Blöch basis, the orbital angular

momentum reads

$$\mathbf{L}_{k,mn} = i \left\langle \frac{\partial u_{km}}{\partial \mathbf{k}} \right| \times \left(\widehat{H}_0 - \frac{\epsilon_{km} + \epsilon_{kn}}{2} \right) \left| \frac{\partial u_{kn}}{\partial \mathbf{k}} \right\rangle, \tag{6.7}$$

where m and n are band indices; ϵ and u are electronic energy and the periodic part of the wavefunction, respectively; $\widehat{H}_0$ is the zero-field Hamiltonian operator. Eq. 6.7 can be proven equivalent to $\mathbf{L} = \mathbf{0.5} * (\mathbf{r} \times \mathbf{p} - \mathbf{p} \times \mathbf{r})$ with $\mathbf{r}$ and $\mathbf{p}$ the position and momentum operator respectively. The detailed implementation of Eq. 6.7 is described in Ref. [238]. Our implementation of $\mathbf{L}$ has been benchmarked against previous theoretical and experimental data for monolayer MoS_2 (Table S1).

***g*-factor of free carriers.** In experimental and model Hamiltonian theory studies[235, 10], g-factor is defined from the ratio between either $\mathbf{B}^{\text{ext}}$-induced energy splitting $\Delta E\left(\mathbf{B}^{\text{ext}}\right)$ or Larmor precession frequency $\Omega\left(\mathbf{B}^{\text{ext}}\right)$ to $\mu_B B$. Therefore, we define g-factor of an electron or a hole at state $\mathbf{k}$,

$$g_k^S = \theta_k^S \left(\widehat{\mathbf{B}^{\text{ext}}} \right) \frac{\Delta E_k \left(\mathbf{B}^{\text{ext}} \right)}{\mu_B B^{\text{ext}}}, \tag{6.8}$$

where g_k^S is g-factor defined based on spin expectation values. $\widehat{\mathbf{B}^{\text{ext}}}$ is the unit vector along $\mathbf{B}^{\text{ext}}$. $\Delta E_k \left(\mathbf{B}^{\text{ext}} \right)$ is the energy splitting due to finite $\mathbf{B}^{\text{ext}}$. $\theta_k^S \left(\widehat{\mathbf{B}^{\text{ext}}} \right)$ is the sign of $S_{k,h}^{\text{exp}} \left(\widehat{\mathbf{B}^{\text{ext}}} \right) - S_{k,l}^{\text{exp}} \left(\widehat{\mathbf{B}^{\text{ext}}} \right)$, where $S_{k,h}^{\text{exp}} \left(\widehat{\mathbf{B}^{\text{ext}}} \right)$ and $S_{k,l}^{\text{exp}} \left(\widehat{\mathbf{B}^{\text{ext}}} \right)$ are the spin expectation value (exp) of the higher (h) and lower (l) energy band at $\mathbf{k}$ projected to the direction of $\widehat{\mathbf{B}^{\text{ext}}}$ respectively.

However, in previous theoretical studies of perovskites [258, 235], g-factors were defined based on pseudo-spins related to the total magnetic momenta J^{at}, which are determined from the atomic-orbital models. The pseudo-spins can have opposite

directions to the actual spins. Most previous experimental studies adopted the same convention for the signs of carrier g-factors. Therefore, to compare with g-factors obtained in previous theoretical and experimental studies, we introduce a correction factor $C^{\mathrm{S}\to\mathrm{J}}$ and define a new g-factor:

$$\widetilde{g}_k\left(\widehat{\mathbf{B}^{\mathrm{ext}}}\right) = C^{S\to J} g_k^S. \tag{6.9}$$

$C^{\mathrm{S}\to\mathrm{J}} = m_S^{\mathrm{at}}/m_J^{\mathrm{at}}$ with m_J^{at} and m_S^{at} the total and spin magnetic momenta respectively, obtained from the atomic-orbital model [235]. $C^{\mathrm{S}\to\mathrm{J}}$ is independent from k-point, and is ∓ 1 for electrons and holes respectively for $CsPbBr_3$.

$\widetilde{g}_k$ is different at different $\mathbf{k}$; therefore we define its statistically averaged value (depending on temperature T and chemical potential $\mu_{F,c}$) as

$$\bar{\widetilde{g}} = \frac{\sum_k \left(-f_k'\right)\widetilde{g}_k}{\sum_k \left(-f_k'\right)}, \tag{6.10}$$

and its fluctuation amplitude as

$$\Delta\widetilde{g} = \sqrt{\frac{\sum_k \left(-f_k'\right)\left(\widetilde{g}_k - \bar{\widetilde{g}}\right)^2}{\sum_k \left(-f_k'\right)}}, \tag{6.11}$$

where f_k' is the derivative of the Fermi-Dirac distribution function. Here for simplicity the band index of f_k' is dropped considering both valence and conduction bands are two-fold degenerate.

We have further defined a more general g-factor as a tensor and its fluctuation amplitude in SI Sec. SV. For $CsPbBr_3$, we find different definitions predict quite similar values (differences are not greater than 10%).

Analysis of e-ph matrix elements. For EY spin relaxation, in the simplified picture of Fermi's golden rule (FGR), τ_s^{-1} is proportional to the modulus square of the

spin-flip scattering matrix element. As the e-ph scattering plays a crucial role in spin relaxation in $CsPbBr_3$, it is helpful to analyze the spin-flip e-ph matrix elements.

Note that most matrix elements are irrelevant to spin relaxation and we need to pick the "more relevant" ones, by defining a weight function related to occupation and energy conservation. Therefore we propose a T and $\mu_{F,c}$ dependent effective modulus square of the spin-flip e-ph matrix element $\overline{|\widetilde{g}^{\uparrow\downarrow}|^2}$ as

$$\overline{|\widetilde{g}^{\uparrow\downarrow}|^2} = \frac{\sum_{kq} \mathrm{w}_{k,k-q} \sum_{\lambda} |g^{\uparrow\downarrow,q\lambda}_{k,k-q}|^2 n_{q\lambda}}{\sum_{kq} \mathrm{w}_{k,k-q}}, \tag{6.12}$$

$$\mathrm{w}_{k,k-q} = f_{k-q}\left(1-f_k\right)\delta\left(\epsilon_k - \epsilon_{k-q} - \omega_c\right), \tag{6.13}$$

where $g^{\uparrow\downarrow,q\lambda}_{k,k-q}$ is e-ph matrix element, related to a scattering event between two electronic states of opposite spins at $\mathbf{k}$ and $\mathbf{k}-\mathbf{q}$ through phonon mode λ at wavevector q; $n_{q\lambda}$ is phonon occupation; f_k is Fermi-Dirac function; ω_c is the characteristic phonon energy specified below, and $\mathrm{w}_{k,k-q}$ is the weight function. Here we drop band indices for simplicity, as $CsPbBr_3$ bands are two-fold Kramers degenerate and only two bands are relevant to electron and hole spin/carrier dynamics.

The matrix element modulus square is weighted by $n_{q\lambda}$ since τ_s^{-1} is approximately proportional to $n_{q\lambda}$ according to Eq. 5 of Ref. [71]. This rules out high-frequency phonons at low T which are not excited. ω_c is chosen as 4 meV at 10 K based on our analysis of phonon-mode-resolved contribution to spin relaxation. The trends of $\overline{|\widetilde{g}^{\uparrow\downarrow}|^2}$ are found not sensitive to ω_c as checked. $\mathrm{w}_{k,k-q}$ selects transitions between states separated by ω_c and around the band edge or $\mu_{F,c}$, which are "more relevant" transitions to spin relaxation.

We also define a q-resolved modulus square of the spin-flip e-ph matrix element $|\widetilde{g}^{\uparrow\downarrow}|^2(q)$ as

$$|\widetilde{g}^{\uparrow\downarrow}|^2(q) = N_k^{-1} \sum_{k\lambda} |g_{k,k-q}^{\uparrow\downarrow,q\lambda}|^2 n_{q\lambda}. \tag{6.14}$$

Note that for spin relaxation, only states around the band edges are relevant. Thus we restrict $|\epsilon_k - \epsilon_{\text{edge}}|$ <180 meV for the calculation of Eq. 6.14, which is about $7k_BT$ at 300 K relative to the band edge energy (ϵ_{edge}).

Analysis of the EY spin relaxation rate. According to FGR, the EY spin relaxation rate of an electronic state should be also proportional to the density of pair states allowing spin-flip scattering between them. Therefore, we propose a scattering density of states D^{S} (which is T and $\mu_{F,c}$ dependent),

$$D^{\text{S}}(T, \mu_{F,c}) = \frac{2N_k^{-2} \sum_{kq} \text{w}_{k,k-q}}{N_k^{-1} \sum_k f_k (1 - f_k)}. \tag{6.15}$$

D^{S} can be regarded as an effective density of spin-flip or spin-conserving e-ph transitions satisfying energy conservation between one state and its pairs (considering that the number of spin-flip and spin-conserving transitions are the same for Kramers degenerate bands).

When $\omega_c = 0$ (i.e. elastic scattering), we have

$$D^{\text{S}} = \int d\epsilon \left(-\frac{df}{d\epsilon}\right) D^2(\epsilon) \Big/ \int d\epsilon \left(-\frac{df}{d\epsilon}\right) D(\epsilon) \tag{6.16}$$

with $D(\epsilon)$ density of electronic states (DOS). So D^{S} can be roughly regarded as an weighted averaged DOS with weight $\left(-\frac{df}{d\epsilon}\right) D(\epsilon)$.

With $\overline{|\widetilde{g}^{\uparrow\downarrow}|^2}$ and D^{S}, we have the approximate relation for spin relaxation rate,

$$\tau_s^{-1} \propto \overline{|\widetilde{g}^{\uparrow\downarrow}|^2} D^{\mathrm{S}}. \tag{6.17}$$

We then discuss $\mu_{F,c}$ dependence of τ_s^{-1} at low n_c limit. For simplicity, we only consider conduction electrons. At low n_c limit, we have $\exp\left[\left(\epsilon - \mu_{F,c}\right)/\left(k_B T\right)\right] \gg 1$, thus

$$f_{k-q}\left(1 - f_k\right) \approx \exp\left(\frac{\mu_{F,c}}{k_B T}\right) \exp\left(\frac{-\epsilon_{k-q}}{k_B T}\right). \tag{6.18}$$

Therefore, according to Eq. 6.12, 6.13 and 6.15, both $\overline{|\widetilde{g}^{\uparrow\downarrow}|^2}$ and D^{S} are independent from $\mu_{F,c}$ (as $\exp\left(\frac{\mu_{F,c}}{k_B T}\right)$ is cancelled out), so τ_s^{-1} is independent from $\mu_{F,c}$ and n_c at low n_c region, e.g. much lower than 10^{16} cm^{-3} for $CsPbBr_3$. We can similarly define spin conserving matrix elements $\overline{|\widetilde{g}^{\uparrow\uparrow}|^2}$ and $|\widetilde{g}^{\uparrow\uparrow}|^2(q)$ by replacing $g_{k,k-q}^{\uparrow\downarrow,q\lambda}$ to $g_{k,k-q}^{\uparrow\uparrow,q\lambda}$ in Eq. 6.12 and 6.14. Then we have the approximate relation for carrier relaxation rate due to e-ph scattering, $\tau_p^{-1} \propto \overline{|\widetilde{g}^{\uparrow\uparrow}|^2} D^{\mathrm{S}}$.

The Hamiltonian for model SOC. In general, the Hamiltonian for model SOC reads

$$H_k^{\mathrm{model}} = \overrightarrow{\Omega}_k^{\mathrm{model}} \cdot \mathbf{s}_k, \tag{6.19}$$

where $\overrightarrow{\Omega}_k^{\mathrm{model}}$ are Larmor precession vectors induced by $\mathbf{k}$-dependent $\mathbf{B}^{\mathrm{in}}$. $\mathbf{s}_k$ is spin operator. With the total electronic Hamiltonian $H_k = H_{0,k} + H_k^{\mathrm{model}}$, τ_s considering the effects of model SOC is obtained by solving the density-matrix master equation in Eq. 7.12.

For the Rashba field, $\overrightarrow{\Omega}_k^{\text{model}}$ in Eq. 6.19 is defined in the plane (xy plane here) surrounding Γ point,

$$\overrightarrow{\Omega}_k^{\text{model}} = \alpha^{\text{R}} f^{\text{cut}}\left(k/k_{\text{cut}}\right) \widehat{z} \times \mathbf{k}, \tag{6.20}$$

where α^{R} is the Rashba SOC strength coefficient. $f^{\text{cut}}\left(k/k_{\text{cut}}\right)$ is 1 at small k but vanishes at large k. It is introduced to truncate the SOC fields at $k > k_{\text{cut}}$ smoothly in order to avoid unphysical band structures around first Brillouin zone boundaries. It is taken as

$$f^{\text{cut}}\left(k/k_{\text{cut}}\right) = \left\{\exp\left[10\left(k/k_{\text{cut}} - 1\right)\right] + 1\right\}^{-1}. \tag{6.21}$$

k_{cut} is taken 0.12 bohr^{-1} for $CsPbBr_3$. This value is about half of the length of the shortest reciprocal lattice vector, about 0.28 bohr^{-1} for orthorhombic $CsPbBr_3$. We can see that f^{cut} is almost 1 at $\mathbf{k} = \Gamma$ but almost vanishes at first Brillouin zone boundaries.

Persistent Spin Helix (PSH) was first proposed by Bernevig et al.[242]. PSH has SU(2) symmetry which is robust against spin-conserving scattering. In general, for PSH SOC,

$$\overrightarrow{\Omega}_k^{\text{model}} \propto k_i \widehat{j}, \tag{6.22}$$

where directions i and j are orthogonal. PSH fields are all along the same axis (y axis here). We take

$$\overrightarrow{\Omega}_k^{\text{model}} = \alpha^{\text{PSH}} f^{\text{cut}}\left(k/k_{\text{cut}}\right) k_z \widehat{y}, \tag{6.23}$$

where α^{PSH} is the PSH SOC strength coefficient.

$T^*_{2,\mathrm{loc}}$ due to nuclear spin fluctuation. The Hamiltonian of hyperfine coupling between an electron spin and nuclear spins approximately reads[246, 10]

$$H^{\mathrm{hf}} = \overrightarrow{\Omega}_N \cdot \mathbf{s}, \tag{6.24}$$

$$\overrightarrow{\Omega}_N = V_u \sum_j A_j \left|\psi\left(\mathbf{R}_j\right)\right|^2 \mathbf{I}_j, \tag{6.25}$$

$$A_j = \frac{16\pi\mu_B\mu_j \left|u_c\left(\mathbf{R}_j\right)\right|^2}{3I_j}, \tag{6.26}$$

where $\overrightarrow{\Omega}_N$ is Larmor precession vector, related to the effective hyperfine field (called Overhauser field) generated by all nuclei and acting on electron spin. $\mathbf{s}$ is the spin operator of the electron. Eq. 6.25 specifically refers to the hyperfine Fermi contact interaction between an electron and nuclear spins. The sum in Eq. 6.25 goes over all nuclei. $\mathbf{I}_j$ is the spin operator of nucleus j. V_u is the unit cell volume. A_j is the hyperfine coupling constant considering only the Fermi contact contribution, which was assumed to be the dominant contribution in Refs. [10, 246, 247] for $CsPbBr_3$ and GaAs. μ_j and I_j are the magnetic moment and spin of nucleus j, respectively. μ_B is the Bohr magneton. $\psi\left(\mathbf{R}_j\right)$ and $u_c\left(\mathbf{R}_j\right)$ are the electron envelope wave function and the electron Bloch function at the j-th nucleus respectively, whose product gives the electronic wavefunction $\Phi(\mathbf{R}_j) = V_u\psi\left(\mathbf{R}_j\right).u_c\left(\mathbf{R}_j\right)$ as in Ref. [246]. The normalization conditions are $\int_V \left|\psi\left(\mathbf{R}_j\right)\right|^2 dv = 1$ and

$$\int_{V_u} \left|u_c\left(\mathbf{R}_j\right)\right|^2 dv = 1. \tag{6.27}$$

With this definition, $|u_c(\mathbf{R}_j)|^2 \propto 1/V_u$, therefore, from Eq. 6.26,

$$A_j \propto 1/V_u. \tag{6.28}$$

The value of A_j depends on the isotope of the nucleus. For $CsPbBr_3$, it was found that the relevant isotopes are ^{207}Pb with natural abundance of about 22% for holes, and ^{79}Br and ^{81}Br for electrons [10]. Since the total abundance of ^{79}Br and ^{81}Br is almost 100% and their nuclear spins are both 3/2, ^{79}Br and ^{81}Br can be treated together.

According to the proportional relation in Eq. 6.28, A_j of orthorhombic $CsPbBr_3$ is approximately 1/4 of A_j of cubic $CsPbBr_3$, considering that their Bloch functions at the band edges are similar [259] (e.g., their hole Bloch functions both have significant Pb-s-orbital contribution), and V_u of orthorhombic $CsPbBr_3$ is about 4 times of that of cubic $CsPbBr_3$. Therefore, using estimated A_j of cubic $CsPbBr_3$ in Ref. [10], we obtain that A_j of ^{207}Pb for holes is about 25 μeV and A_j of Br for electrons is about 1.75 μeV.

When nuclear spins are not polarized (due to $\mathbf{B}^{\text{ext}}$=0), the nuclear field is zero on average. However, due to the finite number of nuclei interacting with the localized electron, there are stochastic nuclear spin fluctuations, which are characterized by the probability distribution function [245]

$$P\left(\overrightarrow{\Omega}_N\right) = \frac{1}{\left(\sqrt{\pi}\sigma_{\Omega_N}\right)^3} \exp\left(-\frac{\Omega_N^2}{\sigma_{\Omega_N}^2}\right), \tag{6.29}$$

where σ_{Ω_N} determines the dispersion of hyperfine field, and the angular brackets denotes the statistical averaging: $\left\langle \Omega_N^2 \right\rangle = 3\sigma_{\Omega_N}^2/2$. For the independent and ran-

domly oriented nuclear spins, we have (at $\mathbf{B}^{\text{ext}}$=0)

$$\sigma_{\Omega_N}^2 = \frac{2V_u^2}{3} \sum_{j_u\xi} \alpha_\xi I_{j_u\xi} \left(I_{j_u\xi}+1\right) A_{j_u\xi}^2 \sum_c \left|\psi\left(\mathbf{R}_{j_uc}\right)\right|^4, \tag{6.30}$$

where j_u is nucleus index in the unit cell, ξ is the isotope, and c is the unit cell index in the whole system. α_ξ is the abundance of isotope ξ. Since $\psi\left(\mathbf{R}_{j_uc}\right)$ usually varies slowly on the scale of a unit cell, $V_u \sum_c \left|\psi\left(\mathbf{R}_{j_uc}\right)\right|^4$ can be replaced by an integral in the whole system - $\int \left|\psi\left(\mathbf{r}\right)\right|^4 d\mathbf{r}$. Define $V^{\text{loc}} = 1/\int \left|\psi\left(\mathbf{r}\right)\right|^4 d\mathbf{r}$. V^{loc} is the localization volume. Therefore (at $\mathbf{B}^{\text{ext}}$=0),

$$\sigma_{\Omega_N}^2 = C^{\text{loc}}/V^{\text{loc}}, \tag{6.31}$$

$$C^{\text{loc}} = \frac{2V_u}{3} \sum_{j_u\xi} \alpha_\xi I_{j_u\xi} \left(I_{j_u\xi}+1\right) A_{j_u\xi}^2. \tag{6.32}$$

With σ_{Ω_N}, $T_{2,\text{loc}}^*$ is often estimated based on FID mechanism[245, 246, 247] (Eq. 6.4) $T_{2,\text{loc}}^* \sim \sigma_{\Omega_N}^{-1}$.

As α_ξ, $I_{j_u\xi}$ and V_u can be easily obtained and with $A_{j_u\xi}$ estimated above, we obtain C^{loc} ~180 and ~530 nm^3 ns^{-2} for electrons and holes respectively. V^{loc} can be estimated from the localization radii r^{loc} of localized carriers,

$$V^{\text{loc}} = \frac{4\pi}{3}\left(r^{\text{loc}}\right)^3. \tag{6.33}$$

In Table S2, we listed values of the parameters used to calculate $T_{2,\text{loc}}^*$.

Experimental synthesis. Growth of $CsPbBr_3$ single crystal: Small $CsPbBr_3$ seeds were first prepared with fresh supersaturated precursor solution at 85 °C. Small and transparent seeds were then picked and put on the bottom of the vials for large crystal growth. The temperature of the vials was set at 80 °C initially with an increasing

rate of 1 °C/ h, and was eventually maintained at 85 °C. Vials were covered with glass slides to avoid fast evaporation of the DMSO. So the growth driving force is supersaturation achieved by slow evaporation of DMSO solvent. After 120-170 hours, a centimeter-sized single crystal was picked from the solution, followed by wiping the residue solution on the surface.

Experimental Spin Lifetime Measurement. For measuring the spin lifetime in $CsPbBr_3$ single crystals, we have used the ultrafast circularly-polarized photoinduced reflectivity (PPR) method at liquid He temperature under the influence of a magnetic field. The experimental setup was described elsewhere [260]. It is a derivative of the well-known 'pump-probe' technique, where the polarization of the pump beam is modulated by a photoelastic modulator between left (δ^+) and right (δ^-) circular polarization, namely LCP and RCP, respectively. Whereas the probe beam is circularly polarized (either LCP or RCP) by a quarter-wave plate. The transient change in the probe reflection, namely c-PPR(t), was recorded. The 405 nm pump beam, having 150 femtoseconds pulse duration at 80 MHZ repetition rate, was generated by frequency doubling the fundamental at 810 nm from the Ti:Sapphire laser (Spectra Physics) using a SHG BBO crystal. The 533 nm probe beam was generated by combining the 810 nm fundamental beam with the 1560 nm infrared beam from an OPA (optical parametric amplifier) onto a BBO type 2 SFG (Sum Frequency Generation) crystal. The pump/probe beams having average intensity of 12 Wcm^{-2} and 3 Wcm^{-2}, respectively were aligned onto the $CsPbBr_3$ crystal that was placed inside a cryostat with a built-in electro-magnet that delivered a field strength, B up to 700 mT at temperatures down

to 4 K. Using this technique we measured both t-PPR responses at both zero and finite B to extract the B-dependent electron and hole spin lifetimes. From the c-PPR(B,t) dynamics measured on (001) facet with B directed along [010] [260] (see example c-PPR(B,t) dynamics in SI Fig. S15), we could obtain the electron and hole T_2^* by fitting the transient quantum beating response with two damped oscillation functions:

$$A_1 e^{\frac{-t}{T_{2,e}^*}} cos(2\pi f_1 t + \phi_1) + A_2 e^{\frac{-t}{T_{2,h}^*}} cos(2\pi f_2 t + \phi_2), \tag{6.34}$$

where $T_{2,e}^*$ and $T_{2,h}^*$ are the spin dephasing times of the electrons and holes; f1 and f2 are the two QB frequencies that can be obtained directly from the fast Fourier transform of the c-PPR dynamics.

Chapter 7

Anisotropy of Spin Lifetime in Perovskites due to Symmetry Breaking

As a continuation of the study on spin dynamics in perovskites presented in Chapter 6, the study in this chapter aims to explain the anisotropy of spin lifetime of the hybrid inorganic-organic perovskite $MAPbBr_3$ that is observed from experiment. The anisotropy of spin lifetime is attributed to the dynamical Rashba splitting in the reciprocal space, caused by symmetry breaking induced by the vibration of organic molecule that transfers to the inorganic sublattice.

In addition, the ferroelectric $MPSnBr_3$, which shows persistent spin helix due to the strong electric dipole that breaks the inversion symmetry, is investigated and found to exhibit stronger anisotropy of spin lifetime of electrons. The study of $MAPbBr_3$ and $MPSnBr_3$ provides more insight into the relationship between spin lifetime and symmetry, offering guidance to the advanced design of materials for spintronics.

7.1 Introduction

The field of spintronics has gained significant attention in recent years, due to its application potential for low-power electronics [210, 30, 211, 212, 213]. Spintronics utilizes the spin degree of freedom to encode and manipulate information, offering a promising alternative to traditional charge-based electronics. However, one of the primary challenges in creating efficient spintronic devices is to achieve both long spin lifetimes and strong spin-orbit coupling (SOC) simultaneously [261, 262, 227]. These two properties are essential for retaining stable quantum information and enabling the precise control of spin states, respectively.

Halide perovskites have emerged as strong candidates for spintronic applications due to their unique combination of long spin lifetimes, strong SOC, and tunable symmetry [33, 10, 216, 9, 34, 217]. Some of these materials also exhibit large Rashba splitting [263, 261] and persistent spin helix (PSH) texture with SU(2) symmetry [34], which highlight their potential for future spintronics applications.

In this first-principles study, we investigate the spin relaxation and dephasing in the three-dimensional hybrid perovskite systems under zero and finite magnetic fields. We found that the spin relaxation of centrosymmetric $MAPbBr_3$ is nearly isotropic and closely resembles that of $CsPbBr_3$ [74, 216], when both materials have the same *Pnma* crystal symmetry. The spin dephasing under magnetic field is slightly anisotropic due to the weak anisotropy of the g factor fluctuation. Therefore, this alone does not explain the large anisotropy of spin lifetime (up to 2.5) observed experimentally. Interestingly, when the symmetry is broken due to structural dynamics such as molecular rotation (which

has the same time scale with spin lifetime at room temperature), the spin relaxation becomes anisotropic, attributed to the spin split induced by symmetry broken. This trend and spin lifetime anisotropy ratio align with the experimental observation and underscores the importance of structural dynamics and symmetry on spin relaxation.

At the end, we used the permanent symmetry broken example, $MPSnBr_3$, to show an significant spin lifetime anisotropy at a range of 20-50. In particular we found such large anisotropy correlates with its PSH spin texture, and the corresponding spin lifetime parallel to spin texture shows dominantly spin-flip Elliot-Yafet mechanism. Our work pointed out the strong tunability of spin dynamics properties in halide pervoskites, and provided fundamental insights to guide materials design of pervoskites for spintronics applications.

7.2 Results and Discussion

7.2.1 Spin Lifetime of $MAPbBr_3$ with Centro-symmetry

By employing our first-principles density-matrix dynamics (FPDM) method (more details in computational detail), first we focus on the intrinsic spin relaxation of centrosymmetric $MAPbBr_3$ at *Pnma* crystal symmetry. This is crucial for understanding its behavior under more complex external conditions. For the intrinsic spin relaxation, we include both electron-electron (e-e) and electron-phonon (e-ph) scattering processes. Since the e-e scattering process is negligible compared to electron-phonon (shown in SM Fig. S1), its spin relaxation is mainly attributed to electron-phonon scat-

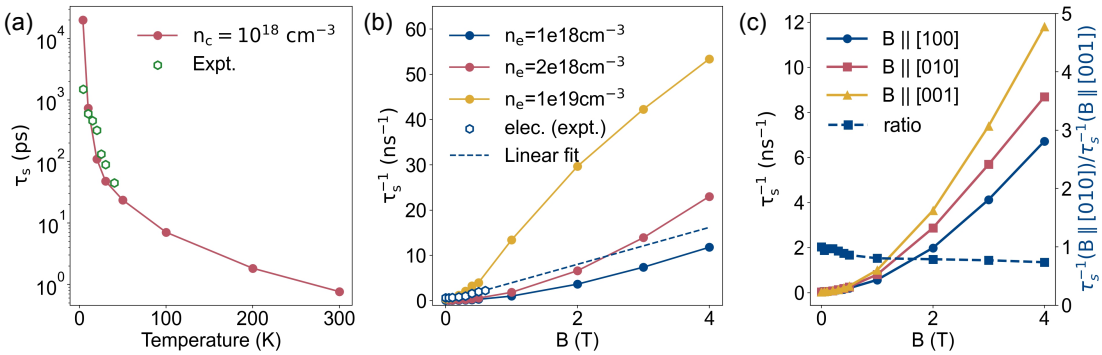

Figure 7.1: Electron Spin lifetime of centrosymmetric $MAPbBr_3$. (a) Temperature-dependent electron spin lifetimes $\tau_{s,z}$ from the FPDM calculations and experiments [15]. The experiment is performed at a laser power of 800 μW, corresponding to carrier concentration of 10^{18} cm^{-3}. (b) Magnetic field-dependent spin dephasing rate of electrons at T = 4 K, with carrier concentrations of 1×10^{18}, 2×10^{18} and 1×10^{19} cm^{-3}. The experimental data measured at $P = 100$ mW, with the dashed line as a linear fit of last three points. $\tau_{s,x}$ is measured with the external **B** along [001]. (c) Anisotropy of spin dephasing rate of electrons. $\tau_{s,y}$ is measured for **B** $\parallel$ [100], and $\tau_{s,x}$ is measured for **B** $\parallel$ [010] and **B** $\parallel$ [001]. The data points with the blue dashed line represent the ratio of $\tau_s^{-1}(B \parallel [010])/\tau_s^{-1}(B \parallel [001])$.

terings and spin-orbit couplings.

As shown in Fig. 7.1(a), under zero magnetic field, the spin relaxation time (T_1) in $MAPbBr_3$ decreases with increasing temperature. This trend is primarily caused by an increased phonon occupation at higher temperatures, and correspondingly, stronger electron-phonon scattering strength, facilitating spin-flip transition dominated by the Elliot-Yafet (EY) mechanism [227, 264], as can be seen in SM Fig. S3. Such temperature dependence is similar to what we found in $CsPbBr_3$ earlier [74].

The phonon contribution to electron-phonon interaction in $MAPbBr_3$ involves complex molecular-inorganic lattice hybrid vibrational modes due to the inclusion of the organic MA molecule comparing with previous studies on $CsPbBr_3$ [74]. Contrary to the common assumption that LO phonons via the Fröhlich interaction are the major contributors to spin relaxation [10, 12, 265], the spin relaxation is primarily caused by lower-energy optical phonons in the energy range from 2-6 meV as shown by the phonon dispersion in SM Fig. S4. This contribution of phonon is evidenced by the spin lifetimes determined by electron interacting with different groups of phonons in SM Fig. S5(a). In particular, the spin-flip electron-phonon matrix elements in SM Fig. S6(a) that are most relevant to spin relaxation, show distinct phonon dependence from the spin-conserving matrix elements. On the other hand, the Fröhlich like phonon modes, giving rise to a large LO-TO splitting at $13 - 21$ meV, consistent with the strong Raman intensity at 12.3 meV, 12.6 meV, 16.2 meV and 22.3 ± 0.6 meV [266, 267]. They have large contribution to carrier relaxation through spin-conserving electron-phonon scattering processes, little to spin-flip processes or spin relaxation, as shown in SM Fig. S5(b) and

SM Fig. S6(b).

Next, we look at the spin dynamics of $MAPbBr_3$ at finite magnetic field. The k-dependent spin vectors, can undergo inhomogenous precession in an external magnetic field that is perpendicular to its initial spin direction, leading to spin dephasing, fundamentally because of g factor induced magnetic field fluctuations [227]. Specifically, the interaction of spin with an external magnetic field $\mathbf{B}$ is described by the following Hamiltonian approximately,

$$H_k(\mathbf{B}) = H_{0,k} + \mu_B \mathbf{B} \cdot (\mathbf{L}_k + g_0 \mathbf{S}_k) \tag{7.1}$$

where μ_B is the Bohr magneton, g_0 is the free-electron g-factor, and $\mathbf{S}$ and $\mathbf{L}$ are the spin and orbital angular momentum, respectively. We calculated $\mathbf{L}$ using Berry phase formalism with details in Refs. [238, 74]. Under the external magnetic field, the total spin decay rate under a magnetic field can be expressed as,

$$\tau_s^{-1}(\mathbf{B}) \approx \left(\tau_s^0\right)^{-1} + \left(\tau_s^{\Delta\Omega}\right)^{-1}(\mathbf{B}) \tag{7.2}$$

where $(\tau_s^0)^{-1}$ is the zero-field spin relaxation rate, $(\tau_s^{\Delta\Omega})^{-1}$ is the spin dephasing rate under external B field, and $\Delta\Omega$ is the fluctuation of the Larmor-precession-frequency expressed as,

$$\Delta\Omega = \mu_B B \Delta\widetilde{g} \tag{7.3}$$

where $\Delta\widetilde{g}$ is the fluctuation (or variation) of g factor, whose detailed derivation can be found in Ref. [74], with result shown in SM Fig. S7. $(\tau_s^{\Delta\Omega})^{-1}$ spin dephasing rate has been mainly discussed with Dyakonov-Perel (DP) mechanism at strong scattering

limit ($\tau_p \Delta\Omega \ll 1$), or free induction decay (FID) mechanisms at weak scattering limit ($\tau_p \Delta\Omega \gtrsim 1$) [223].

In Fig. 7.1(b), we show the spin dephasing at 4 K, at which temperature the spin relaxation due to electron-phonon coupling is weak, where the experimental reference in this work was carried out [74]. In comparison to the experiment, which is carried out at $P = 100$ mW, corresponding to the carrier density $n_c = 10^{18}$ cm^{-3}, our theoretical results show good agreement when $B^{\text{ext}} < 0.5$ T. The experimental data locate in-between $n_c = 1 \times 10^{18}$ cm^{-3} to 1×10^{19} cm^{-3} of the calculated results. The onset of the linear dependence on the magnetic field (FID mechanism) occurs earlier in experiments than theory. Additionally, a slightly higher spin dephasing rate has been observed experimentally, consistent with previous work on $CsPbBr_3$ [74]. This discrepancy may be attributed to the presence of nuclear spins. By estimation, the hyperfine interaction is mainly from the electron spin interacting with the nuclear spin of Pb and Br atoms, which ranges from 4×10^8 Hz to 6×10^9 Hz. The spin dephasing time (T_2^*) of localized carriers due to the hyperfine interaction is 0.6–8.0 ns for electrons and 0.35-4.60 ns for holes, setting the upper bound of spin lifetime at $B = 0$ T [74]. In Fig. 7.1(a), the discrepancy between theory and experiment at T$<$ 10 K could also be attributed to the hyperfine interaction-induced spin relaxation.

An interesting fact from our calculation is that the spin dephasing rate shows slight anisotropy between [001] and [010] at a finite magnetic field, with the factor of rate anisotropy ($\tau_s^{-1}(B \parallel [010])/\tau_s^{-1}(B \parallel [001])$) about 0.8, as can be seen in Fig. 7.1(c). However, the experimental results [15] show a factor of anisotropy $\sim$2.5

between $B \parallel [010]$ and $B \parallel [001]$. The stronger spin relaxation anisotropy in experiments indicates that some additional mechanisms may mediate spin relaxation and dephasing as discussed below.

7.2.2 Strong Spin Lifetime Anisostropy Induced by Dynamical Symmetry Breaking

The dynamical Rashba effect [268, 269, 270] offers a unique perspective for understanding the anisotropy of spin lifetime. According to the past studies [271, 272, 270, 269], the dynamical Rashba effect is induced by the local fluctuation of the organic cation MA that associatively distorts the inorganic sublattice. The local distortion within the nanometer scale at room temperature occurs on a sub-picosecond time scale, which is comparable with the spin lifetime at the same temperature. Given similar time scales of two events, the dynamical Rashba effect can inevitably affect the spin dynamics.

To understand the Rashba effect on the spin dynamics, instead of iterating many possible configurations of structure, we select the structure of $MAPbBr_3$ in the maximally polarized case, where all MA molecules nearly align in x-axis, as shown in Fig. 7.2(a). Such a structure has broken inversion symmetry under structure distortion due to the MA molecule. Because of the alignment of the MA molecules, a net electric polarization occurs in nearly x-axis, which induces a large internal effective magnetic field in y-z plane. Simultaneously, as in Fig. 7.2(b), the originally degenerate Kramer's pairs split (spin split at each k point), providing a Rashba-like spin texture, as shown

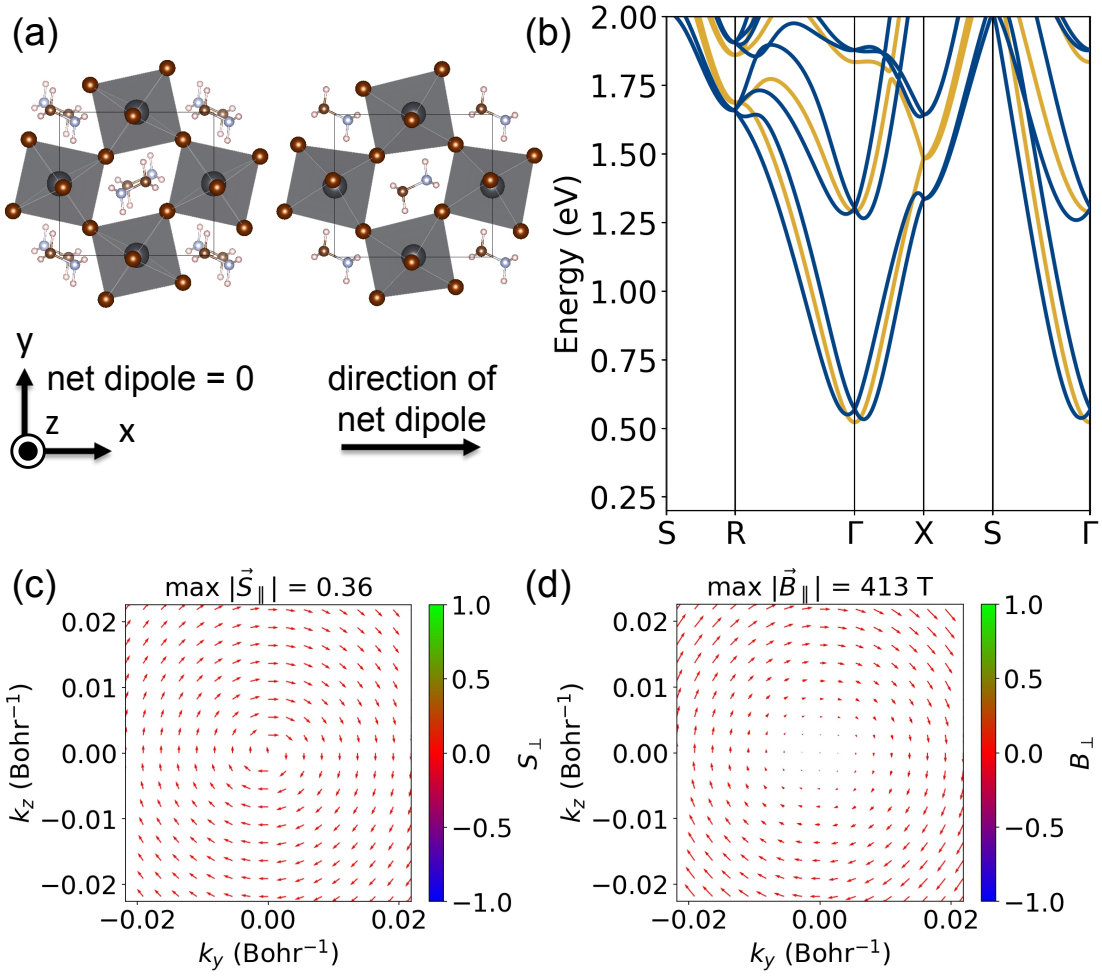

Figure 7.2: (a) Crystal structures of centrosymmetric (left) and asymmetric $MAPbBr_3$ (right), with zero and nonzero net dipole approximately pointing to x-axis, respectively. The choice of asymmetric $MAPbBr_3$ configuration is discussed in the main text. (b) The band structures of the centrosymmetric $MAPbBr_3$ (yellow) and asymmetric $MAPbBr_3$ (blue). The latter shows a band splitting at Γ due to symmetry breaking. (c) The Rashba-like spin texture in the y-z plane near the conduction band minimum. (d) The internal magnetic field in the y-z plane obtained from the product of spin expectation value and the band splitting by Eq. (7.8).

in Fig. 7.2(c). The following Hamiltonian H^{in} describing the interaction between the spin and internal magnetic field (an effective Zeeman Hamiltonian) provides a way to quantify the internal magnetic field of the asymmetric $MAPbBr_3$,

$$H^{\text{in}} = \frac{2g_0\mu_B}{\hbar}\mathbf{B}^{\text{in}}(\mathbf{k}) \cdot \mathbf{S}_{\mathbf{k}} \tag{7.4}$$

$$\mathbf{B}^{\text{in}}(\mathbf{k}) = C \cdot \mathbf{k} \tag{7.5}$$

$$C = C_s + C_v + C_t. \tag{7.6}$$

Here μ_B is the Bohr magneton, g_0 is the free-electron g-factor, $\mathbf{S}_{\mathbf{k}}$ is the spin angular momentum, $\mathbf{B}^{\text{in}}(\mathbf{k})$ is the internal magnetic field vector which can be represented by the product of coefficient tensor C and $\mathbf{k}$ vector. The factor of 2 accounts for the relative shift between two bands. This tensor C can be decomposed into the traceless antisymmetric part (Rashba), the symmetric part (Dresselhaus at the linear order), and the trace (Weyl contributions). More details see SM Sec. VI. As shown in Fig. 7.2(d), the internal B field is Rashba-like, dominated by the Rashba effect ($> 90\%$) with a small mixture of Dresselhaus effect ($< 10\%$). We find the Rashba splitting coefficient from fitting effective Zeeman Hamiltonian to be 1.18 eV Å. Alternatively, we calculate the effective Rashba splitting coefficient from the band splitting by the conventional definition $\alpha = \varepsilon/(2\Delta k) = 1.35$ eV Å, where ε and Δk are the energy difference between splitting bands and k distance from the reference high symmetry point, respectively [269]. Note that such definition assumes the spin split is completely from the Rashba SOC contribution, which is approximately true for this system ($> 90\%$ Rashba contribution from above). The calculated Rashba splitting coefficients from both methods are comparable

with the coefficient 1.4 eV Å extracted from experimental data on the same system [273]. This provides some experimental justification for the asymmetric structural model we used here.

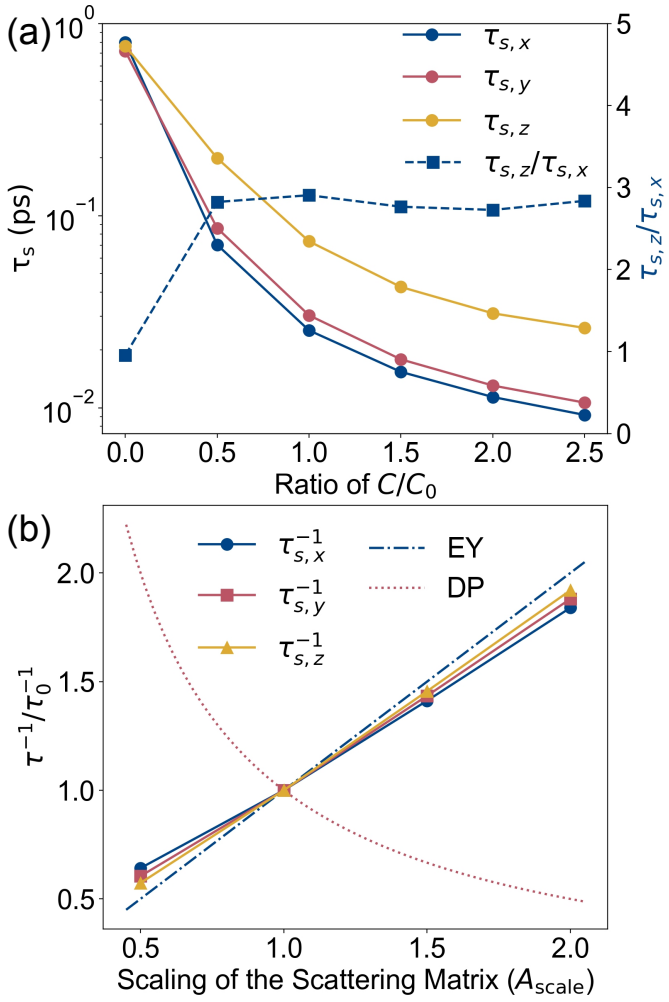

Figure 7.3: (a) Anisotropy of electron spin lifetime due to the internal magnetic field of asymmetric $MAPbBr_3$ at 300 K. The general effect that splits band structure is represented by the C tensor in Eq. (7.5), and C_0 is the fitted tensor for asymmetric $MAPbBr_3$. (b) Spin relaxation mechanism of asymmetric $MAPbBr_3$ at 300 K.

As shown in Fig. 7.3(a), the spin lifetime reduces monotonically by scaling up the coefficient C (increasing C/C_0 ratio), where C_0 is the coefficient directly fitted from the internal magnetic field of the asymmetric $MAPbBr_3$. The Rashba effect creates an inhomogeneous distribution of magnetic field in the momentum space, which is physically equivalent to the fluctuation or variation of Larmor precession ($\Delta\Omega \propto \Delta B^{in}$). This becomes another cause of spin decay ($\left(\tau_s^{-1}\right)^{\Delta\Omega}$) through spin precession in addition to the spin-flip relaxation ($\left(\tau_s^{-1}\right)|_{\Delta\langle B^{\text{in}}\rangle=0}$) as follows,

$$\tau_s^{-1} \approx \left(\tau_s^{-1}\right)|_{\Delta\langle B^{\text{in}}\rangle=0} + \left(\tau_s^{-1}\right)^{\Delta\Omega} \tag{7.7}$$

In particular, the Rashba-like SOC leads to the anisotropy of spin lifetime, i.e., the spin lifetime along y or z direction (in-plane) is longer than that in x direction (out-of-plane). The reason is that the fluctuation of internal magnetic field ($\Delta\langle B^{\text{in}}\rangle$) is stronger in the y-z plane than in the x-y and x-z planes, i.e. $\Delta\langle B^{\text{in}}\rangle_{xy} = 57.3$ T, $\Delta\langle B^{\text{in}}\rangle_{xz} = 119.1$ T and $\Delta\langle B^{\text{in}}\rangle_{yz} = 131.5$ T. Here the internal magnetic field $\mathbf{B^{in}}$ is evaluated according to

$$\mathbf{B}_{nk}^{\text{in}} = \frac{2\Delta_{nk}\mathbf{S}^{\text{exp}}}{g_e\mu_B} \tag{7.8}$$

$$\langle B^{\text{in}}\rangle_i = \sum_{nk} \frac{f'_{nk}B_{i;nk}^{\text{in}}}{\sum_{nk} f'_{nk}} \tag{7.9}$$

$$\Delta\langle B^{\text{in}}\rangle_i = \sqrt{\sum_{nk} \frac{f'_{nk}(B_{i;nk}^{\text{in}} - \langle B^{\text{in}}\rangle_i)^2}{\sum_{nk} f'_{nk}}} \tag{7.10}$$

$$\Delta\langle B^{\text{in}}\rangle_{ij} = \sqrt{\Delta\langle B^{\text{in}}\rangle_i^2 + \Delta\langle B^{\text{in}}\rangle_j^2} \tag{7.11}$$

where $\mathbf{B}_{nk}^{\text{in}}$ is the internal magnetic field as the product of the band splitting Δ_{nk} and spin expectation value $\mathbf{S}^{\text{exp}}$ at band n and k point. $\langle B^{\text{in}}\rangle_i$ and $\Delta\langle B^{\text{in}}\rangle_i$ are the

thermal average of the internal magnetic field and magnetic field fluctuation in i-th Cartesian direction, respectively, with f' being the derivative of Fermi-Dirac distribution function [73].

As the magnetic field fluctuation orthogonal to the spin direction of interest leads to spin relaxation or dephasing, stronger $\Delta\langle B^{\text{in}}\rangle$ effectively gives rise to faster Larmor precession and smaller spin lifetime. The weakest $\Delta\langle B^{\text{in}}\rangle_{xy}$ accounts for the longest spin lifetime $\tau_{s,z}$. The stronger and similar $\Delta\langle B^{\text{in}}\rangle_{xz}$ and $\Delta\langle B^{\text{in}}\rangle_{yz}$ account for the similarity between the shorter $\tau_{s,x}$ and $\tau_{s,y}$. Interestingly, the spin lifetime anisotropy aligns with the experimental observation [15] of ~2.5 across a wide range of the internal B field coefficient, as seen in Fig. 7.3(a). This suggests that the spin lifetime anisotropy has weak dependence on the size of Rashba coefficients, generated by the lattice polarization from molecular rotation.

7.2.3 Strong Spin Lifetime Anisotropy from Persistent Spin Helix

Next, we will show that the PSH spin texture can give rise to a significantly larger anisotropy in spin lifetime, using an example of $MPSnBr_3$, which has a crystal symmetry of Pc and a corresponding point group of C_s, as shown in Fig. 7.4(a). Compared to MA molecules, the MP molecule is more polarized and less likely to rotate around its center due to the high rotation energy barrier [274]. The highly polarized and stable alignment of the MP molecules give rise to a strong net dipole in the x-z plane and mostly along z-axis, which subsequently results in strong distortion in the inorganic sublattice and a permanent symmetry breaking. This results in an effective

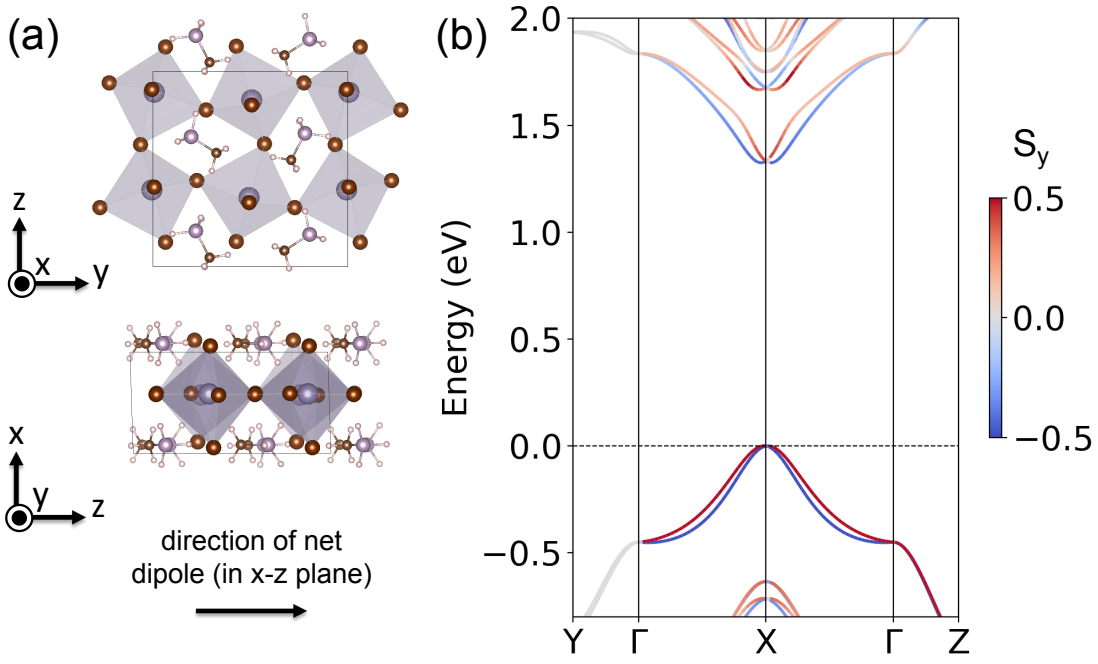

Figure 7.4: (a) Crystal Structure of $MPSnBr_3$ of P_c crystal symmetry. The net dipole due to the alignment of the MP molecules is in the x-z plane and mostly along the z-axis [16]. (b) Band structure of $MPSnBr_3$, showing spin polarization projected along the y-axis. The S_x and S_y spin polarization projection on band structure can be found in SM Fig. S9.

magnetic field in the x-y plane. Due to the C_s symmetry, a significant result is the persistent spin helix in the conduction band [275, 16, 276], with spin highly polarized in the y-axis, as shown in Fig. 7.4(b) and Fig. 7.5(a). We numerically fitted the internal B field Hamiltonian in Eq. 7.5 to confirm PSH, where Rashba and Dresselhaus contributions are nearly equal. Details can be found in SM Sec. X.

As shown in Fig. 7.5(b), the spin lifetime of electrons in the y axis is 20-50 times longer than the spin lifetime along the x and z axes. This remarkable anisotropy between y and the x-z plane is consistent with the strong spin polarization in the y axis. The significantly longer spin lifetime along the y-axis, compared to the x and z axes, can be explained by the suppression of spin scattering in the direction of PSH [277, 242]. Additionally, the spin lifetime of electrons in $MPSnBr_3$ is generally one order of magnitude shorter compared to that of centrosymmetric $MAPbBr_3$. This can be attributed to the exceptionally large internal magnetic field (maximally 956 T in the momentum space) of $MPSnBr_3$ and the small range of PSH in momentum space (approximately 20% of the first Brillouin zone, SM Fig. S10), which quickly transitions to a Rashba-like spin texture as it moves away from the band edge [16]. Consequently, there occurs the fluctuation of internal magnetic field, and $\Delta\langle B^{\text{in}}\rangle_{xz} = 38.1$ T is one order smaller than $\Delta\langle B^{\text{in}}\rangle_{xy} = 508.5$ T and $\Delta\langle B^{\text{in}}\rangle_{yz} = 509.5$ T. The fluctuation of the internal magnetic field leads to additional spin relaxation or dephasing that reduce the spin lifetime, as described by Eq. (7.7), and longer spin lifetime along the y direction than the z and x.

In contrast, as can be seen in SM Fig. S13(a), the spin lifetime of holes in the VBM is less anisotropic, and similar to the spin lifetime anisotropy of the asymmetric

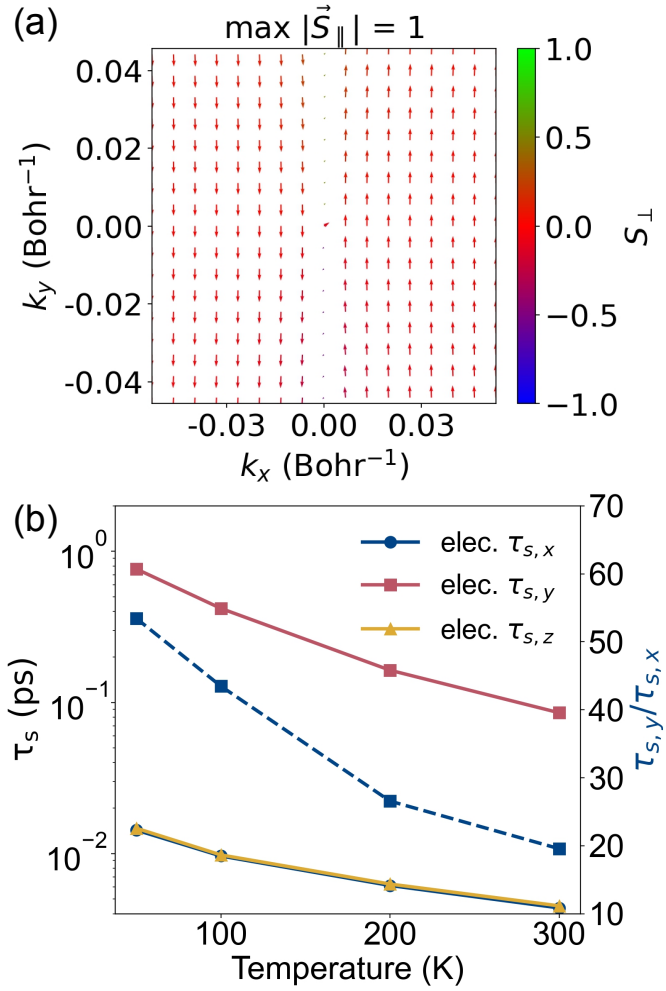

Figure 7.5: (a) The PSH spin texture at CBM centered at high symmetry point X. (b) Temperature-dependent spin lifetime of electrons in $MPSnBr_3$ at zero external magnetic field. The red, blue and yellow data points with solid lines represent the spin lifetime of electrons in x, y and z axes. The blue data points with the dashed line are the anisotropy of spin lifetime between y (parallel to PSH) and x (perpendicular to PSH) directions.

$MAPbBr_3$. This anisotropy is attributed to the Rashba-like spin texture at VBM in SM Fig. S13(b). Compared to the spin lifetime of holes, the spin lifetime of electrons in the y direction is more intringing, highlighting the fact that the spin lifetime can be more reliably controlled by the PSH. The attenuated protection of the PSH to spin relaxation suggests the need of materials that exhibit a larger range of PSH in the k space.

7.3 Conclusion

In summary, we present the spin dynamics study of hybrid inorganic-organic perovskites, $MAPbBr_3$ and $MPSnBr_3$, with a particular focus on elucidating the anisotropy of spin lifetime with the dynamical Rashba effect and permanent symmetry breaking.

We first present the theoretical spin lifetime of the centrosymmetric $MAPbBr_3$, which agrees with experimental observations, particularly in terms of temperature and magnetic field dependence. The EY, DP, and FID mechanisms are identified as the primary origins of spin relaxation and dephasing under zero, weak, and strong external magnetic fields, respectively. Besides, we reveal the distinct phonon mode dependence in carrier and spin relaxation.

However, the anisotropy of spin lifetime in $MAPbBr_3$ is much weaker than what is observed experimentally, suggesting additional mechanism yet to be identified. Specifically, we attribute the observed anisotropy to the dynamical Rashba effect due to molecular rotation, which occurs on a similar timescale as the spin lifetime, and has been observed in several past experiments. Our structural model for studying dynamical Rashba effect is supported by the consistent Rashba coefficient between theoretical

and experimental values. The symmetry breaking induced by the Rashba effect introduces additional DP/FID spin dephasing alongside the EY mechanism, resulting in the observed anisotropy in spin lifetime.

Finally, we calculate the spin lifetime of electrons and holes in $MPSnBr_3$ and find a large anisotropy of spin lifetime of electrons, as a result of permanent symmetry breaking. A significant enhancement of spin lifetime is observed in the parallel direction to PSH compared to the perpendicular directions. Even though the spin lifetime of $MPSnBr_3$ is shorter than the widely studied $CsPbBr_3$ and $MAPbBr_3$, our theoretical results provide in-depth understanding of the PSH effect on spin lifetime, and insights into the design of spintronics materials. We propose materials with strong SOC and a wide-range of PSH in k space to enable the simultaneous effective spin control and long spin lifetime for optimal spintronics applications.

7.4 Computational Methods

We perform electronic structure, phonon, Wannier calculations by using Quantum-Espresso [130] and JDFTx [253]. We choose the energy cutoff of wavefunction 74 Ry using the PseudoDojo Optimized Norm-Conserving Vanderbilt (ONCV) pseudopotential [278, 279]. We use the exchange-correlation functionals with Perdew-Burke-Ernzerhof (PBE) generalized gradient approximation [39] to optimize the lattice constants and internal geometry, and obtain phonon properties as well as single-particle electronic structure. We calculate the phonon and electron-phonon interaction by using the finite difference method with self-consistent SOC from the fully relativistic pseu-

dopotentials. The electron-electron interaction is calculated with screened Coulomb potential with Random-Phase-Approximation [72]. The perovskites involve the orthorhombic $MAPbBr_3$ of the $Pnma$ space group [280], and the monoclinic $MPSnBr_3$ of the Pc space group [274].

We simulate spin and carrier dynamics using the method of first-principles density-matrix dynamics (FPDM) [71, 72]. This involves solving a quantum master equation that governs the time evolution of the density matrix $\rho(t)$, depicted as follows:

$$\begin{aligned}\frac{d\rho_{12}(t)}{dt} &= \big[H(\mathbf{B}),\rho(t)\big]_{12} \\ &+ \frac{1}{2}\sum_{345}\Big\{\big[I-\rho(t)\big]_{13}P_{32,45}\rho_{45}(t) \\ &- \big[I-\rho\,(t)\,\big]_{45}P^{*}_{45,13}\rho_{32}(t)\Big\} + H.C.\end{aligned} \tag{7.12}$$

Here the equation incorporates Larmor precession in the first term, and scattering processes in the second term. Within the first term, $H(\mathbf{B})$ represents the electronic Hamiltonian in the presence of a magnetic field $\mathbf{B}$, and $[H,\rho] = H\rho - \rho H$. The second term includes the general mechanisms that induce spin relaxation through the spin-orbit coupling (SOC). The generalized scattering-rate matrix P encompasses electron-phonon, electron-impurity, and electron- electron scattering processes including spin-orbit couplings, computed from first-principles [75]. The numeric indices are the contracted notation for the k-point and band of electronic states. The notation of $H.C.$ signifies Hermitian conjugate. Beginning with an initial density matrix initialized with a net spin, we evolve $\rho(t)$ over sufficient duration, typically ranging from hundreds of picoseconds to a few microseconds, using the Eq. 7.12. Subsequently, we compute the spin observable $S(t)$ from $\rho(t)$ and determine the spin lifetime from fitting $S(t)$. More

theoretical background and details can be found in Ref. [75].

7.5 Experimental Methods

The $MAPbBr_3$ thin films were prepared by using a precursor solution. Precursors CH_3NH_3Br and $PbBr_2$ are mixed in a molar ratio of 1:1 in solvant N,N-dimethylformamide, and the concentration of 0.8 mol/ml [15]. The $MAPbBr_3$ crystals were grown via antisolvent precipitation. X-ray-diffraction (XRD) measurements confirm the crystal structure and principal axes.

The ultrafast circularly-polarized photoinduced reflectivity (c-PPR) method [260, 15] is used to measure the spin lifetime of carriers in $MAPbBr_3$ single crystals. The PPR method is a derivative of the pump-probe technique, where the polarization of the pump beam is modulated by a photoelastic modulator between left circular polarization (LCP, δ^+) and right circular polarization (RCP, δ^-), and the probe beam is modulated to LCP/RCP by a quarter-wave plate. The pump beam is of 405 nm wavelength, 250 femtoseconds pulse duration, and 80 MHZ repetition rate. It is generated by frequency doubling the fundamental at 810 nm from the Ti:Sapphire laser (Spectra Physics) using a second-harmonic generator (SHG) barium borate (BBO) crystal. The 533 nm probe beam was generated by combining the 810 nm fundamental beam with the 1560 nm infrared beam from an optical parametric amplifier (OPA) onto a BBO type 2 SFG (Sum Frequency Generation) crystal. Using this technique we measured both t-PPR responses at both zero and finite B to extract the B-dependent spin lifetimes of electrons.

Chapter 8

Conclusion

This thesis presents the development and application of advanced first-principles methods to elucidate two key topics: the excited-state dynamics of solid-state spin defects and the spin dynamics of carriers in solids.

Chapter 3 introduces a group theory framework and procedure for describing spin defects, encompassing electronic states, SOC matrix elements, and Jahn-Teller electron-phonon couplings, all from a symmetry perspective. Chapter 4 and Chapter 5 further develop and apply these first-principles approaches, along with group theory, to provide deep insights into the chemical structure, static properties, and excited-state dynamics of solid-state spin defects. The long-debated question of the chemical structure of defects in hBN is addressed by identifying the C_2C_N defect as the candidate responsible for the 2 eV single-photon emitter. For the NV center in diamond, this work resolves long-standing inconsistencies between theory and experiment regarding intersystem crossing and provides the rates of internal conversion for ODMR. The ODMR

simulation tool developed here is demonstrated to be general and capable of providing robust simulations for various spin defects.

Chapter 6 and Chapter 7 detail the development and application of advanced first-principles density-matrix dynamics to study the spin dynamics of carriers in solids. These studies incorporate critical mechanisms, including electron-electron, electron-phonon, and electron-impurity interactions, to provide in-depth insights into the spin dynamics of carriers in various perovskite materials with different symmetries. This work offers valuable guidance for the design and development of spintronic materials.

There are still many challenges associated with spin defects. One is in identifying additional defect candidates with varying characteristics such as ZPL, total spin, ZFS, hyperfine parameters, and ODMR as observed in experiments. Moreover, the temperature has significant influence on the PL spectrum and ODMR of the NV center, as observed experimentally, and this is very challenging for first-principles calculations. Challenges related to spin dynamics in solids include the need for more accurate theoretical developments in electronic structure, a deeper understanding of the anharmonicity of lattice vibration on spin dynamics, and the effects of strong external magnetic fields.

Appendix A

Group Theory Derivation of Symmetry

A.1 Matrix Representations of the Symmetry Operations on Two Spins

Two spin wavefunctions are constructed by direct product

$$(\alpha,\beta)\otimes(\alpha,\beta)=(\alpha\otimes\alpha,\alpha\otimes\beta,\beta\otimes\alpha,\beta\otimes\beta)=(\alpha\alpha,\alpha\beta,\beta\alpha,\beta\beta) \tag{A.1}$$

Because they transform as follows under symmetry operation,

$$P_R[(\alpha,\beta)\otimes(\alpha,\beta)]=(P_R\alpha,P_R\beta)\otimes(P_R\alpha,P_R\beta) \tag{A.2}$$

$$=P_R\otimes P_R(\alpha\otimes\alpha,\alpha\otimes\beta,\beta\otimes\alpha,\beta\otimes\beta) \tag{A.3}$$

$$=P_R\otimes P_R(\alpha\alpha,\alpha\beta,\beta\alpha,\beta\beta) \tag{A.4}$$

the direct product of $P_R\otimes P_R$ can describe the transformation of two spin wavefunctions. A corollary can be deduced from the above that $\Pi^N P_R=P_R^1\otimes P_R^2\otimes\ldots\otimes P_R^{N-1}\otimes P_R^N$ serves as the symmetry operator for N spins.

The matrix representations of the two-spin symmetry operations are derived below by using the symmetry operation matrices in Sec. 3.6.5.

$$E \otimes E = \begin{pmatrix} 1 & 0 \\ 0 & 1 \end{pmatrix} \otimes \begin{pmatrix} 1 & 0 \\ 0 & 1 \end{pmatrix} = \begin{pmatrix} 1 & 0 & 0 & 0 \\ 0 & 1 & 0 & 0 \\ 0 & 0 & 1 & 0 \\ 0 & 0 & 0 & 1 \end{pmatrix} \tag{A.5}$$

$$C_3 \otimes C_3 = \begin{pmatrix} e^{-i\pi/3} & 0 \\ 0 & e^{i\pi/3} \end{pmatrix} \otimes \begin{pmatrix} e^{-i\pi/3} & 0 \\ 0 & e^{i\pi/3} \end{pmatrix} = \begin{pmatrix} e^{-i2\pi/3} & 0 & 0 & 0 \\ 0 & 1 & 0 & 0 \\ 0 & 0 & 1 & 0 \\ 0 & 0 & 0 & e^{i2\pi/3} \end{pmatrix} \tag{A.6}$$

$$C_3^{-1} \otimes C_3^{-1} = \begin{pmatrix} e^{i\pi/3} & 0 \\ 0 & e^{-i\pi/3} \end{pmatrix} \otimes \begin{pmatrix} e^{i\pi/3} & 0 \\ 0 & e^{-i\pi/3} \end{pmatrix} = \begin{pmatrix} e^{i2\pi/3} & 0 & 0 & 0 \\ 0 & 1 & 0 & 0 \\ 0 & 0 & 1 & 0 \\ 0 & 0 & 0 & e^{-i2\pi/3} \end{pmatrix} \tag{A.7}$$

$$\sigma_v \otimes \sigma_v = \begin{pmatrix} 0 & -1 \\ 1 & 0 \end{pmatrix} \otimes \begin{pmatrix} 0 & -1 \\ 1 & 0 \end{pmatrix} = \begin{pmatrix} 0 & 0 & 0 & 1 \\ 0 & 0 & -1 & 0 \\ 0 & -1 & 0 & 0 \\ 1 & 0 & 0 & 0 \end{pmatrix} \tag{A.8}$$

$$\sigma_v' \otimes \sigma_v' = \begin{pmatrix} 0 & e^{-i2\pi/3} \\ e^{-i\pi/3} & 0 \end{pmatrix} \otimes \begin{pmatrix} 0 & e^{-i2\pi/3} \\ e^{-i\pi/3} & 0 \end{pmatrix} = \begin{pmatrix} 0 & 0 & 0 & e^{i2\pi/3} \\ 0 & 0 & -1 & 0 \\ 0 & -1 & 0 & 0 \\ e^{-i2\pi/3} & 0 & 0 & 0 \end{pmatrix} \tag{A.9}$$

$$\sigma_v'' \otimes \sigma_v'' = \begin{pmatrix} 0 & e^{i2\pi/3} \\ e^{i\pi/3} & 0 \end{pmatrix} \otimes \begin{pmatrix} 0 & e^{i2\pi/3} \\ e^{i\pi/3} & 0 \end{pmatrix} = \begin{pmatrix} 0 & 0 & 0 & e^{-i2\pi/3} \\ 0 & 0 & -1 & 0 \\ 0 & -1 & 0 & 0 \\ e^{i2\pi/3} & 0 & 0 & 0 \end{pmatrix} \tag{A.10}$$

$$\bar{E} \otimes \bar{E} = \begin{pmatrix} -1 & 0 \\ 0 & -1 \end{pmatrix} \otimes \begin{pmatrix} -1 & 0 \\ 0 & -1 \end{pmatrix} = \begin{pmatrix} 1 & 0 & 0 & 0 \\ 0 & 1 & 0 & 0 \\ 0 & 0 & 1 & 0 \\ 0 & 0 & 0 & 1 \end{pmatrix} \tag{A.11}$$

$$\bar{C}_3 \otimes \bar{C}_3 = \begin{pmatrix} e^{i2\pi/3} & 0 \\ 0 & e^{-i2\pi/3} \end{pmatrix} \otimes \begin{pmatrix} e^{i2\pi/3} & 0 \\ 0 & e^{-i2\pi/3} \end{pmatrix} = \begin{pmatrix} e^{-i2\pi/3} & 0 & 0 & 0 \\ 0 & 1 & 0 & 0 \\ 0 & 0 & 1 & 0 \\ 0 & 0 & 0 & e^{i2\pi/3} \end{pmatrix} \tag{A.12}$$

$$\bar{C}_3^{-1} \otimes \bar{C}_3^{-1} = \begin{pmatrix} e^{-i2\pi/3} & 0 \\ 0 & e^{i2\pi/3} \end{pmatrix} \otimes \begin{pmatrix} e^{-i2\pi/3} & 0 \\ 0 & e^{i2\pi/3} \end{pmatrix} = \begin{pmatrix} e^{i2\pi/3} & 0 & 0 & 0 \\ 0 & 1 & 0 & 0 \\ 0 & 0 & 1 & 0 \\ 0 & 0 & 0 & e^{-i2\pi/3} \end{pmatrix} \tag{A.13}$$

$$\bar{\sigma}_v \otimes \bar{\sigma}_v = \begin{pmatrix} 0 & 1 \\ -1 & 0 \end{pmatrix} \otimes \begin{pmatrix} 0 & 1 \\ -1 & 0 \end{pmatrix} = \begin{pmatrix} 0 & 0 & 0 & 1 \\ 0 & 0 & -1 & 0 \\ 0 & -1 & 0 & 0 \\ 1 & 0 & 0 & 0 \end{pmatrix} \tag{A.14}$$

$$\bar{\sigma}'_v \otimes \bar{\sigma}'_v = \begin{pmatrix} 0 & e^{i\pi/3} \\ e^{i2\pi/3} & 0 \end{pmatrix} \otimes \begin{pmatrix} 0 & e^{i\pi/3} \\ e^{i2\pi/3} & 0 \end{pmatrix} = \begin{pmatrix} 0 & 0 & 0 & e^{i2\pi/3} \\ 0 & 0 & -1 & 0 \\ 0 & -1 & 0 & 0 \\ e^{-i2\pi/3} & 0 & 0 & 0 \end{pmatrix} \tag{A.15}$$

$$\bar{\sigma}''_v \otimes \bar{\sigma}''_v = \begin{pmatrix} 0 & e^{-i\pi/3} \\ e^{-i2\pi/3} & 0 \end{pmatrix} \otimes \begin{pmatrix} 0 & e^{-i\pi/3} \\ e^{-i2\pi/3} & 0 \end{pmatrix} = \begin{pmatrix} 0 & 0 & 0 & e^{-i2\pi/3} \\ 0 & 0 & -1 & 0 \\ 0 & -1 & 0 & 0 \\ e^{i2\pi/3} & 0 & 0 & 0 \end{pmatrix} \tag{A.16}$$

It can be found that for two-spin wavefunction which can be either $S = 1$ or $S = 0$, there is the equivalence $E = \bar{E}$, $C_3 = \bar{C}_3$, $C_3^{-1} = \bar{C}_3^{-1}$, $\sigma_v = \bar{\sigma}_v$, $\sigma_v' = \bar{\sigma}_v'$ and $\sigma_v'' = \bar{\sigma}_v''$.

Appendix B

ZFS Parameters and Symmetry

B.1 ZFS Parameters and Symmetry

Using the traceless ZFS tensor **D** [281], the ZFS Hamiltonian is written as

$$\begin{aligned} H &= \mathbf{S} \cdot \mathbf{D} \cdot \mathbf{S} \\ &= D_x S_x^2 + D_y S_y^2 + D_z S_z^2 \end{aligned} \tag{B.1}$$

By rewriting D_x and D_y into a symmetric form and an antisymmetric form, then

$$H = \frac{1}{2}(D_x + D_y)(S_x^2 + S_y^2) + \frac{1}{2}(D_x - D_y)(S_x^2 - S_y^2) + D_z S_z^2 \tag{B.2}$$

From the traceless **D** tensor we have

$$D_x + D_y + D_z = 0 \implies D_x + D_y = -D_z \tag{B.3}$$

Decomposing the total spin into the three orthogonal components,

$$\mathbf{S}^2 = S_x^2 + S_y^2 + S_z^2 \implies S_x^2 + S_y^2 = \mathbf{S}^2 - S_z^2 \tag{B.4}$$

when we choose the z-axis as the spin quantization axis, it is easy to find that

$$\begin{aligned} H &= \frac{1}{2}(-D_z)(\mathbf{S}^2 - S_z^2) + \frac{1}{2}(D_x - D_y)(S_x^2 - S_y^2) + D_z S_z^2 \\ &= D(S_z^2 - \frac{\mathbf{S}^2}{3}) + E(S_x^2 - S_y^2) \end{aligned} \tag{B.5}$$

with the axial and rhombic ZFS parameters being defined as [281],

$$D = \frac{3}{2}D_z \tag{B.6}$$

$$E = \frac{1}{2}(D_x - D_y) \tag{B.7}$$

By replacing the operator $\mathbf{S}^2$ with the expectation value $S(S+1)$, the hamiltonian is written as

$$H = D\left[S_z^2 - \frac{S(S+1)}{3}\right] + E(S_x^2 - S_y^2) \tag{B.8}$$

This form of the hamiltonian is convenient for the case that a magnetic field is along the spin quantization axis or spin principle axis (z-axis). For the case of spin quantization along x-axis, we can write the hamiltonian as

$$\begin{aligned} H &= \frac{1}{2}(D_y + D_z)(S_y^2 + S_z^2) + \frac{1}{2}(D_y - D_z)(S_y^2 - S_z^2) + D_x S_x^2 \\ &= \frac{1}{2}(-D_x)(\mathbf{S}^2 - S_x^2) + \frac{1}{2}(D_y - D_z)(S_y^2 - S_z^2) + D_x S_x^2 \\ &= \frac{3}{2}D_x\left(S_x^2 - \frac{\mathbf{S}^2}{3}\right) + \frac{1}{2}(D_y - D_z)(S_y^2 - S_z^2) \end{aligned} \tag{B.9}$$

Here we need to express D_x and $(D_y - D_z)$ in terms of D and E measured in experiments. To do that, we can rewrite Eq. (B.5) in terms of S_x^2 as follows,

$$\begin{aligned}
H &= D\left(S_z^2 - \frac{\mathbf{S}^2}{3}\right) + E(S_x^2 - S_y^2) \\
&= D\left(S_z^2 - \frac{S_x^2 + S_y^2 + S_z^2}{3}\right) + E(S_x^2 - S_y^2) \\
&= \left(E - \frac{D}{3}\right) S_x^2 - \left(\frac{D}{3} + E\right) S_y^2 + \frac{2D}{3} S_z^2 \\
&= \frac{3}{2}\left(E - \frac{D}{3}\right)\left(S_x^2 - \frac{S_x^2 + S_y^2 + S_z^2}{3}\right) + \frac{1}{2}\left(E - \frac{D}{3}\right)(S_y^2 + S_z^2) - \left(\frac{D}{3} + E\right) S_y^2 \\
&\quad + \frac{2D}{3} S_z^2 \\
&= \frac{3}{2}\left(E - \frac{D}{3}\right)\left(S_x^2 - \frac{\mathbf{S}^2}{3}\right) - \frac{D+E}{2}(S_y^2 - S_z^2)
\end{aligned} \tag{B.10}$$

Comparing Eq. (B.9) and Eq. (B.10), we can find the expression of D_x and D_y in terms of D by Eq. (B.6) and E Eq. (B.7) as follows,

$$D_x = E - \frac{D}{3} \tag{B.11}$$

$$D_y - D_z = -(D + E) \tag{B.12}$$

Likewise, in the case of a magnetic field along y-axis, we can find the hamiltonian to be

$$H = \frac{3}{2} D_y \left(S_y^2 - \frac{\mathbf{S}^2}{3}\right) + \frac{1}{2}(D_x - D_z)(S_x^2 - S_z^2) \tag{B.13}$$

$$H = -\frac{3}{2}\left(E + \frac{D}{3}\right)\left(S_y^2 - \frac{\mathbf{S}^2}{3}\right) - \frac{D-E}{2}(S_x^2 - S_z^2) \tag{B.14}$$

with

$$D_y = -\left(E + \frac{D}{3}\right) \tag{B.15}$$

$$D_x - D_z = -(D - E) \tag{B.16}$$

When there is axial symmetry, i.e. systems with x and y being degenerate, e.g. systems described by C_{3v}, D_{3h} and cubic systems, it can be found that $D_x = D_y$ and $E = 0$.

Bibliography

[1] Jeronimo R Maze, Adam Gali, Emre Togan, Yiwen Chu, Alexei Trifonov, Efthimios Kaxiras, and Mikhail D Lukin. Properties of Nitrogen-Vacancy Centers in Diamond: the Group Theoretic Approach. *New J. Phys.*, 13(2):025025, 2011.

[2] Tyler J Smart, Feng Wu, Marco Govoni, and Yuan Ping. Fundamental Principles for Calculating Charged Defect Ionization Energies in Ultrathin Two-Dimensional Materials. *Phys. Rev. Mater.*, 2(12):124002, 2018.

[3] Noah Mendelson, Dipankar Chugh, Jeffrey R Reimers, Tin S Cheng, Andreas Gottscholl, Hu Long, Christopher J Mellor, Alex Zettl, Vladimir Dyakonov, Peter H Beton, et al. Identifying Carbon as the Source of Visible Single-Photon Emission from Hexagonal Boron Nitride. *Nat. Mater.*, 20(3):321–328, 2021.

[4] JP Tetienne, L Rondin, P Spinicelli, M Chipaux, T Debuisschert, JF Roch, and V Jacques. Magnetic-Field-Dependent Photodynamics of Single NV Defects in Diamond: an Application to Qualitative All-Optical Magnetic Imaging. *New J. Phys.*, 14(10):103033, 2012.

[5] Ankit Rohatgi. WebPlotDigitizer User Manual Version 3.4. *WebPlotDigitizer*, pages 1–18, 2014.

[6] Erika Janitz, Konstantin Herb, Laura A Völker, William S Huxter, Christian L Degen, and John M Abendroth. Diamond Surface Engineering for Molecular Sensing with Nitrogen—Vacancy Centers. *J. Mater. Chem. C*, 10(37):13533–13569, 2022.

[7] Yu Jin, Marco Govoni, and Giulia Galli. Vibrationally Resolved Optical Excitations of the Nitrogen-Vacancy Center in Diamond. *npj Comput. Mater.*, 8(1):238, 2022.

[8] RJ Epstein, FM Mendoza, YK Kato, and DD Awschalom. Anisotropic Interactions of a Single Spin and Dark-Spin Spectroscopy in Diamond. *Nat. Phys.*, 1(2):94–98, 2005.

[9] Meng Zhou, Julio S Sarmiento, Chengbin Fei, Xinwen Zhang, and He Wang. Effect of composition on the spin relaxation of lead halide perovskites. *J. Phys. Chem. Lett.*, 11(4):1502–1507, 2020.

[10] Vasilii V Belykh, Dmitri R Yakovlev, Mikhail M Glazov, Philipp S Grigoryev, Mujtaba Hussain, Janina Rautert, Dmitry N Dirin, Maksym V Kovalenko, and Manfred Bayer. Coherent Spin Dynamics of Electrons and Holes in CsPbBr3 Perovskite Crystals. *Nat. Commun.*, 10(1):673, 2019.

[11] Philipp S Grigoryev, Vasilii V Belykh, Dmitri R Yakovlev, Emmanuel Lhuillier,

and Manfred Bayer. Coherent spin dynamics of electrons and holes in cspbbr3 colloidal nanocrystals. *Nano Lett.*, 21(19):8481–8487, 2021.

[12] Matthew J Crane, Laura M Jacoby, Theodore A Cohen, Yunping Huang, Christine K Luscombe, and Daniel R Gamelin. Coherent Spin Precession and Lifetime-Limited Spin Dephasing in CsPbBr3 Perovskite Nanocrystals. *Nano Lett.*, 20(12):8626–8633, 2020.

[13] Zhen Wu, Yuanyuan Zhang, Rongrong Hu, Meizhen Jiang, Pan Liang, Qing Yang, Li Deng, Tianqing Jia, Zhenrong Sun, and Donghai Feng. Hole-acceptor-manipulated electron spin dynamics in cdse colloidal quantum dots. *J. Phys. Chem. Lett.*, 12(8):2126–2132, 2021.

[14] Alex Greilich, R Oulton, EA Zhukov, IA Yugova, DR Yakovlev, M Bayer, A Shabaev, Al L Efros, IA Merkulov, V Stavarache, et al. Optical control of spin coherence in singly charged (in, ga) as/gaas quantum dots. *Phys. Rev. Lett.*, 96(22):227401, 2006.

[15] Uyen N Huynh, Rikard Bodin, Xin Pan, Paul Bailey, Haoliang Liu, Stephen McGill, Dmitry Semenov, Peter C Sercel, and Z Valy Vardeny. Magneto-optical studies of hybrid organic/inorganic perovskite: The case of methyl-ammonium lead bromide. *Phys. Rev. B*, 109(1):014316, 2024.

[16] Ravi Kashikar, PS Ghosh, S Lisenkov, A Stroppa, and I Ponomareva. Rashba effects in lead-free ferroelectric semiconductor [ch 3 ph 3] snbr 3. *Physical Review Materials*, 6(10):104603, 2022.

[17] Simon L Altmann and Peter Herzig. *Point-group theory tables*. Oxford University Press, 1994.

[18] Marcus W Doherty, Neil B Manson, Paul Delaney, and Lloyd CL Hollenberg. The Negatively Charged Nitrogen-Vacancy Centre in Diamond: the Electronic Solution. *New J. Phys.*, 13(2):025019, 2011.

[19] Audrius Alkauskas, Bob B Buckley, David D Awschalom, and Chris G Van de Walle. First-Principles Theory of the Luminescence Lineshape for the Triplet Transition in Diamond NV Centres. *New J. Phys.*, 16(7):073026, 2014.

[20] P Kehayias, MW Doherty, D English, R Fischer, Andrey Jarmola, K Jensen, N Leefer, P Hemmer, NB Manson, and Dmitry Budker. Infrared Absorption Band and Vibronic Structure of the Nitrogen-Vacancy Center in Diamond. *Phys. Rev. B*, 88(16):165202, 2013.

[21] Nicholas R Jungwirth and Gregory D Fuchs. Optical absorption and emission mechanisms of single defects in hexagonal boron nitride. *Phys. Rev. Lett.*, 119(5):057401, 2017.

[22] M Fischer, JM Caridad, A Sajid, S Ghaderzadeh, M Ghorbani-Asl, L Gammelgaard, Peter Bøggild, Kristian Sommer Thygesen, AV Krasheninnikov, Sanshui Xiao, et al. Controlled Generation of Luminescent Centers in Hexagonal Boron Nitride by Irradiation Engineering. *Sci. Adv.*, 7(8):eabe7138, 2021.

[23] Haider I Rasool, Colin Ophus, and Alex Zettl. Atomic defects in two dimensional materials. *Adv. Mater.*, 27(38):5771–5777, 2015.

[24] Jürgen Schneider and Karin Maier. Point defects in silicon carbide. *Physica B: Condens. Matter.*, 185(1-4):199–206, 1993.

[25] Carlo Bradac, Weibo Gao, Jacopo Forneris, Matthew E Trusheim, and Igor Aharonovich. Quantum nanophotonics with group iv defects in diamond. *Nat. Commun.*, 10(1):5625, 2019.

[26] Michael Lurie Goldman, MW Doherty, Alp Sipahigil, Norman Ying Yao, SD Bennett, NB Manson, Alexander Kubanek, and Mikhail D Lukin. State-Selective Intersystem Crossing in Nitrogen-Vacancy Centers. *Phys. Rev. B*, 91(16):165201, 2015.

[27] GD Cheng, YG Zhang, L Yan, HF Huang, Q Huang, YX Song, Y Chen, and Z Tang. A Paramagnetic Neutral CBVN Center in Hexagonal Boron Nitride Monolayer for Spin Qubit Application. *Comput. Mater. Sci.*, 129:247–251, 2017.

[28] Cesar Jara, Tomaýs˘ Rauch, Silvana Botti, Miguel AL Marques, Ariel Norambuena, Raul Coto, JE Castellanos-Aýguila, Jeronimo R Maze, and Francisco Munoz. First-Principles Identification of Single Photon Emitters Based on Carbon Clusters in Hexagonal Boron Nitride. *J. Phys. Chem. A*, 125(6):1325–1335, 2021.

[29] A Avsar, H Ochoa, Francisco Guinea, B Özyilmaz, BJ Van Wees, and Ivan J

Vera-Marun. Colloquium: Spintronics in graphene and other two-dimensional materials. *Rev. Mod. Phys.*, 92(2):021003, 2020.

[30] Juan F Sierra, Jaroslav Fabian, Roland K Kawakami, Stephan Roche, and Sergio O Valenzuela. Van der waals heterostructures for spintronics and opto-spintronics. *Nat. Nanotech.*, 16(8):856–868, 2021.

[31] Jose H Garcia, Marc Vila, Chuang-Han Hsu, Xavier Waintal, Vitor M Pereira, and Stephan Roche. Canted persistent spin texture and quantum spin hall effect in wte 2. *Phys. Rev. Lett.*, 125(25):256603, 2020.

[32] Libor Šmejkal, Yuriy Mokrousov, Binghai Yan, and Allan H MacDonald. Topological antiferromagnetic spintronics. *Nat. Phys.*, 14(3):242–251, 2018.

[33] Young-Hoon Kim, Yaxin Zhai, Haipeng Lu, Xin Pan, Chuanxiao Xiao, E Ashley Gaulding, Steven P Harvey, Joseph J Berry, Zeev Valy Vardeny, Joseph M Luther, et al. Chiral-induced spin selectivity enables a room-temperature spin light-emitting diode. *Sci.*, 371(6534):1129–1133, 2021.

[34] Lifu Zhang, Jie Jiang, Christian Multunas, Chen Ming, Zhizhong Chen, Yang Hu, Zonghuan Lu, Saloni Pendse, Ru Jia, Mani Chandra, et al. Room-temperature electrically switchable spin–valley coupling in a van der waals ferroelectric halide perovskite with persistent spin helix. *Nat. Photonics*, 16(7):529–537, 2022.

[35] Paul Adrien Maurice Dirac. Quantum mechanics of many-electron systems. *Proc.*

R. soc. Lond. Ser. A-Contain. Pap. Math. Phys. Character, 123(792):714–733, 1929.

[36] Pierre Hohenberg and Walter Kohn. Inhomogeneous electron gas. *Phys. Rev.*, 136(3B):B864, 1964.

[37] Walter Kohn and Lu Jeu Sham. Self-consistent equations including exchange and correlation effects. *Phys. Rev.*, 140(4A):A1133, 1965.

[38] John P Perdew and Alex Zunger. Self-interaction correction to density-functional approximations for many-electron systems. *Phys. Rev. B*, 23(10):5048, 1981.

[39] John P Perdew, Kieron Burke, and Matthias Ernzerhof. Generalized Gradient Approximation Made Simple. *Phys. Rev. Lett.*, 77(18):3865, 1996.

[40] David M Ceperley and Berni J Alder. Ground state of the electron gas by a stochastic method. *Phys. Rev. Lett.*, 45(7):566, 1980.

[41] Richard M Martin. *Electronic structure: basic theory and practical methods*. Cambridge university press, 2020.

[42] Jianwei Sun, John P Perdew, and Adrienn Ruzsinszky. Semilocal density functional obeying a strongly tightened bound for exchange. *Proc. Natl. Acad. Sci.*, 112(3):685–689, 2015.

[43] John P Perdew. Density functional theory and the band gap problem. *Int. J. Quantum Chem.*, 28(S19):497–523, 1985.

[44] John P Perdew and Mel Levy. Physical content of the exact kohn-sham orbital energies: band gaps and derivative discontinuities. *Physical Review Letters*, 51(20):1884, 1983.

[45] Axel D Becke. A new mixing of hartree–fock and local density-functional theories. *J. Chem. Phys.*, 98(2):1372–1377, 1993.

[46] Jochen Heyd, Gustavo E. Scuseria, and Matthias Ernzerhof. Erratum: "Hybrid functionals based on a screened Coulomb potential" [J. Chem. Phys. 118, 8207 (2003)]. *The Journal of Chemical Physics*, 124(21):219906, 06 2006.

[47] Jochen Heyd, Gustavo E Scuseria, and Matthias Ernzerhof. Hybrid Functionals Based on a Screened Coulomb Potential. *J. Chem. Phys.*, 118(18):8207–8215, 2003.

[48] Tyler J Smart, Kejun Li, Junqing Xu, and Yuan Ping. Intersystem Crossing and Exciton–Defect Coupling of Spin Defects in Hexagonal Boron Nitride. *npj Comput. Mater.*, 7(1):1–8, 2021.

[49] Kejun Li, Vsevolod D Dergachev, Ilya D Dergachev, Shimin Zhang, Sergey A Varganov, and Yuan Ping. Excited-state dynamics and optically detected magnetic resonance of solid-state spin defects from first principles. *arXiv preprint arXiv:2404.05917*, 2024.

[50] Viktor Ivády, Gergely Barcza, Gergő Thiering, Song Li, Hanen Hamdi, Jyh-Pin Chou, Örs Legeza, and Adam Gali. Ab Initio Theory of the Negatively Charged

Boron Vacancy Qubit in Hexagonal Boron Nitride. *npj Comput. Mater.*, 6(41):1–6, 2020.

[51] Mark E Turiansky, Audrius Alkauskas, Lee C Bassett, and Chris G Van de Walle. Dangling Bonds in Hexagonal Boron Nitride as Single-Photon Emitters. *Phys. Rev. Lett.*, 123(12):127401, 2019.

[52] Gergő Thiering and Adam Gali. Ab Initio Calculation of Spin-Orbit Coupling for an NV Center in Diamond Exhibiting Dynamic Jahn-Teller Effect. *Phys. Rev. B*, 96(8):081115, 2017.

[53] Lars Hedin. New method for calculating the one-particle green's function with application to the electron-gas problem. *Phys. Rev.*, 139(3A):A796, 1965.

[54] Mark S Hybertsen and Steven G Louie. Electron correlation in semiconductors and insulators: Band gaps and quasiparticle energies. *Phys. Rev. B*, 34(8):5390, 1986.

[55] Edwin E Salpeter and Hans Albrecht Bethe. A relativistic equation for bound-state problems. *Phys. Rev.*, 84(6):1232, 1951.

[56] Alexander L Fetter and John Dirk Walecka. *Quantum theory of many-particle systems*. Courier Corporation, 2012.

[57] Gerald D Mahan. *Many-particle physics*. Springer Science & Business Media, 2013.

[58] (Jun John) Sakurai Sakurai and Jim J Napolitano. *Modern Quantum Mechanics*. Pearson, 2014.

[59] Feng Wu, Dario Rocca, and Yuan Ping. Dimensionality and Anisotropicity Dependence of Radiative Recombination in Nanostructured Phosphorene. *J. Mater. Chem. C*, 7(41):12891–12897, 2019.

[60] Maurizia Palummo, Marco Bernardi, and Jeffrey C Grossman. Exciton Radiative Lifetimes in Two-Dimensional Transition Metal Dichalcogenides. *Nano Lett.*, 15(5):2794–2800, 2015.

[61] Kejun Li, Tyler J Smart, and Yuan Ping. Carbon Trimer as a 2 eV Single-Photon Emitter Candidate in Hexagonal Boron Nitride: A First-Principles Study. *Phys. Rev. Mater.*, 6(4):L042201, 2022.

[62] Shimin Zhang, Kejun Li, Chunhao Guo, and Yuan Ping. Effect of Environmental Screening and Strain on Optoelectronic Properties of Two-Dimensional Quantum Defects. *2D Mater.*, 2023.

[63] V Lawetz, G Orlandi, and W Siebrand. Theory of Intersystem Crossing in Aromatic Hydrocarbons. *J. Chem. Phys.*, 56(8):4058–4072, 1972.

[64] Jörg Tatchen, Natalie Gilka, and Christel M Marian. Intersystem Crossing Driven by Vibronic Spin–Orbit Coupling: a Case Study on Psoralen. *Phys. Chem. Chem. Phys.*, 9(38):5209–5221, 2007.

[65] Isaac Bersuker. Cambridge University Press, 2006.

[66] Audrius Alkauskas, Qimin Yan, and Chris G Van de Walle. First-Principles Theory of Nonradiative Carrier Capture via Multiphonon Emission. *Phys. Rev. B*, 90(7):075202, 2014.

[67] Feng Wu, Tyler J Smart, Junqing Xu, and Yuan Ping. Carrier Recombination Mechanism at Defects in Wide Band Gap Two-Dimensional Materials from First Principles. *Phys. Rev. B*, 100(8):081407(R), 2019.

[68] Gergő Thiering and Adam Gali. Theory of the Optical Spin-Polarization Loop of the Nitrogen-Vacancy Center in Diamond. *Phys. Rev. B*, 98(8):085207, 2018.

[69] A Dréau, M Lesik, L Rondin, P Spinicelli, O Arcizet, J-F Roch, and V Jacques. Avoiding Power Broadening in Optically Detected Magnetic Resonance of Single NV Defects for Enhanced DC Magnetic Field Sensitivity. *Phys. Rev. B*, 84(19):195204, 2011.

[70] Peter L Knight and Peter W Milonni. The Rabi Frequency in Optical Spectra. *Phys. Rep.*, 66(2):21–107, 1980.

[71] J. Xu, A. Habib, S. Kumar, F. Wu, R. Sundararaman, and Y. Ping. Spin-Phonon Relaxation from a Universal Ab Initio Density-Matrix Approach. *Nat. Commun.*, 11(1):2780, 2020.

[72] Junqing Xu, Adela Habib, Ravishankar Sundararaman, and Yuan Ping. Ab initio ultrafast spin dynamics in solids. *Phys. Rev. B*, 104(18):184418, 2021.

[73] Junqing Xu, Hiroyuki Takenaka, Adela Habib, Ravishankar Sundararaman,

and Yuan Ping. Giant spin lifetime anisotropy and spin-valley locking in silicene and germanene from first-principles density-matrix dynamics. *Nano Lett.*, 21(22):9594–9600, 2021.

[74] Junqing Xu, Kejun Li, Uyen N Huynh, Mayada Fadel, Jinsong Huang, Ravishankar Sundararaman, Valy Vardeny, and Yuan Ping. How Spin Relaxes and Dephases in Bulk Halide Perovskites. *Nat. Commun.*, 15(1):188, 2024.

[75] Junqing Xu and Yuan Ping. Ab initio predictions of spin relaxation, dephasing, and diffusion in solids. *Journal of Chemical Theory and Computation*, 20(2):492–512, 2024. PMID: 38157422.

[76] F. Rossi and T. Kuhn. Theory of Ultrafast Phenomena in Photoexcited Semiconductors. *Rev. Mod. Phys.*, 74(3):895–950, 2002.

[77] M. Bonitz. *Quantum Kinetic Theory*, volume 412. Springer, Cham, 2016.

[78] V M Axt and A Stahl. A dynamics-controlled truncation scheme for the hierarchy of density matrices in semiconductor optics. *Z. Physik B - Condensed Matter*, 93(2):195–204, 1994.

[79] Mildred S Dresselhaus, Gene Dresselhaus, and Ado Jorio. *Group theory: application to the physics of condensed matter*. Springer Science & Business Media, 2007.

[80] Michael Tinkham. *Group Theory and Quantum Mechanics*. Courier Corporation, 2003.

[81] D.B. Boyd and K.B. Lipkowitz. *Reviews in Computational Chemistry, Volume 17*. Reviews in Computational Chemistry. Wiley, 2003.

[82] Marcus W Doherty, Neil B Manson, Paul Delaney, Fedor Jelezko, Jörg Wrachtrup, and Lloyd CL Hollenberg. The Nitrogen-Vacancy Colour Centre in Diamond. *Phys. Rep.*, 528(1):1–45, 2013.

[83] Arthur Marshall Stoneham. *Theory of defects in solids: electronic structure of defects in insulators and semiconductors*. Oxford University Press, 2001.

[84] Claude Cohen-Tannoudji, Bernard Diu, and Frank Laloe. Quantum mechanics, volume 2. *Quantum Mechanics*, 2:626, 1986.

[85] A Lenef and SC Rand. Electronic Structure of the N-V Center in Diamond: Theory. *Physical Review B*, 53(20):13441, 1996.

[86] Christel M Marian. Spin–orbit coupling and intersystem crossing in molecules. *Wiley Interdisciplinary Reviews: Computational Molecular Science*, 2(2):187–203, 2012.

[87] Jeronimo Maze Rios. *Quantum manipulation of nitrogen-vacancy centers in diamond: from basic properties to applications*. Harvard University, 2010.

[88] Michael Lurie Goldman, Alp Sipahigil, MW Doherty, Norman Ying Yao, SD Bennett, M Markham, DJ Twitchen, NB Manson, Alexander Kubanek, and Mikhail D Lukin. Phonon-Induced Population Dynamics and Intersystem Crossing in Nitrogen-Vacancy Centers. *Phys. Rev. Lett.*, 114(14):145502, 2015.

[89] Lucio Robledo, Hannes Bernien, Toeno Van Der Sar, and Ronald Hanson. Spin Dynamics in the Optical Cycle of sSingle Nitrogen-Vacancy Centres in Diamond. *New J. Phys.*, 13(2):025013, 2011.

[90] A Batalov, V Jacques, F Kaiser, P Siyushev, P Neumann, LJ Rogers, RL McMurtrie, NB Manson, F Jelezko, and J Wrachtrup. Low Temperature Studies of the Excited-State Structure of Negatively Charged Nitrogen-Vacancy Color Centers in Diamond. *Phys. Rev. Lett.*, 102(19):195506, 2009.

[91] Lukas Razinkovas, Marcus W Doherty, Neil B Manson, Chris G Van de Walle, and Audrius Alkauskas. Vibrational and Vibronic Structure of Isolated Point Defects: The Nitrogen-Vacancy Center in Diamond. *Phys. Rev. B*, 104(4):045303, 2021.

[92] S. Ernst, P. J. Scheidegger, S. Diesch, and C. L. Degen. Modeling Temperature-Dependent Population Dynamics in the Excited State of the Nitrogen-Vacancy Center in Diamond. *Phys. Rev. B*, 108:085203, Aug 2023.

[93] S. Ernst, P. J. Scheidegger, S. Diesch, L. Lorenzelli, and C. L. Degen. Temperature Dependence of Photoluminescence Intensity and Spin Contrast in Nitrogen-Vacancy Centers. *Phys. Rev. Lett.*, 131:086903, Aug 2023.

[94] Dmitry Ganyushin and Frank Neese. A fully variational spin-orbit coupled complete active space self-consistent field approach: Application to electron paramagnetic resonance g-tensors. *J. Chem. Phys.*, 138(10):104113, 2013.

[95] Bernardo de Souza, Giliandro Farias, Frank Neese, and Robert Izsak. Predicting

Phosphorescence Rates of Light Organic Molecules Using Time-Dependent Density Functional Theory and the Path Integral Approach to Dynamics. *J. Chem. Theory Comput.*, 15(3):1896–1904, 2019.

[96] Jianwei Wang, Fabio Sciarrino, Anthony Laing, and Mark G Thompson. Integrated Photonic Quantum Technologies. *Nat. Photon.*, 14(5):273–284, 2020.

[97] Hui Wang, Jian Qin, Xing Ding, Ming-Cheng Chen, Si Chen, Xiang You, Yu-Ming He, Xiao Jiang, L You, Z Wang, et al. Boson Sampling with 20 Input Photons and a 60-Mode Interferometer in a 1 0 14-Dimensional Hilbert Space. *Phys. Rev. Lett.*, 123(25):250503, 2019.

[98] Jonathan Barrett, Lucien Hardy, and Adrian Kent. No Signaling and Quantum Key Distribution. *Phys. Rev. Lett.*, 95(1):010503, 2005.

[99] Guillaume Cassabois, Pierre Valvin, and Bernard Gil. Hexagonal Boron Nitride is an Indirect Bandgap Semiconductor. *Nat. Photon.*, 10(4):262–266, 2016.

[100] Christine Elias, Pierre Valvin, Thomas Pelini, A Summerfield, CJ Mellor, TS Cheng, L Eaves, CT Foxon, PH Beton, SV Novikov, et al. Direct Band-Gap Crossover in Epitaxial Monolayer Boron Nitride. *Nat. Commun.*, 10(1):2639–2645, 2019.

[101] Gabriele Grosso, Hyowon Moon, Benjamin Lienhard, Sajid Ali, Dmitri K Efetov, Marco M Furchi, Pablo Jarillo-Herrero, Michael J Ford, Igor Aharonovich, and Dirk Englund. Tunable and High-Purity Room Temperature Single-Photon Emis-

sion from Atomic Defects in Hexagonal Boron Nitride. *Nat. Commun.*, 8(1):705–712, 2017.

[102] Xiangzhi Li, Robert A Scully, Kamran Shayan, Yue Luo, and Stefan Strauf. Near-Unity Light Collection Efficiency from Quantum Emitters in Boron Nitride by Coupling to Metallo-Dielectric Antennas. *ACS Nano*, 13(6):6992–6997, 2019.

[103] Toan Trong Tran, Kerem Bray, Michael J Ford, Milos Toth, and Igor Aharonovich. Quantum Emission from Hexagonal Boron Nitride Monolayers. *Nat. Nanotechnol.*, 11(1):37–41, 2016.

[104] Toan Trong Tran, Cameron Zachreson, Amanuel Michael Berhane, Kerem Bray, Russell Guy Sandstrom, Lu Hua Li, Takashi Taniguchi, Kenji Watanabe, Igor Aharonovich, and Milos Toth. Quantum Emission from Defects in Single-Crystalline Hexagonal Boron Nitride. *Phys. Rev. Appl.*, 5(3):034005, 2016.

[105] LJ Martínez, Thomas Pelini, V Waselowski, JR Maze, Bernard Gil, Guillaume Cassabois, and Vincent Jacques. Efficient Single Photon Emission from a High-Purity Hexagonal Boron Nitride Crystal. *Phys. Rev. B*, 94(12):121405(R), 2016.

[106] Andreas Dietrich, M Bürk, Elena S Steiger, Lukas Antoniuk, Trong Toan Tran, Minh Nguyen, Igor Aharonovich, Fedor Jelezko, and Alexander Kubanek. Observation of Fourier Transform Limited Lines in Hexagonal Boron Nitride. *Phys. Rev. B*, 98(8):081414(R), 2018.

[107] Fariah Hayee, Leo Yu, Jingyuan Linda Zhang, Christopher J Ciccarino, Minh

Nguyen, Ann F Marshall, Igor Aharonovich, Jelena Vučković, Prineha Narang, Tony F Heinz, et al. Revealing Multiple Classes of Stable Quantum Emitters in Hexagonal Boron Nitride with Correlated Optical and Electron Microscopy. *Nat. Mater.*, 19(5):534–539, 2020.

[108] Minh Nguyen, Sejeong Kim, Toan Trong Tran, Zai-Quan Xu, Mehran Kianinia, Milos Toth, and Igor Aharonovich. Nanoassembly of Quantum Emitters in Hexagonal Boron Nitride and Gold Nanospheres. *Nanoscale*, 10(5):2267–2274, 2018.

[109] Zai-Quan Xu, Christopher Elbadawi, Toan Trong Tran, Mehran Kianinia, Xiuling Li, Daobin Liu, Timothy B Hoffman, Minh Nguyen, Sejeong Kim, James H Edgar, et al. Single Photon Emission from Plasma Treated 2D Hexagonal Boron Nitride. *Nanoscale*, 10(17):7957–7965, 2018.

[110] Prince Khatri, Andrew J Ramsay, Ralph Nicholas Edward Malein, Harold MH Chong, and Isaac J Luxmoore. Optical Gating of Photoluminescence from Color Centers in Hexagonal Boron Nitride. *Nano Lett.*, 20(6):4256–4263, 2020.

[111] Snežana Lazić, André Espinha, Sergio Pinilla Yanguas, Carlos Gibaja, Félix Zamora, Pablo Ares, Manish Chhowalla, Wendel S Paz, Juan José Palacios Burgos, Alberto Hernández-Mínguez, et al. Dynamically Tuned Ton-Classical Light Emission from Atomic Defects in Hexagonal Boron Nitride. *Commun. Phys.*, 2(113):1–8, 2019.

[112] Wei Liu, Yi-Tao Wang, Zhi-Peng Li, Shang Yu, Zhi-Jin Ke, Yu Meng, Jian-Shun Tang, Chuan-Feng Li, and Guang-Can Guo. An Ultrastable and Robust

Single-Photon Emitter in Hexagonal Boron Nitride. *Physica E Low Dimens. Syst. Nanostruct.*, 124:114251, 2020.

[113] Tobias Vogl, Geoff Campbell, Ben C Buchler, Yuerui Lu, and Ping Koy Lam. Fabrication and Deterministic Transfer of High-Quality Quantum Emitters in Hexagonal Boron Nitride. *ACS Photon.*, 5(6):2305–2312, 2018.

[114] Toan Trong Tran, Mehran Kianinia, Minh Nguyen, Sejeong Kim, Zai-Quan Xu, Alexander Kubanek, Milos Toth, and Igor Aharonovich. Resonant Excitation of Quantum Emitters in Hexagonal Boron Nitride. *ACS Photon.*, 5(2):295–300, 2018.

[115] Noah Mendelson, Zai-Quan Xu, Toan Trong Tran, Mehran Kianinia, John Scott, Carlo Bradac, Igor Aharonovich, and Milos Toth. Engineering and Tuning of Quantum Emitters in Few-Layer Hexagonal Boron Nitride. *ACS Nano*, 13(3):3132–3140, 2019.

[116] Annemarie L Exarhos, David A Hopper, Richard R Grote, Audrius Alkauskas, and Lee C Bassett. Optical Signatures of Quantum Emitters in Suspended Hexagonal Boron Nitride. *ACS Nano*, 11(3):3328–3336, 2017.

[117] Toan Trong Tran, Christopher Elbadawi, Daniel Totonjian, Charlene J Lobo, Gabriele Grosso, Hyowon Moon, Dirk R Englund, Michael J Ford, Igor Aharonovich, and Milos Toth. Robust Multicolor Single Photon Emission from Point Defects in Hexagonal Boron Nitride. *ACS Nano*, 10(8):7331–7338, 2016.

[118] Hanh Ngoc My Duong, Minh Anh Phan Nguyen, Mehran Kianinia, Takeshi Ohshima, Hiroshi Abe, Kenji Watanabe, Takashi Taniguchi, James H Edgar, Igor Aharonovich, and Milos Toth. Effects of High-Energy Electron Irradiation on Quantum Emitters in Hexagonal Boron Nitride. *ACS Appl. Mater. Interfac.*, 10(29):24886–24891, 2018.

[119] Sumin Choi, Toan Trong Tran, Christopher Elbadawi, Charlene Lobo, Xuewen Wang, Saulius Juodkazis, Gediminas Seniutinas, Milos Toth, and Igor Aharonovich. Engineering and Localization of Quantum Emitters in Large Hexagonal Boron Nitride Layers. *ACS Appl. Mater. Interfac.*, 8(43):29642–29648, 2016.

[120] Gabriele Grosso, Hyowon Moon, Christopher J Ciccarino, Johannes Flick, Noah Mendelson, Lukas Mennel, Milos Toth, Igor Aharonovich, Prineha Narang, and Dirk R Englund. Low-Temperature Electron–Phonon Interaction of Quantum Emitters in Hexagonal Boron Nitride. *ACS Photon.*, 7(6):1410–1417, 2020.

[121] Elke Neu, David Steinmetz, Janine Riedrich-Möller, Stefan Gsell, Martin Fischer, Matthias Schreck, and Christoph Becher. Single Photon Emission from Silicon-Vacancy Colour Centres in Chemical Vapour Deposition Nano-Diamonds on Iridium. *New J. Phys.*, 13(2):025012, 2011.

[122] Kumarasiri Konthasinghe, Chitraleema Chakraborty, Nikhil Mathur, Liangyu Qiu, Arunabh Mukherjee, Gregory D Fuchs, and A Nick Vamivakas. Rabi Oscillations and Resonance Fluorescence from a Single Hexagonal Boron Nitride Quantum Emitter. *Optica*, 6(5):542–548, 2019.

[123] Qixing Wang, Qi Zhang, Xiaoxu Zhao, Xin Luo, Calvin Pei Yu Wong, Junyong Wang, Dongyang Wan, T Venkatesan, Stephen J Pennycook, Kian Ping Loh, et al. Photoluminescence Upconversion by Defects in Hexagonal Boron Nitride. *Nano Lett.*, 18(11):6898–6905, 2018.

[124] Andreas W Schell, Hideaki Takashima, Toan Trong Tran, Igor Aharonovich, and Shigeki Takeuchi. Coupling Quantum Emitters in 2D Materials with Tapered Fibers. *ACS Photon.*, 4(4):761–767, 2017.

[125] Annemarie L Exarhos, David A Hopper, Raj N Patel, Marcus W Doherty, and Lee C Bassett. Magnetic-Field-Dependent Quantum Emission in Hexagonal Boron Nitride at Room Temperature. *Nat. Commun.*, 10(222):222–229, 2019.

[126] Donggyu Yim, Mihyang Yu, Gichang Noh, Jieun Lee, and Hosung Seo. Polarization and Localization of Single-Photon Emitters in Hexagonal Boron Nitride Wrinkles. *ACS Appl. Mater. Interfac.*, 12(32):36362–36369, 2020.

[127] Ondrej L Krivanek, Matthew F Chisholm, Valeria Nicolosi, Timothy J Pennycook, George J Corbin, Niklas Dellby, Matthew F Murfitt, Christopher S Own, Zoltan S Szilagyi, Mark P Oxley, et al. Atom-by-Atom Structural and Chemical Analysis by Annular Dark-Field Electron Microscopy. *Nature*, 464(7288):571–574, 2010.

[128] A Sajid and Kristian S Thygesen. VNCB Defect as Source of Single Photon Emission from Hexagonal Boron Nitride. *2D Mater.*, 7(3):031007, 2020.

[129] Mark E Turiansky and Chris G Van de Walle. Impact of Dangling Bonds on Properties of h-BN. *2D Mater.*, 8(2):024002, 2021.

[130] Paolo Giannozzi, Stefano Baroni, Nicola Bonini, Matteo Calandra, Roberto Car, Carlo Cavazzoni, Davide Ceresoli, Guido L Chiarotti, Matteo Cococcioni, Ismaila Dabo, Andrea Dal Corso, Stefano de Gironcoli, Stefano Fabris, Guido Fratesi, Ralph Gebauer, Uwe Gerstmann, Christos Gougoussis, Anton Kokalj, Michele Lazzeri, Layla Martin-Samos, Nicola Marzari, Francesco Mauri, Riccardo Mazzarello, Stefano Paolini, Alfredo Pasquarello, Lorenzo Paulatto, Carlo Sbraccia, Sandro Scandolo, Gabriele Sclauzero, Ari P Seitsonen, Alexander Smogunov, Paolo Umari, and Renata M Wentzcovitch. QUANTUM ESPRESSO: A Modular and Open-Source Software Project for Quantum Simulations of Materials. *J. Phys.: Condens. Matter*, 21(39):395502, sep 2009.

[131] Chunhao Guo, Junqing Xu, Dario Rocca, and Yuan Ping. Substrate Screening Approach for Quasiparticle Energies of Two-Dimensional Interfaces with Lattice Mismatch. *Phys. Rev. B*, 102(20):205113, 2020.

[132] Chunhao Guo, Junqing Xu, and Yuan Ping. Substrate Effect on Excitonic Shift and Radiative Lifetime of Two-Dimensional Materials. *J. of Phys. Condens. Matter*, 33(23):234001, 2021.

[133] Mark E Turiansky and Chris G Van de Walle. Boron Dangling Bonds in a Monolayer of Hexagonal Boron Nitride. *J. Appl. Phys.*, 129(6):064301, 2021.

[134] Marie Krečmarová, Rodolfo Canet-Albiach, Hamid Pashaei-Adl, Setatira Gorji,

Guillermo Muñoz-Matutano, Miloš Nesládek, Juan P Martínez-Pastor, and Juan F Sánchez-Royo. Extrinsic Effects on the Optical Properties of Surface Color Defects Generated in Hexagonal Boron Nitride Nanosheets. *ACS Appl. Mater. Interfac.*, 13(38):46105–46116, 2021.

[135] D. R. Hamann. Optimized Norm-Conserving Vanderbilt Pseudopotentials. *Phys. Rev. B*, 88(8):085117, aug 2013.

[136] Feng Wu, Tyler J. Smart, Junqing Xu, and Yuan Ping. Erratum: Carrier Recombination Mechanism at Defects in Wide Band Gap Two-Dimensional Materials from First Principles [Phys. Rev. B 100, 081407(R) (2019)]. *Phys. Rev. B*, 104:079901(E), Aug 2021.

[137] Tyler J Smart, Kejun Li, Junqing Xu, and Yuan Ping. Intersystem Crossing and Exciton–Defect Coupling of Spin Defects in Hexagonal Boron Nitride. *npj Comput. Mater.*, 7(1):59, 2021.

[138] Ravishankar Sundararaman and Yuan Ping. First-principles Electrostatic Potentials for Reliable Alignment at Interfaces and Defects. *J. Chem. Phys.*, 146(10):104109, 2017.

[139] Feng Wu, Andrew Galatas, Ravishankar Sundararaman, Dario Rocca, and Yuan Ping. First-Principles Engineering of Charged Defects for Two-Dimensional Quantum Technologies. *Phys. Rev. Mater.*, 1(7):071001(R), 2017.

[140] Ravishankar Sundararaman, Kendra Letchworth-Weaver, Kathleen A. Schwarz,

Deniz Gunceler, Yalcin Ozhabes, and T.A. Arias. JDFTx: Software for Joint Density-Functional Theory. *SoftwareX*, 6:278 – 284, 2017.

[141] Andrea Marini, Conor Hogan, Myrta Grüning, and Daniele Varsano. Yambo: An *ab initio* Tool for Excited State Calculations. *Comput. Phys. Commun.*, 180(8):1392 – 1403, 2009.

[142] *See Supplemental Materials for electronic properties of* C_2C_N *in hBN, ZPL of defects at charged states, defect-related exciton wave function,* G_0W_0*-BSE convergence tests, electronic, optical, radiative, and nonradiative recombination properties of* C_2C_B*, ZPL of* C_2C_N *with different levels of theory, configuration coordinate diagrams of* C_2C_N*, implementation details of PL line shape as well as its benchmark and convergence test, and a comprehensive summary table of past experimental data.*

[143] F Fuchs, J Furthmüller, F Bechstedt, M Shishkin, and G Kresse. Quasiparticle Band Structure Based on a Generalized Kohn-Sham Scheme. *Phys. Rev. B*, 76(11):115109, 2007.

[144] Friedhelm Bechstedt. *Many-Body Approach to Electronic Excitations.* Springer-Verlag, Berlin, 2016.

[145] Miroslav Kolos and František Karlickỳ. Accurate Many-Body Calculation of Electronic and Optical Band Gap of Bulk Hexagonal Boron Nitride. *Phys. Chem. Chem. Phys.*, 21(7):3999–4005, 2019.

[146] Falco Hüser, Thomas Olsen, and Kristian S Thygesen. Quasiparticle GW Calculations for Solids, Molecules, and Two-Dimensional Materials. *Phys. Rev. B*, 87(23):235132, 2013.

[147] Lorenzo Sponza, Hakim Amara, François Ducastelle, Annick Loiseau, and Claudio Attaccalite. Exciton Interference in Hexagonal Boron Nitride. *Phys. Rev. B*, 97(7):075121, 2018.

[148] Fulvio Paleari, Thomas Galvani, Hakim Amara, François Ducastelle, Alejandro Molina-Sánchez, and Ludger Wirtz. Excitons in Few-Layer Hexagonal Boron Nitride: Davydov Splitting and Surface Localization. *2D Mater.*, 5(4):045017, 2018.

[149] Diana Y Qiu, H Felipe, and Steven G Louie. Screening and Many-Body Effects in Two-Dimensional Crystals: Monolayer MoS 2. *Phys. Rev. B*, 93(23):235435, 2016.

[150] Rex W Godby and RJ Needs. Metal-Insulator Transition in Kohn-Sham Theory and Quasiparticle Theory. *Phys. Rev. Lett.*, 62(10):1169, 1989.

[151] A Oschlies, RW Godby, and RJ Needs. GW Self-Energy Calculations of Carrier-Induced Band-Gap Narrowing in n-type Silicon. *Phys. Rev. B*, 51(3):1527, 1995.

[152] Carlo A Rozzi, Daniele Varsano, Andrea Marini, Eberhard KU Gross, and Angel Rubio. Exact Coulomb Cutoff Technique for Supercell Calculations. *Phys. Rev. B*, 73(20):205119, 2006.

[153] C. Attaccalite, M. Bockstedte, A. Marini, A. Rubio, and L. Wirtz. Coupling of Excitons and Defect States in Boron-Nitride Nanostructures. *Phys. Rev. B*, 83:144115, Apr 2011.

[154] Lukas Novotny and Bert Hecht. *Principles of Nano-Optics*. Cambridge University Press, 2012.

[155] Johann A Preuß, Eduard Rudi, Johannes Kern, Robert Schmidt, Rudolf Bratschitsch, and Steffen Michaelis de Vasconcellos. Assembly of Large hBN Nanocrystal Arrays for Quantum Light Emission. *2D Mater.*, 8(3):035005, 2021.

[156] Tatiana Korona and Michał Chojecki. Exploring Point Defects in Hexagonal Boron-Nitrogen Monolayers. *Int. J. of Quantum Chem.*, 119(14):e25925, 2019.

[157] M Mackoit-Sinkevičienė, Marek Maciaszek, Chris G Van de Walle, and Audrius Alkauskas. Carbon Dimer Defect as a Source of the 4.1 eV Luminescence in Hexagonal Boron Nitride. *Appl. Phys. Lett.*, 115(21):212101, 2019.

[158] Luc Museur, Eduard Feldbach, and Andrei Kanaev. Defect-Related Photoluminescence of Hexagonal Boron Nitride. *Phys. Rev. B*, 78(15):155204, 2008.

[159] Sergey I Bozhevolnyi and Jacob B Khurgin. Fundamental Limitations in Spontaneous Emission Rate of Single-Photon Sources. *Optica*, 3(12):1418–1421, 2016.

[160] Ruben Esteban, TV Teperik, and Jean-Jacques Greffet. Optical Patch Antennas for Single Photon Emission Using Surface Plasmon Resonances. *Phys. Rev. Lett.*, 104(2):026802, 2010.

[161] Philipp Auburger and Adam Gali. Towards *ab initio* Identification of Paramagnetic Substitutional Carbon Defects in Hexagonal Boron Nitride Acting as Quantum Bits. *Phys. Rev. B*, 104(7):075410, 2021.

[162] Constantinos A Valagiannopoulos, Marios Mattheakis, Sharmila N Shirodkar, and Efthimios Kaxiras. Manipulating Polarized Light with a Planar Slab of Black Phosphorus. *J. Phys. Commun.*, 1(4):045003, 2017.

[163] Xinrong Zong, Huamin Hu, Gang Ouyang, Jingwei Wang, Run Shi, Le Zhang, Qingsheng Zeng, Chao Zhu, Shouheng Chen, Chun Cheng, et al. Black Phosphorus-Based van der Waals Heterostructures for Mid-Infrared Light-Emission Applications. *Light Sci. Appl.*, 9(1):1–8, 2020.

[164] Jamison Sloan, Nicholas Rivera, Marin Soljacic, and Ido Kaminer. Tunable UV-Emitters through Graphene Plasmonics. *Nano Lett.*, 18(1):308–313, 2018.

[165] Pankaj K. Jha, Ghazaleh K. Shirmanesh, Hamidreza Akbari, Meir Y. Grajower, Claudio G. Parazzoli, Benjamin E. C. Koltenbah, and Harry A. Atwater. Emitter-Metasurface Interface for Manipulating Emission Characteristics of Quantum Defects. In *Conference on Lasers and Electro-Optics*, page FM4C.2. Optica Publishing Group, 2020.

[166] Zhenisbek Tagay and Constantinos Valagiannopoulos. Highly Selective Transmission and Absorption from Metasurfaces of Periodically Corrugated Cylindrical Particles. *Phys. Rev. B*, 98(11):115306, 2018.

[167] Nicholas V Proscia, Harishankar Jayakumar, Xiaochen Ge, Gabriel Lopez-Morales, Zav Shotan, Weidong Zhou, Carlos A Meriles, and Vinod M Menon. Microcavity-Coupled Emitters in Hexagonal Boron Nitride. *Nanophotonics*, 9(9):2937–2944, 2020.

[168] Constantinos A Valagiannopoulos and Vassilios Kovanis. Judicious Distribution of Laser Emitters to Shape the Desired Far-Field Patterns. *Phys. Rev. A*, 95(6):063806, 2017.

[169] HJ Mamin, M Kim, MH Sherwood, CT Rettner, K Ohno, DD Awschalom, and D Rugar. Nanoscale Nuclear Magnetic Resonance with a Nitrogen-Vacancy Spin Sensor. *Sci.*, 339(6119):557–560, 2013.

[170] Colm A Ryan, Jonathan S Hodges, and David G Cory. Robust Decoupling Techniques to Extend Quantum Coherence in Diamond. *Phys. Rev. Lett.*, 105(20):200402, 2010.

[171] Florian Dolde, Ville Bergholm, Ya Wang, Ingmar Jakobi, Boris Naydenov, Sébastien Pezzagna, Jan Meijer, Fedor Jelezko, Philipp Neumann, Thomas Schulte-Herbrüggen, et al. High-fidelity Spin Entanglement Using Optimal Control. *Nat. Commun.*, 5(1):3371, 2014.

[172] Andreas Gottscholl, Matthias Diez, Victor Soltamov, Christian Kasper, Andreas Sperlich, Mehran Kianinia, Carlo Bradac, Igor Aharonovich, and Vladimir Dyakonov. Room Temperature Coherent Control of Spin Defects in Hexagonal Boron Nitride. *Sci. Adv.*, 7(14):eabf3630, 2021.

[173] Hannes Bernien, Bas Hensen, Wolfgang Pfaff, Gerwin Koolstra, Machiel S Blok, Lucio Robledo, Tim H Taminiau, Matthew Markham, Daniel J Twitchen, Lilian Childress, et al. Heralded Entanglement Between Solid-State Qubits Separated by Three Metres. *Nat.*, 497(7447):86–90, 2013.

[174] A Gruber, A Drabenstedt, C Tietz, L Fleury, J Wrachtrup, and C von Borczyskowski. Scanning Confocal Optical Microscopy and Magnetic Resonance on Single Defect Centers. *Sci.*, 276(5321):2012–2014, 1997.

[175] DM Toyli, DJ Christle, A Alkauskas, BB Buckley, CG Van de Walle, and DD Awschalom. Measurement and Control of Single Nitrogen-Vacancy Center Spins Above 600 K. *Phys. Rev. X*, 2(3):031001, 2012.

[176] Patrick J Scheidegger, Simon Diesch, Marius L Palm, and Christian L Degen. Scanning Nitrogen-Vacancy Magnetometry Down to 350 mK. *Appl. Phys. Lett.*, 120(22), 2022.

[177] Emre Togan, Yiwen Chu, Alexei S Trifonov, Liang Jiang, Jeronimo Maze, Lilian Childress, MV Gurudev Dutt, Anders Søndberg Sørensen, Phillip R Hemmer, Alexander S Zibrov, et al. Quantum Entanglement Between an Optical Photon and a Solid-State Spin Qubit. *Nat.*, 466(7307):730–734, 2010.

[178] Simon Baber, Ralph Nicholas Edward Malein, Prince Khatri, Paul Steven Keatley, Shi Guo, Freddie Withers, Andrew J Ramsay, and Isaac J Luxmoore. Excited State Spectroscopy of Boron Vacancy Defects in Hexagonal Boron Nitride Using

Time-Resolved Optically Detected Magnetic Resonance. *Nano Lett.*, 22(1):461–467, 2021.

[179] Yuchen Ma, Michael Rohlfing, and Adam Gali. Excited States of the Negatively Charged Nitrogen-Vacancy Color Center in Diamond. *Phys. Rev. B*, 81(4):041204, 2010.

[180] Nan Sheng, Christian Vorwerk, Marco Govoni, and Giulia Galli. Green's Function Formulation of Quantum Defect Embedding Theory. *J. Chem. Theory Comput.*, 18(6):3512–3522, 2022.

[181] Churna Bhandari, Aleksander L Wysocki, Sophia E Economou, Pratibha Dev, and Kyungwha Park. Multiconfigurational Study of the Negatively Charged Nitrogen-Vacancy Center in Diamond. *Phys. Rev. B*, 103(1):014115, 2021.

[182] NB Manson, JP Harrison, and MJ Sellars. Nitrogen-Vacancy Center in Diamond: Model of the Electronic Structure and Associated Dynamics. *Phys. Rev. B*, 74(10):104303, 2006.

[183] Peter Deák, Bálint Aradi, Thomas Frauenheim, Erik Janzén, and Adam Gali. Accurate Defect Levels Obtained from the HSE06 Range-Separated Hybrid Functional. *Phys. Rev. B*, 81(15):153203, 2010.

[184] Adam Gali, Erik Janzén, Péter Deák, Georg Kresse, and Efthimios Kaxiras. Theory of Spin-Conserving Excitation of the N-V- Center in Diamond. *Phys. Rev. Lett.*, 103(18):186404, 2009.

[185] Björn O. Roos. Theory and Applications of Computational Chemistry. In *Multiconfigurational quantum chemistry*, pages 725–764. Elsevier, 2005.

[186] Marco Govoni and Giulia Galli. Large Scale GW Calculations. *J. Chem. Theory Comput.*, 11(6):2680–2696, 2015.

[187] Victor Wen-zhe Yu and Marco Govoni. Gpu acceleration of large-scale full-frequency gw calculations. *J. Chem. Theory Comput.*, 18(8):4690–4707, 2022.

[188] Dario Rocca, Deyu Lu, and Giulia Galli. Ab initio calculations of optical absorption spectra: Solution of the bethe–salpeter equation within density matrix perturbation theory. *J. Chem. Phys.*, 133(16), 2010.

[189] Dario Rocca, Yuan Ping, Ralph Gebauer, and Giulia Galli. Solution of the Bethe-Salpeter Equation without Empty Electronic States: Application to the Absorption Spectra of Bulk Systems. *Phys. Rev. B*, 85:045116, Jan 2012.

[190] Frank Neese. The ORCA program system. *Wiley Interdiscip. Rev. Comput. Mol. Sci.*, 2(1):73–78, 2012.

[191] Frank Neese, Frank Wennmohs, Ute Becker, and Christoph Riplinger. The ORCA quantum chemistry program package. *J. Chem. Phys.*, 152(22):224108, 2020.

[192] K. Andersson, P.-A. Malmqvist, B.O. Roos, A.J. Sadlej, and K. Wolinski. Secon Order Perturbation Theory with a CASSCF Reference Function. *J. Phys. Chem.*, 94:5483, March 1990.

[193] C. Angeli, R. Cimiraglia, S. Evangelisti, T. Leininger, and J.-P. Malrieu. Introduction of N-electron Valence States for Multireference Perturbation Theory. *J. Chem. Phys.*, 114:10252, June 2001.

[194] Markus Reiher. Douglas–Kroll–Hess Theory: a Relativistic Electrons-Only Theory for Chemistry. *Theor. Chem. Acc.*, 116:241–252, 2006.

[195] Thom H. Jr. Dunning. Gaussian Basis Sets for Use in Correlated Molecular Calculations. I. The Atoms Boron Through Neon and Hydrogen. *J. Chem. Phys.*, 90(2):1007–1023, 1989.

[196] Benjamin P. Pritchard, Doaa Altarawy, Brett Didier, Tara D. Gibson, and Theresa L. Windus. New Basis Set Exchange: An Open, Up-to-Date Resource for the Molecular Sciences Community. *J. Chem. Inf. Model.*, 59(11):4814–4820, 2019.

[197] Frank Neese. Efficient and Accurate Approximations to the Molecular Spin-Orbit Coupling Operator and Their Use in Molecular g-Tensor Calculations. *J. Chem. Phys.*, 122(3):034107, 2005.

[198] Sang-Yun Lee, Matthias Widmann, Torsten Rendler, Marcus W Doherty, Thomas M Babinec, Sen Yang, Moritz Eyer, Petr Siyushev, Birgit JM Hausmann, Marko Loncar, et al. Readout and Control of a Single Nuclear Spin with a Metastable Electron Spin Ancilla. *Nat. Nanotechnol.*, 8(7):487–492, 2013.

[199] Priyadharshini Balasubramanian, Mathias H Metsch, Prithvi Reddy, Lachlan J

Rogers, Neil B Manson, Marcus W Doherty, and Fedor Jelezko. Discovery of ST1 Centers in Natural Diamond. *Nanophotonics*, 8(11):1993–2002, 2019.

[200] VM Acosta, A Jarmola, E Bauch, and D Budker. Optical Properties of the Nitrogen-Vacancy Singlet Levels in Diamond. *Phys. Rev. B*, 82(20):201202, 2010.

[201] LJ Rogers, S Armstrong, MJ Sellars, and NB Manson. Infrared Emission of the NV Centre in Diamond: Zeeman and Uniaxial Stress Studies. *New J. Phys.*, 10(10):103024, 2008.

[202] Gordon Davies and MF Hamer. Optical Studies of the 1.945 eV Vibronic Band in Diamond. *Proc. Math. Phys. Eng. Sci.*, 348(1653):285–298, 1976.

[203] S. Haldar, A. Mitra, M. R. Hermes, and L. Gagliardi. Local Excitations of a Charged Nitrogen Vacancy in Diamond with Multireference Density Matrix Embedding Theory. *J. Phys. Chem. Lett.*, 14:4273, May 2023.

[204] Michel Bockstedte, Felix Schütz, Thomas Garratt, Viktor Ivády, and Adam Gali. Ab Initio Description of Highly Correlated States in Defects for Realizing Quantum Bits. *npj Quantum Mater.*, 3(1):31, 2018.

[205] Anchal Gupta, Luke Hacquebard, and Lilian Childress. Efficient Signal Processing for Time-Resolved Fluorescence Detection of Nitrogen-Vacancy Spins in Diamond. *J. Opt. Soc. Am. B*, 33(3):B28–B34, 2016.

[206] IB Bersuker. The Jahn-Teller and Pseudo Jahn-Teller Effect in Materials Science. In *J. Phys. Conf. Ser.*, volume 833, page 012001. IOP Publishing, 2017.

[207] Tesfaye A Abtew, YY Sun, Bi-Ching Shih, Pratibha Dev, SB Zhang, and Peihong Zhang. Dynamic Jahn-Teller Effect in the NV- Center in Diamond. *Phys. Rev. Lett.*, 107(14):146403, 2011.

[208] Nicholas P Brawand, Márton Vörös, and Giulia Galli. Surface Dangling Bonds are a Cause of B-Type Blinking in Si Nanoparticles. *Nanoscale*, 7(8):3737–3744, 2015.

[209] P Neumann, R Kolesov, V Jacques, J Beck, J Tisler, A Batalov, Lachlan Rogers, NB Manson, G Balasubramanian, F Jelezko, et al. Excited-State Spectroscopy of Single NV Defects in Diamond Using Optically Detected Magnetic Resonance. *New J. Phys.*, 11(1):013017, 2009.

[210] Alberto Privitera, Marcello Righetto, Franco Cacialli, and Moritz K Riede. Perspectives of Organic and Perovskite-Based Spintronics. *Adv. Opt. Mater.*, 9(14):2100215, 2021.

[211] Qing Lin He, Taylor L Hughes, N Peter Armitage, Yoshinori Tokura, and Kang L Wang. Topological Spintronics and Magnetoelectronics. *Nat. Mater.*, 21(1):15–23, 2022.

[212] Se Kwon Kim, Geoffrey SD Beach, Kyung-Jin Lee, Teruo Ono, Theo Rasing, and Hyunsoo Yang. Ferrimagnetic Spintronics. *Nat. Mater.*, 21(1):24–34, 2022.

[213] See-Hun Yang, Ron Naaman, Yossi Paltiel, and Stuart SP Parkin. Chiral Spintronics. *Nat. Rev. Phys.*, 3(5):328–343, 2021.

[214] Jaeki Jeong, Minjin Kim, Jongdeuk Seo, Haizhou Lu, Paramvir Ahlawat, Aditya Mishra, Yingguo Yang, Michael A Hope, Felix T Eickemeyer, Maengsuk Kim, et al. Pseudo-halide anion engineering for α-fapbi3 perovskite solar cells. *Nature*, 592(7854):381–385, 2021.

[215] Kebin Lin, Jun Xing, Li Na Quan, FPG De Arquer, Xiwen Gong, Jianxun Lu, Liqiang Xie, Weijie Zhao, Di Zhang, Chuanzhong Yan, et al. Perovskite light-emitting diodes with external quantum efficiency exceeding 20 per cent. *Nature*, 562(7726):245–248, 2018.

[216] Uyen N Huynh, Ye Liu, Ashish Chanana, Dipak R Khanal, Peter C Sercel, Jinsong Huang, and Z Valy Vardeny. Transient quantum beatings of trions in hybrid organic tri-iodine perovskite single crystal. *Nat. Commun.*, 13(1):1428, 2022.

[217] Yuan Ping and Jin Zhong Zhang. Spin-optotronic properties of organometal halide perovskites. *J. Phys. Chem. Lett.*, 9(20):6103–6111, 2018.

[218] Claudiu M Iaru, Annalisa Brodu, Niels JJ van Hoof, Stan ET Ter Huurne, Jonathan Buhot, Federico Montanarella, Sophia Buhbut, Peter CM Christianen, Daniël Vanmaekelbergh, Celso de Mello Donega, et al. Fröhlich interaction dominated by a single phonon mode in CsPbBr3. *Nat. Commun.*, 12(1):5844, 2021.

[219] Manoj K. Jana, Ruyi Song, Haoliang Liu, Dipak Raj Khanal, Svenja M. Janke, Rundong Zhao, Chi Liu, Z. Valy Vardeny, Volker Blum, and David B. Mitzi. Organic-to-inorganic structural chirality transfer in a 2D hybrid perovskite and

impact on Rashba-Dresselhaus spin-orbit coupling. *Nat. Commun.*, 11(1):4699, 2020.

[220] Fanhao Jia, Shunbo Hu, Shaowen Xu, Heng Gao, Guodong Zhao, Paolo Barone, Alessandro Stroppa, and Wei Ren. Persistent spin-texture and ferroelectric polarization in 2d hybrid perovskite benzylammonium lead-halide. *J. Phys. Chem. Lett.*, 11(13):5177–5183, 2020.

[221] Adela Habib, Junqing Xu, Yuan Ping, and Ravishankar Sundararaman. Electric fields and substrates dramatically accelerate spin relaxation in graphene. *Phys. Rev. B*, 105(11):115122, 2022.

[222] Junqing Xu and Yuan Ping. Substrate effects on spin relaxation in two-dimensional dirac materials with strong spin-orbit coupling. *Npj Comput. Mater.*, 9(1):47, 2023.

[223] MW Wu, JH Jiang, and MQ Weng. Spin dynamics in semiconductors. *Phys. Rep.*, 493(2-4):61–236, 2010.

[224] C Lü, JL Cheng, MW Wu, and IC da Cunha Lima. Spin relaxation time, spin dephasing time and ensemble spin dephasing time in n-type gaas quantum wells. *Phys. Lett. A*, 365(5-6):501–504, 2007.

[225] VV Belykh, A Yu Kuntsevich, MM Glazov, KV Kavokin, DR Yakovlev, and M Bayer. Quantum interference controls the electron spin dynamics in n-gaas. *Phys. Rev. X*, 8(3):031021, 2018.

[226] Zhi-Gang Yu and Yan S Li. Unraveling the spin relaxation mechanism in hybrid organic–inorganic perovskites. *J. Phys. Chem. C*, 123(23):14701–14706, 2019.

[227] I. Žutić, J. Fabian, and S. D. Sarma. Spintronics: Fundamentals and Applications. *Rev. Mod. Phys.*, 76(2):323, 2004.

[228] David Giovanni, Hong Ma, Julianto Chua, Michael Graötzel, Ramamoorthy Ramesh, Subodh Mhaisalkar, Nripan Mathews, and Tze Chien Sum. Highly spin-polarized carrier dynamics and ultralarge photoinduced magnetization in ch3nh3pbi3 perovskite thin films. *Nano Lett.*, 15(3):1553–1558, 2015.

[229] Xihan Chen, Haipeng Lu, Kang Wang, Yaxin Zhai, Vladimir Lunin, Peter C Sercel, and Matthew C Beard. Tuning spin-polarized lifetime in two-dimensional metal–halide perovskite through exciton binding energy. *J. Am. Chem. Soc.*, 143(46):19438–19445, 2021.

[230] Erik Kirstein, Evgeny A Zhukov, Dmitri R Yakovlev, Nataliia E Kopteva, Carolin Harkort, Dennis Kudlacik, Oleh Hordiichuk, Maksym V Kovalenko, and Manfred Bayer. Coherent spin dynamics of electrons in two-dimensional (pea) 2pbi4 perovskites. *Nano Lett.*, 23(1):205–212, 2022.

[231] Weijie Zhao, Rui Su, Yuqing Huang, Jinqi Wu, Chee Fai Fong, Jiangang Feng, and Qihua Xiong. Transient circular dichroism and exciton spin dynamics in all-inorganic halide perovskites. *Nat. Commun.*, 11(1):5665, 2020.

[232] Jing Li, M Goryca, K Yumigeta, H Li, S Tongay, and Scott A Crooker. Valley

relaxation of resident electrons and holes in a monolayer semiconductor: Dependence on carrier density and the role of substrate-induced disorder. *Phys. Rev. Mater.*, 5(4):044001, 2021.

[233] Prasenjit Dey, Luyi Yang, Cedric Robert, Gang Wang, Bernhard Urbaszek, Xavier Marie, and Scott A Crooker. Gate-controlled spin-valley locking of resident carriers in wse 2 monolayers. *Phys. Rev. Lett.*, 119(13):137401, 2017.

[234] Chenhao Jin, Jonghwan Kim, M Iqbal Bakti Utama, Emma C Regan, Hans Kleemann, Hui Cai, Yuxia Shen, Matthew James Shinner, Arjun Sengupta, Kenji Watanabe, et al. Imaging of pure spin-valley diffusion current in ws2-wse2 heterostructures. *Science*, 360(6391):893–896, 2018.

[235] E Kirstein, DR Yakovlev, MM Glazov, EA Zhukov, D Kudlacik, IV Kalitukha, VF Sapega, GS Dimitriev, MA Semina, MO Nestoklon, et al. The landé factors of electrons and holes in lead halide perovskites: universal dependence on the band gap. *Nat. Commun.*, 13(1):3062, 2022.

[236] Simone Strohmair, Amrita Dey, Yu Tong, Lakshminarayana Polavarapu, Bernhard J Bohn, and Jochen Feldmann. Spin polarization dynamics of free charge carriers in cspbi3 nanocrystals. *Nano Lett.*, 20(7):4724–4730, 2020.

[237] Carla Verdi and Feliciano Giustino. Fröhlich electron-phonon vertex from first principles. *Phys. Rev. Lett.*, 115(17):176401, 2015.

[238] Christian Multunas, Andrew Grieder, Junqing Xu, Yuan Ping, and Ravishankar

Sundararaman. Circular dichroism of crystals from first principles. *Phys. Rev. Mater.*, 7(12):123801, 2023.

[239] J. P. Perdew, K. Burke, and M. Ernzerhof. Generalized Gradient Approximation Made Simple. *Phys. Rev. Lett.*, 77(18):3865, 1996.

[240] Michel I Dyakonov and AV Khaetskii. *Spin physics in semiconductors*, volume 157. Springer, 2008.

[241] JM Kikkawa and DD Awschalom. Resonant spin amplification in n-type gaas. *Phys. Rev. Lett.*, 80(19):4313, 1998.

[242] B Andrei Bernevig, J Orenstein, and Shou-Cheng Zhang. Exact su (2) symmetry and persistent spin helix in a spin-orbit coupled system. *Phys. Rev. Lett.*, 97(23):236601, 2006.

[243] J D Koralek, C P Weber, J Orenstein, B A Bernevig, Shou-Cheng Zhang, S Mack, and D D Awschalom. Emergence of the persistent spin helix in semiconductor quantum wells. *Nature*, 458(7238):610–613, April 2009.

[244] Guy Fishman and Georges Lampel. Spin relaxation of photoelectrons in p-type gallium arsenide. *Phys. Rev. B*, 16(2):820, 1977.

[245] DS Smirnov, EA Zhukov, DR Yakovlev, E Kirstein, M Bayer, and A Greilich. Spin polarization recovery and hanle effect for charge carriers interacting with nuclear spins in semiconductors. *Phys. Rev. B*, 102(23):235413, 2020.

[246] M Syperek, DR Yakovlev, IA Yugova, J Misiewicz, IV Sedova, SV Sorokin, AA Toropov, SV Ivanov, and M Bayer. Long-lived electron spin coherence in cdse/zn (s, se) self-assembled quantum dots. *Phys. Rev. B*, 84(8):085304, 2011.

[247] IA Merkulov, Al L Efros, and M Rosen. Electron spin relaxation by nuclei in semiconductor quantum dots. *Phys. Rev. B*, 65(20):205309, 2002.

[248] Qi Qian, Zhong Wan, Hiroyuki Takenaka, Jong K Keum, Tyler J Smart, Laiyuan Wang, Peiqi Wang, Jingyuan Zhou, Huaying Ren, Dong Xu, et al. Photocarrier-induced persistent structural polarization in soft-lattice lead halide perovskites. *Nat. Nanotechnol.*, 18:357–364, 2023.

[249] Detlev M Hofmann, Albrecht Hofstaetter, Frank Leiter, Huijuan Zhou, Frank Henecker, Bruno K Meyer, Sergei B Orlinskii, Jan Schmidt, and Pavel G Baranov. Hydrogen: a relevant shallow donor in zinc oxide. *Phys. Rev. Lett.*, 88(4):045504, 2002.

[250] Kiyoshi Miyata, Daniele Meggiolaro, M Tuan Trinh, Prakriti P Joshi, Edoardo Mosconi, Skyler C Jones, Filippo De Angelis, and X-Y Zhu. Large polarons in lead halide perovskites. *Sci. Adv.*, 3(8):e1701217, 2017.

[251] Kyle T Munson, Eric R Kennehan, Grayson S Doucette, and John B Asbury. Dynamic disorder dominates delocalization, transport, and recombination in halide perovskites. *Chem*, 4(12):2826–2843, 2018.

[252] Pericles Philippopoulos, Stefano Chesi, and WA Coish. First-principles hyperfine

tensors for electrons and holes in gaas and silicon. *Phys. Rev. B*, 101(11):115302, 2020.

[253] R. Sundararaman, K. Letchworth-Weaver, K. A. Schwarz, D. Gunceler, Y. Ozhabes, and T. A. Arias. JDFTx: Software for Joint Density-Functional Theory. *SoftwareX*, 6:278–284, 2017.

[254] N. Marzari and D. Vanderbilt. Maximally Localized Generalized Wannier Functions for Composite Energy Bands. *Phys. Rev. B*, 56(20):12847, 1997.

[255] A. M. Brown, R. Sundararaman, P. Narang, W. A. Goddard, and H. A. Atwater. Nonradiative Plasmon Decay and Hot Carrier Dynamics: Effects of Phonons, Surfaces, and Geometry. *ACS Nano*, 10:957–966, 2016.

[256] A. Habib, R. Florio, and R. Sundararaman. Hot Carrier Dynamics in Plasmonic Transition Metal Nitrides. *J. Opt.*, 20:064001, 2018.

[257] Christopher J Ciccarino, Thomas Christensen, Ravishankar Sundararaman, and Prineha Narang. Dynamics and spin-valley locking effects in monolayer transition metal dichalcogenides. *Nano Lett.*, 18(9):5709–5715, 2018.

[258] ZG Yu. Effective-mass model and magneto-optical properties in hybrid perovskites. *Sci. Rep.*, 6(1):1–14, 2016.

[259] Mujtaba Hussain, Muhammad Rashid, Faisal Saeed, and AS Bhatti. Spin–orbit coupling effect on energy level splitting and band structure inversion in cspbbr3. *J. Mater. Sci.*, 56(1):528–542, 2021.

[260] Uyen N Huynh, Teddy Feng, Dipak Raj Khanal, Haoliang Liu, Paul Bailey, Rikard Bodin, Peter C Sercel, Jinsong Huang, and Z Valy Vardeny. Transient and steady state magneto-optical studies of the cspb br 3 crystal. *Phys. Rev. B*, 106(9):094306, 2022.

[261] Ying Lu, Qian Wang, Lei Han, Yuzhen Zhao, Zemin He, Wenqi Song, Cheng Song, and Zongcheng Miao. Spintronic phenomena and applications in hybrid organic–inorganic perovskites. *Adv. Funct. Mater.*, page 2314427, 2024.

[262] Samuel D Bader and Stuart Stephen Papworth Parkin. Spintronics. *Annu. Rev. Condens. Matter Phys.*, 1(1):71–88, 2010.

[263] Jiajia Chen, Kai Wu, Wei Hu, and Jinlong Yang. Tunable rashba spin splitting in two-dimensional polar perovskites. *J. Phys. Chem. Lett.*, 12(7):1932–1939, 2021.

[264] J Fabian and S Das Sarma. Spin Relaxation of Conduction Electrons in Polyvalent Metals: Theory and a Realistic Calculation. *Phys. Rev. Lett.*, 81(25):5624, 1998.

[265] Weng Hong Sio and Feliciano Giustino. Unified ab initio description of fröhlich electron-phonon interactions in two-dimensional and three-dimensional materials. *Phys. Rev. B*, 105(11):115414, 2022.

[266] K Matsuishi, T Ishihara, S Onari, YH Chang, and CH Park. Optical Properties and Structural Phase Transitions of Lead-Halide Based Inorganic–Organic 3D and 2D Perovskite Semiconductors Under High Pressure. *Phys. Stat. Sol. (b)*, 241(14):3328–3333, 2004.

[267] Martin Ledinský, Philipp Löper, Bjoern Niesen, Jakub Holovský, Soo-Jin Moon, Jun-Ho Yum, Stefaan De Wolf, Antonín Fejfar, and Christophe Ballif. Raman Spectroscopy of Organic–Inorganic Halide Perovskites. *J. Phys. Chem. Lett.*, 6(3):401–406, 2015.

[268] Artem A Bakulin, Oleg Selig, Huib J Bakker, Yves LA Rezus, Christian Muöller, Tobias Glaser, Robert Lovrincic, Zhenhua Sun, Zhuoying Chen, Aron Walsh, et al. Real-time observation of organic cation reorientation in methylammonium lead iodide perovskites. *J. Phys. Chem. Lett.*, 6(18):3663–3669, 2015.

[269] Thibaud Etienne, Edoardo Mosconi, and Filippo De Angelis. Dynamical origin of the rashba effect in organohalide lead perovskites: A key to suppressed carrier recombination in perovskite solar cells? *J. Phys. Chem. Lett.*, 7(9):1638–1645, 2016.

[270] Yuri D Glinka, Rui Cai, Junzi Li, Tingchao He, and Xiao Wei Sun. Observing Dynamic and Static Rashba Effects in a Thin Layer of 3D Hybrid Perovskite Nanocrystals Using Transient Absorption Spectroscopy. *AIP Adv.*, 10(10):105034, 2020.

[271] Martin Schlipf and Feliciano Giustino. Dynamic rashba-dresselhaus effect. *Phys. Rev. Lett.*, 127:237601, Dec 2021.

[272] Daniel Niesner, Martin Hauck, Shreetu Shrestha, Ievgen Levchuk, Gebhard J Matt, Andres Osvet, Miroslaw Batentschuk, Christoph Brabec, Heiko B Weber, and Thomas Fauster. Structural fluctuations cause spin-split states in tetragonal

(CH3NH3)PbI3 as evidenced by the circular photogalvanic effect. *Proceedings of the National Academy of Sciences*, 115(38):9509–9514, 2018.

[273] Maryam Sajedi, Maxim Krivenkov, Dmitry Marchenko, Andrei Varykhalov, Jaime Sánchez-Barriga, Emile DL Rienks, and Oliver Rader. Absence of a giant rashba effect in the valence band of lead halide perovskites. *Phys. Rev. B*, 102(8):081116, 2020.

[274] Han-Yue Zhang, Xiao-Gang Chen, Zhi-Xu Zhang, Xian-Jiang Song, Tie Zhang, Qiang Pan, Yi Zhang, and Ren-Gen Xiong. Methylphosphonium tin bromide: a 3d perovskite molecular ferroelectric semiconductor. *Adv. Mater.*, 32(47):2005213, 2020.

[275] Ravi Kashikar, PS Ghosh, S Lisenkov, BRK Nanda, and I Ponomareva. Chemically and electrically tunable spin polarization in ferroelectric cd-based hybrid organic-inorganic perovskites. *Phys. Rev. B*, 104(23):235132, 2021.

[276] Xue-Zeng Lu and James M Rondinelli. Strain engineering a persistent spin helix with infinite spin lifetime. *Phys. Rev. B*, 107(3):035155, 2023.

[277] Y Ohno, R Terauchi, T Adachi, F Matsukura, and H Ohno. Spin relaxation in gaas (110) quantum wells. *Phys. Rev. Lett.*, 83(20):4196, 1999.

[278] D. R. Hamann. Optimized Norm-Conserving Vanderbilt Pseudopotentials. *Phys. Rev. B*, 88(8):085117, 2013.

[279] Michiel J Van Setten, Matteo Giantomassi, Eric Bousquet, Matthieu J Verstraete,

Don R Hamann, Xavier Gonze, and G-M Rignanese. The PseudoDojo: Training and Grading a 85 Element Optimized Norm-Conserving Pseudopotential Table. *Comput. Phys. Commun.*, 226:39–54, 2018.

[280] IP Swainson, RP Hammond, C Soullière, O Knop, and W Massa. Phase transitions in the perovskite methylammonium lead bromide, ch3nd3pbbr3. *J. Solid State Chem.*, 176(1):97–104, 2003.

[281] Anatole Abragam and Brebis Bleaney. *Electron Paramagnetic Resonance of Transition Ions*. Oxford University Press, 2012.

[282] Giovanni Onida, Lucia Reining, and Angel Rubio. Electronic excitations: density-functional versus many-body green's-function approaches. *Reviews of modern physics*, 74(2):601, 2002.

[283] Giancarlo Strinati. Application of the green's functions method to the study of the optical properties of semiconductors. *La Rivista del Nuovo Cimento (1978-1999)*, 11(12):1–86, 1988.

[284] XZ Du, J Li, JY Lin, and HX Jiang. The Origin of Deep-Level Impurity Transitions in Hexagonal Boron Nitride. *Appl. Phys. Lett.*, 106(2):021110, 2015.

[285] Romain Bourrellier, Sophie Meuret, Anna Tararan, Odile Stéphan, Mathieu Kociak, Luiz HG Tizei, and Alberto Zobelli. Bright UV Single Photon Emission at Point Defects in h-BN. *Nano Lett.*, 16(7):4317–4321, 2016.

[286] Koh Era, Fujio Minami, and Takashi Kuzuba. Fast Luminescence from Carbon-Related Defects of Hexagonal Boron Nitride. *J. Lumin.*, 24:71–74, 1981.

[287] Alexander Vokhmintsev, Ilya Weinstein, and Dmitry Zamyatin. Electron-Phonon Interactions in Subband Excited Photoluminescence of Hexagonal Boron Nitride. *J. Lumin.*, 208:363–370, 2019.

[288] MG Silly, P Jaffrennou, J Barjon, J-S Lauret, F Ducastelle, A Loiseau, E Obraztsova, B Attal-Tretout, and E Rosencher. Luminescence Properties of Hexagonal Boron Nitride: Cathodoluminescence and Photoluminescence Spectroscopy Measurements. *Phys. Rev. B*, 75(8):085205, 2007.

[289] Natasha Tomm, Alisa Javadi, Nadia Olympia Antoniadis, Daniel Najer, Matthias Christian Löbl, Alexander Rolf Korsch, Rüdiger Schott, Sascha René Valentin, Andreas Dirk Wieck, Arne Ludwig, et al. A Bright and Fast Source of Coherent Single Photons. *Nat. Nanotechnol.*, pages 1–5, 2021.

[290] Mehdi Abdi, Jyh-Pin Chou, Adam Gali, and Martin B Plenio. Color Centers in Hexagonal Boron Nitride Monolayers: a Group Theory and Ab Initio Analysis. *ACS Photon.*, 5(5):1967–1976, 2018.

[291] Tri C Doan, Jing Li, JY Lin, and HX Jiang. Bandgap and Exciton Binding Energies of Hexagonal Boron Nitride Probed by Photocurrent excitation spectroscopy. *Appl. Phys. Lett.*, 109(12):122101, 2016.

[292] R Geick, CH Perry, and G Rupprecht. Normal Modes in Hexagonal Boron Nitride. *Phys. Rev.*, 146(2):543, 1966.

[293] Pratibha Dev. Fingerprinting Quantum Emitters in Hexagonal Boron Nitride Using Strain. *Phys. Rev. Res.*, 2(2):022050, 2020.

[294] Robin Camphausen, Loris Marini, Sherif Abdulkader Tawfik, Toan Trong Tran, Michael J Ford, and Stefano Palomba. Observation of Near-Infrared Sub-Poissonian Photon Emission in Hexagonal Boron Nitride at Room Temperature. *APL Photon.*, 5(7):076103, 2020.

[295] Yuan Ping, Dario Rocca, and Giulia Galli. Optical Properties of Tungsten Trioxide from First-Principles Calculations. *Phys. Rev. B*, 87:165203, Apr 2013.

[296] Yuan Ping, Dario Rocca, Deyu Lu, and Giulia Galli. Ab Initio Calculations of Absorption Spectra of Semiconducting Nanowires within Many-Body Perturbation Theory. *Phys. Rev. B*, 85:035316, Jan 2012.

[297] Sohrab Ismail-Beigi and TA Arias. New Algebraic Formulation of Density Functional Calculation. *Comput. Phys. Commun.*, 128(1-2):1–45, 2000.

[298] Tomás A Arias, MC Payne, and JD Joannopoulos. Ab Initio Molecular Dynamics: Analytically Continued Energy Functionals and Insights into Iterative Solutions. *Phys. Rev. Lett.*, 69(7):1077, 1992.

[299] Dan Wang and Ravishankar Sundararaman. Layer Dependence of Defect Charge

Transition Levels in Two-Dimensional Materials. *Phys. Rev. B*, 101(5):054103, 2020.

[300] Martin Schlipf and François Gygi. Optimization Algorithm for the Generation of ONCV Pseudopotentials. *Comput. Phys. Commun.*, 196:36–44, 2015.

[301] J. Towns, T. Cockerill, M. Dahan, I. Foster, K. Gaither, A. Grimshaw, V. Hazlewood, S. Lathrop, D. Lifka, G. D. Peterson, R. Roskies, J. R. Scott, and N. Wilkins-Diehr. XSEDE: Accelerating Scientific Discovery. *Comput. Sci. Eng.*, 16(5):62–74, Sept.-Oct. 2014.

[302] Yuan Ping, Dario Rocca, and Giulia Galli. Electronic Excitations in Light Absorbers for Photoelectrochemical Energy Conversion: First Principles Calculations Based on Many Body Perturbation Theory. *Chem. Soc. Rev.*, 42(6):2437–2469, 2013.

[303] Huy-Viet Nguyen, T Anh Pham, Dario Rocca, and Giulia Galli. Improving Accuracy and Efficiency of Calculations of Photoemission Spectra within the Many-Body Perturbation Theory. *Phys. Rev. B*, 85(8):081101, 2012.

[304] Hsiao-Yi Chen, Davide Sangalli, and Marco Bernardi. Exciton-Phonon Interaction and Relaxation Times from First Principles. *Phys. Rev. Lett.*, 125(10):107401, 2020.

[305] Chris G Van de Walle and Jörg Neugebauer. First-Principles Calculations for

Defects and Impurities: Applications to III-Nitrides. *J. Appl. Phys.*, 95(8):3851–3879, 2004.

[306] Hannu-Pekka Komsa, Natalia Berseneva, Arkady V. Krasheninnikov, and Risto M. Nieminen. Charged Point Defects in the Flatland: Accurate Formation Energy Calculations in Two-Dimensional Materials. *Phys. Rev. X*, 4:031044, Sep 2014.

[307] Dan Wang, Dong Han, Xian-Bin Li, Sheng-Yi Xie, Nian-Ke Chen, Wei Quan Tian, Damien West, Hong-Bo Sun, and S. B. Zhang. Determination of Formation and Ionization Energies of Charged Defects in Two-Dimensional Materials. *Phys. Rev. Lett.*, 114:196801, May 2015.

[308] MJ Rayson and PR Briddon. First Principles Method for the Calculation of Zero-Field Splitting Tensors in Periodic Systems. *Phys. Rev. B*, 77(3):035119, 2008.

[309] John Wertz. *Electron Spin Resonance: Elementary Theory and Practical Applications*. Springer Science & Business Media, 2012.

[310] C.J. Foot, D.P.C.J. Foot, and C.J.F. Foot. *Atomic Physics*. Oxford Master Series in Physics. OUP Oxford, 2005.

[311] Fedor Jelezko, T Gaebel, I Popa, A Gruber, and Jorg Wrachtrup. Observation of Coherent Oscillations in a Single Electron Spin. *Phys. Rev. Lett.*, 92(7):076401, 2004.

[312] Giacomo Mariani, Shuhei Nomoto, Satoshi Kashiwaya, and Shintaro Nomura.

System for the Remote Control and Imaging of MW Fields for Spin Manipulation in NV Centers in Diamond. *Sci. Rep.*, 10(1):1–10, 2020.

[313] Nathan Chejanovsky, Amlan Mukherjee, Jianpei Geng, Yu-Chen Chen, Youngwook Kim, Andrej Denisenko, Amit Finkler, Takashi Taniguchi, Kenji Watanabe, Durga Bhaktavatsala Rao Dasari, et al. Single-Spin Resonance in a van der Waals Embedded Paramagnetic Defect. *Nat. Mater.*, pages 1–6, 2021.

[314] Aharon Blank, Guy Shapiro, Ran Fischer, Paz London, and David Gershoni. Optically Detected Magnetic Resonance Imaging. *Appl. Phys. Lett.*, 106(3):034102, 2015.

[315] SangKook Choi, Manish Jain, and Steven G. Louie. Mechanism for optical initialization of spin in NV- center in diamond. *Phys. Rev. B*, 86(4):041202, 2012.

[316] Paul Delaney, James C. Greer, and J. Andreas Larsson. Spin-Polarization Mechanisms of the Nitrogen-Vacancy Center in Diamond. *Nano Lett.*, 10(2):610–614, 2010.

[317] A.C. Zyubin, A.M. Mebel, M. Hayashi, H.C. Chang, and S.H. Lin. Quantum Chemical Modeling of Photoadsorption Properties of the Nitrogen-Vacancy Point Defect in Diamond. *J. Comput. Chem.*, 30(1):119–131, 2009.

[318] Chih-Kai Lin, Yi-Hsieh Wang, Huan-Cheng Chang, and S.H. Lin. One- and Two-Photon Absorption Properties of Diamond Nitrogen-Vacancy Defect Centers: A Theoretical Study. *J. Chem. Phys.*, 129(12):124714, 2008.

[319] Gordon Davies. The Jahn-Teller Effect and Vibronic Coupling at Deep Levels in Diamond. *Rep. Prog. Phys.*, 44(7):787, 1981.

[320] Otfried Madelung. *Semiconductors: Group IV Elements and III-V Compounds.* Springer Science & Business Media, 2012.

[321] Ph Tamarat, NB Manson, JP Harrison, RL McMurtrie, A Nizovtsev, C Santori, RG Beausoleil, P Neumann, T Gaebel, F Jelezko, et al. Spin-Flip and Spin-Conserving Optical Transitions of the Nitrogen-Vacancy Centre in Diamond. *New J. Phys.*, 10(4):045004, 2008.

[322] Kai-Mei C Fu, Charles Santori, Paul E Barclay, Lachlan J Rogers, Neil B Manson, and Raymond G Beausoleil. Observation of the Dynamic Jahn-Teller Effect in the Excited States of Nitrogen-Vacancy Centers in Diamond. *Phys. Rev. Lett.*, 103(25):256404, 2009.

[323] Carlos L Benavides-Riveros, Nektarios N Lathiotakis, and Miguel AL Marques. Towards a Formal Definition of Static and Dynamic Electronic Correlations. *Phys. Chem. Chem. Phys.*, 19(20):12655–12664, 2017.

[324] Ph Tamarat, T Gaebel, JR Rabeau, M Khan, AD Greentree, H Wilson, LCL Hollenberg, S Prawer, P Hemmer, F Jelezko, et al. Stark Shift Control of Single Optical Centers in Diamond. *Phys. Rev. Lett.*, 97(8):083002, 2006.

[325] He Ma, Marco Govoni, and Giulia Galli. PyZFS: A Python Package for First-

Principles Calculations of Zero-Field Splitting Tensors. *J. Open Source Softw.*, 5(47):2160, 2020.

[326] Krishnendu Ghosh, He Ma, Mykyta Onizhuk, Vikram Gavini, and Giulia Galli. Spin–Spin Interactions in Defects in Solids from Mixed All-Electron and Pseudopotential First-Principles Calculations. *npj Comput. Mater.*, 7(1):123, 2021.

[327] Carlos Fiolhais, Fernando Nogueira, and Miguel AL Marques. *A Primer in Density Functional Theory*, volume 620. Springer Science & Business Media, 2003.

[328] Tian Lu and Feiwu Chen. Multiwfn: A Multifunctional Wavefunction Analyzer. *J. Comput. Chem.*, 33(5):580–592, 2012.

[329] Audrius Alkauskas, Matthew D McCluskey, and Chris G Van de Walle. Tutorial: Defects in Semiconductors—Combining Experiment and Theory. *J. Appl. Phys.*, 119(18), 2016.

[330] Andrei Faraon, Paul E Barclay, Charles Santori, Kai-Mei C Fu, and Raymond G Beausoleil. Resonant Enhancement of the Zero-Phonon Emission from a Colour Centre in a Diamond Cavity. *Nat. Photonics*, 5(5):301–305, 2011.

[331] Bi-Ching Shih, Yu Xue, Peihong Zhang, Marvin L Cohen, and Steven G Louie. Quasiparticle band gap of zno: High accuracy from the conventional g 0 w 0 approach. *Phys. Rev. Lett.*, 105(14):146401, 2010.

[332] J Katriel. Second quantization and the general two-centre harmonic oscillator integrals. *J. Phys. B: Atom. Molec. Opt. Phys.*, 3(10):1315, 1970.

[333] PJ Dean, EC Lightowlers, and DR Wight. Intrinsic and extrinsic recombination radiation from natural and synthetic aluminum-doped diamond. *Phys. Rev.*, 140(1A):A352, 1965.

[334] Dandan Zhang, Yiming Yang, Yehonadav Bekenstein, Yi Yu, Natalie A Gibson, Andrew B Wong, Samuel W Eaton, Nikolay Kornienko, Qiao Kong, Minliang Lai, et al. Synthesis of composition tunable and highly luminescent cesium lead halide nanowires through anion-exchange reactions. *J. Am. Chem. Soc.*, 138(23):7236–7239, 2016.

[335] Yizhi Zhu, Qiannan Cui, Jinping Chen, Feng Chen, Zengliang Shi, Xiangwei Zhao, and Chunxiang Xu. Inhomogeneous trap-state-mediated ultrafast photocarrier dynamics in cspbbr3 microplates. *ACS Appl. Mater. Interfaces*, 13(5):6820–6829, 2021.

[336] Brent A Koscher, Zachary Nett, and A Paul Alivisatos. The underlying chemical mechanism of selective chemical etching in cspbbr3 nanocrystals for reliably accessing near-unity emitters. *ACS Nano*, 13(10):11825–11833, 2019.

[337] Yihui He, Zhifu Liu, Kyle M McCall, Wenwen Lin, Duck Young Chung, Bruce W Wessels, and Mercouri G Kanatzidis. Perovskite cspbbr3 single crystal detector for alpha-particle spectroscopy. *Nucl. Instrum. Methods Phys. Res. A*, 922:217–221, 2019.

[338] Haotong Wei and Jinsong Huang. Halide lead perovskites for ionizing radiation detection. *Nat. Commun.*, 10(1):1066, 2019.

[339] Christian Wehrenfennig, Giles E Eperon, Michael B Johnston, Henry J Snaith, and Laura M Herz. High charge carrier mobilities and lifetimes in organolead trihalide perovskites. *Adv. Mater.*, 26(10):1584–1589, 2014.

[340] Jingying Wang, Chuang Zhang, Haoliang Liu, Ryan McLaughlin, Yaxin Zhai, Shai R Vardeny, Xiaojie Liu, Stephen McGill, Dmitry Semenov, Hangwen Guo, et al. Spin-optoelectronic devices based on hybrid organic-inorganic trihalide perovskites. *Nat. Commun.*, 10(1):129, 2019.

[341] Yulu Li, Xiao Luo, Yuan Liu, Xin Lu, and Kaifeng Wu. Size-and composition-dependent exciton spin relaxation in lead halide perovskite quantum dots. *ACS Energy Lett.*, 5(5):1701–1708, 2020.

[342] Tue Gunst, Troels Markussen, Kurt Stokbro, and Mads Brandbyge. First-principles method for electron-phonon coupling and electron mobility: Applications to two-dimensional materials. *Phys. Rev. B*, 93(3):035414, 2016.

[343] Gerald D. Mahan. *Many-Particle Physics*. Springer US, 2000.

[344] Paolo Giannozzi, Stefano Baroni, Nicola Bonini, Matteo Calandra, Roberto Car, Carlo Cavazzoni, Davide Ceresoli, Guido L Chiarotti, Matteo Cococcioni, Ismaila Dabo, et al. Quantum espresso: a modular and open-source software project for quantum simulations of materials. *J. Phys. Condens. Matter*, 21(39):395502, 2009.

[345] Ravishankar Sundararaman and Yuan Ping. First-principles electrostatic po-

tentials for reliable alignment at interfaces and defects. *J. Chem. Phys.*, 146(10):104109, 2017.

[346] Xavier Gonze and Changyol Lee. Dynamical matrices, born effective charges, dielectric permittivity tensors, and interatomic force constants from density-functional perturbation theory. *Phys. Rev. B*, 55(16):10355, 1997.

[347] Tomasz Woźniak, Paulo E Faria Junior, Gotthard Seifert, Andrey Chaves, and Jens Kunstmann. Exciton g factors of van der waals heterostructures from first-principles calculations. *Phys. Rev. B*, 101(23):235408, 2020.

[348] Thorsten Deilmann, Peter Krüger, and Michael Rohlfing. Ab initio studies of exciton g factors: Monolayer transition metal dichalcogenides in magnetic fields. *Phys. Rev. Lett.*, 124(22):226402, 2020.

[349] Fengyuan Xuan and Su Ying Quek. Valley zeeman effect and landau levels in two-dimensional transition metal dichalcogenides. *Phys. Rev. Research*, 2(3):033256, 2020.

[350] AA Mitioglu, Krzysztof Galkowski, Alessandro Surrente, L Klopotowski, D Dumcenco, A Kis, Duncan Kennedy Maude, and Paulina Plochocka. Magnetoexcitons in large area cvd-grown monolayer mos 2 and mose 2 on sapphire. *Phys. Rev. B*, 93(16):165412, 2016.

[351] Eberhard Engel and Seymour H Vosko. Exact exchange-only potentials and the

virial relation as microscopic criteria for generalized gradient approximations. *Phys. Rev. B*, 47(20):13164, 1993.

[352] Jianwei Sun, Adrienn Ruzsinszky, and John P Perdew. Strongly constrained and appropriately normed semilocal density functional. *Phys. Rev. Lett.*, 115(3):036402, 2015.

[353] Samuel Poncé, Wenbin Li, Sven Reichardt, and Feliciano Giustino. First-principles calculations of charge carrier mobility and conductivity in bulk semiconductors and two-dimensional materials. *Rep. Prog. Phys.*, 83(3):036501, 2020.

[354] Rep Kubo. The fluctuation-dissipation theorem. *Rep. Prog. Phys.*, 29(1):255, 1966.

[355] Pedro Borlido, Jonathan Schmidt, Ahmad W Huran, Fabien Tran, Miguel AL Marques, and Silvana Botti. Exchange-correlation functionals for band gaps of solids: benchmark, reparametrization and machine learning. *Npj Comput. Mater.*, 6(1):1–17, 2020.

[356] Michele Puppin, Serhii Polishchuk, Nicola Colonna, Alberto Crepaldi, DN Dirin, Olga Nazarenko, Riccardo De Gennaro, Gianmarco Gatti, Silvan Roth, Thomas Barillot, et al. Evidence of large polarons in photoemission band mapping of the perovskite semiconductor cspbbr 3. *Phys. Rev. Lett.*, 124(20):206402, 2020.

[357] T Paul, BK Chatterjee, S Maiti, S Sarkar, N Besra, BK Das, KJ Panigrahi, S Thakur, UK Ghorai, and KK Chattopadhyay. Tunable cathodoluminescence

over the entire visible window from all-inorganic perovskite cspbx 3 1d architecture. *J. Mater. Chem. C*, 6(13):3322–3333, 2018.

[358] AA Sirenko, VI Belitsky, T Ruf, M Cardona, AI Ekimov, and C Trallero-Giner. Spin-Flip and Acoustic-Phonon Raman Scattering in CdS Nanocrystals. *Phys. Rev. B*, 58(4):2077, 1998.

[359] Claudio Grimaldi and Peter Fulde. Theory of Screening of the Phonon-Modulated Spin-Orbit Interaction in Metals. *Phys. Rev. B*, 55(23):15523, 1997.

[360] Christian Illg, Michael Haag, and Manfred Fähnle. Ultrafast Demagnetization After Laser Irradiation in Transition Metals: Ab Initio Calculations of the Spin-Flip Electron-Phonon Scattering with Reduced Exchange Splitting. *Phys. Rev. B*, 88(21):214404, 2013.

[361] Miguel A Pérez-Osorio, Rebecca L Milot, Marina R Filip, Jay B Patel, Laura M Herz, Michael B Johnston, and Feliciano Giustino. Vibrational Properties of the Organic–Inorganic Halide Perovskite CH3NH3PbI3 from Theory and Experiment: Factor Group Analysis, First-Principles Calculations, and Low-Temperature Infrared Spectra. *J. Phys. Chem. C*, 119(46):25703–25718, 2015.

[362] Kousuke Nakada, Yuki Matsumoto, Yukihiro Shimoi, Koji Yamada, and Yukio Furukawa. Temperature-Dependent Evolution of Raman Spectra of Methylammonium Lead Halide Perovskites, CH3NH3PbX3 (X= I, Br). *Molecules*, 24(3):626, 2019.

[363] Michael Sendner, Pabitra K Nayak, David A Egger, Sebastian Beck, Christian Müller, Bernd Epding, Wolfgang Kowalsky, Leeor Kronik, Henry J Snaith, Annemarie Pucci, et al. Optical Phonons in Methylammonium Lead Halide Perovskites and Implications for Charge Transport. *Mater. Horiz.*, 3(6):613–620, 2016.

[364] Florian Knoop, Nina Shulumba, Aloïs Castellano, José Pedro Alvarinhas Batista, Roberta Farris, Matthieu J Verstraete, Matthew Heine, David Broido, Dennis S Kim, Johan Klarbring, et al. Tdep: Temperature dependent effective potentials. *J. Open Source Softw.*, 9(94), 2024.

[365] Olle Hellman, Peter Steneteg, Igor A Abrikosov, and Sergei I Simak. Temperature dependent effective potential method for accurate free energy calculations of solids. *Phys. Rev. B Condens. Matter.*, 87(10):104111, 2013.

[366] Nina Shulumba, Olle Hellman, and Austin J Minnich. Intrinsic localized mode and low thermal conductivity of pbse. *Phys. Rev. B*, 95(1):014302, 2017.

[367] Georg Kresse and Jürgen Furthmüller. Efficient iterative schemes for ab initio total-energy calculations using a plane-wave basis set. *Phys. Rev. B*, 54(16):11169, 1996.

[368] Peter E Blöchl. Projector augmented-wave method. *Phys. Rev. B*, 50(24):17953, 1994.

[369] André TJB Eppink and DH Parker. Energy partitioning following photodissocia-

tion of methyl iodide in the a band: A velocity mapping study. *J. Chem. Phys.*, 110(2):832–844, 1999.